Geofluids

Hydro-Mechanical Behaviors of Rock Fractures and Fracture Networks 2021

Lead Guest Editor: Richeng Liu
Guest Editors: Bo Li and Na Huang

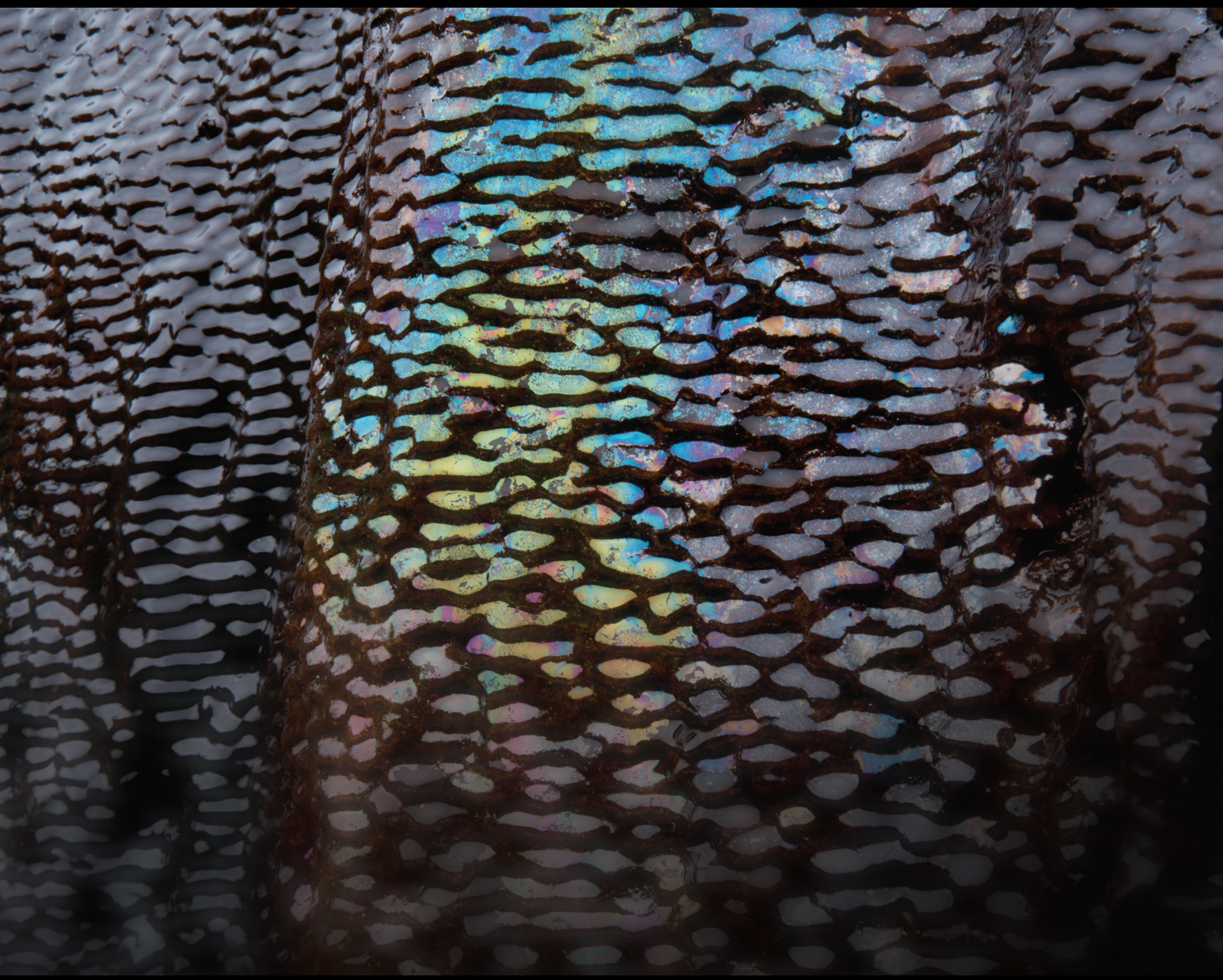

Hydro-Mechanical Behaviors of Rock Fractures and Fracture Networks 2021

Geofluids

Hydro-Mechanical Behaviors of Rock Fractures and Fracture Networks 2021

Lead Guest Editor: Richeng Liu
Guest Editors: Bo Li and Na Huang

Chief Editor

Associate Editors

Academic Editors

Contents

Study on Deformation and Fracture Evolution of Underground Reservoir Coal Pillar Dam under Different Mining Conditions
Liu Xuesheng, Song Shilin, Wu Baoyang, Li Xuebin, and Yang Kang
Research Article (11 pages), Article ID 2186698, Volume 2022 (2022)

Rock Deformation Estimated by Groundwater-Level Monitoring: A Case Study at the Xianshuihe Fault, China
Yuqing Zhao, You-Kuan Zhang, Xiuyu Liang, Zheming Shi, Yonglin Yang, and Feifei Li
Research Article (14 pages), Article ID 8011733, Volume 2022 (2022)

Numerical Simulation and Field Measurement Analysis of Fracture Evolution and Seepage Response of Key Aquiclude Strata in Backfill Mining
Qiang Sun, Yong Chen, Jianli Huang, Dan Ma, Cunli Zhu, and Yue Liu
Research Article (12 pages), Article ID 8416485, Volume 2021 (2021)

Dynamic Mechanical Properties and Damage Mechanism of Freeze-Thaw Sandstone under Acid Corrosion
Xiaoxiao Cao, Meimei Feng, and Kangsheng Yuan
Research Article (15 pages), Article ID 7335284, Volume 2021 (2021)

A Study of Millisecond Blasting on High Bench at Barun Iron Ore Operation
Pengfei Zhang, Runcai Bai, Xue Sun, Haoran Li, Honglu Fei, and Shijie Bao
Research Article (13 pages), Article ID 3645438, Volume 2021 (2021)

Experimental Study of the Water-Sediment Two-Phase Seepage Characteristics in Rock Fractures and the Influencing Factors
Kui Di, Ming Li, Xianbiao Mao, Zhanqing Chen, Lianying Zhang, and Yu Han
Research Article (14 pages), Article ID 9808238, Volume 2021 (2021)

Analytical Solution for the Deformation and Support Parameters of Coal Roadway in Layered Roof Strata
Kai Wang, Bao-gui Yang, Zhong-kui Wang, and Xiao-long Wang
Research Article (9 pages), Article ID 6669234, Volume 2021 (2021)

Study on the Mechanical Behavior and Acoustic Emission Properties of Granite under Triaxial Compression
Jiaqi Guo, Pengfei Liu, Junqi Fan, and Hengyuan Zhang
Research Article (17 pages), Article ID 3954097, Volume 2021 (2021)

Mechanical Behavior of Frozen Porous Sandstone under Uniaxial Compression
Hong-Ying Wang and Qiang Zhang
Research Article (6 pages), Article ID 1872065, Volume 2021 (2021)

Influence of Clay on Solute Transport in Saturated Homogeneous Mixed Media
Albert Kwame Kwaw, Zhi Dou, Jinguo Wang, Yuting Zhang, Xueyi Zhang, Wenyuan Zhu, and Portia Annabelle Opoku
Research Article (14 pages), Article ID 1207971, Volume 2021 (2021)

Exploring the Effect of Asperity Order on Mechanical Character of Joint Specimen from the Perspective of Damage
Zhouhao Yuan, Yicheng Ye, and Binyu Luo
Research Article (17 pages), Article ID 4901231, Volume 2021 (2021)

Hindawi
Geofluids
Volume 2022, Article ID 2186698, 11 pages
https://doi.org/10.1155/2022/2186698

Research Article

Study on Deformation and Fracture Evolution of Underground Reservoir Coal Pillar Dam under Different Mining Conditions

Liu Xuesheng,[1,2] **Song Shilin**,[2] **Wu Baoyang**,[1] **Li Xuebin**,[2] **and Yang Kang**[2,3]

[1]*State Key Laboratory of Water Resources Protection and Utilization in Coal Mining, National Energy Investment Group, Co., Ltd, Beijing 100013, China*
[2]*College of Energy and Mining Engineering, Shandong University of Science and Technology, Shandong, Qingdao 266590, China*
[3]*Yushuwan Coal Mine of Yushen Coal Co., Ltd, China*

Correspondence should be addressed to Song Shilin; shilinsong1995@163.com and Li Xuebin; xuebin9311@163.com

Received 15 September 2021; Accepted 14 March 2022; Published 30 March 2022

Academic Editor: Richeng Liu

Coal mine underground reservoir water storage technology is an effective technical way to achieve high efficiency of coal mining and protection of water resources. The stability of coal pillar dam plays a decisive role in the safe and stable operation of underground reservoirs. Mining of adjacent working faces and long-term water erosion are the main influencing factors of stability of coal pillar dam. In this paper, a fluid-solid coupling calculation model for the deformation and evolution of coal pillar dam was established by FLAC3D numerical simulation software and the underground brine reservoir of Lingxin Coal Mine of Shenning group as an engineering background. The paper studied systematically the deformation, failure, and stress evolution of the dam with coal pillars soaked in water for a long time under different working face inclining length, coal pillar width, mining height, and water pressure. The simulation results showed that the degree of deformation and failure of the coal pillar dam continued to increase with the continuous advancement of the working face. The plastic zone of the coal pillar dam was increased by approximately 23.53%, the maximum vertical stress was increased by approximately 95.78%, and the maximum vertical deformation was increased by approximately 68.18%. The influence of each factor on the deformation and failure of overburden strata is quite different. The development range of plastic zone, the maximum vertical stress, and the maximum vertical deformation were increasing with the increased of working face inclined length and mining height. The increasing width of coal pillar would lead to the decrease of maximum vertical stress. The increase of water pressure would lead to the decrease of maximum vertical deformation. It can be seen that the inclined length of the working face is the main factor affecting the deformation and failure of the coal pillar dam. Coal pillar width and mining height are the main factors affecting the development of plastic zone. This study reveals the law of deformation and fracture evolution of coal pillar dam under different mining conditions, which can provide a reference for the design of coal pillar dam of coal mine underground reservoir.

1. Introduction

A major problem in green mining of China is the protection and utilization of water resources, especially in western regions such as Inner Mongolia, Shanxi, Shaanxi, Ningxia, and Xinjiang. The proven coal resources in these regions account for about 80% of the country's total reserves. However, due to its location in the arid-semiarid zone of China, water resources have become the dominant factor restricting coal mining and ecological protection in these regions [1–9]. Therefore, in order to reduce the loss of water resources caused by mining, Gu and others propose to store water by using underground goaf, by connecting the safety coal pillars at the borders of the goaf with artificial dams to form underground storage reservoirs. This technology plays a key role in many fields, such as preventing and controlling water disasters, reducing surface losses, and ensuring the stability of roadways. It is an effective way to solve the protection

Columnar lithology	Thickness (m)	Lithology description
Coarse sandstone	18.0	Light gray, gray-green, the main components are feldspar, quartz
Siltstone and fine sand interbed	10.0	Grayish green and grayish green with purple spots
Coarse sandstone	2.0	Light gray, gray-green, the main components are feldspar, quartz
Siltstone and fine sand interbed	11.0	Grayish green and grayish green with purple spots
Mudstone	7.0	Gray green, brown red and others
Siltstone and fine sand interbed	17.5	Gray-green, purple-grey, brown-gray thick layer to massive fine grain, siltstone
Mudstone	4.5	Gray green, brown red and others
Coarse sandstone	3.0	Light gray, gray-green, the main components are feldspar, quartz
Mudstone	4.5	Gray green, brown red and others
14# coal seam	2.5	The thickness is 2.2~2.9 m, can be mined in the whole mine field
Siltstone and fine sand interbed	20.0	Gray-green, purple-grey, brown-gray thick layer to massive fine grain, siltstone

Figure 1: Geological histogram.

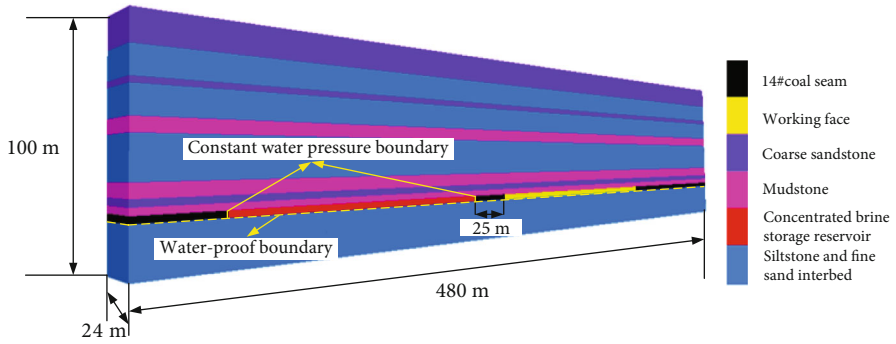

Figure 2: FLAC3D model diagram.

and utilization of water resources in ecologically fragile areas in the west [10–15].

The coal safety pillars at the boundary of the goaf play an important part of the reservoir dams, and its stability directly determines the normal operation of the underground water reservoir. The stability of coal pillar dam is essentially the deformation and failure of the dam under the influence of overburden pressure, water pressure, and coal mining [16–22]. And scholars at home and abroad have achieved many research results about this. Gu et al. [23] explored the destruction form of coal pillar dams through similar simulation tests under dynamic loading conditions and proposed the safety factor of coal pillar dams in underground water reservoirs. Zhang [24] analyzed the safety for the dam of the groundwater reservoir by establishing a mathematical model for dam safety analysis. Through numerical simulation research, Yao et al. [25] found that the water content, buried depth, and coal seam mining thickness all have a great influence on the width of the coal pillar dam. Bai et al. [26] found that under the influence of water storage pressure in goaf and the pressure of the overlying strata, the bottom of the outer surface and the top of the inner surface of the artificial dam were prone to instability and damage, and instability in other locations was less likely. Wang et al. [27] found that the development area and depth of the plastic zone of coal pillar surrounding rock increased significantly under the dynamic load, and the vertical stress extreme point developed in the depth direction. Most of the above studies are aimed at the stability of coal pillar dam under the effect of overburden pressure and water pressure, and there is still insufficient research on the influence of mining on adjacent working faces. If the law of

deformation and fracture evolution of coal pillar dam under different mining conditions can be grasped and by combining with the research results of the influence of overburden pressure and water pressure, so the correlative design of coal pillar dam can be carried out in order to achieve the best effect.

In this paper, FLAC3D fluid structure coupling calculation model is established based on the engineering background of underground concentrated brine reservoir in Lingxin Coal Mine of Shenning group. The laws of deformation, fracture, and stress evolution of coal pillar dam under different mining conditions are studied. This study provides a reference for the design of coal pillar dam of underground reservoir.

2. Engineering Geological Conditions

Lingxin Coal Mine is located in Ciyaobao Town, Lingwu City, Ningxia Hui Autonomous Region. It is a key construction project of the "Eighth Five-year Plan" of China, with a designed production capacity of 3.2 million tons per year. It is the main production mine of Shenning Company. In order to save water resources and reduce water pollution, Lingxin Coal Mine constructed a high-mineralization mine water quality and utilization treatment station underground in the first mining area. The purpose is to recycle 85% of Lingxin coal mine water and permanently store 15% of concentrated brine in underground goaf. To this end, Lingxin Coal Mine built an underground water reservoir in the north wing of the first mining area to store concentrated brine. The water level of the reservoir is +1050 m to +1145 m, and the head pressure is 0.9842 MPa. Because the location of the brine storage is affected by the mining and water pressure of the adjacent working face all the year round, the requirements for the coal pillar dam are also relatively high.

The main coal seam in the first mining area is 14# coal, which is located at the level of +1050 m underground, and the mining ended in 2008. The average thickness of 14# coal is 2.8 m. The thickness of the coal seam is simple in structure, with a bedded structure and the lower coal quality hardness. The immediate roof is mudstone, and the upper part and the floor are fine sand and rock interbedded. The specific histogram is shown in Figure 1. In the first mining area, the strike length of working face is 1040.8 m, the inclined length is 180~200 m, and the width of protective coal pillar between working faces is 25 m.

3. Numerical Simulation

3.1. Model Building. According to the geological profile of 14# coal in Lingxin Coal Mine, the abovementioned concentrated brine storage reservoir was used as the research prototype, and a three-dimensional numerical model was established by using the finite difference software FLAC3D. The model is shown in Figure 2, and the size is determined to be length × width × height = 480 m × 24 m × 100 m. A total of 351,5000 grids and 3682710 nodes are divided. The physical and mechanical properties of each strata are set according to reference [28].

Table 1: Simulation scheme of orthogonal experiment.

Test	Length of working face/m	Width of coal pillar/m	Mining height/m	Water pressure/MPa
1	100	20	1.5	0.5
2	100	25	2	1
3	100	30	2.5	1.5
4	100	35	3	2
5	150	20	2	1.5
6	150	25	1.5	2
7	150	30	3	0.5
8	150	35	2.5	1
9	200	20	2.5	2
10	200	25	3	1.5
11	200	30	1.5	1
12	200	35	2	0.5
13	250	20	3	1
14	250	25	2.5	0.5
15	250	30	2	2
16	250	35	1.5	1.5

Set an 80 m area on the left and right sides of the model to reduce the boundary effect. Model boundary conditions: (1) mechanical boundary, the X direction of the model constrains the left and right boundary displacements, the Y direction constrains the front and rear boundary displacements, and the Z direction constrains the lower boundary displacements. The fix command is used to control the model boundary velocity, and the upper boundary of the model is imposed with a self-weight stress of 5.35 MPa in the overlying strata. (2) Seepage boundary conditions, the bottom plate of the reservoir is the water-proof boundary, and the two sides are the boundary of constant water pressure, and a certain water pressure is applied here according to the experimental design.

The Mohr-Coulomb yield criterion is used to judge the deformation and fracture evolution of coal pillar dam under different mining conditions.

3.2. Design of Orthogonal Experiment Simulation Scheme. Orthogonal experiment method is a design method to study multifactor and multilevel. It can select some representative level combinations to test and analyze the results to find the optimal level combination.

The stability of the coal pillar dam is often affected by coal mining. Considering that there is a working face on the side of the reservoir and the coal pillar dam is immersed in water for a long time, therefore, the influencing factors of the stability of the coal pillar dam are selected as the inclined length and the mining height of the adjacent working face, the width of the coal pillar dam, and the water pressure exerted on the coal pillar dam. According to the actual geological and production conditions, the above four factors take 4 levels, the permeability coefficient of the coal pillar is 1.36×10^{-6}, the working face is simulated by step mining,

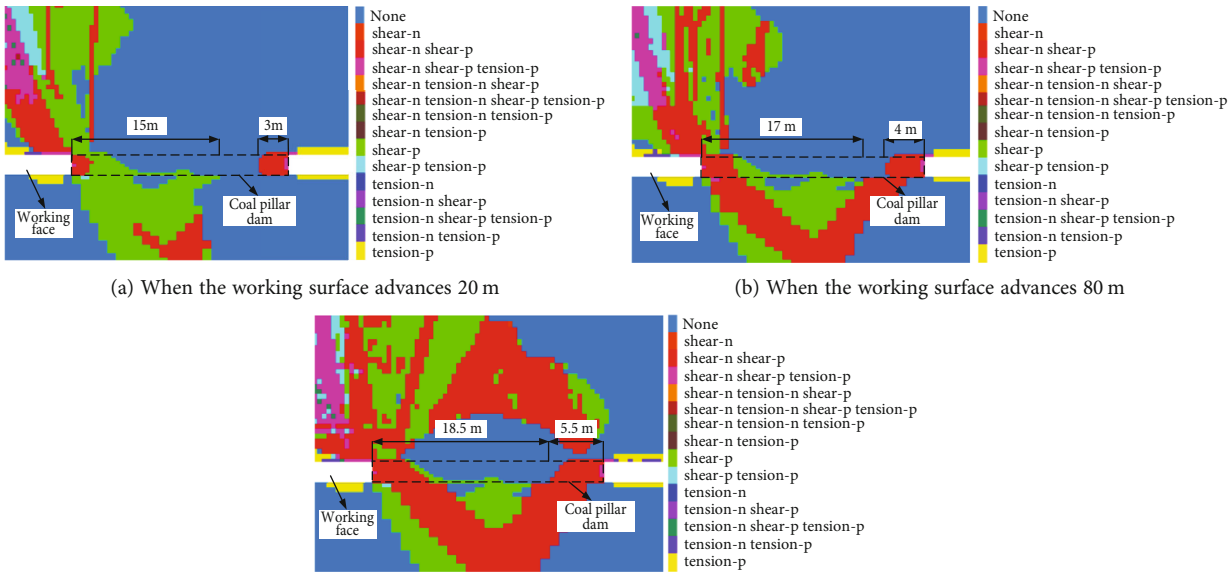

(a) When the working surface advances 20 m

(b) When the working surface advances 80 m

(c) When the working surface advances 180 m

Figure 3: Cloud diagram of plastic zone change during mining.

the orthogonal test has a total of 4 factors, and each factor has 4 levels. Regardless of the interaction between factors, the $L16$ (4^4) orthogonal Tab. is selected, and the test indicators are the development height of the plastic zone, maximum vertical stress, and maximum vertical deformation of the coal pillar dam, and the test scheme under different parameter combinations is numerically simulated. The orthogonal experiment simulation scheme is shown in Table 1.

4. Analysis of Simulation Results

4.1. Evolution of Deformation and Fracture of Coal Pillar Dam during Mining. In the simulation calculation, the step excavation method is adopted to mine the working face. The experiment 14 is used as an example to analyze the law of deformation and fracture evolution of the coal pillar dam. The plastic zone distribution cloud map, vertical stress cloud map, and vertical deformation cloud map of some excavation stages are as shown in Figures 3–5.

It can be seen from Figure 3 that when the face is pushed 20 m, the coal pillar face is slightly damaged, there is a plastic zone of about 3 m, and the top and floor of the face are also partially damaged; when the face is pushed 80 m, the plastic zone on the working face side of the coal pillar dam continues to develop into the interior of the coal pillar dam. The plastic zone in the lower part of the dam is connected with the reservoir side, and the plastic zone appears in the side wall angle of the coal pillars of the working face and continues to extend deeper; the roof damage range is further expanded; when the working face is pushed 180 m away, the plastic zone in the coal pillar dam is further expanded, and the plastic zone above the coal pillar dam is combined with the plastic zone on the side of the working face. During the mining process, with the advancement of the working face, the horizontal development range of the plastic zone on the reservoir side continues to increase. It can also be seen from the figure that the failure mode of the coal pillar dam is mainly shear failure, and the horizontal development range of the plastic zone in the coal pillar dam has expanded by about 23.53%.

It can be seen from Figure 4 that as the working face continues to push, the maximum vertical stress in the coal pillar dam continues to increase. When the working face is pushed 20 m, the maximum vertical stress in the coal pillar dam is 27.73 MPa, the maximum vertical stress is mainly distributed on the reservoir side, and the side of working face is slightly distributed; when the working face is pushed 80 m, the maximum vertical stress is 34.04 MPa. The maximum vertical stress is mainly distributed on the working face side, but less on the reservoir side. When the working face is pushed 180 m, the maximum vertical stress is 25.14 MPa, and the maximum vertical stress on the side of the working face is further increased. The working face is pushed from 20 m to the end of mining, and the maximum vertical stress is increased by about 95.78%.

It can be seen from Figure 5 that when the working face is pushed 20 m, the maximum vertical deformation of the coal pillar dam is about 0.66 m; when the working face is advanced by 80 m, the maximum vertical deformation of the coal pillar dam is about 0.84 m. When the working face is pushed 180 m, the maximum vertical deformation of coal pillar dam is about 1.03 m. The working face was pushed from 20 m to the end of mining, and the maximum vertical deformation increased by about 68.18%.

4.2. Influence of Various Factors on Deformation and Fracture of Coal Pillar Dam. The simulation is carried out according to the experimental design, and the development range of the plastic zone, vertical stress, and vertical deformation inside the coal pillar dam under different mining conditions were obtained, respectively. In some of the

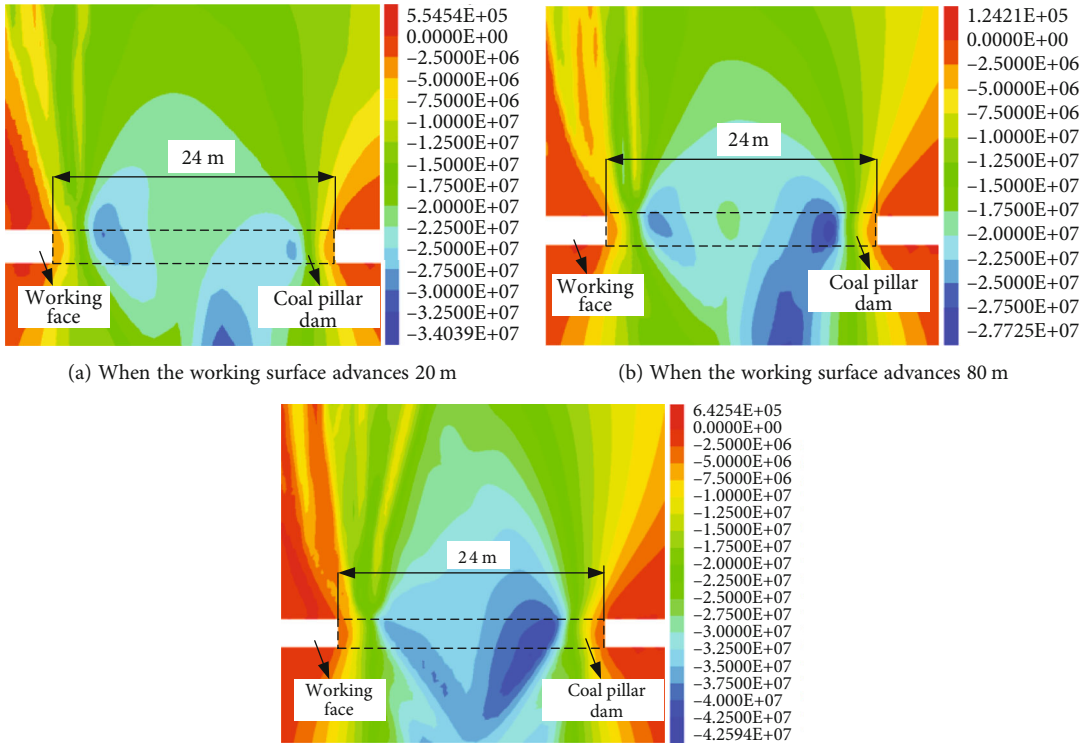

(a) When the working surface advances 20 m

(b) When the working surface advances 80 m

(c) When the working surface advances 180 m

Figure 4: Stress cloud diagram during mining.

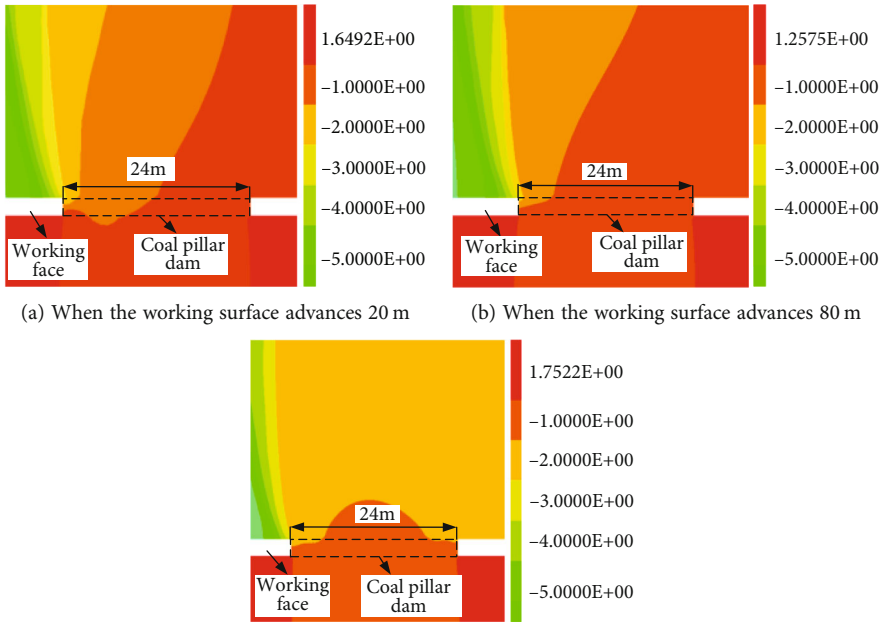

(a) When the working surface advances 20 m

(b) When the working surface advances 80 m

(c) When the working surface advances 180 m

Figure 5: Deformation cloud diagram during mining.

simulation results, the distribution cloud map of the plastic zone, stress distribution cloud map, and deformation distribution cloud map of coal pillar dam are shown in Figures 6–8, respectively. The simulation results are shown in Table 2.

It can be seen from Figures 6–8 that under different mining conditions, the development range and height of the plastic zone on the reservoir side of the coal pillar dam are larger than the working face side, and the horizontal

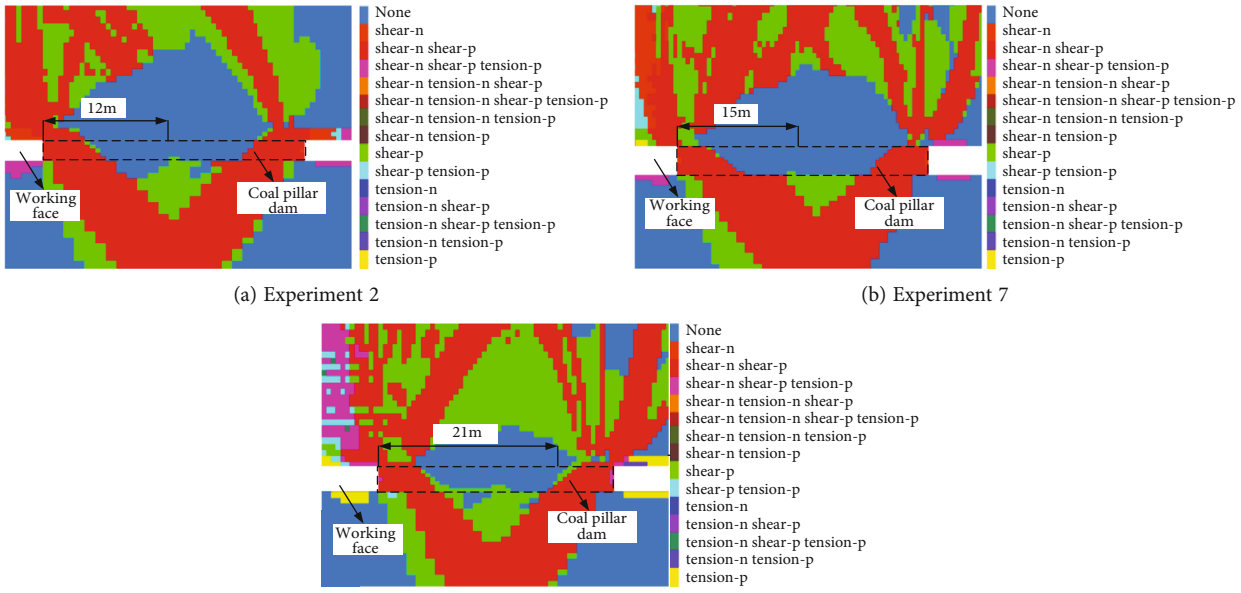

(a) Experiment 2

(b) Experiment 7

(c) Experiment 14

Figure 6: Plastic zone cloud diagram of partial coal pillar dams.

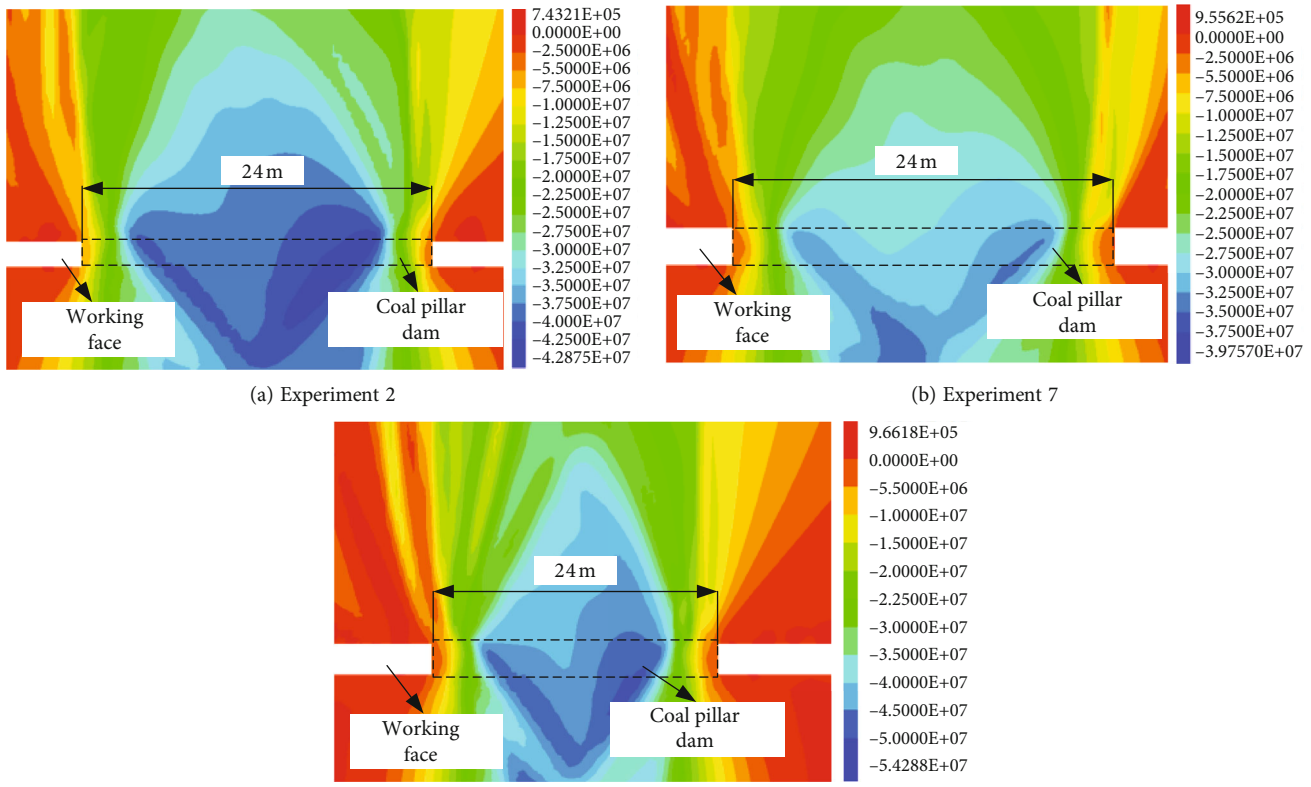

(a) Experiment 2

(b) Experiment 7

(c) Experiment 14

Figure 7: Vertical stress cloud diagram of partial coal pillar dams.

development depth of the plastic zone on the reservoir side is greater about 2~3 m than that on the working face side; the stress concentration area of the coal pillar dam is approximately symmetrically distributed, but the maximum vertical stress is mostly distributed on the working face side; the deformation of the coal pillar dam is divided into upper and lower parts, and the upper deformation is significantly larger than the lower deformation.

By further analyzing the simulation results, the average value of the development height of the plastic zone, the

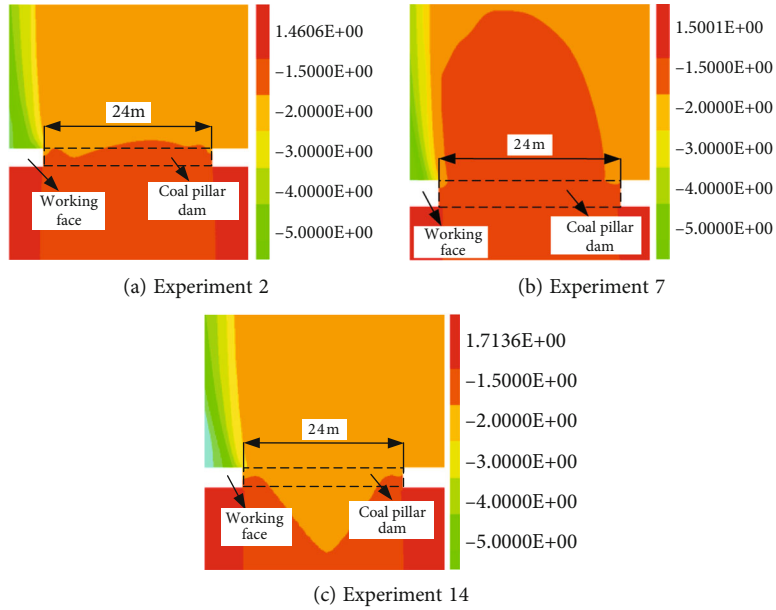

(a) Experiment 2

(b) Experiment 7

(c) Experiment 14

Figure 8: Vertical deformation cloud diagram of partial coal pillar.

Table 2: Simulation results.

Test	Development range of the plastic zone/m	Maximum vertical stress/MPa	Vertical deformation/m
1	11.0	45.57	0.63
2	12.0	39.76	0.61
3	15.0	38.21	0.54
4	12.5	36.24	0.53
5	13.5	51.67	0.81
6	12.5	43.06	0.75
7	15.0	42.88	0.82
8	19.0	43.56	0.78
9	18.0	51.16	0.80
10	14.5	53.30	0.72
11	13.5	46.11	1.23
12	16.5	43.61	1.20
13	16.5	58.87	1.05
14	21.0	54.29	1.11
15	19.0	48.93	0.98
16	21.5	41.75	1.25

maximum vertical stress, and the maximum vertical deformation in the coal pillar dam with different levels under the same mining conditions are calculated. The calculation results are shown in Tables 3–5, respectively.

It can be seen from the Tab. that when the inclined length of the working face increases from 100 m to 250 m, the horizontal development range of the plastic zone in the coal pillar dam gradually increases from 12.38 m to 19.50 m, the maximum vertical stress gradually increases from 39.95 MPa to 50.96 MPa, and vertical deformation increases from 0.58 m to 1.07 m. When the width of the coal pillar dam increases from 20 m to 35 m, the horizontal development range of the plastic zone gradually increases from 14.75 m to 17.13 mm, the maximum vertical stress increases from 51.82 MPa to 41.29 MPa, and the vertical deformation increases from 0.77 m to 0.94 m. When the mining height increases from 1.5 m to 3 m, the development height of the plastic zone increases from 14.38 m to 18.25 m and finally reduces to 20.96 m; the maximum vertical stress increases from 44.12 MPa to 47.82 MPa, and the vertical deformation increases from 0.70 m gradually increases to 0.96 m. When the water pressure increases from 0.5 MPa to 2 MPa, the development height of the plastic zone gradually increases from 15.25 m to 16.13 m, the maximum vertical stress increases from 44.85 MPa to 47.08 MPa, and the vertical deformation decreases from 0.92 m to 0.77 m and finally increases to 1.57 m.

In order to more intuitively observe the influence of various factors on the deformation and fracture of the coal pillar dam, the average results in Tables 2–4 were fitted with the horizontal number to obtain the average result trend chart of each factor under different horizontal combinations as shown in Figure 9.

It can be found that different factors have different degrees of influence on the horizontal development range of the coal pillar dam plastic zone, but the effect is the same, and with the increase of inclined length of working face, width of coal pillar, mining height, and water pressure, the horizontal development range of plastic zone of coal pillar dam also increases. Different factors have different effects on the maximum vertical stress inside the coal pillar dam. With the increase of the inclined length of working face, mining height, and water pressure, the maximum vertical stress in the coal pillar dam also increases, and as the width of the coal pillar increases, the maximum vertical stress in the coal pillar dam gradually decreases. This is because the

Table 3: Orthogonal experiment range analysis Tab. (plastic zone development height).

Factor	Length of working face/m	Width of coal pillar/m	Mining height/m	Water pressure/MPa
Average results of the first level	12.38	14.75	14.38	15.25
Average results of the second level	15.00	15.00	14.63	15.50
Average results of the third level	15.63	15.63	15.25	15.88
Average results of the fourth level	19.50	17.13	18.25	16.13
Range	7.13	2.38	3.88	0.88

Table 4: Orthogonal experiment range analysis Tab. (maximum vertical stress).

Factor	Length of working face/m	Width of coal pillar/m	Mining height/m	Water pressure/MPa
Average results of the first level	39.95	51.82	44.12	44.85
Average results of the second level	45.29	47.60	45.99	46.23
Average results of the third level	48.55	44.03	46.81	46.59
Average results of the fourth level	50.96	41.29	47.82	47.08
Range	11.02	10.53	3.70	2.23

Table 5: Orthogonal experiment range analysis Tab. (maximum vertical deformation).

Factor	Length of working face/m	Width of coal pillar/m	Mining height/m	Water pressure/MPa
Average results of the first level	0.58	0.77	0.70	0.92
Average results of the second level	0.79	0.82	0.78	0.91
Average results of the third level	0.99	0.89	0.90	0.83
Average results of the fourth level	1.07	0.94	0.96	0.77
Range	0.50	0.17	0.26	0.15

wider the coal pillar is, the better the roof integrity is, the pressure it bears will be reduced, and the stress concentration in the coal pillar will be reduced accordingly. Different factors have different effects on the vertical deformation of the coal pillar dam. With the increase of the inclined length of working face, coal pillar width, and mining height, the vertical deformation of the coal pillar dam gradually increases, and with the increase of water pressure, the vertical deformation of the coal pillar dam gradually decreases, and this is because under the action of the horizontal water pressure, a certain horizontal deformation will occur in the coal pillar, which offsets a part of the vertical deformation, so that the vertical deformation in the coal pillar gradually decreases.

4.3. Significance Analysis of Different Influencing Factors. Perform a range analysis on the orthogonal test results, and calculate the range based on the average of the index results corresponding to each factor and level obtained in Tables 2–4. The calculation results are shown in Tables 2–4.

It can be seen from Table 2 that the range of the four factors by calculating that influence the development height of the plastic zone in the coal pillar dam are 7.13, 2.38, 3.88, and 0.88, respectively, and the sensitivity of the parameters from large to small is the inclined length of working face, mining height, the width of coal pillar, and water pressure. Due to the large range of indicators corresponding to the inclined length of working face, mining height, and the width of pillar, it can be judged that the inclined length of the working face, the mining height, and the width of the coal pillar are the main factors affecting the development of the plastic zone of the coal pillar dam. While the range of the corresponding index of water pressure is relatively small, it can be considered that water pressure is a secondary factor affecting the development of the plastic zone of coal pillar dam.

It can be seen from Table 3 that the range of the four factors by calculating that influence the maximum vertical stress of the coal pillar dam is 11.02, 10.53, 3.70, and 2.23, respectively, and the sensitivity of the parameters from large to small is the inclined length of working face, the width of coal pillar, mining height, and water pressure. Due to the large range of indicators corresponding to the inclined length of working face and the width of pillar, it can be judged that the inclined length of the working face is the main factor affecting the maximum vertical stress of the coal pillar dam. While the range of the corresponding index of mining height and water pressure is relatively small, it can be considered that mining height and water pressure are the secondary factors affecting the maximum vertical stress of the coal pillar dam.

It can be seen from Table 4 that the range of the four factors by calculating that influence the vertical deformation of the coal pillar dam is 0.50, 0.26, 0.17, and 0.15, respectively, and the sensitivity of the parameters from large to small is the inclined length of working face, mining height, the width of coal pillar, and water pressure. Due to the large range of indicators corresponding to the inclined length of working

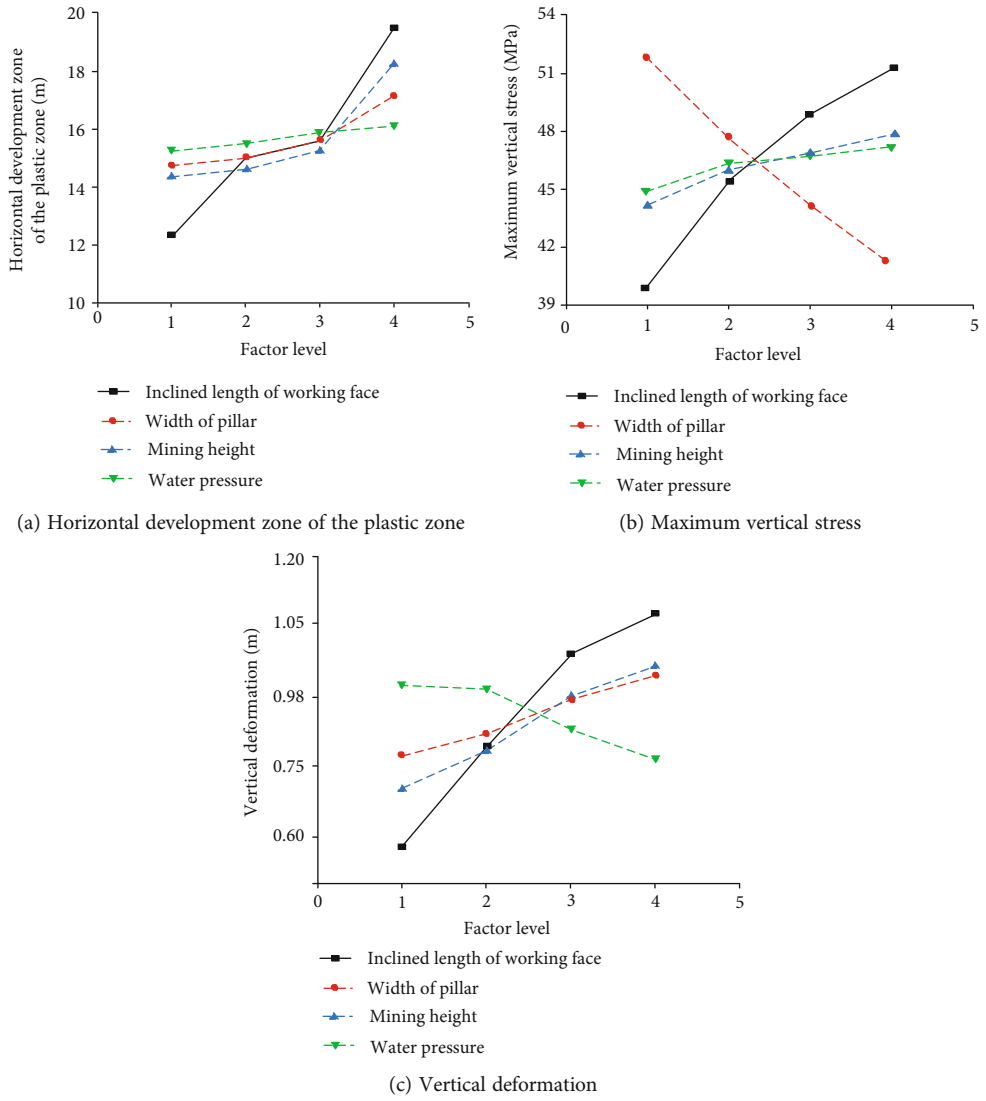

(a) Horizontal development zone of the plastic zone

(b) Maximum vertical stress

(c) Vertical deformation

Figure 9: Trend chart of average results under different levels of factors.

face and the mining height, it can be judged that the inclined length of the working face and mining height are the main factors affecting the vertical deformation of the coal pillar dam. While the range of the corresponding index of the width of coal pillar and water pressure is relatively small, it can be considered that the width of coal pillar and water pressure are the secondary factors affecting the vertical deformation of the coal pillar dam.

According to the comprehensive range analysis, the range of the three indicators corresponding to the inclined length of the working face is the largest, and it is larger than the range obtained by the other three factors. Therefore, it can be judged that the inclined length of the working face is the main factor affecting deformation and fracture of coal pillar dam, and the width of coal pillar, mining height, and water pressure are the secondary factors affecting deformation and fracture of coal pillar dam.

5. Conclusions

In this study, the fluid-solid coupling calculation model of coal pillar dam affected by mining is established. The long-term immersion of water in coal pillar dam is taken into account. Then, through systematic analysis of the law of deformation and fracture evolution and stress distribution of coal pillar dam under different mining conditions, the main conclusions are as follows:

(1) The development range and degree of plastic zone, the maximum principal stress, and deformation of coal pillar dam increase with the mining process are affected by the mining of adjacent working face. The horizontal development range of plastic zone increases by 23.53%, the maximum vertical stress increases by 95.78%, and the maximum vertical deformation increases by 68.18%. The advance of

working face has the greatest influence on the maximum vertical stress in coal pillar dam and the smallest influence on the horizontal development range of plastic zone

(2) The width of coal pillar, inclined length of working face, mining height, and water pressure all have great influence on the deformation and failure of coal pillar dam. The horizontal development range, the maximum vertical stress, and the maximum vertical deformation of the plastic zone increase continuously with the increase of the inclined length of the working face. The height of plastic zone and the maximum vertical deformation gradually increase, and the maximum vertical stress gradually decreases with the increase of coal pillar width. The horizontal development range, the maximum vertical stress, and the maximum vertical deformation of plastic zone are increasing with the increase of mining height. The horizontal development range and the maximum vertical stress of plastic zone increase, and the maximum vertical deformation decreases gradually with the increase of water pressure

(3) The influence of the different factors on the deformation and failure of coal pillar dam is different. Through the analysis of the range of the simulation results, it is found that the inclined length of the working face is the main factor affecting the development of the plastic zone of the coal pillar dam, the width of the coal pillar, and the mining height. The inclined length of working face and the width of coal pillar are the main factors affecting the maximum vertical stress of coal pillar dam. The inclined length and mining height of working face are the main factors affecting the maximum vertical deformation of coal pillar dam

Data Availability

The data used to support the findings of this study are available from the corresponding author upon request.

Conflicts of Interest

The authors declare that there are no conflicts of interest regarding the publication of this paper.

Acknowledgments

This work is supported by the Open Fund of State Key Laboratory of Water Resource Protection and Utilization in Coal Mining (No. GJNY-18-73.5), the National Natural Science Foundation of China (Nos. 52174122 and 51874190), and the Climbing Project of Taishan Scholar in Shandong Province (No. tspd20210313).

References

[1] Q. Minggao, "On sustainable coal mining in China," *Journal of China Coal Society*, vol. 35, no. 4, pp. 529–534, 2010.

[2] X. S. Liu, Y. L. Tan, J. G. Ning, Y. W. Lu, and Q. H. Gu, "Mechanical properties and damage constitutive model of coal in coal-rock combined body," *International Journal of Rock Mechanics and Mining Sciences*, vol. 110, pp. 140–150, 2018.

[3] S. Song, X. Liu, Y. Tan, D. Fan, Q. Ma, and H. Wang, "Study on failure modes and energy evolution of coal–rock combination under cyclic loading," *Shock and Vibration*, vol. 2020, 16 pages, 2020.

[4] H. Qingxiang, "Research on roof control of water conservation mining in shallow seam," *Journal of China Coal Society*, vol. 42, no. 1, pp. 50–55, 2017.

[5] F. Limin, M. Xiongde, and J. Ruijun, "Progress in engineering practice of water-preserved coal mining in western eco-environment frangible area," *Journal of China Coal Society*, vol. 40, no. 8, pp. 1711–1717, 2015.

[6] G. Yongxia, Z. Zhongning, and L. Yimin, "Research on resource utilization of mine water in goaf," *Coal Science and Technology*, vol. 35, no. 4, pp. 94–96, 2007.

[7] S. Liu, J. Bai, X. Wang, B. Wu, and W. Wu, "Mechanisms of floor heave in roadways adjacent to a goaf caused by the fracturing of a competent roof and controlling technology," *Shock and Vibration*, vol. 2020, 17 pages, 2020.

[8] X. Liu, D. Fan, Y. Tan et al., "Failure evolution and instability mechanism of surrounding rock for close-distance parallel chambers with super-large section in deep coal mines," *International Journal of Geomechanics*, vol. 21, no. 5, article 04021049, 2021.

[9] R. Liu, H. Jing, X. Li, Q. Yin, Z. Xu, and M. He, "An experimental study on fractal pore size distribution and hydro-mechanical properties of granites after high temperature treatment," *Fractals*, vol. 29, no. 4, p. 2150083, 2021.

[10] G. Dazhao, "Theory framework and technological system of coal mine underground reservoir," *Journal of China Coal Society*, vol. 40, no. 2, pp. 239–246, 2015.

[11] X. Li, X. Liu, Y. Tan, Q. Ma, B. Wu, and H. Wang, "Creep constitutive model and numerical realization of coal-rock combination deteriorated by immersion," *Minerals*, vol. 12, no. 3, p. 292, 2022.

[12] G. Dazhao, Z. Yong, and C. Zhiguo, "Technical progress of water resource protection and utilization by coal mining in China," *Coal Science and Technology*, vol. 44, no. 1, pp. 1–7, 2016.

[13] C. Zhiguo, H. Ruimin, and W. Xingfeng, "Coal mining affected to underground water and underground water storage and utilization technology," *Coal Science and Technology*, vol. 42, no. 12, pp. 113–116, 2014.

[14] X. Liu, S. Song, Y. Tan et al., "Similar simulation study on the deformation and failure of surrounding rock of a large section chamber group under dynamic loading," *International Journal of Mining Science and Technology*, vol. 31, no. 3, pp. 495–505, 2021.

[15] X. Liu, D. Fan, Y. Tan et al., "New detecting method on the connecting fractured zone above the coal face and a case study," *Rock Mechanics and Rock Engineering*, vol. 54, no. 8, pp. 4379–4391, 2021.

[16] X. Jinhai, M. Xiexing, and Z. Xiaochun, "Analysis of the time-dependence of the coal pillar stability," *Journal of China Coal Society*, vol. 29, no. 4, pp. 433–437, 2005.

[17] T. Shihao, B. Qingsheng, and T. Hongsheng, "Pillar size determination and panel layout optimization for fully mechanized faces in shallow seams," *Journal of Mining & Safety Engineering*, vol. 28, no. 4, pp. 505–510, 2011.

[18] J. Jinquan and S. Zhenqi, "Study on working face floor activities and its impact on water-inrush," *Journal of Shandong Institute of Mining*, vol. 4, pp. 1–11, 1987.

[19] Q. L. Yao, T. Chen, X. H. Li, and A. Wang, "Experimental study on coarsely water - bearing sandstone in roof of Jurassic coal seam," *Journal of China Coal Society*, vol. 42, no. 1, pp. 183–188, 2017.

[20] D. Y. Fan, X. S. Liu, Y. L. Tan, S. L. Song, J. G. Ning, and Q. Ma, "Numerical simulation research on response characteristics of surrounding rock for deep super-large section chamber under dynamic and static combined loading condition," *Journal of Central South University*, vol. 27, no. 12, pp. 3544–3566, 2020.

[21] D. Fan, X. Liu, Y. Tan et al., "Roof cutting parameters design for gob-side entry in deep coal mine: a case study," *Energies*, vol. 12, no. 10, p. 2032, 2019.

[22] R. Liu, C. Wang, B. Li, Y. Jiang, and H. Jing, "Modeling linear and nonlinear fluid flow through sheared rough-walled joints taking into account boundary stiffness," *Computers and Geotechnics*, vol. 120, article 103452, 2020.

[23] D. Z. Gu, Y. G. Yan, Y. Zhang, E. Z. Wang, and Z. G. Cao, "Experimental study and numerical simulation for dynamic response of coal pillars in coal mine underground reservoir," *Journal of China Coal Society*, vol. 41, no. 7, pp. 1589–1597, 2016.

[24] Z. Guoen, "Safety analysis of artificial blocking dam in underground coal mine reservoir," *China Coal*, vol. S1, pp. 78–81, 2014.

[25] Q. L. Yao, Q. Hao, X. Y. Chen, B. J. Zhou, and J. Fang, "Design on the width of coal pillar dam in coal mine groundwater reservoir," *Journal of China Coal Society*, vol. 44, no. 3, pp. 890–898, 2019.

[26] D. Y. Bai, J. F. Ju, J. L. Xu, and J. H. Li, "Stability analysis of mine underground reservoir artificial dam in Lijiahao Mine," *Journal of China Coal Society*, vol. 42, no. 7, pp. 1839–1845, 2017.

[27] F. Wang, N. Liang, G. Li, and B. Zhao, "Failure evolution mechanism of coal pillar dams in complex stress environment," *Journal of Mining & Safety Engineering*, vol. 36, no. 6, pp. 1145–1152, 2019.

[28] Z. Xiaowu, C. Xin, and L. Zhen, "Numerical simulation study of the development height of water flowing fracture zone in Lingxin Coal Mine," *Exploration Engineering (Rock & Soil Drilling and Tunneling)*, vol. 46, no. 7, pp. 64–69, 2019.

Hindawi
Geofluids
Volume 2022, Article ID 8011733, 14 pages
https://doi.org/10.1155/2022/8011733

Research Article

Rock Deformation Estimated by Groundwater-Level Monitoring: A Case Study at the Xianshuihe Fault, China

Yuqing Zhao,[1,2,3] **You-Kuan Zhang**,[4] **Xiuyu Liang**,[4] **Zheming Shi**,[5] **Yonglin Yang**,[6] **and Feifei Li**[6]

[1]*College of Environmental Science and Engineering, Guilin University of Technology, Guilin 541004, China*
[2]*Guangxi Key Laboratory of Environmental Pollution Control Theory and Technology, Guilin University of Technology, Guilin 541004, China*
[3]*Collaborative Innovation Center for Water Pollution Control and Water Safety in Karst Area, Guilin University of Technology, Guilin 541004, China*
[4]*School of Environmental Science and Engineering, Southern University of Science and Technology, Shenzhen 518055, China*
[5]*School of Water Resources and Environment, China University of Geoscience, Beijing 100083, China*
[6]*Survey Engineering Institute, Sichuan Earthquake Administration, Yaan 625099, China*

Correspondence should be addressed to Yuqing Zhao; 2020163@glut.edu.cn and You-Kuan Zhang; zhangyk@sustech.edu.cn

Received 8 September 2021; Accepted 20 December 2021; Published 10 March 2022

Academic Editor: Na Huang

Rock deformations induced by active faults is an important topic in earthquake studies. Such deformations are usually measured with crossfault measurements (CFM), which are time-consuming and labor-intensive. In this study, rock deformations induced by the famous Xianshuihe fault in Xialatuo of China were estimated by groundwater-level monitoring (GLM) and CFM for the period of January 1, 2016 to December 31, 2018. The pattern of the variations in areal strain estimated with GLM matches that from CFM well. The estimated strain by the GLM and CFM both changed from positive to negative with time, indicating that the fault plane switched from tensile to compressive. This indicates that the rate of rock deformation had slowed down during this period, which is consistent with the long-term creep rates obtained by CFM at the site, implying that the fault may have gradually entered the next relock state. The estimated strain changes using the GLM method lag slightly behind those of CFM, which is probably due to the diffusive effects of pore pressure propagation that is caused by the rock deformation under the crustal stress. This study demonstrates that GLM is a more convenient and efficient addition to traditional geophysical techniques and raises the possibility for the characterization of continuous rock deformations. The method may be used to obtain the changing regional strain field with a network of monitoring wells.

1. Introduction

Estimation of rock deformation and ground movement induced by active faults is an important task in earthquake studies [1–5]. Several techniques, e.g., satellite- and ground-based methods, are commonly used in the measurement of the ground displacement at the regional and local scales. Different measurement methods generally have different accuracies and resolutions. As a satellite-based method, GPS observation has been widely used in previous regional deformation and/or ground movement studies [1, 6–12]. GPS data can be used to analyze plate movement with a measurement accuracy of 10^{-8} and regional deformations with a measurement accuracy of 10^{-9} [2, 4]. GPS data can be further used to analyze the creep movement of faults, with its accuracy reaching 10^{-10} [2, 4]. The measurement accuracy is determined by the density of the GPS monitoring stations. The cost of building a GPS network is relatively high, especially in southwestern China where topography varies dramatically. Consequently, there are fewer GPS observation stations in this region than in other regions [13, 14]. Therefore, it is

difficult to accurately estimate local rock deformation and crustal movement based on the sparseness of the GPS stations in the southwestern region of China.

As a ground-based method, crossfault measurements (CFM) are usually carried out with conventional baseline and leveling arrays, alignment arrays, and trilateration networks to provide highly accurate observations for fault movement in the vertical, orthogonal, and oblique directions [15]. CFMs are reliable for measuring surface deformation and have been widely adopted to monitor fault activity [3, 5, 16–18]. The accuracy of this method is 10^{-4}–10^{-5} m, and the frequency of measurements can be daily to monthly [3, 19]. However, this method is time-consuming and labor-intensive and thus may not be an appropriate method for the analysis of active faults in remote areas, especially if frequent measurements are needed.

The changes in groundwater level, temperature, and chemical composition caused by the crustal movements, which reflect the interaction between tectonic activities and hydrological systems [20–37]. Such changes can be captured and observed by the physical and chemical parameters monitoring in the groundwater wells. Groundwater-level monitoring (GLM) can be used to obtain rock deformations, and the accuracy of the strain estimated with GLM can be as high as 10^{-9}–10^{-11} [21, 22], higher than the GPS and CFM methods mentioned above. Groundwater level oscillations in the deep well, responding to a pressure disturbance, can be caused by the earth tide dilatation of the aquifer [25, 28–30, 38, 39]. Responses of groundwater level to earth tides reflect the pore pressure changes that are closely related to the changes in crustal stress. Groundwater level monitoring (GLM) in the fault provides a way to obtain the changes of the rock properties in response to the fault activity and other tectonic movements [32, 33]. The hydraulic properties of fault zones responding to the pore pressure development are closely related to the fault stability [40–42]. Well water level responses to earth tides provide an effective method to monitor continuously in site properties of fault zone [2, 29, 33, 36, 43]. Previous research [44, 45] studied the tectonic stress field of north China using groundwater levels in deep wells while there is other data to prove the results. Despite a rich observation history of groundwater level changes in rock deformation, little is known regarding the temporal variations of groundwater level tidal response in rock deformation in regions with active faults [25]; furthermore, less is known whether the estimated deformation from the groundwater level tidal response is accordant with that obtained by traditional geophysical measurements, such as GPS or CFM, mainly because of the high costs of drilling and instrumenting geophysical facilities.

In short, the groundwater level tidal response might serve as an additional and economic method of characterizing the variations in rock deformation in remote areas where geophysical facilities are rare and continuous measurements are needed. As is well known, these different measurement methods have different accuracies and resolutions. Do the temporal variations of rock deformation estimated with GLM match those measured continuously by CFM in a region with an active fault? This question can be answered at a site where both GLM and CFM are available. The field site at the active Xianshuihe fault (XF) zone in southwest China, built in Xialatuo in 2015 and chosen for this study, is such a site. The rock deformation induced by the active fault was estimated by GLM and compared with that measured by CFM at the site. The results show that the pattern of the variations in the areal strain estimated with GLM matches well with that obtained by CFM. This demonstrates that GLM is a more convenient and economic method of estimating rock deformation with observed groundwater levels than CFM. The GLM method may be used to obtain the changing regional rock deformations and crustal movements with a network of monitoring wells. In the following, the field site and data collected are described first; then, the methodology and results and discussion are presented, and finally, some conclusions are drawn.

2. Field Site and Data Collection

2.1. Field Site. The field site is located in Xialatuo in the eastern Tibetan Plateau. This area belongs to the subhumid climate zone of the Qinghai-Tibet Plateau (Figure 1(a)). The annual average temperature and annual precipitation are 7.4°C and 572.5 mm, respectively. The site is situated in Xialatuo Basin, which is a pull-apart basin formed by the left-lateral strike-slip movements of the XF (red lines in Figure 1(b)). The XF is one of the most tectonically active intracontinental faults in China, and more than 20 earthquakes ($M > 6.5$) have occurred along this fault since 1700 [41]. Xialatuo Basin is located in the northwest XF, which strikes NNW-SSE and dips NE at approximately 85°, surrounded by a high mountainous region (Figures 1(b) and 1(e)). The formations in the XF region range from Neoproterozoic to Cenozoic, whereas Cretaceous and Jurassic formations are absent owing to the uplift and denudation that occurred in this region [46]. The formation outcropping in the Xialatuo is mainly Triassic, and some Permian formations also occur. Granite is mainly formed during the Himalayan tectonic movement. The study area is mainly covered by Quaternary sediments, which are underlain by the fractured slate rock of the Triassic, according to the well log at borehole ZK01 (Figure 1(c)).

2.2. Crossfault Measurements. In this study, CFMs of the XF (Figure 1(d)) are constructed by baseline and leveling measurements based on trilateral and quadrilateral networks, which provide an accurate accounting of the deformation in the area. A closed quadrilateral network of four stations labeled *D*, *E*, *F*, and *G* (Figure 1(d)) across the XF was built in December 2015 for the performance of ground deformation measurements. These stations form a measured network that includes six baselines and four leveling lines (white lines in Figure 1(d)). The baseline measurements of the changes in distance among the stations can be indicated by six baselines as in Figure 1(d) (white lines), in which lines EF and DG are orthogonal to the XF, lines DF and EG are oblique to the XF, and lines DE and FG are parallel to the XF. Baselines measurements conducted by Leica TM 50 Monitoring Station with a distance accuracy of 0.6 mm + 1

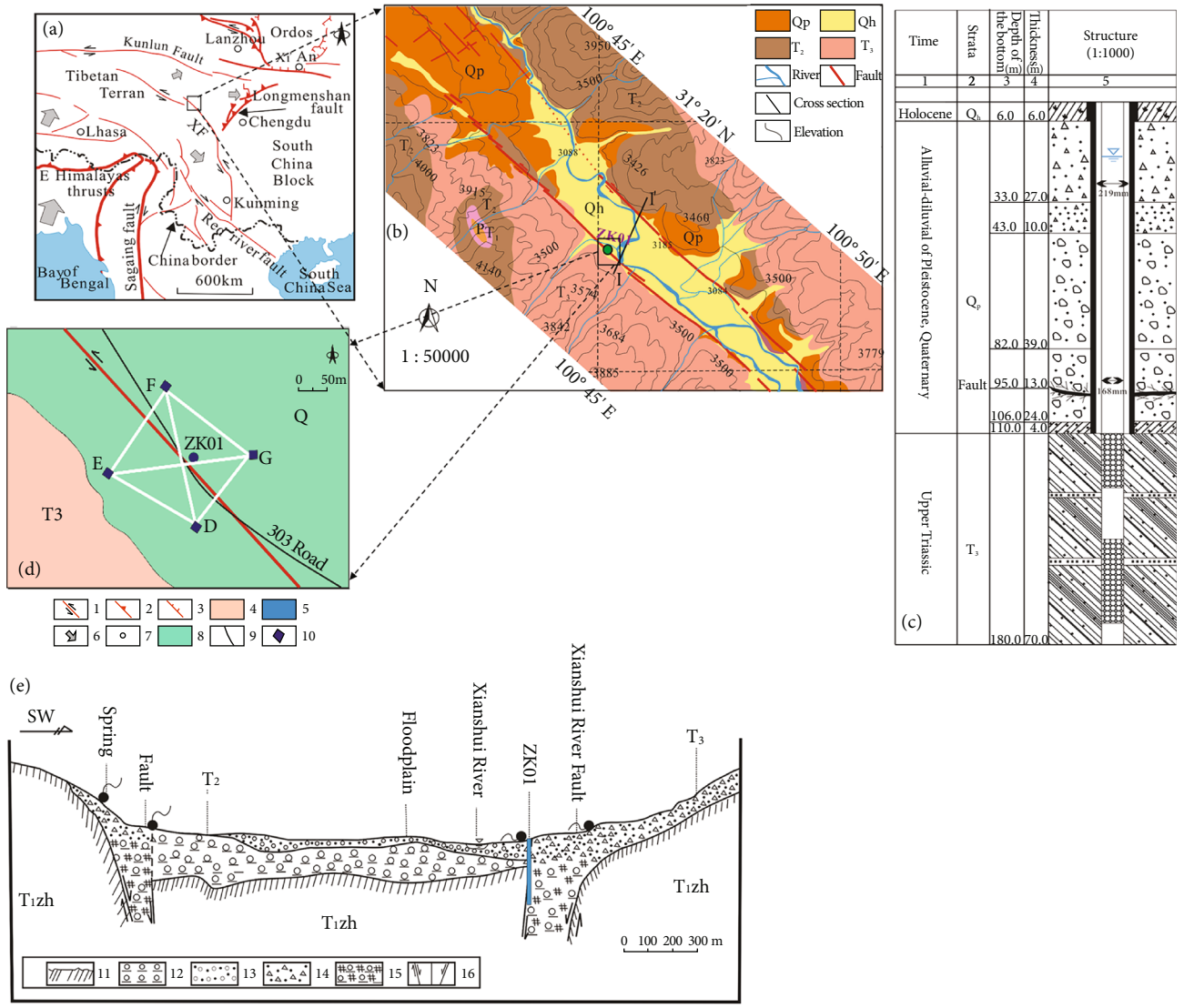

FIGURE 1: (a) Location of the study area (modified from Zhang [5]), (b) hydrogeological map of the study area (Q_h and Q_p represent the quaternary, P is the Permian, and T_1, T_2, and T_3 represent the Lower, Middle, and Upper layers of Triassic, respectively), (c) the simplified diagram about the lithology of ZK01, (d) ZK01, and the site of the crossfault measurements of XF ((1) strike-slip fault; (2) reverse fault and its dip direction; (3) normal fault and its dip direction; (4) Upper Triassic; (5) sea; (6) plate/block movement relative to Eurasia Plate; (7) town; (8) quaternary sediment; (9) road; and (10) D, E, F, and G are the crossfault geodetic measuring stations), and (e) the cross-section map of I-I′ in Figure 1(b) ((11) Upper Triassic, (12) Middle Triassic, (13) alluvium of the Upper Pleistocene–Holecene, (14) Lower Triassic, (15) bedrock fractured zone, and (16) fault) (modified from Zhang [47]).

ppm (Leica Geosystems) are used to measure the horizontal displacements of the XF. Leveling measurements conducted by Leica DNA03 Digital Level Surveying with a distance accuracy of 0.3 mm (Leica Geosystems) are carried out to quantify the vertical displacement of the XF. Note that both F and G are located on the hanging wall block of the XF, while both D and E are located on the footwall block.

Leveling measurements among the four stations (D, E, F, and G) were conducted daily from January 1, 2016 to December 31, 2018. The elevation variations of station D relative to station E and station F relative to station G were defined as h_{DE} and h_{FG}, respectively. A total of 1095 pairs of h_{DE} and h_{FG} were obtained. The leveling change of the hanging wall relative to the footwall of XF was defined as $h_{DE-FG} = h_{FG} - h_{DE}$, and the temporal variation of h_{DE-FG} is presented in Figure 2(a), which shows that the hanging wall block was uplifted relative to the footwall block during the measurement period. Specifically, this uplift (decrease in slope of h_{DE-FG} with time is not shown in the paper) decreased from January of 2016 to December of 2018, and several factors, such as atmospheric pressure, earth tides, were responsible for producing the annual variations in h_{DE-FG} (Figure 2(a)). The baseline measurements among the four stations (D, E, F, and G) were conducted every 5 (from January of 2016 to December of 2017) or 10 days (from January of 2017 to December of 2018) during the

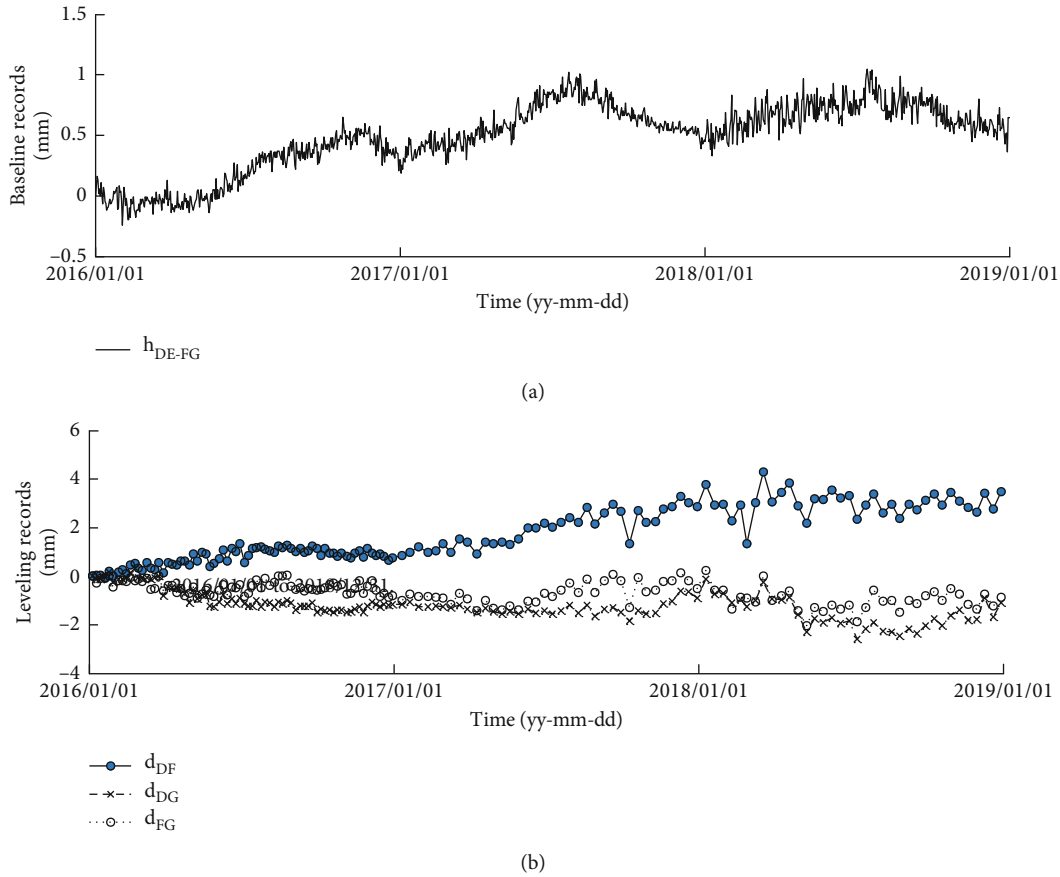

Figure 2: (a) Leveling records and (b) baseline records of the crossfault measurements from 2016/01/01 to 2018/12/31.

same period as the leveling measurements. The baseline changes between stations D and F, F and G, and D and G were defined as d_{DF}, d_{FG}, and d_{DG}, respectively. A total of 144 groups data were obtained, and the temporal variations of d_{DF}, d_{FG}, and d_{DG} are displayed in Figure 2(b).

Specifically, the minus sign describes the fact that d_{DG} and d_{FG} generally decrease relative to the displacements on January 1, 2016, meaning that the displacement between D and G and F and G continued to decrease during the measurement period. The plus sign means that d_{DF} increases relative to the displacements on January 1, 2016, indicating that the displacement between stations D and F continued to increase during the measurement period. This showed that the deformation tends to be compressed along the orthogonal direction of XF, while the deformation along the strike of XF is stretched.

2.3. Observed Groundwater Levels. A monitoring well (ZK01) was installed near the centre of the site at E100°45′7.28″ and N31°17′34.18″ (Figure 1(d)), and the ground elevation was 3140 m. The well is about 200 m deep and open to the aquifers at depths from 110 to 128 m and 145 to 173 m (Figure 1(d)). It was drilled approximately 15 m north of the XF, intersecting the fault at a depth of approximately 95 m (Figure 1(c)). The well is open to fluid flow in the formation below 110 m and provides a unique opportunity to directly measure the fault activities over time. The water table was 14-17 m below the ground. Daily precipitations (Figure 3(a)) were recorded by the local meteorological station approximately several hundred meters away from the well. The groundwater levels (Figure 3(b)) were observed using the Diver logger with the accuracy of ±0.5 cmH_2O from January 1, 2016 to December 31, 2018 with 15 min sample interval. To evaluate the effects of the barometric pressure on groundwater levels (Figure 3(c)), the barometric pressure was observed by a Baro Diver logger with the accuracy of ±0.06 cmH_2O during the same period.

In the end of 2017, a new Diver logger was deployed to measure pressure 6.5 m higher than the old one (Figure 3(c)). The logger recorded the barometric pressures was temporarily jammed; so, there were no recorded barometric pressure fluctuations during two periods; otherwise, the time series are uninterrupted for three years period (Figure 3(b)). One mysterious feature of the data is the change of water pressure that occurred during April-July 2017. These water pressure abnormal fluctuations were not related to any local earthquakes, quarry blast events, or surface hydrological events according to the local investigations. The cause of these water pressure fluctuations was not clear, which requires further and more data to evaluate. Therefore, the study of these abnormal fluctuations is beyond the scope of this paper. The tidal response analysis pursued here

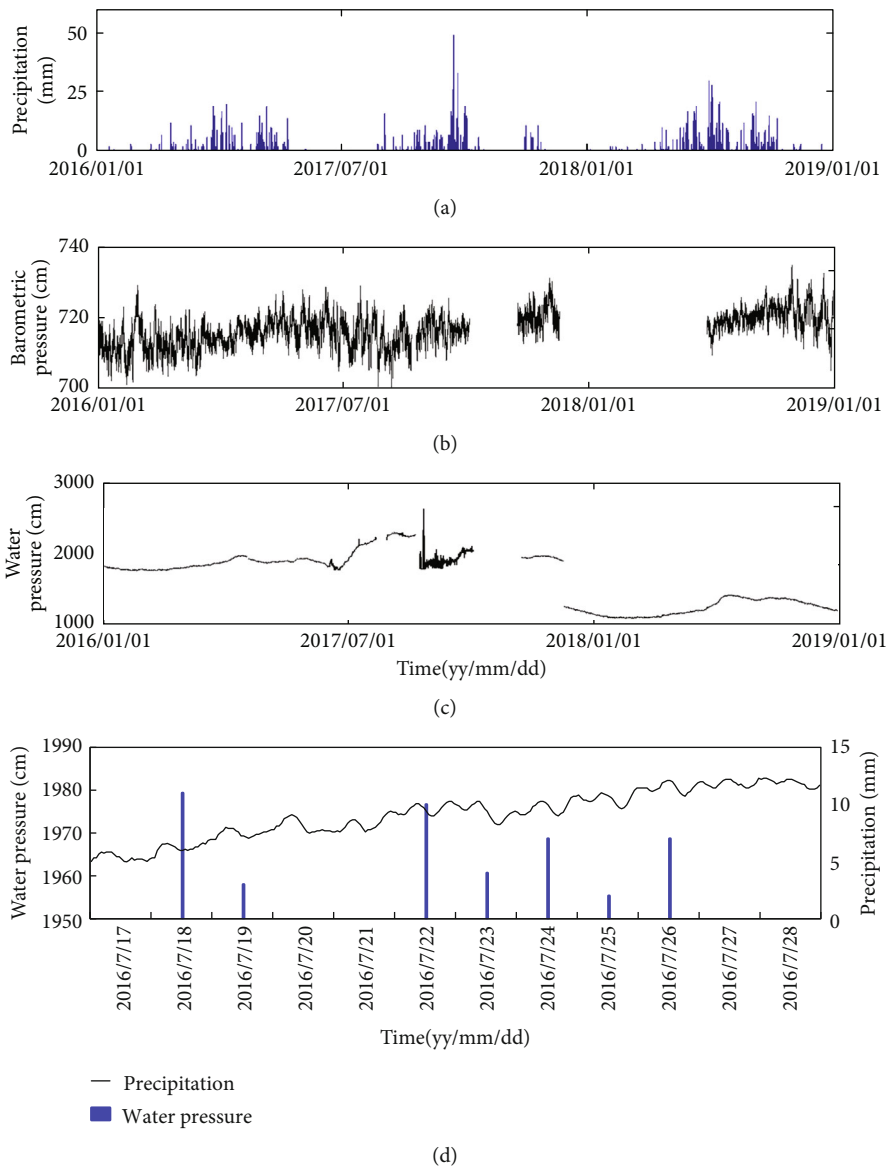

Figure 3: (a) Daily precipitation, (b) hourly barometric pressure, (c) hourly ground-water levels of ZK01, and (d) enlarged view of water pressure showing that water pressure recorded by the Diver logger are not affected by local precipitation.

focused on a specific harmonic and is therefore unaffected by these abnormal fluctuations and the resulting errors displayed by the error bars of the tidal analysis (Figure 4).

The water pressure fluctuates in a seasonal pattern, such that it increases from March to October and decreases after October. Furthermore, the water pressure does not respond to local precipitation (Figure 3(d)). This is demonstrated by the fact that if local precipitation recharged an aquifer, one would expect an increase in the water pressure with increasing local precipitation, rather than the uncorrelated patterns shown in Figure 3(d). Thus, the annual change in the water pressure in the well is likely due to the distant seasonal recharge (well located in the basin that is surrounded by mountainous region) [48]. The water pressure data were resampled to hourly intervals for tidal analysis, revealing that the water level in the well recorded a clear tidal signal and showed a strong response to earth tides (Figure 3(c) and Figure 5(a)).

3. Methodology

3.1. Tidal Analysis. The main work of tidal analysis is to estimate the tidal factors and phase shifts of the measured groundwater levels. The tidal factor is defined as the ratio of amplitudes of the groundwater levels induced by earth tides to that of the theoretical earth tides, and the phase shift is defined as the time lag between earth tides and water level, which is caused by the time required for water to flow into and out of the well. Both the tidal factor and phase shift are commonly used to represent responses of aquifer systems to earth tides. Variations in both the tidal factor and phase shift imply changes of aquifer parameters and/or force

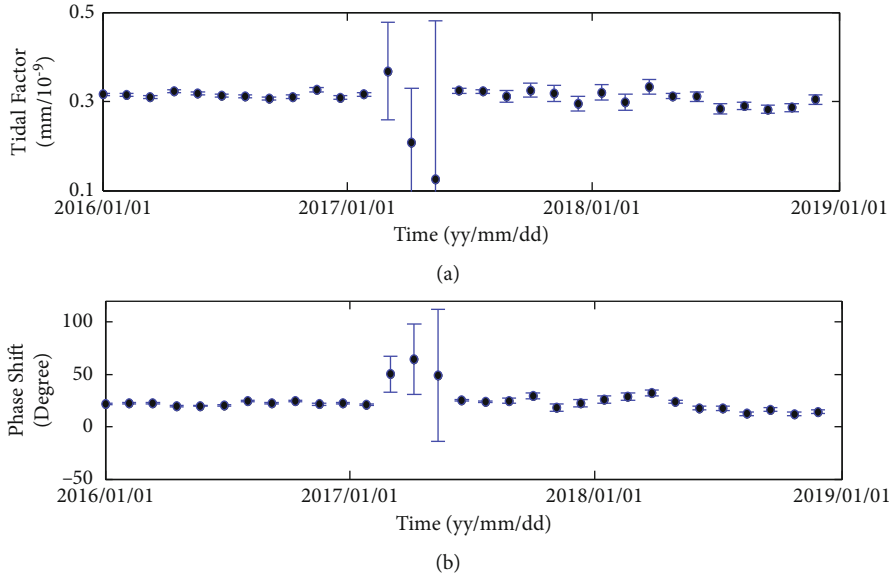

Figure 4: (a) Estimated tidal factors and (b) estimated phase shifts of M_2 Earth tide from 2016/01/01 to 2018/12/31, where the blue error bars indicate the root mean square error of the tidal analysis.

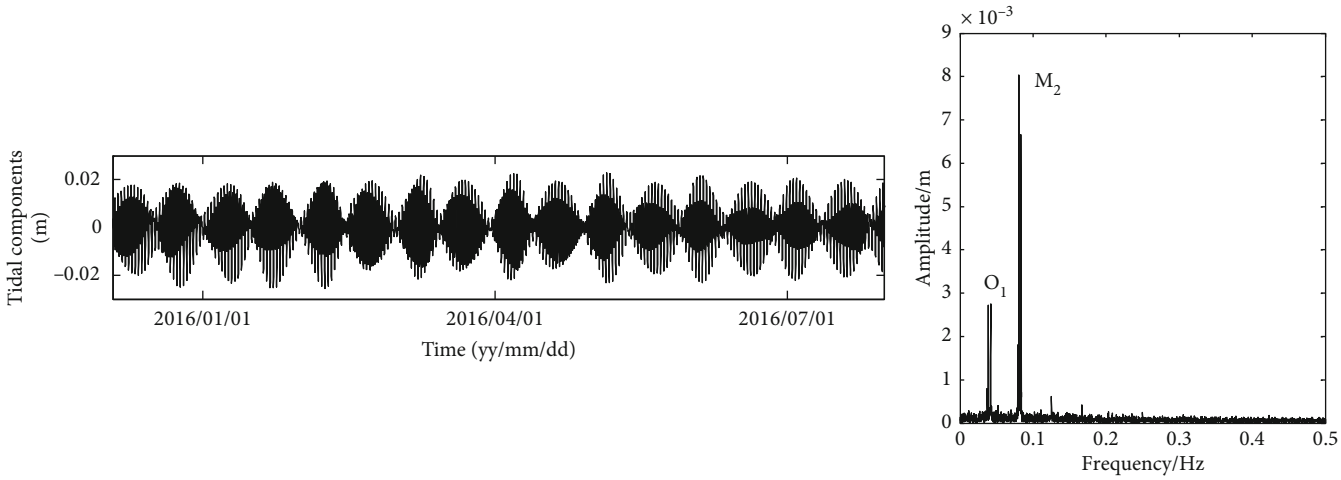

Figure 5: (a) The detrended water level time series showing the response of the water level to Earth tides and (b) normalized fast Fourier transform spectrum analysis of the measured groundwater levels.

sources. In this study, the tidal signals were extracted from the groundwater level using Baytap08, a modified version of the Bayesian Analysis Program-Grouping Model program (BAYTAP-G), which is a popular software package for tidal analysis [31, 33, 35, 49–51]. Baytap08 assumes that a signal y_i can be decomposed into the following parts:

$$y_i = \sum_{m=1}^{M} (A_m C_{mi} + B_m S_{mi}) + d_i + \sum_{k=0}^{K} b_k x_{i-k} + e_i, \quad (1)$$

where $\sum_{m=1}^{M}(A_m C_{mi} + B_m S_{mi})$ is the tidal component, M is the number of tidal waves in the tidal group, C_{mi} and S_{mi} are the summation of the cosine and sine parts of the theoretical values of different tidal components, respectively, A_m and B_m are the tidal constants, d_i is the long-term trend; $\sum_{k=0}^{K} b_k x_{i-k}$ is the local barometric response component in which b_k is the response coefficient, x_{i-k} is the observed barometric pressure, K is the lag time between the groundwater level response and barometric pressure, and e_i is the noise. This software package incorporates a Bayesian inversion process that allows the parameters A_m and B_m to be evaluated by minimising Akaike's Bayesian Information Criterion, which is formulated by Equation (1).

Several possible causes of water level fluctuation in the well include periodic effects of the earth tides, the barometric tide, ocean tidal loading and seismic waves and aperiodic effects related to seasonal aquifer recharge or discharge,

and pumping from nearby wells [31, 37, 52]. The observation well in this study are situated where the effects of ocean tidal loading and pumping can be neglected. The impacts of seismic waves can also be neglected as their periods (0.1–100 s) are much shorter than that of the earth tide. The barometric pressure includes periodic and aperiodic signals accounting for approximately 10% of the total tidal signals [53], which was eliminated by Baytap08 as well. If the aquifer is imperfectly confined, rainfall can contribute to aperiodic water level changes.

The periodic and aperiodic fluctuations, which are evident on the records in Figure 3, can be separated by well-known tidal harmonic analysis method of Baytap08. This method requires at least 28-day tide record [53]. The tidal factors and phase shifts of the constituents of the well tide were obtained from harmonic analyses of the periodic fluctuations. Some features of the spectrum of tidal harmonic constituents are revealed by the normalized fast Fourier transform spectrum analysis of the periodic water pressure data (Figure 5(b)). Note that the earth tides include 386 tidal groups with different periods [54]. The O_1, K_1, M_2, S_2, and N_2 tides account for 95% of all earth tides, and M_2 is more stable with a larger amplitude and is less disturbed by external perturbations [38, 53]. Therefore, M_2 has been widely used in the tidal analysis for aquifer system in previous studies [31, 34, 37, 48, 52, 55–57]. The M_2 tide is also adopted for the tidal analysis in this study, and responses of the groundwater level to the M_2 tide are very distinct from the normalized fast Fourier transform spectrum analysis (Figure 5(b)). In the analysis of the observed period, a time interval of 720 hour (30 days) with a sliding window of a half-month (15 days) was adopted to extract the various tidal parameters in a full time series and obtained time-dependent tidal parameters, such as the tidal factors, phase shifts, and amplitudes of the tidal constituents, from the output of Baytap08. The average value of the tidal factor was used in the subsequent calculation. Both the M_2 phase shift and tidal amplitude are at least twice as large as their root mean square error (RMSE), which were presented in Figure 6.

3.2. Estimations of Areal Strains Using GLM. For a confined aquifer, the period of earth tide is much shorter than that of discharge or recharge of the aquifer, and the fluctuations of the groundwater level caused by the dilatations or contractions of the aquifer can be approximated as being done under the undrained condition [35, 37, 57–59]. Strictly speaking, it is ideal that an aquifer is completely confined, and an aquifer in fact is generally the combination of confined and unconfined state. In this study, we just focus on the ideal case. In such a case, the relationship between the groundwater level in the deep well and volumetric strain induced by the dilation or contraction of the aquifer can be described by the following equation [21, 58, 60].

$$\delta = -\frac{\Delta \mathrm{H}}{\varepsilon_v}, \tag{2}$$

where δ is the tidal factor (mm/10^{-9}), which represents the variation of water levels (L) per volumetric strain of 10^{-9}, and it can be obtained directly from the tidal analysis of Baytap08, ε_v is the volumetric strain of the aquifer (-), and ΔH is the changes of groundwater levels in the well (L). Based on Equation (2), the volumetric strain can be calculated using the tidal factors and the change of the groundwater level.

The areal strain and volumetric strain model were set up under the plane stress (σ_1, σ_2) based on the Evertson theory [61] and later improved by Pan [62] and Zhang [63, 64] under the condition of the shallow crust, $\varepsilon_v = (2k - \mu)(\sigma_1 + \sigma_2)/E_3$ (is the elastic modulus of rock) and $\varepsilon_a = 2k(\sigma_1 + \sigma_2)/E_3$. Therefore, the relationship between the areal strain and volumetric strain in the shallow crust of the earth can be written as

$$\varepsilon_a = \frac{(2k - \mu)}{2k}\varepsilon_v, \tag{3}$$

where ε_a is the areal strain, and μ is the Poisson ratio of the host rock. The typical value of the drained Poisson ratio of rocks is approximately 0.25, which was widely adopted in previous studies [52, 65, 66]. Therefore, this typical value is adopted in this study. Meanwhile, k is the ratio of the areal strain of the inner wall of the strain instrument probe to that of the borehole rock and is usually equal to 1, inferred from the elastic modulus of rock [61, 63, 64].

3.3. Elimination of Annual Periodic Variation from Baseline Measurements. The CFM is a geodetic measurement that conducted on the ground surface, which are sensitive to a variety of surface noises like anthropogenic and natural factors [67–69]. Effect of human activities on the measurements can be negligible because there are no any human activities like pumping or large buildings constructing in the site. Therefore, only the effect of natural noises like temperature, barometric pressure, and solid tidal effect influences the CFM [4, 70]. The baseline measurements among the four stations (*D*, *E*, *F*, and *G*) were conducted every 5 (from January of 2016 to December of 2017) or 10 days (from January of 2017 to December of 2018) from January 1, 2016 to December 31, 2018; thus, we just focus on the elimination of annual periodic variations rather than the daily variations in this study.

For the annual periodic variation caused by the nontectonic movements during the crossfault measurements, the generalized analysis shows that it is a combined result of several factors like temperature, barometric pressure, and solid earth tides that results from the rotation of the earth around the sun [63, 64, 67]. In order to extract the annual periodic variation of baselines from CFM, Empirical Mode Decomposition (EMD) is applied. The raw data is decomposed into different group data with different frequencies by EMD, and the data with frequency of one year can be extracted from the raw data. EMD, a very powerful and efficient tool for the analysis of nonstationary and nonlinear time series data [71], has been widely used for different geophysical data

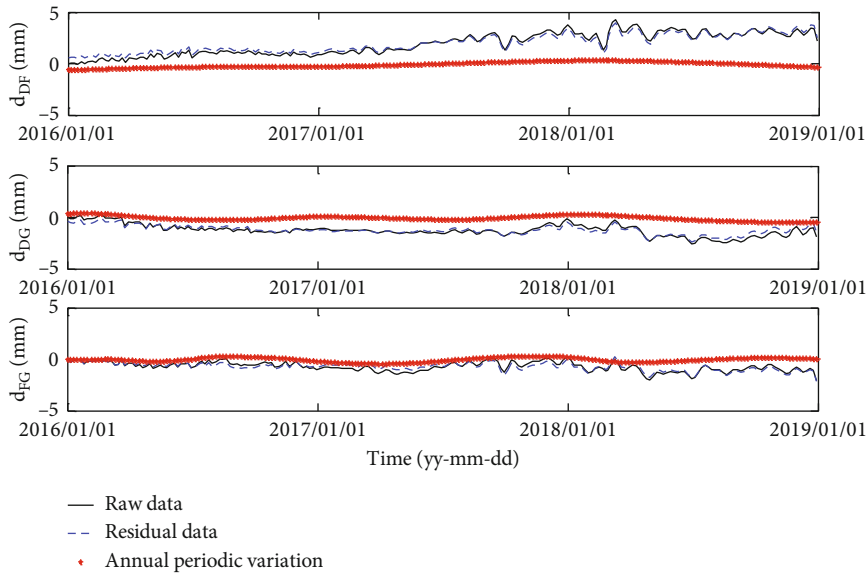

FIGURE 6: The raw data, annual periodic variation, and the long-term trend of over more than one year for (a) d_{DF}, (b) d_{DF}, and (c) d_{FG} from 2016/01/01 to 2018/12/31.

analyses, such as seismic waves [72, 73], river tides [74], and oceanic waves [75, 76].

If a real signal $X_{real}(t)$ is contaminated by a noise $n(t)$, then the raw measured signal $X_{raw}(t) = X_{real}(t) + n(t)$. The shifting process first determines the mean $m_1(t) = U(t) + L(t)/2$, where $U(t)$ and $L(t)$ are the upper and lower envelopes of $X_{raw}(t)$, obtained from a cubic spline function fitting. Subtracting $m_1(t)$ from $X_{raw}(t)$ yields the first intrinsic mode function (IMF) component $h_1(t) = X_{raw}(t) - m_1(t)$, and the shifting process needs to be iterated several times using the equation $h_{1k}(t) = h_{1(k-1)}(t) - m_{1k}(t)$, where k denotes the number of iterations until $C_{1k}(t) = h_{1k}(t)$ which satisfies the definition of IMF. The function $C_1(t)$ is the first IMF with the highest instantaneous frequency and can be separated from $X_{raw}(t)$ by $R_1(t) = X_{raw}(t) - C_1(t)$. The shifting process is again conducted on the residual $R_1(t)$ to extract the second IMF. This process is continued until either the residual is a constant value or it becomes a monotonic function. Finally, $X_{raw}(t) = \sum_{i=1}^{N} C_i(t) + R_N(t)$ where $R_N(t)$ is the trend function, n is the number of IMFs, and $C_i(t)$ is the i^{th} IMF. The decomposed IMFs are orthogonal to one another and thus can be used as the basis to represent the raw measured signal. From the above, a time series of the baseline measurements data $X_{raw}(t)$ can be decomposed into different groups with different frequencies.

Because of the observation periods of baseline measurements are not the same, the baseline measurements were conducted every 5 days from January of 2016 to December of 2017 and every 10 days from January of 2017 to December of 2018. Thus, the first thing for the raw data before decomposed by EMD is to preprocess the raw data with the three spline interpolation to obtain a value of the baseline measurements every 5 days. Annual periodic variations (the red star line shown in Figure 6) of baseline DF, DG, and FG extracted from EMD are eliminated from the raw data (the solid line shown in Figure 6). The standard deviations (STD) of the residuals between the raw data and the residual data (the dotted line shown in Figure 6) without the annual periodic variations are 0.2668, 0.2321, and 0.2154, respectively. The residual data without the annual periodic variations are applied to estimate the areal strain.

The effect of hydrological processes with period ranges from a few days to annual period on the rock deformation. The original raw data is probably the most reliable if interference information like the hydrological processes for the strain is excluded with significant uncertainties; thus, in this study, we did not exclude the effect of hydrological processes caused by precipitations on the strain estimated by both groundwater level monitoring and crossfault measurements. Therefore, the study of hydrological processes caused by precipitations on the rock deformation is the next research plan, which is beyond the scope of this paper.

3.4. Estimations of Areal Strains Using CFM. Deformation in a local place can be conventionally obtained by CFM, a method proposed by Jaeger [77] that calculates the main strain, shear strain, and areal strain from variations of the baseline lengths in two or more measurements:

$$\frac{\Delta S}{S} = \frac{\varepsilon_x + \varepsilon_y}{2} + \frac{\varepsilon_x - \varepsilon_y}{2} \cos 2\alpha + \frac{\gamma_{xy}}{2} \sin 2\alpha, \quad (4)$$

where S is the baseline length, i.e., the distance between two observation stations (L), ΔS is the variations of baseline length relative to that at the beginning of the measurement, i.e., change in the distance between two stations (L), ε_x is the strain in the direction parallel to the strike of the fault, ε_y is the strain in the direction perpendicular to the fault, γ_{xy} is the shear strain, and α is the angle between the baseline and the fault. Angles between the DF, DG, and FG baselines

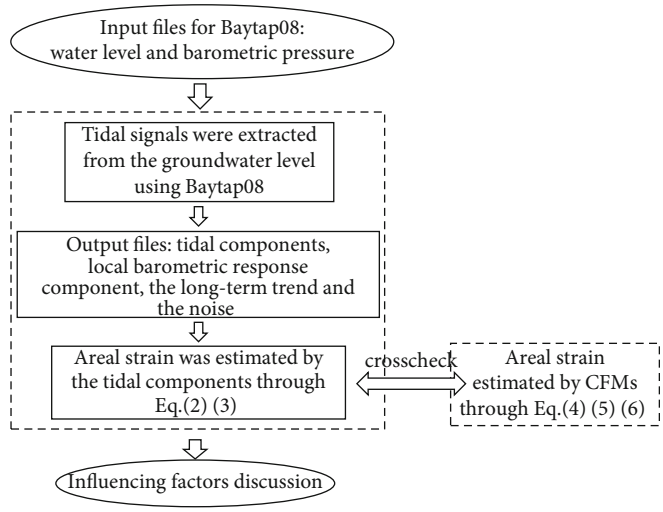

Figure 7: A flowchart of the analysis processes.

and the fault are $\alpha_1 = 35.6^\circ$, $\alpha_2 = 89.65^\circ$, and $\alpha_3 = 3.02^\circ$, respectively. The strains can be obtained by

$$\begin{bmatrix} \frac{\Delta S_{01}}{S_{01}} \\ \frac{\Delta S_{02}}{S_{02}} \\ \frac{\Delta S_{03}}{S_{03}} \end{bmatrix} = \begin{bmatrix} \frac{1+\cos 2\alpha_1}{2} & \frac{1-\cos 2\alpha_1}{2} & \frac{\sin 2\alpha_1}{2} \\ \frac{1+\cos 2\alpha_2}{2} & \frac{1-\cos 2\alpha_2}{2} & \frac{\sin 2\alpha_2}{2} \\ \frac{1+\cos 2\alpha_3}{2} & \frac{1-\cos 2\alpha_3}{2} & \frac{\sin 2\alpha_3}{2} \end{bmatrix} \begin{bmatrix} \varepsilon_x \\ \varepsilon_y \\ \gamma_{xy} \end{bmatrix}. \tag{5}$$

And the areal strain ε_a can be obtained by

$$\varepsilon_a = \varepsilon_x + \varepsilon_y. \tag{6}$$

In order to help readers better understand the analysis steps, a flowchart shown in Figure 7 showing the connection of different physical processes.

4. Results and Discussion

Both tidal factors (Figure 4(a)) and phase shifts (Figure 4(b)) are time-dependent parameters, and they range from 0.1255 to 0.3681 and 12.181° to 64.411°, respectively. The blue error bars indicate the RMSE of the tidal analysis. Theoretically, the periodical fluctuations of the tidal factor and phase shift are mainly caused by the elastic deformation of an aquifer forced by the earth tides [78]. In this study, the abnormal jumps in both tidal factors and phase shifts are consistent with the abnormal fluctuations in the observed groundwater level during the April-July 2017. Specifically, the tidal factors and phase shifts changed little with time except those from April to July 2017, in which the abnormal groundwater level fluctuations result from some reasons that require further and more data to evaluate. Therefore, a large RMSE resulted for both the phase shifts and tidal factors during the time.

According to Hsieh's model, a single, homogeneous, isotropic, laterally extensive, and confined aquifer in which the water table drainage effect is negligible, and the phase shifts should be negative [34, 59, 79]. However, if the phase shifts are positive which may be caused by the vertical drainage of the water table and the aquifer is unconfined [39, 80], sometimes, the phase shift of an aquifer can be switched from negative to positive under strong ground movements, such as earthquakes, the water table drainage happened through the reopening of vertical fractures during earthquakes, and the water table drainage is ignored as vertical fractures resealed over time after earthquakes [2, 29, 34]. As shown in Figure 4(b), the phase shifts in this study are positive, indicating that the connection between the aquifer and the water table is strong, and the vertical drainage of the water table cannot be ignored. It seems like that ZK01 is an unconfined aquifer, and the connection with water table is important, which will be discussed further later.

The temporal variation of the areal strain estimated with the GLM method is presented in Figure 8 (the green stars). It should be noted that the estimated strain was defined as the relative strain, which is calculated with respect to the reference of the strain on January 1, 2016. Positive strain means that the rock becomes tensile with respect to the reference, and negative strain means that the rock becomes compressive with respect to the reference. The strain was positive in the early time and then became negative after June 1, 2016, and the slope of the linear regression analysis is negative (not shown in the article), meaning that the rock around the well switched from tensile to compressive state relative to the reference, resulting from the local crustal stress redistribution under the crustal movement. Figure 8 shows that the estimated areal strain significantly oscillated over time, which may be induced by the dynamic responses of the groundwater level to the crust movement and precipitation infiltrations, similar oscillations also exist in the strain estimated by the CFM method.

The temporal variation of the estimated areal strain calculated by the CFM method was also presented in Figure 8 (solid curve with blue dots). The strain, similar to that by the GLM method, also was the relative strain with respect to the reference on January 1, 2016. It shows that the areal

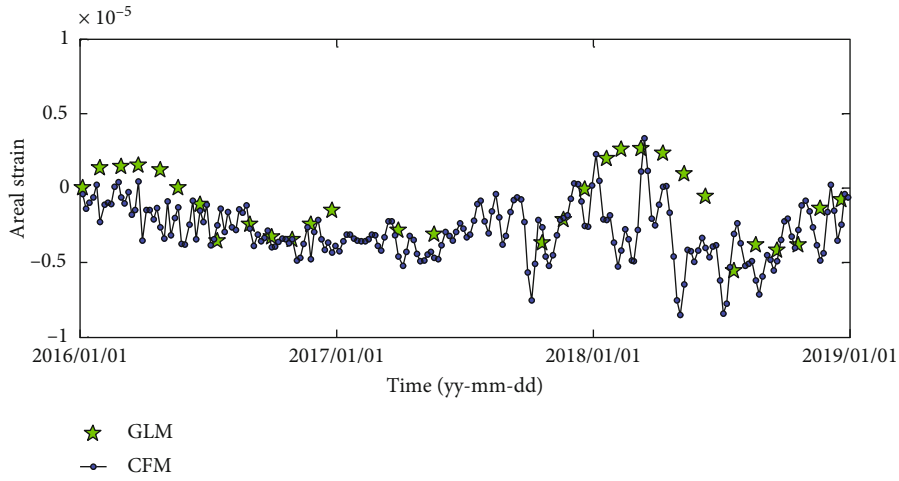

Figure 8: Comparison of the estimated areal strains from the GLM and CFM methods.

strain estimated by the CFM method was positive early and became negative after April 1, 2016, and the slope of the linear regression analysis is negative (not shown in the article), meaning that the rock switched from tensile to compressive state relative to the reference as time progressed. The areal strain fluctuated dramatically over time as well. The reason is the same as that of the estimated strain using the GLM method mentioned above.

Comparison of the areal strains estimated by different methods in the study area during the period of January 1, 2016 to December 31, 2018 was shown in Figure 8. It shows that the pattern of the strain variations estimated by the GLM method matches well with that obtained by the CFM method. The fluctuations of the areal strain during the period of January 1, 2016 to December 31, 2016 are weaker than those during the period of January 1, 2017 to December 31, 2018, which is probably caused by the precipitation loading in the rainy season, i.e., the precipitation of 2016, 2017, and 2018 was 508 mm, 572 mm, and 800 mm, respectively, and rain falls mainly in the rainy season. Although with different maximum areal strain values, the interannual variation of the estimated strain appeared near January 2016, January 2017, and January 2018 is apparently. This interannual characteristic of the estimated strain occurs in both methods, which is likely caused by annual infiltration loading [48]. The temporal variations in the estimated strains using both GLM and CFM method show that XF switched from tensile to compressive state relative to the reference on January 1, 2016, owing to the areal strain changed from positive to negative with time relative to the reference on January 1, 2016.

The long-term creep rates of the site with CFM were measured by the Survey Engineering Institute of Sichuan Earthquake Administration (SEISEA) (Figure 9). The creep rate is negative in the vertical direction of XF (blue line with diamonds) and decreases quickly before 1992; then, it decreases slowly in the remaining period of the measurements. The creep rate that oblique with XF (red line with squares) was positive and approximately constant before 2015, then decreased significantly, and became negative after 2016. The creep rate that orthogonal to XF (green line with triangles) has decreased significantly after 1980. The temporal variations of the creep rates in the three directions implied that the left-lateral creep rate of XF at this segment has decreased gradually since 1980.

For the period of this study, specifically, the creep rate that obliques with XF (red line with squares) is negative with respect to the reference of the creep rate on January 1, 2016, owing to the creep rate in the opposite direction kept increasing since 2016. It illustrates that XF changed from the stretched state (before 2016) to the compressed state (after 2016) in the direction that oblique with XF with respect to the state on January 1, 2016. Besides, the creep rate that orthogonal to XF (green line with triangles) is also negative relative to the creep rate on January 1, 2016, owing to the creep rate that orthogonal to XF kept decreasing since 1980s. It also illustrates that the fault had a tendency from the stretched state to the compressed state in the direction that orthogonal to XF with respect to the state on January 1, 2016. The vertical creep rate of XF also decreased gradually since 1980s. Above all, it can be concluded that the fault has tended to the compressed state from the stretched state.

Moreover, previous studies on XF [5, 68, 81] have indicated that the fault at this segment behaved as tensional creeping in the first few years following the 1973 Luhuo earthquake; however, the creep rate has slowed down since 1980, speculating that the fault has gradually entered the relock state (a state in the seismic cycle described from Du et al., 2010) before the next earthquake happen. This deformation pattern is consistent with the areal strain state of the study area using both GLM and CFM, proving the reliability of the estimated strain in this study.

It is recognized that there are some discrepancies in the estimated strains using the two methods. First, the magnitude of the estimated strain using the CFM method is smaller than that of the GLM method. The reason is that the estimated strain using the CFM method mainly represents the ground deformation, whereas the estimated strain using the GLM method mainly represents the rock deformation at a depth of 200 m. Second, the strain changes

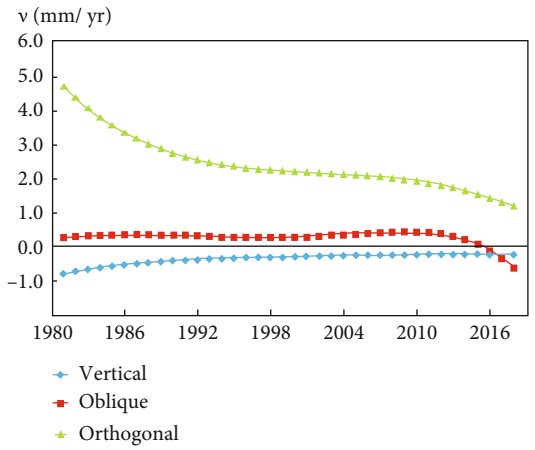

Figure 9: Measured long-term creep rates of three directions from the cross-fault measurements that have been conducted by SEISEA since 1980s.

estimated by the GLM method lag slightly behind that of the CFM method. This lag is probably owing to the diffusive effects of pore pressure propagation caused by the rock deformation under crustal stress. Besides, the CFM method only considers the surface rock deformation. Thus the change of the strain estimated using CFM is a little earlier than that obtained by GLM. A comparison of the two methods indicates that the readily available groundwater level monitoring data provide a convenient and economic tool to investigate the rock deformation. The GLM method can be used to obtain the regional strain field or crustal movement with a network of monitoring wells, which is the next study we intend to conduct.

5. Conclusions

In this study, rock deformation at the Xianshuihe fault in Xialatuo, China, was estimated using GLM and compared with that of using CFM. Groundwater levels were measured with two dataloggers in a monitoring well installed in the center of the study area from Jan 1, 2016 to Dec 31, 2018. The baseline and leveling measurements have been conducted in this study area since 1980s. The main conclusions were drawn from this study as follows.

(1) The pattern of the areal strain variations estimated using the GLM method matches well with that obtained by the CFM method

(2) The strains estimated by the GLM and the CFM method both changed from positive to negative, indicating that the fault switched from tensile to compressive, which is consistent with the long-term creep rates measurements of the fault

(3) The strain estimated by the GLM method lag slightly behind that of the CFM method, which is probably owing to the diffusive effects of pore pressure propagation caused by rock deformations under the crustal stress

(4) GLM is an additional method that is effective at characterizing variations in rock deformation in remote areas where geophysical facilities are rare while continuous measurements are needed

Data Availability

The data used in the study can be found at the documentary called "original data" on the https://github.com/2019Yuqing/HESS/blob/master/originaldata.xlsx.

Conflicts of Interest

The authors declare that they have no known competing financial interests or personal relationships that could have appeared to influence the work reported in this paper.

Authors' Contributions

Y.-K. Zhang, Y.Q. Zhao, X.Y. Liang, and other co-authors conceived the idea and designed the experiments based on weekly workshops and discussions. Y.L. Yang and F.F. Li conducted the field experiments in the Xialatuo study area. Y.Q. Zhao analyzed the field data and wrote the first draft of the paper.

Acknowledgments

The authors would like to thank the journal for the invitation to write this article. Thanks are due to everyone for their efforts in this article. This work was supported with the research grants from Guangxi Science and Technology Planning Project (Grant No. GuiKe AD21075013), Guangxi "Bagui Scholar" Construction Projection, Guangxi Science and Technology Planning Project (Grant No. GuiKe-AD18126018), and the research fund provided by the Guangdong Provincial Key Laboratory of Soil and Groundwater Pollution Control, State Environmental Protection Key Laboratory of Integrated Surface Water-Groundwater Pollution Control, and Shenzhen Municipal Engineering Lab of Environmental IoT Technologies of the School of Environmental Sciences and Engineering, Southern University of Science and Technology, China.

References

[1] F. Masson, M. Lehujeur, Y. Ziegler, and C. Doubre, "Strain rate tensor in Iran from a new Gps velocity field," *Geophysical Journal International*, vol. 197, no. 1, pp. 10–21, 2014.

[2] L. Xue, *Investigations of Fault Zone Behavior During Earthquake Cycles Using Hydrology and Geodesy, [Ph.D. thesis]*, University of California, California, 2015, https://escholarship.org/content/qt90p323z6/qt90p323z6.pdf.

[3] S. Wang, C. Zhang, W. Liu, and G. Su, "Study on fault activity and seismic risk in the capital region by the cross-fault measurements data," *Technology for Earthquake Disaster Prevention*, vol. 12, no. 3, pp. 547–556, 2017.

[4] X. Su, G. Meng, H. Sun, and W. Wu, "Positioning performance of Bds observation of the crustal movement observation

network of China and its potential application on crustal deformation," *Sensors*, vol. 18, no. 10, p. 3353, 2018.

[5] J. Zhang, X. Z. Wen, J. Cao, W. Yan, Y. Y. Yang, and Q. Su, "Surface creep and slip-behavior segmentation along the northwestern Xianshuihe fault zone of southwestern China determined from decades of fault-crossing short-baseline and short-level surveys," *Tectonophysics*, vol. 722, pp. 356–372, 2018.

[6] J. Beavan and J. Haines, "Contemporary horizontal velocity and strain rate fields of the Pacific-Australian plate boundary zone through New Zealand," *Journal of Geophysical Research*, vol. 106, no. B1, pp. 741–770, 2001.

[7] R. W. Allmendinger, R. Reilinger, and J. Loveless, "Strain and rotation rate from Gps in Tibet, Anatolia, and the Altiplano," *Tectonics*, vol. 26, no. 3, 2007.

[8] M. Hackl, R. Malservisi, and S. Wdowinski, "Strain rate patterns from dense Gps networks," *Natural Hazard and Earth System Sciences*, vol. 9, no. 4, pp. 1177–1187, 2009.

[9] S. Ergintav, R. E. Reilinger, R. Cakmak et al., "Istanbul's earthquake hot spots: geodetic constraints on strain accumulation along faults in the Marmara seismic gap," *Geophysical Research Letters*, vol. 41, no. 16, pp. 5783–5788, 2014.

[10] R. Devoti, D. Zuliani, C. Braitenberg, P. Fabris, and B. Grillo, "Hydrologically induced slope deformations detected by Gps and clinometric surveys in the Cansiglio Plateau, southern Alps," *Earth and Planetary Science Letters*, vol. 419, pp. 134–142, 2015.

[11] H. S. Kutoglu, M. Toker, and C. Mekik, "The 3-D strain patterns in Turkey using geodetic velocity fields from the RTK-CORS (TR) network," *Journal of African Earth Sciences*, vol. 115, pp. 246–270, 2016.

[12] D. Cheloni, V. D. Novellis, M. Albano, and A. Antonioli, "Geodetic model of the 2016 Central Italy earthquake sequence inferred from Insar and Gps data," *Geophysical Research Letters*, vol. 44, no. 13, pp. 6778–6787, 2017.

[13] S. M. Liang, W. J. Gan, W. W. Shen et al., "Three-dimensional velocity field of present-day crustal motion of the Tibetan Plateau derived from Gps measurements," *Journal of Geophysical Research: Solid Earth*, vol. 118, no. 10, pp. 5722–5732, 2013.

[14] G. Zheng, H. Wang, T. J. Wright et al., "Crustal deformation in the India-Eurasia Collision Zone from 25 years of Gps measurements," *Journal of Geophysical Research: Solid Earth*, vol. 122, no. 11, pp. 9290–9312, 2017.

[15] J. Zhang, Y. Zhu, Y. Wu, X. Zhang, and G. Yang, "Intermediate to long-term estimation of strong earthquake risk areas in the chinses mainland based on geodesic measurements," *Earthquake Research in China*, vol. 32, no. 2, pp. 153–172, 2018.

[16] J. Langbein, J. R. Murray, and H. A. Snyder, "Coseismic and initial postseismic deformation from the 2004 Parkfield, California, earthquake, observed by global positioning system, electronic distance meter, creepmeters, and borehole strainmeters," *Bulletin of the Seismological Society of America*, vol. 96, no. 4B, pp. S304–S320, 2006.

[17] J. Lienkaemper, B. Baker, and F. S. McFarland, "Surface slip associated with the 2004 Parkfield, California, earthquake measured on alinement arrays," *Bulletin of the Seismological Society of America*, vol. 96, no. 4B, pp. S239–S249, 2006.

[18] B. Li, K. Atakan, M. B. Sorensen, and J. Havskov, "Stress pattern of the Shanxi Rift System, North China, inferred from the inversion of new focal mechanisms," *Geophysical Journal International*, vol. 201, no. 2, pp. 505–527, 2015.

[19] A. Niu, G. Gu, J. Cao et al., "On the preseismic deformation changes prior to the Lushan Ms 7.0 earthquake," *Acta Seismologica Sinca*, vol. 35, no. 5, pp. 670–680, 2013.

[20] A. W. Bishop, *The Principle of Effective Stress*, Teknisk Ukeblad, 1960.

[21] J. D. Bredehoeft, "Response of well-aquifer systems to earth tides," *Journal of Geophysical Research*, vol. 72, no. 12, pp. 3075–3087, 1967.

[22] G. Bodvarsson, "Confined Fluids as Strain meters," *Journal Geophysical Research*, vol. 75, no. 14, pp. 2711–2718, 1970.

[23] D. R. Bower, "Bedrock fracture parameters from the interpretation of well tides," *Journal of Geophysical Research Solid Earth*, vol. 88, no. B6, pp. 5025–5035, 1983.

[24] T. N. Narasimhan, B. Y. Kanehiro, and P. A. Witherspoon, "Interpretation of earth tide response of three deep, confined aquifers," *Journal of Geophysical Research Solid Earth*, vol. 89, no. B3, pp. 1913–1924, 1984.

[25] A. J. Barbour, "Pore pressure sensitivities to dynamic strains: observations in active tectonic regions," *Journal of Geophysical Research: Solid Earth*, vol. 120, no. 8, pp. 5863–5883, 2015.

[26] H. Zhang, Z. Shi, G. Wang, X. Sun, R. Yan, and C. Liu, "Large earthquake reshapes the groundwater flow system: insight from the water-level response to Earth tides and atmospheric pressure in a deep well," *Water Resources Research*, vol. 55, no. 5, pp. 4207–4219, 2019.

[27] C.-Y. Wang, Z. Ai-Yu, L. Xin, M. Michael, and W. Lee-Ping, "Capillary effects on groundwater response to Earth tides," *Water Resources Research*, vol. 55, no. 8, pp. 6886–6895, 2019.

[28] T. Shibata, N. Matsumoto, F. Akita, N. Okazaki, H. Takahashi, and R. Ikeda, "Linear poroelasticity of groundwater levels from observational records at wells in Hokkaido, Japan," *Tectonophysics*, vol. 483, no. 3-4, pp. 305–309, 2010.

[29] L. Xue, H.-B. Li, E. E. Brodsky et al., "Continuous permeability measurements record healing inside the Wenchuan earthquake fault zone," *Science*, vol. 340, no. 6140, pp. 1555–1559, 2013.

[30] G. Lai, H. Ge, L. Xue, E. E. Brodsky, F. Huang, and W. Wang, "Tidal response variation and recovery following the Wenchuan earthquake from water level data of multiple wells in the nearfieldTidal response variation and recovery following the Wenchuan earthquake from water level data of multiple wells in the nearfield," *Tectonophysics*, vol. 619-620, pp. 115–122, 2014.

[31] Z. Shi, G. Wang, M. Manga, and C. Wang, "Mechanism of co-seismic water level change following four great earthquakes - insights from co-seismic responses throughout the Chinese mainland," *Earth and Planetary Science Letters*, vol. 430, pp. 66–74, 2015.

[32] R. Yan, F. W. Gao, and H. Chen, "Study on volume strain version from water level change of well-aquifer system," *Earthquake Research in China*, vol. 23, no. 3, pp. 303–309, 2007.

[33] R. Yan, G. Wang, and Z. Shi, "Sensitivity of hydraulic properties to dynamic strain within a fault damage zone," *Journal of hydrology*, vol. 543, pp. 721–728, 2016.

[34] Z. Shi and G. Wang, "Aquifers switched from confined to semiconfined by earthquakes," *Geophysical Research Letters*, vol. 43, no. 21, pp. 166–172, 2016.

[35] M. Tang, H. Zhao, H. Ma, S. Lu, and Y. Chen, "Study on Co_2 huff-N-puff of horizontal wells in continental tight oil reservoirs," *Fuel*, vol. 188, pp. 140–154, 2017.

[36] Z. Shi and G. Wang, "Evaluation of the permeability properties of the Xiaojiang fault zone using Hot Springs and water Wells," *Geophysical Journal International*, vol. 209, no. 3, pp. 1526–1533, 2017.

[37] Z. M. Shi, G. Wang, C. Liu, and Y. Che, "Tectonically induced anomalies without large earthquake occurrences," *Pure and Applied Geophysics*, vol. 175, no. 7, pp. 2513–2526, 2018.

[38] H. H. Cooper, J. D. Bredehoeft, I. S. Papadopulos, and R. R. Bennett, "The response of well-aquifer systems to seismic waves," *Journal of Geophysical Research*, vol. 70, no. 16, pp. 3915–3926, 1965.

[39] E. Roeloffs, "Poroelastic techniques in the study of earthquake-related hydrologic phenomena," *Advances in Geophysics*, vol. 37, pp. 135–195, 1996.

[40] Z. Fan, P. Eichhubl, and P. Newell, "Basement fault reactivation by fluid injection into sedimentary reservoirs: poroelastic effects," *Journal of Geophysical Research: Solid Earth*, vol. 124, no. 7, pp. 7354–7369, 2019.

[41] Z. Fan and R. Parashar, "Transient flow to a finite-radius well with wellbore storage and skin effect in a poroelastic confined aquifer," *Advances in water resources*, vol. 142, article 103604, 2020.

[42] Z. Shi, Z. Shouchuan, Y. Rui, and W. Guangcai, "Fault zone permeability decrease following large earthquakes in a hydrothermal system," *Geophysical Research Letters*, vol. 45, no. 3, pp. 1387–1394, 2018.

[43] V. Allègre, E. Brodsky Emily, X. Lian, M. Nale Stephanie, L. Parker Beth, and A. Cherry John, "Using Earth-tide induced water pressure changes to measure in situ permeability: a comparison with long-term pumping tests," *Water Resources Research*, vol. 52, no. 4, pp. 3113–3126, 2016.

[44] F. Q. Huang, R. Yun, Y. Chen, W.-X. Wang, J. Geng, and J.-P. Gu, "Study of present tectonic stress field of Pan-North China region based on ground water level dynamic in deep wells," *Earth*, vol. 24, no. 1, pp. 112–118, 2004.

[45] L. Yang, J. Y. Ma, J. Q. Cao, and Y. Shao, "Inversion of the volumetric strain of aquifer according to the tidal effect of groundwater in the North China region," *Earthquake Research in China*, vol. 30, no. 2, pp. 249–259, 2014.

[46] Y. Du, C. Guo, Y. Zhang, G. Zhang, and M. Zhang, "Luhuo fault distribution characteristics and quaternary activity along the Xianshui River fault, east Tibetan plateau," in *Proceedings of conferences on Chanllenges and countermeasures for the construction of Sichuan-Tibet railway*, pp. 54–65, Chengdu, 2016.

[47] X. J. Zhang, "Preliminary study on characteristics of Xialatuo Basin in Xianshui River fault zone," *Sichuan Earthquake*, vol. 2, pp. 29–34, 1988.

[48] X. Liao and C.-Y. Wang, "Seasonal permeability change of the shallow crust inferred from deep well ,onitoring," *Geophysical Research Letters*, vol. 45, no. 20, pp. 11130–11136, 2018.

[49] G. Igarashi and H. Wakita, "Geochemical and hydrological observations for earthquake prediction in Japan," *Journal of Physics of the Earth*, vol. 43, no. 5, pp. 585–598, 1995.

[50] S. Rojstaczer and D. C. Agnew, "The influence of formation material properties on the response of water levels in wells to earth tides and atmospheric loading," *Journal of Geophysical Research*, vol. 94, no. B9, pp. 12403–12411, 1989.

[51] Y. Tamura, T. Sato, M. Ooe, and M. Ishiguro, "A procedure for tidal analysis with a Bayesian information criterion," *Geophysical Journal International*, vol. 104, no. 3, pp. 507–516, 1991.

[52] T. J. Burbey and M. Zhang, "Assessing hydrofracing success from earth tide and barometric response," *Groundwater*, vol. 48, no. 6, pp. 825–835, 2010.

[53] M.-L. Doan, E. E. Brodsky, R. Prioul, and C. Signer, *Tidal Analysis of Borehole Pressure: A Tutorial*, University of California, Santa Cruz, 2006.

[54] G. Godin, *The Analysis of Tides*, University of Toronto Press, Toronto, 1972.

[55] R. Yan, L. Zhang, and C. L. Jian, "Dynamic analysis of well water level tides in Qujing well, Yunan Province," *Acta Seicmologica Sinica*, vol. 34, no. 3, pp. 363–373, 2012.

[56] R. A. Darner and R. A. Sheets, "Using existing data to estimate aquifer properties, Great Lakes region, USA," *Groundwater*, vol. 50, no. 3, pp. 477–484, 2012.

[57] Z. M. Shi, G. C. Wang, C. L. Liu, J. Mei, J. Wang, and H. Fang, "Coseismic response of groundwater level in the three gorges well network and its relationship to aquifer parameters," *Chinese Science Bulletin*, vol. 58, no. 25, pp. 3080–3087, 2013.

[58] Z. Shi and G. Wang, "Hydrological response to multiple large distant earthquakes in the mile well, China," *Journal of Geophysical Research Earth Surface*, vol. 119, no. 11, pp. 2448–2459, 2014.

[59] L. Xue, E. E. Brodsky, J. Erskine, P. M. Fulton, and R. Carter, "A permeability and compliance contrast measured hydrogeologically on the San Andreas Fault," *Geochemistry, Geophysics, Geosystems*, vol. 17, no. 3, pp. 858–871, 2016.

[60] G. H. Rhoads and S. R. Edwin, "Determination of aquifer parameters from well tides," *Journal of Geophysical Research*, vol. 84, no. B11, pp. 6071–6082, 1979.

[61] D. W. Evertson, *Borehole Strainmeters for Seismology, [Ph.D. Austin]*, Thesis of Texas University, 1975, https://www.researchgate.net/publication/252904358.

[62] Institute of Geomechanics, *Chinese Academy of Geological Sciences 1981*Application and Measurement Principle of the in-Site Stress, Beijinghttp://img.sslibrary.com/n/slib/book/slib/11027732/9f67e5c79a944258b74710ac9961ae95/6f999da7aedd8571f67a4000ace17b52.shtml?dxbaoku=false&deptid=288&fav=http%3A%2F%2Fwww.sslibrary.com%2Freader%2Fpdg%2Fpdgreader%3Fd%3D2589f3f57b24fd34c5abf0712561f710%26ssid%3D11027732&fenlei=1403010502&spage=1&t=5&username=202.103.243.78&view=-1.

[63] L. K. Zhang, A. F. Niu, and L. J. Wu, "Conversion factors from volume to areal strain in crustal strain observation," *Acta Seismologica Sinica*, vol. 34, no. 4, pp. 476–486, 2012.

[64] L. K. Zhang and A. F. Niu, "Calculation of borehole volumetric strain and area strain observation parameters K," *Earthquake Research in China*, vol. 29, no. 3, pp. 335–346, 2013.

[65] M. L. Merritt, *Estimating Hydraulic Properties of the Floridan Aquifer System by Analysis of Earth-Tide, Ocean-Tide, and Barometric Effects*, Florida, 2004https://pubs.usgs.gov/wri/wri034267/wri03_4267.pdf.

[66] T. J. Burbey, "Fracture characterization using earth tide analysis," *Journal of Hydrology*, vol. 380, no. 3-4, pp. 237–246, 2010.

[67] M. J. S. Johnston, R. D. Borcherdt, A. T. Linde, and M. T. Gladwin, "Continuous borehole strain and pore pressure in the near field of the 28 September 2004 M 6.0 Parkfield, California, earthquake: implications for nucleation, fault response, earthquake prediction, and tremor," *Bulletin of the Seismological Society of America*, vol. 96, no. 4B, pp. s56–s72, 2006.

[68] G. Liu, J. Ma, H. Zhang, J. Wang, Y. Yang, and L. Wang, "Study on activity features of Xianshuihe fault zone with fault creep and short baseline observation for the last 20 years," *Chinese Journal of Geophysics*, vol. 56, no. 3, pp. 878–891, 2013.

[69] G. Z. Liu, J. Ma, Y. L. Yang, and Q. Su, "Effect of long-term surface temperature variation on fault displacement observation and anomalous fault movement in Western Sichuan before the Lushan Ms.7.0 earthquake," *Chinese Journal of Geophysics*, vol. 57, no. 7, pp. 2150–2164, 2014.

[70] K. Hirahara, Y. Ooi, M. Ando, Y. Hoso, Y. Wada, and T. Ohkura, "Dense Gps array observations across the Atotsugawa Fault, Central Japan," *Geophysical Research Letters*, vol. 30, no. 6, 2003.

[71] N. E. Huang, Z. Shen, S. R. Long et al., "The empirical mode decomposition and the Hilbert spectrum for nonlinear and non-stationary time series analysis," *Proceedings of the Royal Society of London a: mathematical, physical and engineering sciences*, vol. 454, pp. 903–995, 1998.

[72] N. E. Huang, C. C. Chern, K. Huang, L. W. Salvino, S. R. Long, and K. L. Fan, "A new spectral representation of earthquake data: Hilbert spectral analysis of Station Tcu 129, Chi-Chi, Taiwan, 21 September 1999," *Bulletin of the Seismological Society of America*, vol. 91, pp. 1310–1338, 2004.

[73] N. E. Huang and Z. H. Wu, "A Review on Hilbert-Huang Transform: Method and Its Applications to Geophysical Studies," *Reviews of Geophysics*, vol. 46, no. 2, article 2007RG000228, 2008.

[74] H. Pan, Z. Guo, Y. Wang, and X. Lv, "Application of the Emd method to river tides," *Journal of Atmospheric & Oceanic Technology*, vol. 35, no. 4, pp. 809–819, 2018.

[75] T. Ezer and W. B. Corlett, "Is sea level rise accelerating in the Chesapeake Bay? A demonstration of a novel new approach for analyzing sea level data," *Geophysical Research Letters*, vol. 39, no. 19, 2012.

[76] Y. Cheng, T. Ezer, L. P. Atkinson, and Q. Xu, "Analysis of tidal amplitude changes using the Emd method," *Continental Shelf Research*, vol. 148, no. 2017, pp. 44–52, 2017.

[77] J. C. Jaeger, *Elasticity, Fracture and Flow*, MeThuen and Co. Ltd, London, 1964, http://link.springer.com/978-94-011-6024-7.

[78] W. Lowrie, *Fundamentals of Geophysics*, Cambridge University Press, Cambridge, 2007, http://gen.lib.rus.ec/book/index.php?md5=31E4E48407A2D46A40D16FA67176C29E.

[79] P. A. Hsieh, J. D. Bredehoeft, and J. M. Farr, "Determination of aquifer transmissivity from earth tide analysis," *Water Resources Research*, vol. 23, no. 10, pp. 1824–1832, 1987.

[80] H. F. Wang, *Theory of Linear Poroelasticity*, Princeton Univ. Press, Princeton, 2000, https://www.researchgate.net/publication/240345534_Theory_of_Linear_Poroelasticity.

[81] F. Du, X. Wen, and P. Zhang, "Post-seismic slip and deformation on the Luhuo segment of the Xianshuihe fault zone," *Chinese Journal of Geophysics*, vol. 53, no. 10, pp. 2355–2366, 2010.

Hindawi
Geofluids
Volume 2021, Article ID 8416485, 12 pages
https://doi.org/10.1155/2021/8416485

Research Article

Numerical Simulation and Field Measurement Analysis of Fracture Evolution and Seepage Response of Key Aquiclude Strata in Backfill Mining

Qiang Sun,[1,2] **Yong Chen**,[3] **Jianli Huang**,[3] **Dan Ma**,[1] **Cunli Zhu**,[1] **and Yue Liu**[1]

[1]*School of Mines, China University of Mining & Technology, Xuzhou, 221116 Jiangsu, China*
[2]*State Key Laboratory for Geomechanics and Deep Underground Engineering, China University of Mining & Technology, Xuzhou, 221116 Jiangsu, China*
[3]*Yanzhou Coal Mining Company Limited, Jining, 272101 Shandong, China*

Correspondence should be addressed to Qiang Sun; kkysun@126.com

Received 3 August 2021; Accepted 29 November 2021; Published 13 December 2021

Academic Editor: Jianwei Cheng

Solid waste backfill mining can effectively deal with gangue and other mining wastes, as well as control the movement and damage of rock strata. In this paper, the RFPA^{2D} rock failure process analysis software is used to study the fracture evolution and seepage response mechanism of the key aquiclude strata (KAS) under the conditions of different structural characteristics, interlayer rock thickness, and backfilling ratios in backfill mining. The simulation results show that, in backfill mining, soft rock plays a crucial role in the fracture repair of KAS with different structural characteristics. An increase in the KAS thickness from 15 to 35 m is shown to results in a continuously improved repair of KAS fractures. At the advancing distance of the working face of 50~100 m and the KAS thickness of 35 m, the minimum vertical seepage velocity of $(0.06\text{-}0.78) \times 10^{-2}$ m/s is reached. An increase in the backfilling ratio from 45 to 80% improves the control effect on the overlying strata. A case study of backfill mining in the Wugou Coal Mine located in the Anhui Province of China was conducted. At the goaf backfilling ratio of 80%, the composite KAS's good control effect was achieved, which minimized seepage and avoided the water in rush phenomena. The above engineering application ensured the safe backfill mining of coal resources.

1. Introduction

The global demand for green energy is related to the inevitable exhaustion of fossil fuels and increasing concern about the environment and air quality. China has also increased the direct use of renewables via wind and bioenergy for industry needs, solar thermal energy for heating, and biofuels for transport. However, the current share of coal in China's total power generation still exceeds 50% and is not expected to drop below 40% by 2040 [1]. China's demand for coal resources was about 3.55 billion tons in 2019, and further coal production envisages this sector restructuring, making most mines profitable and closing the least efficient mines [2].

Safe underground coal mining became increasingly challenging due to the complex hydrogeological conditions of numerous coal mines in China [3]. In the last seventy years, many coal resources under water bodies have been successfully mined out. However, most mining areas adopted waterproof coal pillar reservation methods, strip mining, thickness limiting mining, and drainage pressure reduction for coal mining under water bodies, which resulted in a large-scale waste of coal and water resources [4–6]. According to statistics, in Northern and Eastern China, mining coal-bearing strata, which are affected by confined aquifers, has sterilized over five billion tons of coal in waterproof coal pillars. In the past 20 years, there have been more than 800 water inrush disasters in mines, causing more than 4,000 deaths [7, 8]. These facts necessitate selecting a reasonable mining method for areas with aquifers, improving the coal recovery rate, ensuring production safety, and protecting water resources.

As a typical example of green mining technology, solid backfill mining (SBM) has been successfully applied to coal mining below large rivers, aquifers, and other water bodies [9, 10]. The theoretical research and field measurement results related to this technology show that under the coupling effect of the backfill body and surrounding rock, the development height of the water-conducting fractured zone (HWFZ) in the overlying strata can be limited, and the surrounding rock fractures readily compacted and closed. This greatly reduces the water inrush risk, improves the coal recovery rate, and protects water resources. SBM technology has become one of the important measures to realize water conservation mining, groundwater environment protection, and premining water table maintenance in green mines [11, 12]. However, theoretical research efforts of the global scientific community on safe mining, such as caving and backfill mining, under surface water bodies and aquifers, are mostly focused on controlling the development height of overburden water diversion fracture zone, HWFZ, which should not reach the water body and aquifer [13, 14]. The seepage and water inrush problem, influenced by the lithologic structure and the water isolation performance of each coal measure strata, has received much less attention.

To this end, the fracture evolution and seepage response mechanism of the key aquiclude strata (KAS) under conditions of different structural parameters, geologic characteristics, and backfilling ratios (backfilling materials' compaction bearing ratio in goaf) [15] in SBM mining are numerically simulated in this study using the RFPA^{2D} rock failure process analysis software. This paper investigates the effect of different geological structural parameters and multilayer characteristics of KAS on repairing damage caused by mining to overlying strata and the related vertical seepage velocity. Field measurements verify the simulation results obtained. The positive control effect of the composite KAS on the mitigation of excessive seepage and water inrush is demonstrated. The adopted method ensured safety for the SBM method and provided a reference for engineering applications under similar conditions.

2. Numerical Simulation Model and Scheme

2.1. Numerical Simulation Model. The rock failure process analysis (RFPA) is mainly used for numerical simulations of rock fracture progression. RFPA is a numerical analysis tool and calculation method based on finite element stress analysis and modeled statistical damage interpretation. RFPA fully considers the characteristics of nonlinearity, nonuniformity, and anisotropy in progressive fracturing and the potential failure of rock. In this software, the heterogeneity of rock material is fully considered, and complex macrononlinear mechanical problems are transformed into simple continuous media problems. At the same time, the effect and change of the coupling of stress, damage, and seepage resulting from the interaction between existing and newly initiated cracks are considered [16–20]. Therefore, the mining rock mass's failure principle and failure process align with the actual site situation. The RFPA mainly includes static, dynamic, combined dynamic and static, seepage, temperature, and multifield coupling analyses [21–24]. The basic principle of the RFPA^{2D} flow coupling module is based on the following assumptions.

(a) The seepage process in rock satisfies the Biot consolidation theory:

Equilibrium equation:

$$\frac{\partial \sigma_{ij}}{\partial x_{ij}} + \rho X_j = 0 (i, j = 1, 2, 3). \tag{1}$$

Geometric equation:

$$\varepsilon_{ij} = \frac{1}{2}\left(\mu_{i,j} + \mu_{j,i}\right)\varepsilon_v = \varepsilon_{11} + \varepsilon_{22} + \varepsilon_{33}. \tag{2}$$

Constitutive equation:

$$\sigma_{ij} = \sigma_{ij} - \alpha p \delta_{ij} = \lambda \sigma_{ij} \varepsilon_v + 2G\varepsilon_{ij}. \tag{3}$$

Seepage equation:

$$K\nabla^2 p = \frac{1}{Q}\frac{\partial p}{\partial t} - \alpha \frac{\partial \varepsilon_v}{\partial t}. \tag{4}$$

where ρ is density; σ_{ij} is stress tensor; ε_v is volume strain; δ is Kronecker constant; Q is Biot constant; G is shear modulus; λ is Lame coefficient; and ∇^2 is Laplace operator.

(b) The mesoelement in rock is elastic and brittle and has a certain residual strength, while its mechanical behavior conforms to the elastic damage theory. The maximum tensile strength and the Mohr-Coulomb criteria are taken as the threshold conditions of damage; that is, when the element satisfies both the maximum tensile stress-strain and the Mohr-Coulomb criteria, the initial damage occurs

(c) The rock structure is nonuniform. The damage parameters of the mesounit are assigned according to the Weibull distribution. The nonuniform Weibull distribution function and integral are derived as follows:

$$\varphi(E) = \frac{n}{E_0}\left(\frac{E}{E_0}\right)^{n-1} e^{-(E/E_0)n},$$

$$\varphi(E) = \int_0^e \varphi(x)dx = \int_0^e \left\{\frac{n}{E_0}\left(\frac{E}{E_0}\right)^{n-1} e^{-(E/E_0)n}\right\} dx = 1 - e^{-(E/E_0)n}, \tag{5}$$

where E and E_0 are the elastic modulus and the statistically average value of the mesounit of the rock medium, respectively, n is the homogeneity (smaller values of n correspond to more dispersed material properties), and $\varphi(E)$ is the statistical distribution density.

Table 1: The model geometry, physical, and mechanical parameters of overlying strata.

Lithology	Elastic modulus, GPa	Poisson's ratio	Cohesion, MPa	Internal friction angle, °	Density, kN·m^{-3}	Permeability coefficient, ×10^{-7} m·s^{-1}	Porosity
Overlying strata	8.5	0.28	4.5	32.0	24.0	0.20	0.10
Aquifer	22.0	0.25	8.0	34.0	26.0	11.57	0.25
Mudstone	6.7	0.32	2.7	24.0	22.0	0.05	0.01
Siltstone	16.3	0.28	8. 8	35.9	24.0	0.12	0.12
Fine sandstone	20.1	0.26	14.2	36.7	26.0	0.14	0.15
Immediate roof	7.2	0.32	3.5	28.0	22.0	0.08	0.05
Coal seam	5.5	0.30	2.5	26.0	14.0	0.30	0.20
Floor	25.0	0.25	12.0	32.0	25.0	0.15	0.02

(d) The relationship between permeability and stress-strain function is satisfied in the elastic state of the mesounit, and the permeability increases obviously after damage and fracture. The equation linking the stress σ_{ij} and permeability coefficient K of the model has the following form:

$$K = \xi K_0 \exp\left[-\beta\left(\frac{\sigma_{ij}}{3} - \alpha p\right)\right], \quad (6)$$

where K and K_0 are the permeability coefficient and its initial value, respectively; p is the pore water pressure; ξ is the sudden jump rate of permeability coefficient, α is the pore water pressure coefficient, and β is the stress-sensitive factor.

The effective stress and damage variables influence element's permeability variation, while its permeability also affects the stress distribution through the water pressure variation. Thus, the element stress and seepage fields are coupled. Based on the particular geological conditions of the Wugou Coal Mine mining face located in the north of Anhui Province, China, a basic 2D mechanical simplified model with length × height of 180 m × 80 m was established along the coal seam strike. The numerical simulation was selected to study the fracture evolution characteristics and seepage distribution law under the different influencing factors of the structural geology parameters, interlayer rock thickness, and KAS's backfilling ratios. The horizontal and vertical displacement constraints were applied to both sides and the bottom of the model. The model's upper surface applied the equivalent crustal stress uniform load of 5.75 MPa (corresponding to a buried depth of 300 m). The thickness of the model aquifer was 15 m. The water head boundary of 200 m was applied to both sides of the aquifer, while the remaining boundary was set as a water separation boundary. The mining area boundary was set as a zero-water head boundary. The numerical model was subdivided into 22,500 units in total. The revised Mohr-Coulomb model was used for the rock material within the framework of the plane strain simplified model. Physical and mechanical parameters, as well as seepage characteristics of the rock, are listed in Table 1.

2.2. Numerical Simulation Scheme. The analysis revealed that structural parameters, interlayer rock thickness, and backfilling ratios in the goaf were the key factors influencing the KAS control effect in the backfill mining under the aquifer. Using the RFPA^{2D} software, the effect of the above three influencing factors on the KAS water-holding performance in the backfill mining control was analyzed. A total of three schemes and ten groups of numerical models were designed (as shown in Table 2).

2.2.1. Scheme 1. Under the condition of backfilling ratio 65% and distance of 20 m between the coal seam and aquifer, the fracture evolution characteristics and seepage response of the KAS with four different structural features, namely, single-layer soft rock (mudstone), single-layer hard rock (fine sandstone), double-layer soft/hard composite KAS (mudstone and fine sandstone), and four-layer soft/hard composite KAS (mudstone, siltstone, mudstone, and fine sandstone), were analyzed. The distribution patterns used in the numerical simulation of the respective schemes are depicted in Figure 1.

2.3. Scheme 2. The mining geological conditions of the working face in the Wugou Coal Mine were combined with the three-layer composite KAS's occurrence characteristics composed of mudstone, siltstone, and fine sandstone. Fractures of the composite KAS were analyzed under the condition that the working face was 15, 25, and 35 m below the aquifer, and the backfilling ratio was 65%. For scheme 2, the evolution characteristics and seepage response distributions were derived via the numerical simulation for the respective schemes depicted in Figures 2(a), 2(c), and 2(d).

2.3.1. Scheme 3. Scheme 3 was used to analyze the fracture evolution characteristics and seepage distribution rules of the three-layer composite KAS composed of mudstone, siltstone, and fine sandstone during the mining process. The working face was 21.8 m below the overlying aquifer, while the goaf backfilling ratios were 45%, 65%, and 80%,

Table 2: Numerical simulation schemes and parameters.

Scheme no.	Lithology and parameters of KAS	Backfilling ratio, %	Interlayer rock thickness, m
1	Mudstone 18 m Fine sandstone 16 m Mudstone 9 m, fine sandstone 9 m Mudstone 5 m, siltstone 5 m, mudstone 5 m, fine sandstone 5 m	65	20
2	Mudstone 5.8 m, siltstone 1.3 m, fine sandstone 5.4 m	65	15
	Mudstone 10.5 m, siltstone 4.4 m, fine sandstone 7.6 m		25
	Mudstone 15.2 m, siltstone 7.5 m, fine sandstone 9.8 m		35
3	Mudstone 8.8 m, siltstone 3.4 m, fine sandstone 7.1 m	45	21.8
	Mudstone 8.8 m, siltstone 3.4 m, fine sandstone 7.1 m	65	
	Mudstone 8.8 m, siltstone 3.4 m, fine sandstone 7.1 m	80	

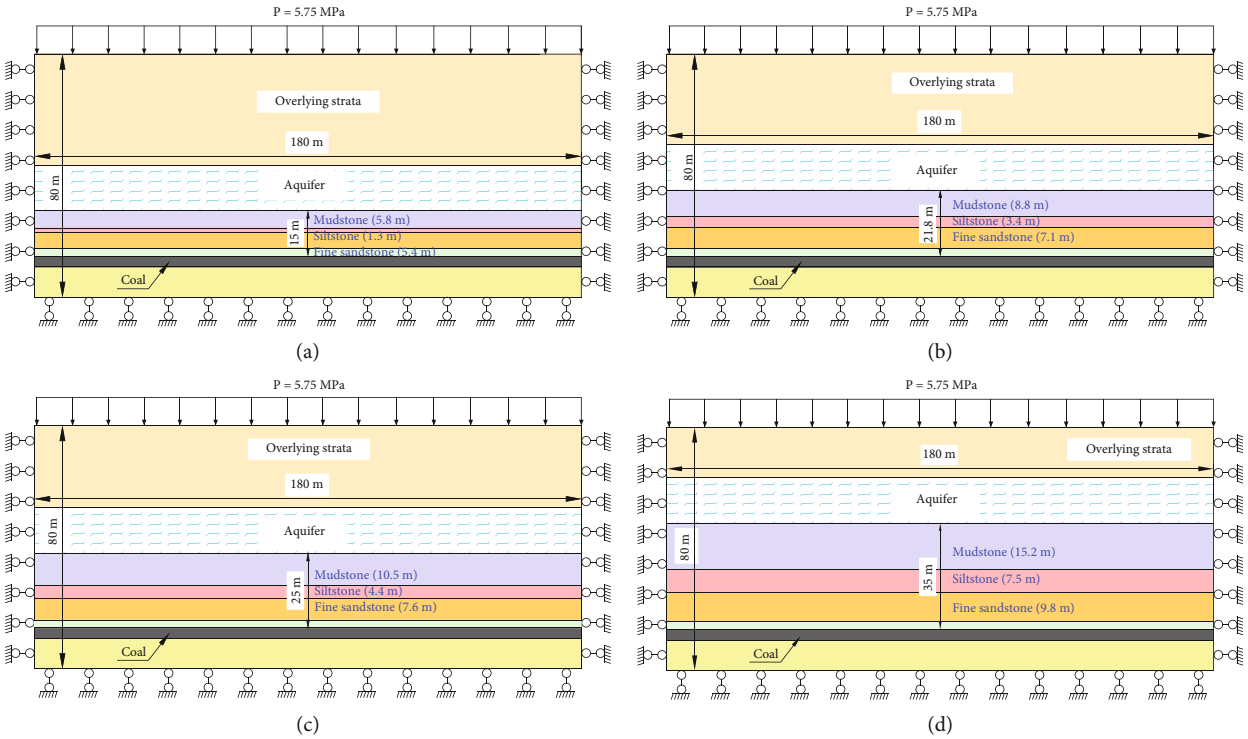

Figure 1: Numerical simulation model of KAS with different structural features: (a) single-layer soft KAS; (b) single-layer hard KAS; (c) double-layer soft/hard composite KAS; (d) four-layer soft/hard composite KAS.

respectively. The distribution pattern used in the numerical simulation is depicted in Figure 2(b).

3. Results and Discussion

According to the above schemes, the fracture evolution characteristics and seepage response patterns of the overlying rock in SBM with the mining height of 3.5 m, mining depth of 300 m, and the backfilling ratio of 65% were analyzed for different structural characteristics of single-layer soft rock, single-layer hard rock, and double- and four-layer soft/hard composites. For the working face advance of 100 m and the backfilling ratio of 65%, the cloud chart of the evolution of the overlying rock fracture and the seepage vector's distribution pattern for the above structural features were plotted (as shown in Figure 3).

The simulation results show that the fracture evolution characteristics of the KAS with the structural characteristics of a single-layer soft rock are relatively low. In contrast, the evolution process involves fracture initiation, development, compaction, and closure. This kind of rock structure is readily subjected to fracture compaction and closure under the coupling action of the backfill materials, overburden stress, water pressure, and good repair characteristics. Under the structural characteristics of single-layer hard rock, KAS's initial fracture development is relatively slow. With a continuous increase in the coal face's advance distance, when the first collapse and the periodic collapse step distance are

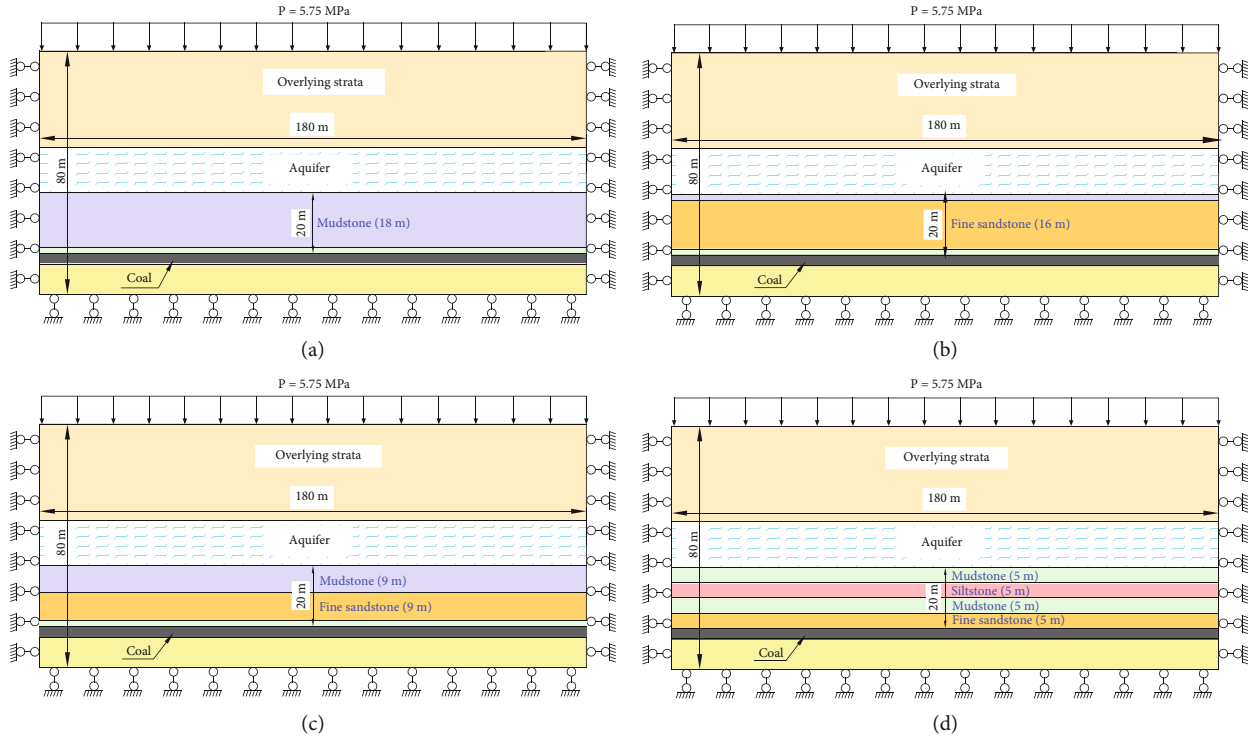

Figure 2: Numerical model with different interlayer rock thickness: (a) 15 m; (b) 21.8 m; (c) 25 m; (d) 35 m.

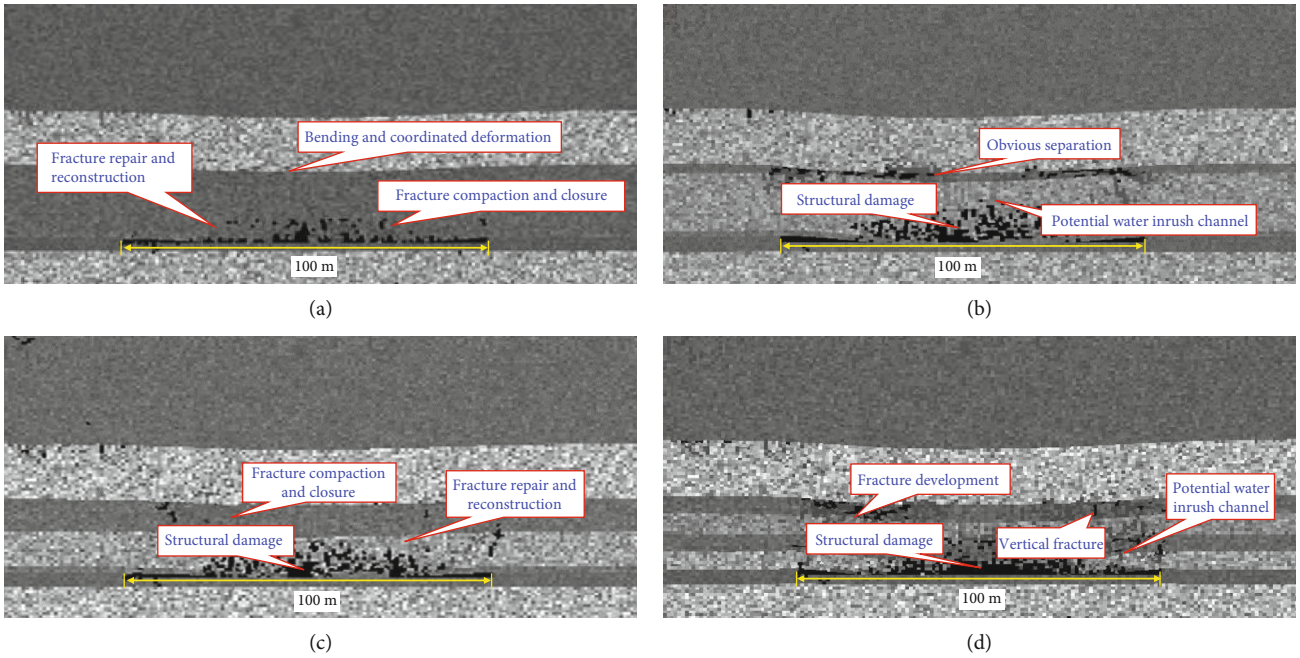

Figure 3: Fracture evolution and seepage response of different overlying strata structures: (a) single-layer soft KAS; (b) single-layer hard KAS; (c) double-layer composite KAS; (d) four-layer composite KAS.

reached, the rock stratum breaks suddenly and forms a fractured water inrush channel. After the fracture development and expansion, the compaction and closure of joints are unlikely, which leads to an extreme risk of a water inrush disaster. Therefore, the surrounding rock's stress state before fracture and damage should be controlled for this kind of KAS. Under the backfill materials' influence, a hinged supporting structure is readily formed after the hard rock's damage in the lower part of double- and four-layer soft/hard composites. This hinged fracture can be repaired to different degrees under the compaction of the soft upper rock. Noteworthy is that the overall control effect of the double-layer

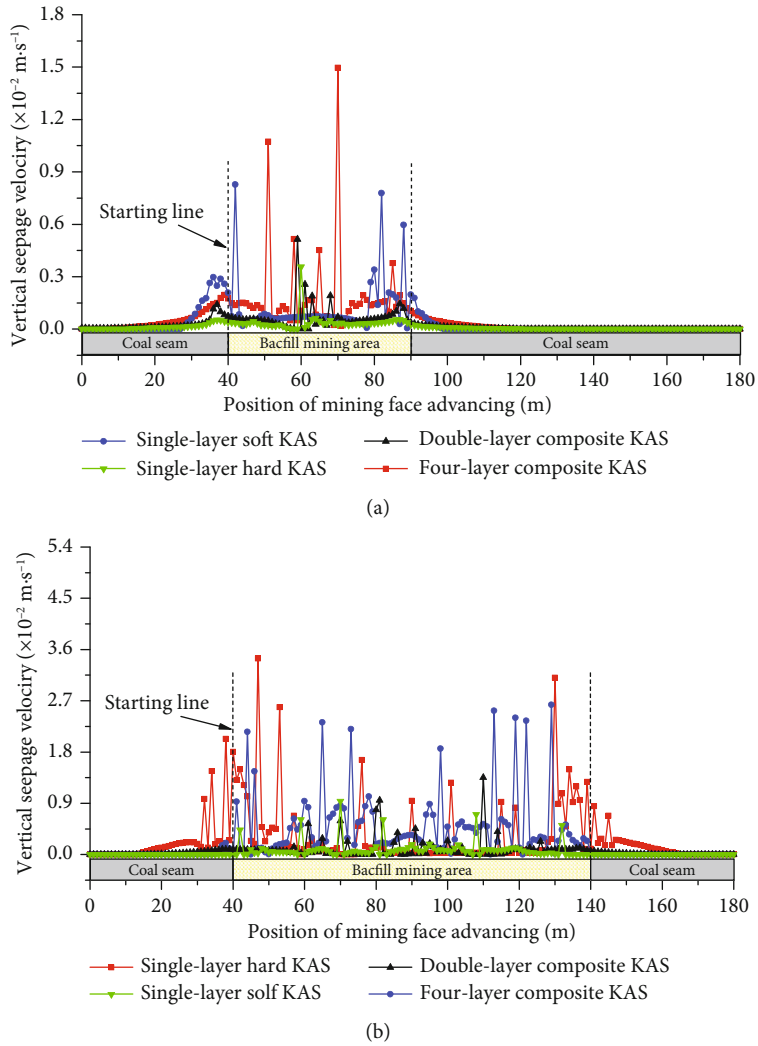

Figure 4: Vertical seepage flow distribution of KAS with different structural features: (a) advancing distance 50 m; (b) advancing distance 100 m.

soft/hard composite KAS is better than that of four-layer one, while the fracture development degree in both cases is relatively mild.

According to different structural characteristics, the vertical seepage velocity distribution curves in the middle of the KAS along the advancing direction of the working face were constructed, for advancing distances of 50 and 100 m, as shown in Figures 4(a) and 4(b), respectively.

It can be seen in Figure 4 that under different structural characteristics, the KAS seepage flow in the SBM water separation increases gradually with the continuous advance of the working face. The seepage flow's peak value is mainly distributed in the rear of the goaf, in front of the working face, and in the middle of the stope. At the mining distance of the working face of 50~100 m, under different structural characteristics of single-layer soft rock, single-layer hard rock, and double- and four-layer soft/hard composite, the variation ranges of the peak value of seepage velocity of the key layer are $(0.83 \sim 0.94) \times 10^{-2}$, $(0.36 \sim 3.40) \times 10^{-2}$, $(0.51 \sim 1.35) \times 10^{-2}$, and $(1.49 \sim 2.53) \times 10^{-2}$ m/s, respectively. Under different structural characteristics, the KAS variation in peak seepage flow is 1.13-2.63 times under the rock layering sequences of single-layer soft rock and double-layer soft/hard composite structures, which is relatively smooth as a whole and has a good control effect. In contrast, the variation in peak seepage flow in the key layer of water separation is 1.69-9.50 times under the rock layering sequences of single-layer hard rock and four-layer soft/hard composite structures, which is relatively large as a whole and easy to cause water inrush. Under the condition of the same backfilling ratio, the SBM control effect is closely related to the structural characteristics of the KAS. The structural hard rock mainly plays a mechanical load-bearing role, making self-repair after breaking quite problematic and promoting damage to this rock layer. The occurrence characteristics of the weak rock layer result in an obvious improvement in fracture compaction and repair. When the hard rock is damaged, the adjacent soft rock is compacted to close the potential water inrush fissures and form the water-resisting rock stratum, achieving the water-resisting layer's repair effect.

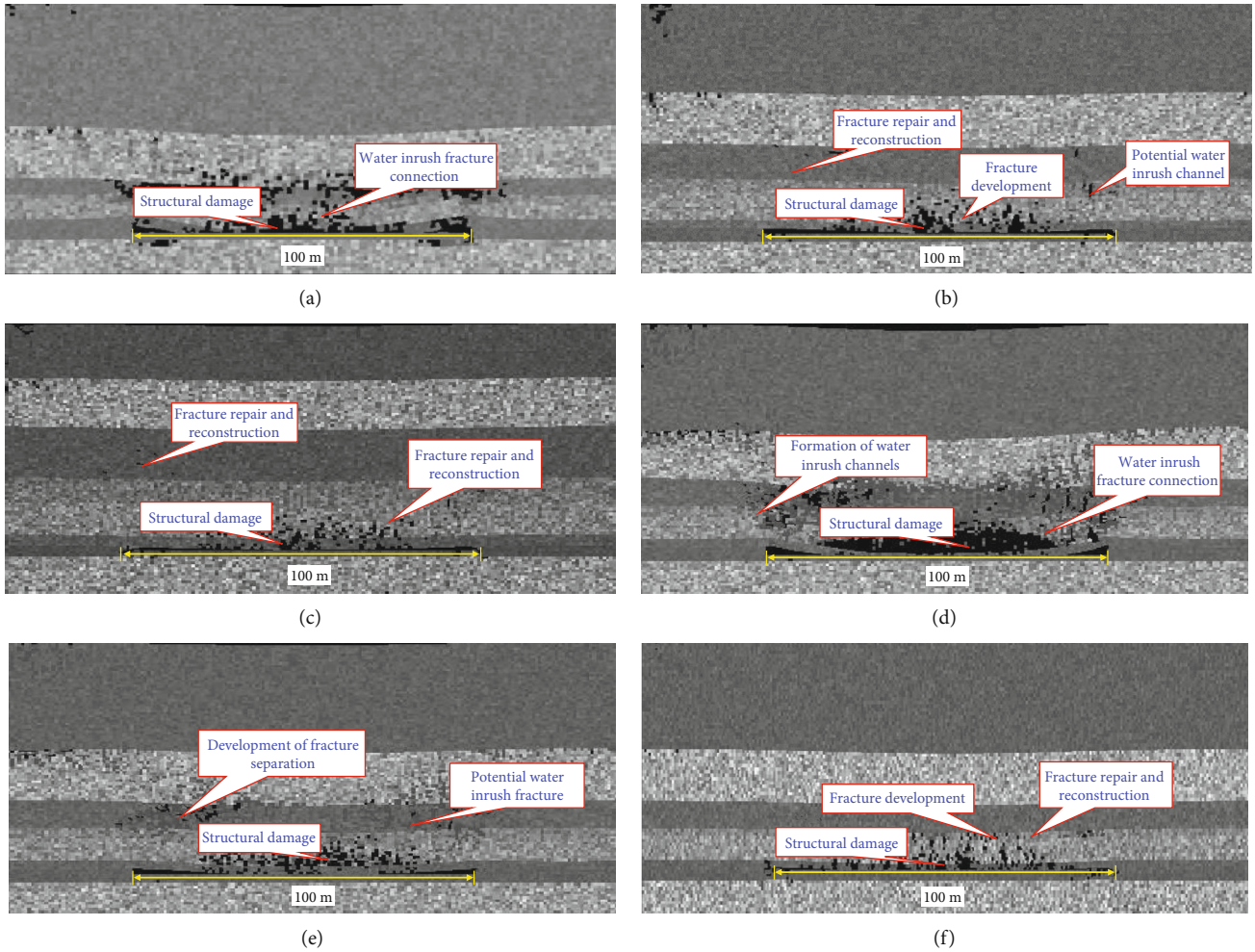

Figure 5: Fracture evolution characteristics and seepage response of overlying strata with different interlayer rock thickness and backfilling ratios: (a) 15 m; (b) 25 m; (c) 35 m; (d) 45%; (e) 65%; (f) 80%.

The overlying strata's fracture evolution characteristics and seepage response were also simulated for the mining height of 3.5 m, mining depth below ground of 300 m, backfilling ratio of 65%, and rock thicknesses of 15, 25, and 35 m between the working face and aquifer. At a backfilling ratio of 65% and the working face advance of 100 m, the cloud charts of the evolution of the overlying rock fracture under the influence of three different layer thicknesses were constructed (as shown in Figures 5(a)–5(c)). At the goaf backfilling ratio of 45, 65, and 80%, the overlying strata's fracture evolution characteristics and seepage response were further simulated. At the interlayer rock thickness of 21.8 m and the advancing distance of the working face of 100 m, the cloud chart of fracture evolution of overburden under the influence of different backfilling ratios was constructed (as shown in Figures 5(d)–5(f)).

It can be seen in Figures 5(a)–5(c) that when the rock thickness between the mining void and the aquifer is 15 m, the overall thickness of the KAS is relatively thin. With the continuous advancement of the backfill working face, the rock stratum is broken, and the mining-induced fractures expand to connect to the aquifer, and then, the water inrush fracture channel is formed. With an increasing rock thickness between the mining void and the aquifer, the overall performance of the composite KAS improves and tends to be beneficial. After backfilling the mining void (Figures 5(d)–5(f)), the lower fine sandstone and siltstone are damaged. However, they still maintain some mechanical load-bearing capacity. Under the soft upper rock action, the mining fractures are readily compacted and closed, and the rock mass has some integrity based on visual inspection of the number of fractures. Under the influence of the backfilling body's effective bearing capacity, with the continuous increase of the KAS thickness from 15 to 35 m, the overall control effect of the KAS in the backfill mining is significantly improved.

It can be seen in Figures 5(d)–5(f) that at a backfilling ratio of 45%, the overall damage of overburden is relatively severe. When the working face is mined for 50 m, the lower fine sandstone has been damaged. When the working face is mined 100 m in advance of the backfill, a large area of fracture and damage occurs in the composite KAS, and mining-induced fractures penetrate the aquifer, causing a water inrush disaster. Overall mining-induced damage to the KAS is reduced at a backfilling ratio of 65% and a 100 m mining advance. After mining the working face, a

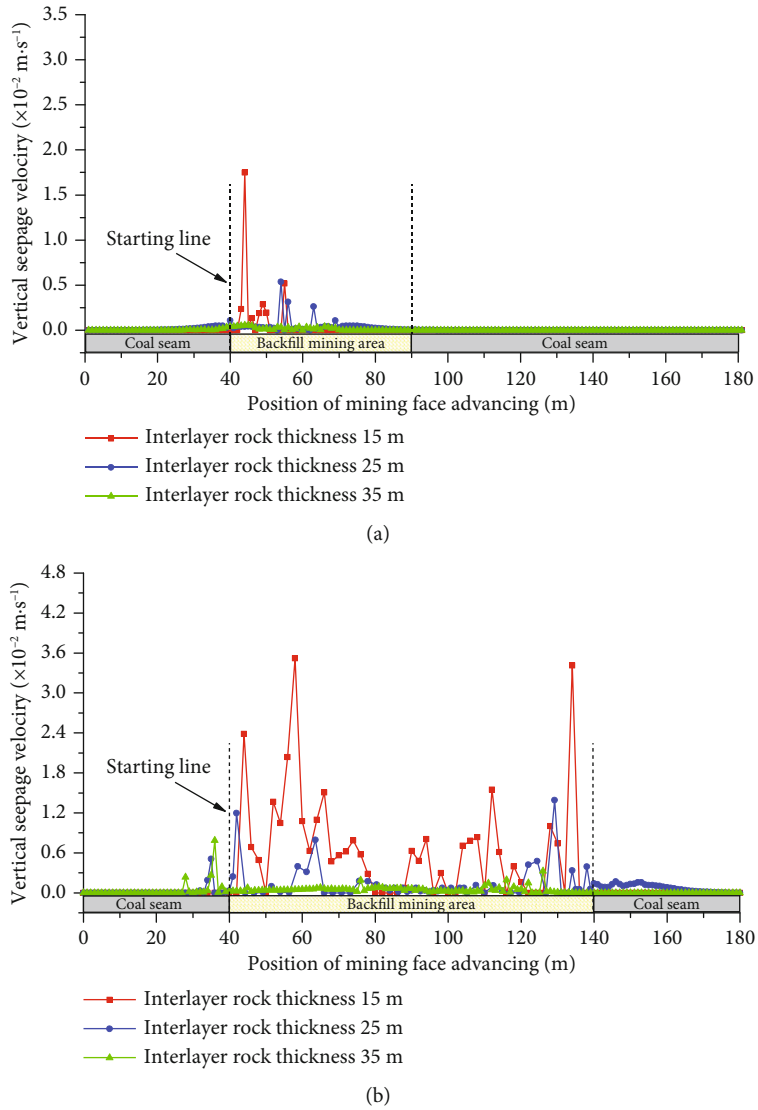

Figure 6: Vertical seepage flow distribution of KAS with different interlayer rock thickness: (a) advancing distance 50 m; (b) advancing distance 100 m.

mechanical bearing structure can be formed after the mining damage of the lower fine sandstone and siltstone. Compaction of the upper mudstone layer in the KAS plays an important role in maintaining water separation and seepage prevention. At a backfilling ratio of 80%, the fine sandstone and siltstone in the lower part of the composite KAS remain relatively intact after mining. The overall development of mining-induced rock fractures is restrained, while the soft mudstone layer in the upper part is unaffected by mining damage. Thus, the KAS can maintain the original water separation performance.

According to the characteristics of different layers, the vertical seepage velocity distribution curve in the middle of the KAS along the working face's advancing direction is shown in Figure 6. Corresponding to different backfilling ratios, the vertical seepage velocity distribution curve of the middle part of the KAS along the working face's advancing direction is shown in Figure 7.

It can be seen in Figure 6 that under the influence of different interlayer rock thicknesses, the seepage flow in the KAS increases gradually with the continuous advance of the working face. The peak value of seepage flow is also mainly distributed in the rear of the goaf, the front of the working face, and the middle of the stope. When the working face's advancing distance was 50~100 m, the variation ranges of the peak value of the seepage velocity of KAS were $(1.75 \sim 3.52) \times 10^{-2}$, $(0.54 \sim 1.55) \times 10^{-2}$, and $(0.06 \sim 0.78) \times 10^{-2}$ m/s for the working face thickness of 15, 25, and 35 m from the aquifer, respectively. With increase in KAS's thickness, the seepage flow peak value decreased at the same advance distance. Under the same backfill mining conditions, KAS's layer characteristics differ in the SBM control effect.

It can be seen in Figure 7 that at different backfilling ratios, the seepage flow of the KAS increases gradually with the continuous advance of the working face. The peak value of seepage flow is mainly concentrated in the fracture

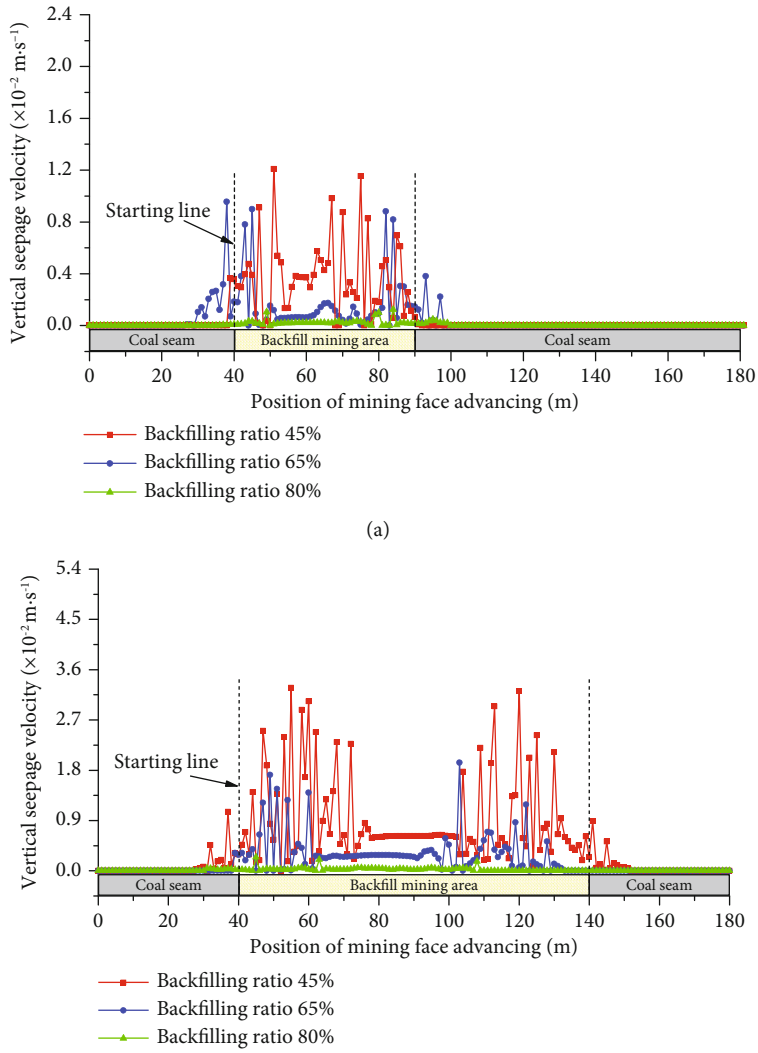

Figure 7: Vertical seepage flow distribution of KAS with various backfilling ratios: (a) advancing distance 50 m; (b) advancing distance 100 m.

development and failure position behind the goaf, in front of the working face, and in the middle of the stope. At the advancing distance of the working face of 50~100 m, the variation ranges of the peak values of the key layer's seepage velocity are $(1.21 \sim 3.28) \times 10^{-2}$, 2, and $(0.10 \sim 0.24) \times 10^{-2}$ m/s for the backfilling ratios of 45, 65, and 80%, respectively. With the continuous improvement of the filling rate, the backfilling body can effectively carry KAS's stress load, inhibiting the development and expansion of cracks. Under the joint action of the backfilling body, overlying rock, and water flow, cracks are readily compacted and bridged, which is beneficial to the KAS repair effect.

The Wugou Coal Mine with a field area of 21.74 km^2 is located in the Suixi County, Anhui Province, China. The eastern mining area is located in the northeastern part of the mine field with the ground elevations 26.37~7.67 m, which is a stable horizon and simple structure. With the strike length of 2.51 km and incline of 0.93 km, the average thickness of the primary mineable coal seam is 3.5 m. The bottom aquifer of Cenozoic thick and loose strata directly covers the outcrop of the main coal resources, which poses a serious threat to the safety of coal seam mining. Based on the simulation and theoretical assessments of the parameters related to the washing gangue material with particle size 0~50 mm on the ground, it was concluded that the mining starting position of the first CT101 backfilling coal face should be 21.8 m from the upper aquifer [25]. Considering that site's working face is dip mining and upward backfilling, a certain safety factor was applied to ensure the safe production of the first backfilling working face and improve the proficiency of the backfill mining technology. The final designed backfilling ratio was determined to be 80%. The KAS control effect was measured and analyzed by the transient electromagnetic method, which is practical and easy to operate. It is widely used in fracture damage and evaluation of aquifer rock mass above the mine. With the continuous mining of the working face, within the cumulative advance distance of 90 m of the working face, according to

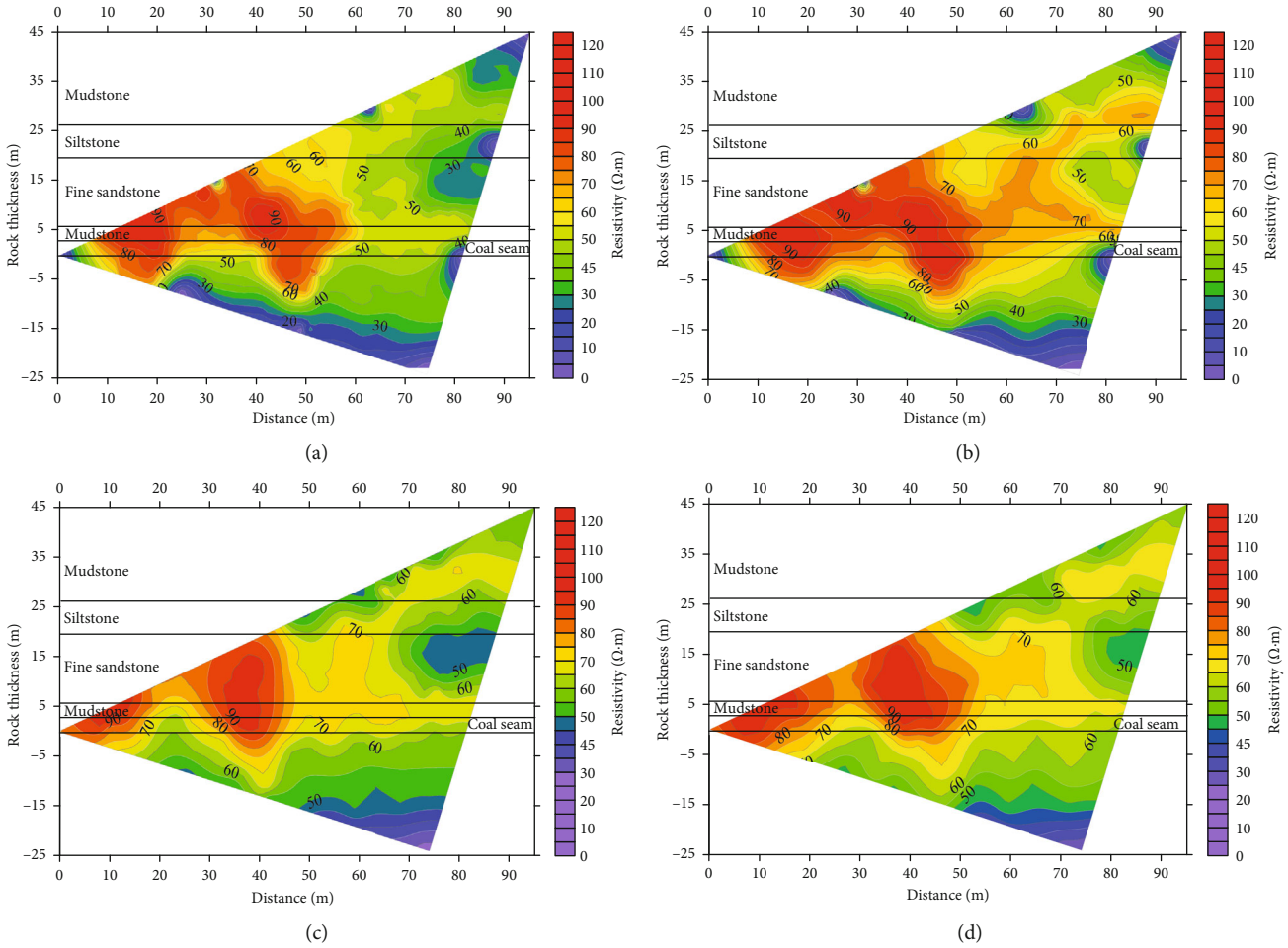

Figure 8: Detected resistivity profile during the backfill mining: (a) 40 m; (b) 60 m; (c) 70 m; (d) 90 m.

the field observation frequency requirements, the monitoring control area has been monitored many times, and resistivity results were obtained shown in Figure 8.

It can be seen in Figure 8 that with the mining of the working face, the roof fracture develops, and the resistivity value increases gradually. The area with an abnormal increase of resistivity is mainly within 25 m of the coal seam roof. The mudstone layer's resistivity in the upper part of the KAS is stable and mainly distributed within the range of 40~50 Ω·M. Using the KAS occurrence characteristics in the monitoring area and measured results, it was found that the fine sandstone and siltstone in the lower part of the KAS were partially damaged after the backfill mining. At the same time, the upper mudstone is free of fracture development. Under the coupling effect of the filling body and the overburden, the KAS is still stable. There is no water seepage and gushing in the underground working face, which shows that the control effect of backfill mining on the KAS is good, ensuring site production safety.

4. Conclusions

(1) Under the conditions of different structural parameters, interlayer rock thickness, and backfilling ratios, with the continuous advance of the backfill working face, the overlying rock fissures show different degrees of gradual development and evolution characteristics. Affected by this, KAS's seepage flow increases gradually with the continuous advance of the working face. The peak value of seepage flow is mainly observed in the rear of the goaf, in front of the working face, and in the middle of the stope damage location

(2) Different structural characteristics in SBM have different KAS control effects. KAS's backfilling control effect is gradually deteriorated when the structural characteristics correspond to single-layer soft rocks, double-layer soft/hard composites, four-layer soft/hard composites, and single-layer hard rocks. With a change in the working face's layer characteristics at distances of 15, 25, and 35 m from aquifers, the backfilling control effect of the KAS is gradually enhanced. The main factor controlling the KAS is the backfilling ratio, which determines KAS's repair effect. With an increase in the backfilling ratio, the backfill can effectively carry the overlying rock layer load. The inhibition of the development and expansion of fractures can enhance the compaction and bridging of previously formed fractures to ensure

the recovery and improvement of KAS's water separation performance

(3) The results obtained show that after the SBM technology application in the Wugou Coal Mine in the Anhui Province of China, the mudstone layer's resistivity in the KAS was stable, and the main distribution was within the range of 40~50 Ω·M. The overall control effect of the KAS was good: there was no seepage or water gushing phenomena. This ensured the safe mining of coal resources and achieved a good engineering application effect

Data Availability

All the data used to support the findings of this study are included within the article.

Conflicts of Interest

The authors have declared that we have no financial and personal relationships with other people or organizations that can inappropriately influence our work.

Acknowledgments

The authors appreciate the financial support of this work provided by the National Natural Science Foundation of China (grant no. 52104152) and the China Postdoctoral Science Foundation (grant no. 2020M671650).

References

[1] M. G. Qian and J. L. Xu, "Discussion of several issues concerning the development of coal industry in China," *Journal of Mining and Safety Engineering*, vol. 23, no. 2, pp. 127–132, 2006.

[2] Q. Wu, K. Tu, Y. F. Zeng, and S. Q. Liu, "Discussion on the main problems and countermeasures for building an upgrade version of main energy(coal) industry in China," *Journal of China Coal Society*, vol. 44, no. 6, pp. 1625–1636, 2019.

[3] J. F. Lou, F. Q. Gao, J. H. Yang et al., "Characteristics of evolution of mining-induced stress field in the longwall panel: insights from physical modeling," *International Journal of Coal Science & Technology*, vol. 8, no. 5, pp. 938–955, 2021.

[4] S. M. Wang, Q. X. Huang, L. M. Fan, Z. Y. Yang, and T. Shen, "Study on overburden aquiclude and water protection mining regionalization in the ecologically fragile area," *Journal of China Coal Society*, vol. 35, no. 1, pp. 7–14, 2010.

[5] Q. Wu, "Progress, problems, and prospects of prevention and control technology of mine water and reutilization in China," *Journal of China Coal Society*, vol. 39, no. 5, pp. 4–14, 2014.

[6] D. Z. Gu, Y. Zhang, and Z. G. Cao, "Technical progress of water resource protection and utilization by coal mining in China," *Coal Science and Technology*, vol. 44, no. 1, pp. 1–7, 2016.

[7] Z. Huang, *Seepage Evolution in Rock Masses and Catastrophe Mechanism of Water Inrush under Liquid-Solid Coupling Effect*, China University of Mining and Technology, 2016.

[8] L. M. Yin, K. Ma, J. T. Chen, Y. C. Xue, Z. Q. Wang, and B. Q. Cui, "Mechanical model on water inrush assessment related to deep mining above multiple aquifers," *Mine Water and the Environment*, vol. 38, no. 4, pp. 827–836, 2019.

[9] Q. Sun, J. X. Zhang, N. Zhou, and W. Y. Qi, "Roadway backfill coal mining to preserve surface water in western China," *Mine Water and the Environment*, vol. 37, no. 2, pp. 366–375, 2018.

[10] J. X. Zhang, Q. Sun, M. Li, and X. Zhao, "The mining-induced seepage effect and reconstruction of key aquiclude strata during backfill mining," *Mine Water and the Environment*, vol. 38, no. 3, pp. 590–601, 2019.

[11] D. Ma, J. X. Zhang, H. Y. Duan et al., "Reutilization of gangue wastes in underground backfilling mining: overburden aquifer protection," *Chemosphere*, vol. 264, article 128400, 2021.

[12] Q. X. Huang, B. N. Wei, and W. Z. Zhang, "Study of downward crack closing of clay aquiclude in shallow buried coal seam," *Journal of Mining and Safety Engineering*, vol. 27, no. 1, pp. 39–43, 2010.

[13] W. X. Wang, W. H. Sui, Q. H. Dong, W. W. Hu, and S. X. Gu, "Closure effect of mining-induced fractures under sand aquifers and prediction of overburden failure due to re-mining," *Journal of China Coal Society*, vol. 38, no. 10, pp. 1728–1734, 2013.

[14] J. W. Qu, Q. S. Liu, J. He, and Z. P. Liu, "Study of elastoplastic damage-healing model for argillite," *Chinese Journal of Rock Mechanics and Engineering*, vol. 33, no. s1, pp. 3192–3197, 2014.

[15] Q. Sun, *Mechanism and Method of Key Aquiclude Strata Reconstruction by Backfill Mining Technology*, China University of Mining and Technology, 2019.

[16] Q. Sun, G. H. Meng, K. Sun, and J. X. Zhang, "Physical simulation experiment on prevention and control of water inrush disaster by backfilling mining under aquifer," *Environmental Earth Sciences*, vol. 79, no. 18, 2020.

[17] J. Zhang, T. Yang, Y. P. Tian, and B. Wang, "Experimental test for destruction law of aquiclude under action of mining and seepage," *Rock and Soil Mechanics*, vol. 36, no. 1, pp. 219–224, 2015.

[18] C. H. Park and A. Bobet, "Crack initiation, propagation and coalescence from frictional flaws in uniaxial compression," *Engineering Fracture Mechanics*, vol. 77, no. 14, pp. 2727–2748, 2010.

[19] S. F. Wang, X. B. Li, and D. M. Wang, "Mining-induced void distribution and application in the hydro-thermal investigation and control of an underground coal fire: a case study," *Process Safety and Environmental Protection*, vol. 102, pp. 734–756, 2016.

[20] S. F. Wang, X. B. Li, and S. Y. Wang, "Separation and fracturing in overlying strata disturbed by longwall mining in a mineral deposit seam," *Engineering Geology*, vol. 226, pp. 257–266, 2017.

[21] S. Q. Yang, X. R. Liu, and H. W. Jing, "Experimental investigation on fracture coalescence behavior of red sandstone containing two unparallel fissures under uniaxial compression," *International Journal of Rock Mechanics and Mining Sciences*, vol. 63, pp. 82–92, 2013.

[22] M. Prudencio and M. van Sint Jan, "Strength and failure modes of rock mass models with non-persistent joints," *International Journal of Rock Mechanics and Mining Sciences*, vol. 44, no. 6, pp. 890–902, 2007.

[23] W. Han, Y. Jiang, H. Luan, Y. Du, Y. Zhu, and J. Liu, "Numerical investigation on the shear behavior of rock-like materials

containing fissure-holes with FEM-CZM method," *Computers and Geotechnics*, vol. 125, article 103670, 2020.

[24] B. Vásárhelyi and A. Bobet, "Modeling of crack initiation, propagation and coalescence in uniaxial compression," *Rock Mechanics and Rock Engineering*, vol. 33, no. 2, pp. 119–139, 2000.

[25] C. A. Tang, H. Y. Liu, W. C. Zhu et al., "Numerical approach to particle breakage under different loading conditions," *Powder Technology*, vol. 143-144, no. 26, pp. 130–143, 2004.

Hindawi
Geofluids
Volume 2021, Article ID 7335284, 15 pages
https://doi.org/10.1155/2021/7335284

Research Article

Dynamic Mechanical Properties and Damage Mechanism of Freeze-Thaw Sandstone under Acid Corrosion

Xiaoxiao Cao[1,2] **Meimei Feng**[1,2] **and Kangsheng Yuan**[1,2]

[1]*State Key Laboratory for Geomechanics & Deep Underground Engineering, China University of Mining & Technology, Xuzhou, Jiangsu 221116, China*
[2]*School of Mechanics & Civil Engineering, China University of Mining & Technology, Xuzhou, Jiangsu 221116, China*

Correspondence should be addressed to Meimei Feng; fengmeimei@cumt.edu.cn

Received 8 September 2021; Revised 9 October 2021; Accepted 12 November 2021; Published 8 December 2021

Academic Editor: Afshin Davarpanah

During the construction of geotechnical engineering in cold regions, the stability of rock is inevitably affected by freeze-thaw cycles and hydrochemical corrosion. In order to study the effect of hydrochemical corrosion on dynamic mechanical properties of freeze-thaw rocks, dynamic compression tests were carried out on sandstone samples corroded by four different concentrations of HCl solutions with the same number of freeze-thaw cycles using split-Hopkinson pressure bar (SHPB) test system. The coupling effects of freeze-thaw cycles with different concentrations of HCl solutions and strain rate on mechanical properties of sandstones were explored. The results showed that strain rate could enhance the dynamic compressive strength and peak strain but had no significant effect on the elastic modulus. The coupling effect of freeze-thaw cycles and acid corrosion weakened the dynamic compressive strength, and elastic modulus but enhanced the peak strain. In addition, X-ray diffractometer (XRD) and scanning electron microscope (SEM) were used to analyze the changes of mineral composition and microstructure damage of sandstone samples under the coupling effect of acid corrosion and freeze-thaw cycles. The analysis results were basically consistent with the damage characteristics of macro mechanical properties. The research results can provide reference for open pit coal mining in cold regions.

1. Introduction

China has abundance of coal resources, but they are not evenly distributed. More than 95% of open-pit coal mines are located in cold regions north of 38°N latitude. To increase the efficiency of coal mining via safety and stability, many scholars have conducted extensive study in areas such as roadway excavation [1, 2], stability monitoring [3, 4], and resource utilization [5]. However, due to seasonal variations and the diurnal cycle, freeze-thaw damage is unavoidable in coal mining. There have been episodes of low temperatures below 0°C in the past 8 months at the Xinjiang Beitashan Pasture Open-Pit Coal Mine [6]. In open-pit coal mines, bench blasting is the primary method of production. The intensity of blasting steadily increases in high-intensity mining conditions. According to real measurements, the stress wave produced by blasting may cause strain rates in the range of 10^1-10^3 s^{-1} in the rock mass [7], which corresponds to normal high impact dynamic loading. Several investigations reveal that the mechanical response characteristics and failure law of rock mass under dynamic stress differ considerably from those under static load [8, 9]. As a result, it is critical to investigate the dynamic impact test of rock under freeze-thaw cycles for coal mining in cold regions.

Rock materials are cemented by various mineral particles, and there are holes and fissures in the process of diagenesis. Under the influence of freeze-thaw cycles, the frost heaving force caused by the transformation of fracture water into ice is the main damage mechanism of rock freeze-thaw cycles [10, 11]. The factors affecting rock freeze-thaw strength mainly include rock type, temperature, water content, and freeze-thaw cycle times [12, 13]. Scholars at home and abroad have done a lot of research on changes of static mechanical properties of rock under freeze-thaw cycles [14, 15]. With the development of coal mining in cold regions, some scholars have paid attention to dynamic mechanical

properties of rock under freeze-thaw cycles. Li et al. [16] carried out a dynamic impact test on sandstone after freeze-thaw cycle, analyzed the change of pore structure after freeze-thaw cycle by combining with nuclear magnetic resonance technology, and explained the reason of degradation of dynamic strength. Based on the energy change during the dynamic failure process of red sandstone, Wang et al. [17] proposed an analysis method of damage evolution process after freeze-thaw cycles. Zhou et al. [18] carried out nuclear magnetic resonance (NMR) and dynamic compression tests on the frozen and thawed sandstone. The results showed that the dynamic elastic modulus and peak strength of sandstone decreased with the increase of freeze-thaw cycles, and the relationship between porosity and dynamic peak strength was polynomial. Ma et al. [19] carried out dynamic compression tests on sandy mudstone and mudstone with different freeze-thaw cycles. The results showed that the compressive strength decreased logarithmically with the increase of freeze-thaw cycles. Lu et al. [20] verified the influence trend of damage effect on the compressive strength of concrete by observing the microcrack growth trend. At present, the research achievements in this field mainly focus on dynamic compression mechanical properties of rock under freeze-thaw cycles. However, the actual underground environment is often intricate, and water-rock interaction has become a problem that cannot be ignored in geological engineering. Existing scholars have done related research on water-rock interaction, for example, Liu et al. [21, 22] and Yu et al. [23] have done related research on the permeability of rock fissures. But obviously these studies are far from enough. Groundwater, as the main factor affecting freeze-thaw cycle, contains different ionic components and pH. It is a complex hydrochemical solution. Under the action of freeze-thaw cycle, ground water produces frost heaving force and corrodes rocks in varying degrees. Therefore, not only freeze-thaw cycles but also water-rock interaction should be considered in rock mass engineering in cold regions.

In recent years, the mechanical properties of rock under freeze-thaw cycles and water-rock interaction have been concerned by scholars all over the world. Han et al. [24] analyzed the variation of mechanical properties of sandstone under different chemical solutions and freeze-thaw cycles. They concluded that strong alkaline solution can inhibit the freeze-thaw damage of sandstone when the freeze-thaw cycles were less than 25. Han et al. [25] quantitatively analyzed the damage degree of mechanical properties of sandstone under freeze-thaw cycles and different chemical solutions. Yang et al. [26] studied the damage effect of the mechanical properties of quartz sandstone, quartzite, and four different chemical solutions under the action of freeze-thaw cycles and verified it by analyzing the microstructure damage mechanism with scanning electron microscope (SEM). Gao et al. [27] studied the influence of the chemical environment and freeze-thaw cycle coupling on the damage characteristics of red sandstone. Qu et al. [28] and Li et al. [29] established damage evolution models, respectively, for the mechanical properties of sandstone under chemical corrosion and freeze-thaw cycles. Zhang et al. [30] studied the degradation of mechanical properties of sandstone under rapid freeze-thaw cycles and chemical corrosion and further studied the variation of rock splitting tensile strength and point load index with freeze-thaw cycles by using the attenuation function model. However, the current research results mainly focus on the study of static mechanical properties of rocks under freeze-thaw cycles and water-rock interactions. There are few studies on dynamic mechanical properties of rocks under freeze-thaw cycles and water-rock interaction. Under such background, this paper will study dynamic mechanical properties of rocks under freeze-thaw cycles and water-rock interaction, hoping to provide references for further related research.

In this paper, HCl solution will be used to simulate the hydrochemical environment of rock samples. Dynamic compression tests will be carried out on sandstone samples with different concentrations of HCl solutions under freeze-thaw cycles. The influence of varying concentrations of HCl solutions and freeze-thaw cycles on the strength and deformation properties of sandstone samples will be discussed, as well as the effect of strain rate. In order to accurately analyze the micromechanism change of samples, X-ray diffractometer (XRD) and scanning electron microscopy (SEM) will be used to analyze the mineral composition, variation, and internal damage of samples.

2. Materials and Methods

2.1. Preparation of Test Materials and Samples. The sandstone samples selected in this test were taken from a coal mine slope in Xinjiang, China. The main components are quartz, kaolinite, and muscovite. The longitudinal wave velocity of the sample is 1.7 km/s, the density is 2.14 g/m^3, and the static compressive strength is 14.7 MPa. According to the requirements of rock mechanics testing regulations, rock samples were cut into $\Phi 50 \times 25$ mm cylindrical standard specimens. After that, specimens were ground to ensure that the parallelism of the end face was less than 0.05 mm and the flatness was less than 0.02 mm [31].

In order to study the effect of acid corrosion of groundwater on mechanical properties of sandstones in cold regions, four concentrations of HCl solutions (0 mol/L, 0.01 mol/L, 0.1 mol/L, and 1 mol/L) were selected. After the solution preparation was completed, we used a high-precision pH detection pen to measure the pH value of the solution. The corresponding pH values were 7.0, 5.8, 3.2, and 1.1, respectively. Considering the time effect of initial compressive strength and chemical corrosion, 10 freeze-thaw cycles were carried out for all rock samples. Firstly, the specimens were dried in the drying oven. Then, the samples were immersed in HCl solutions. Finally, put the sample and solution into the freeze-thaw tester shown in Figure 1 for freeze-thaw cycles. According to the China Meteorological Administration, the annual minimum temperature is about −20°C, and the maximum temperature is about 20°C. Therefore, we set the freeze-thaw cycles temperature to -20°C. Each cycle lasted about 4 hours, and the number of cycles was 10 times.

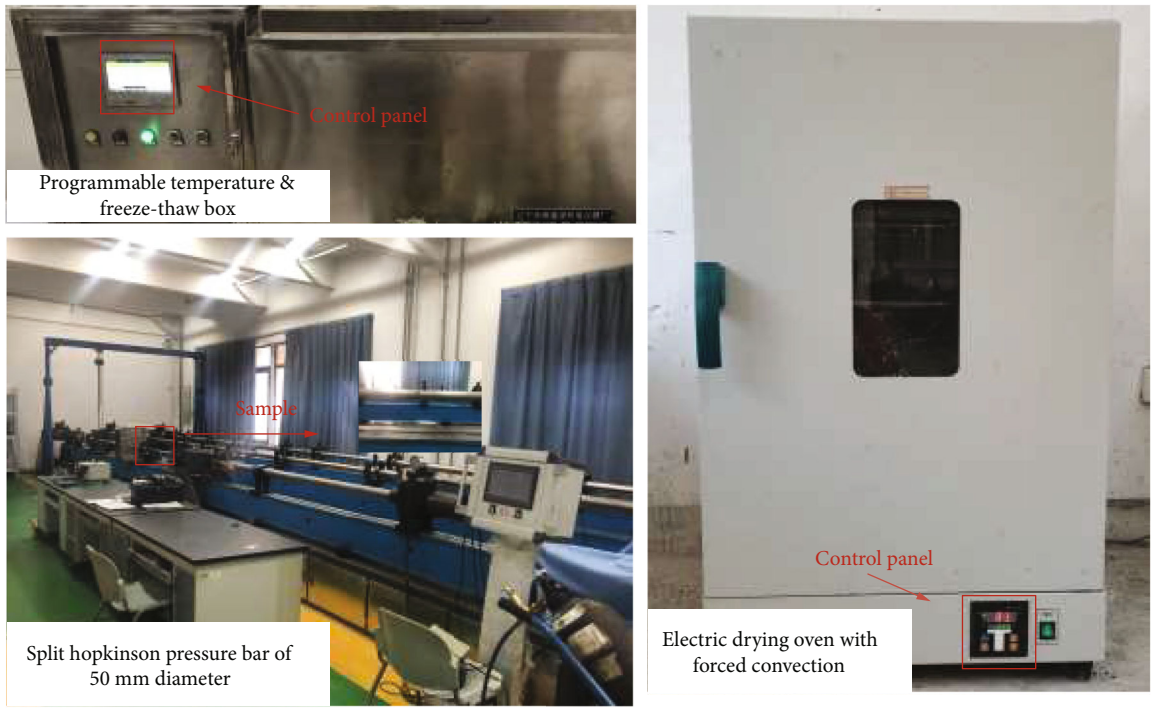

Figure 1: Experimental devices.

2.2. Test System. The split Hopkinson pressure bar (SHPB) device was the main test equipment. The variable cross-section SHPB test device with a diameter of 50 mm was adopted, as shown in Figure 2. The device consists of transmitter, pressure bar, energy absorption device, signal acquisition system, and signal processing system. The principle of the test was mainly to measure the incident wave, reflected wave, and transmission pulse in the transmission rod by using the strain gauge. Then, based on the assumption of one-dimensional stress wave and stress uniformity, the stress-strain relationship of the test sample was calculated by using the three-wave method in Equation (1) [32].

$$\begin{cases} \sigma = \dfrac{A}{2A_0} E(\varepsilon_i + \varepsilon_r + \varepsilon_t), \\ \varepsilon = \dfrac{c_0}{l_0} \displaystyle\int_0^t (\varepsilon_i - \varepsilon_r - \varepsilon_t) dt, \\ \dot{\varepsilon} = \dfrac{c_0}{l_0} (\varepsilon_i - \varepsilon_r - \varepsilon_t), \end{cases} \tag{1}$$

where E is Young's modulus of bars; c_0 is the elastic wave velocity in the pressure bar; ε_i, ε_r, and ε_t are the strain in the bar corresponding to the incident wave, reflected wave, and transmitted wave, respectively; l_0 and A_0 are the original length and cross-sectional area of the sample, respectively; and A is the cross-sectional area of the pressure bar.

2.3. Test Process. In the process of SHPB test, the prepared sample was taken out from the freeze-thaw test instrument and dried and then installed between the incident bar and the transmission bar to ensure that the sample was coaxial with the incident bar and the transmission bar. Subsequently, the SHPB tests were carried out under four impact pressures (0.3 MPa, 0.4 MPa, 0.5 MPa, and 0.6 MPa). After the tests, the incident wave, reflected wave, and transmitted wave signals were recorded by the strain gauge.

Dynamic stress equilibrium is the premise to verify the validity of SHPB test [33]. It can be seen from Equation (2) that the dynamic force at the incident bar was proportional to the sum of the incident wave and the reflected wave, and the dynamic force at the transmission bar was proportional to the transmitted wave. Figure 3 shows the dynamic stress balance process of the concrete test. It could be found that the sum of the strains corresponding to the incident wave and the reflected wave was approximately equal to the strain corresponding to the transmitted wave, while the cross-sectional area and Young's modulus of the bar remained unchanged. Therefore, the test could meet the dynamic stress equilibrium.

$$\begin{cases} F_1 = AE(\varepsilon_i + \varepsilon_r), \\ F_2 = AE\varepsilon_t, \end{cases} \tag{2}$$

where F_1 is the force on the incident bar and F_2 is the force on the transmission bar.

3. Experimental Results and Analysis

In order to reduce the dispersion, three effective tests were carried out under each test condition. According to the principle of SHPB test, the three-wave method is used for data processing. The average compressive strength, average elastic modulus, average strain rate, and other mechanical parameters of sandstone samples under different

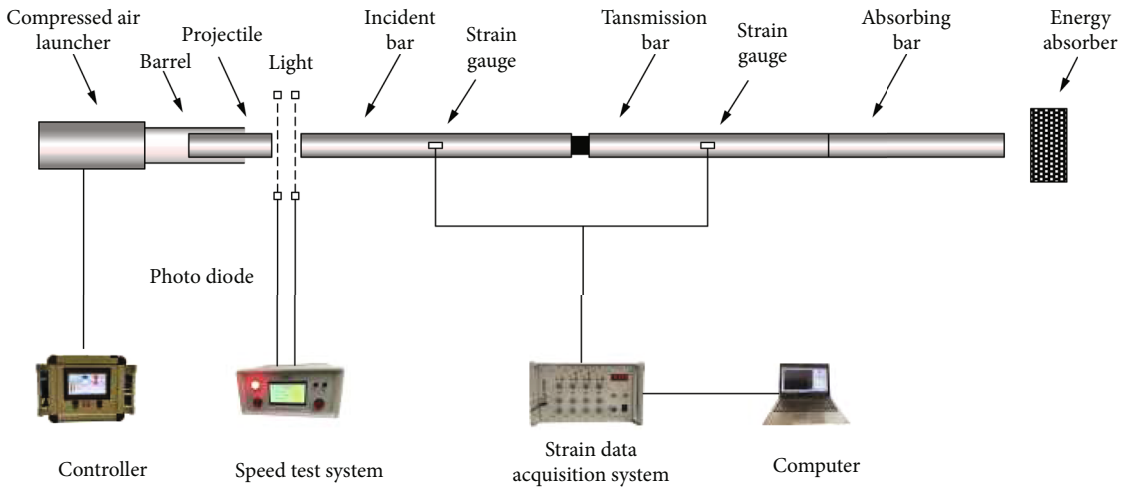

Figure 2: Split Hopkinson pressure bar of 50 mm diameter.

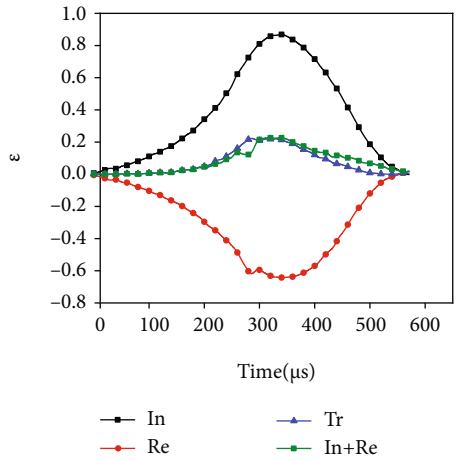

Figure 3: Strain balance check for a typical dynamic compression test.

concentrations of HCl solution and freeze-thaw cycle are obtained, as shown in Table 1.

3.1. Variation of Dynamic Stress-Strain Curves. The typical dynamic stress-strain curve of sandstone specimen is shown in Figure 4. Under the action of impact loads, sandstone mainly experienced the following deformation stages: (I) initial compaction stage, (II) linear elastic deformation stage, (III) plastic deformation stage, and (IV) failure stage.

Figure 5 shows the stress-strain curves of sandstone samples subjected to SHPB dynamic compression test under the coupling effect of HCl solutions with various concentrations and freeze-thaw cycles. Compared with Figure 3, it can be seen that variation characteristics of the stress-strain curves are as follows:

(1) The stress-strain curves of various concentrations of HCl solutions under freeze-thaw cycles had obvious compaction stages. When the pH value decreased from 7.0 to 1.1, the compactness of the prepeak region increased gradually. As the pH value

Table 1: Test results of samples at different pH values and impact speeds.

No.	pH	v (m·s^{-1})	$\dot{\varepsilon}$ (s^{-1})	σ_d (MPa)	ε_d (10^{-3})	E (GPa)
1	7.0	5.5	66.2	33.6	16.4	1.4
2	7.0	6.0	89.5	34.1	16.9	1.3
3	7.0	7.0	120.3	35.9	17.3	1.33
4	7.0	7.8	133.5	38.5	17.9	1.5
5	5.8	5.5	71.8	32.8	17.5	1.08
6	5.8	6.0	97.1	33.3	18.1	1.22
7	5.8	7.0	107.7	35.0	18.7	1.23
8	5.8	7.8	142.6	37.4	19.1	1.28
9	3.2	5.5	68.4	30.1	19.9	0.87
10	3.2	6.0	86.6	31.9	20.6	0.91
11	3.2	7.0	118.3	34.1	21.0	1.05
12	3.2	7.8	147.7	37.1	22.1	0.99
13	1.1	5.5	75.9	28.8	22.4	0.76
14	1.1	6.0	93.1	30.9	23.6	0.78
15	1.1	7.0	115.3	33.3	24.3	0.75
16	1.1	7.8	145.6	36.2	25.0	0.80

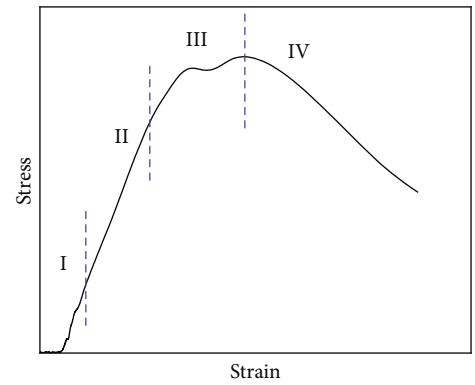

Figure 4: Typical dynamic stress-strain curve.

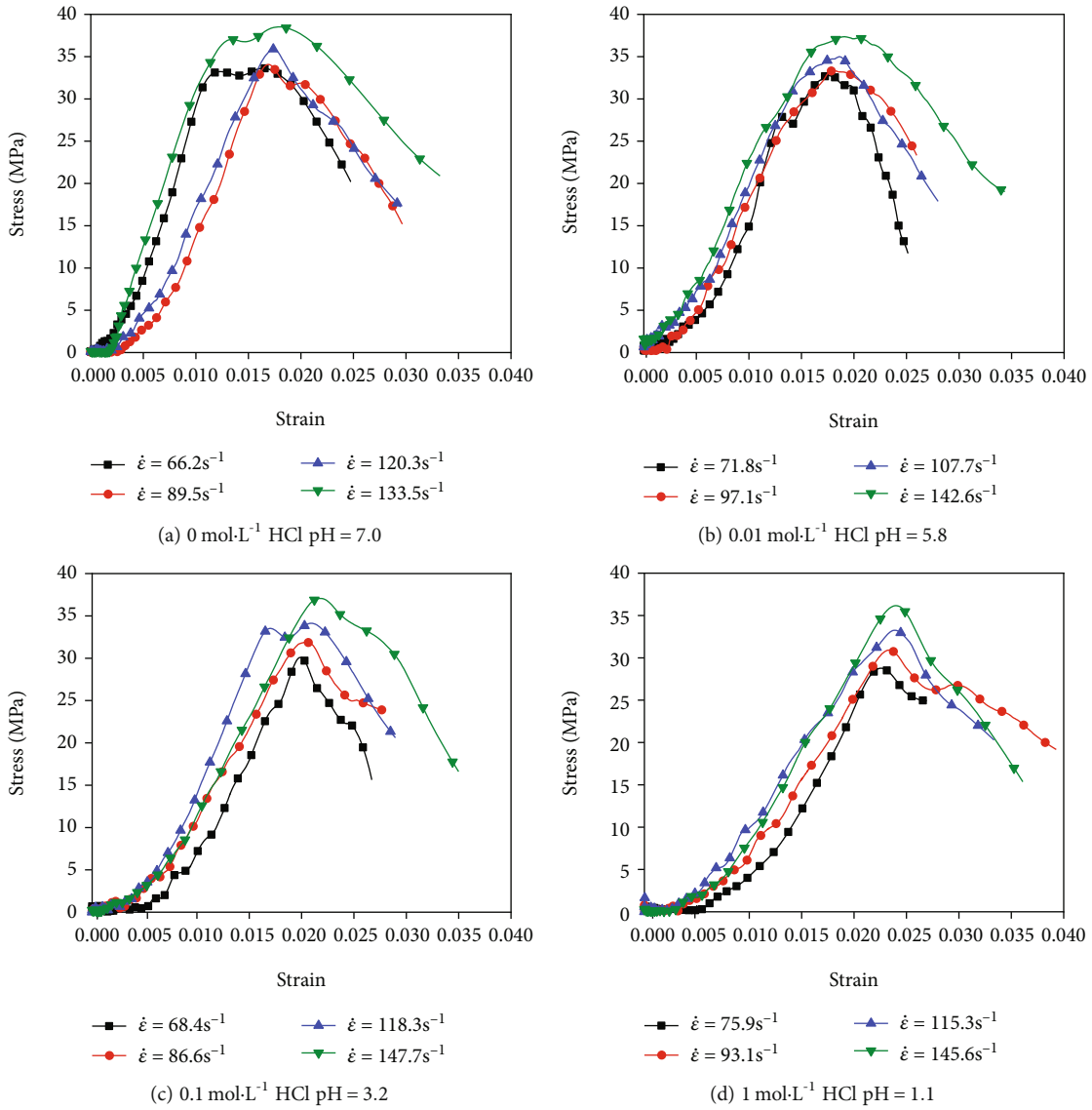

Figure 5: The dynamic stress-strain curves of the specimens with variation concentrations of hydrochloric acid solution affected by variation loading rates.

decreased, the internal corrosion of the sandstone increased. And the pores and fissures gradually expanded, which further increased the degree of compaction

(2) The stress-strain curves of each concentration of HCl solution had obvious linear elastic stages. In the prepeak region, the proportion of linear elastic deformation decreased to a certain extent with the increase of the solution concentration. When the pH value was 1.1, the proportion was the smallest. Thus, with the decrease of pH value, the influence of impact loads on the linear elastic deformation of sandstone became smaller

3.2. Variation of Dynamic Compressive Strength. Figure 6 shows the spatial surface characterizing the compressive strength σ_d to describe the coupling effect of pH and strain rate on the compressive strength. It can be seen from the figure that σ_d is positively correlated with the pH value and also positively correlated with strain rate. Figure 7 shows the relationship between the dynamic compressive strength of sandstone samples with the pH value and strain rate under the coupling effect of different concentrations of HCl solutions and freeze-thaw cycles. It can be found that

(1) The dynamic compressive strength of sandstone samples increased with the increase of strain rate under the coupling effect of the same concentration of HCl solution and freeze-thaw cycle. At pH of 7.0, as the strain rate increased from 66.2 s^{-1} to 133.45 s^{-1}, the compressive strength increased by 14.6%. At pH of 1.1, as the strain rate increased from 75.85 s^{-1} to 145.6 s^{-1}, the compressive strength increased by 25.7%. Equation (3) shows the linear fitting relationship of compressive strength with

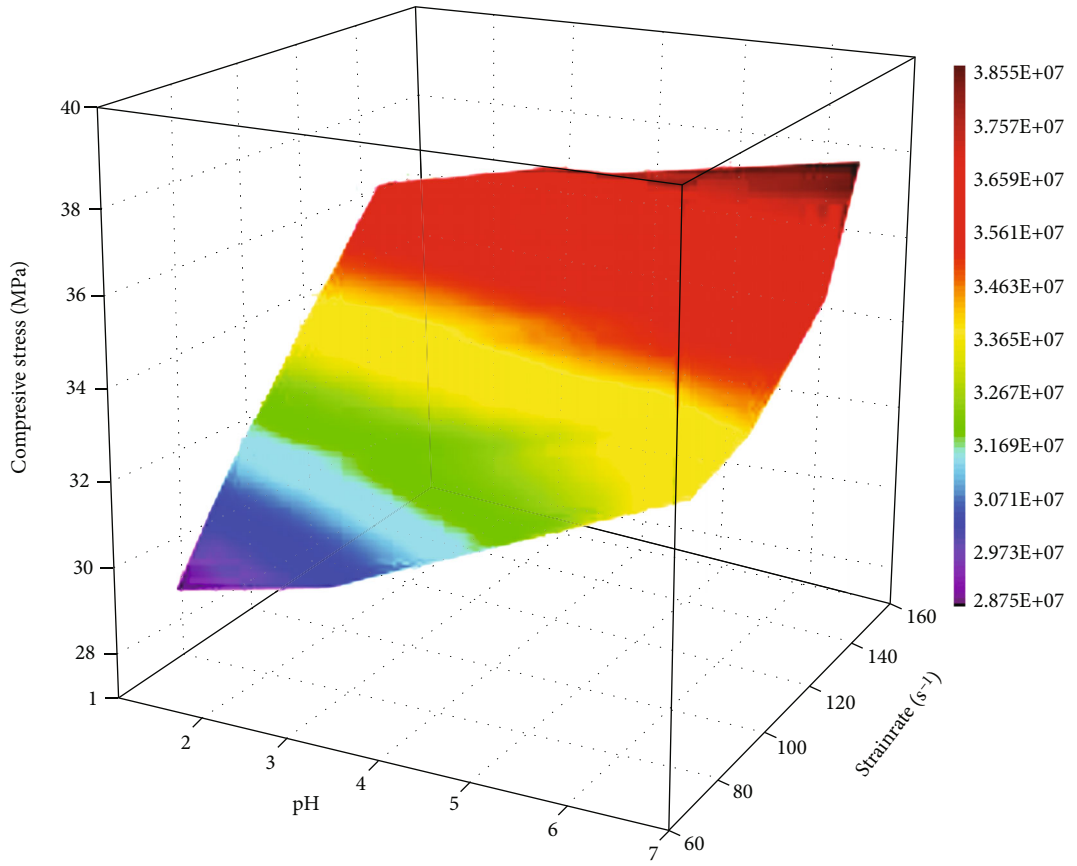

Figure 6: Coupling effect of the pH value and strain rate on compressive strength.

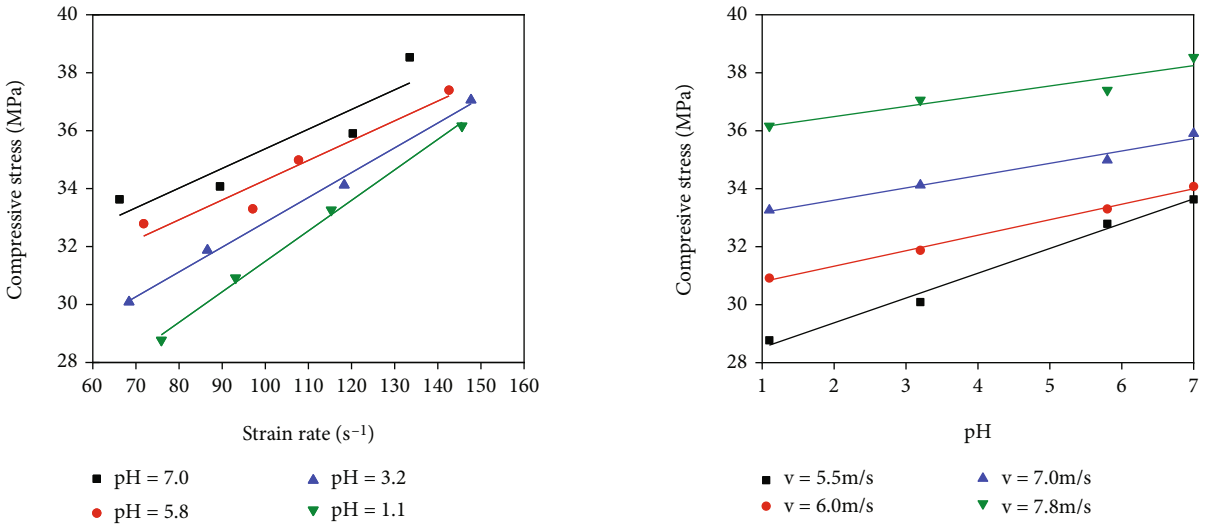

(a) Effect of strain rate on compressive strength under different pH values (b) Effect of pH value on compressive strength under different strain rates

Figure 7: Variation curves of compressive strength.

strain rate. As the pH value of the solution decreased, the slope of the linear fitting equation gradually increased. It showed that the dynamic compressive strength of sandstone samples became more sensitive to strain rate as the pH value decreased

(2) As the pH value of the HCl solution decreased, the dynamic compressive strength of the sample decreased successively. Specifically, when the strain rate is in the range of 66.2 s^{-1} to 75.9 s^{-1}, the compressive strength increased by 16.9% with the increase of pH value from 1.1 to 7.0. When the strain

rate is in the range of 133.5 s^{-1} to 147.7 s^{-1}, the compressive strength increased by 6.6% with the increase of pH value from 1.1 to 7.0. Equation (4) shows the linear fitting relationship of compressive strength with the pH value. As the strain rate increased, the slope of the linear fitting equation gradually increased. It showed that the dynamic compressive strength of sandstone samples became less sensitive to the pH value as the strain rate increased

$$\sigma_d = \begin{cases} 2.86 \times 10^7 + 6.79 \times 10^4 \dot{\varepsilon}, & R^2 = 0.86, \\ 2.75 \times 10^7 + 6.83 \times 10^4 \dot{\varepsilon}, & R^2 = 0.93, \\ 2.43 \times 10^7 + 8.57 \times 10^4 \dot{\varepsilon}, & R^2 = 0.99, \\ 2.24 \times 10^7 + 10.52 \times 10^4 \dot{\varepsilon}, & R^2 = 0.99, \end{cases} \tag{3}$$

$$\sigma_d = \begin{cases} 2.77 \times 10^7 + 8.55 \times 10^4 \mathrm{pH}, & R^2 = 0.99, \\ 3.03 \times 10^7 + 5.34 \times 10^4 \mathrm{pH}, & R^2 = 0.99, \\ 3.28 \times 10^7 + 4.25 \times 10^4 \mathrm{pH}, & R^2 = 0.98, \\ 3.58 \times 10^7 + 3.52 \times 10^4 \mathrm{pH}, & R^2 = 0.90. \end{cases} \tag{4}$$

3.3. Variation of Dynamic Peak Strain. Figure 8 shows the spatial surface characterizing the peak strain ε_d to describe the coupling effect of pH and strain rate on the peak strain. It can be seen from the figure that ε_d is positively correlated with strain rate and negatively correlated with pH. Figure 9 shows the relationship between peak strain and strain rate of sandstone samples under different concentrations of HCl solutions coupled with freeze-thaw cycles. It can be found that

(1) Equation (5) is the linear fitting relationship between the peak strain and the strain rate. It can be seen that the strain rate had a certain influence on the peak strain of the sample under the coupling effect of different concentrations of HCl solutions and freeze-thaw cycles. With the increase of strain rate, the peak strain of each concentration increased linearly. When pH = 7.0, as the strain rate increased from 66.2 s^{-1} to 133.45 s^{-1}, the peak strain increased by 9.1%; When pH = 1.1, as the strain rate increased from 75.85 s^{-1} to 145.6 s^{-1}, the peak strain increased by 11.6%. It showed that as the pH value decreased, the sensitivity of peak strain to strain rate increased

(2) The dynamic peak strain of the sample decreased with the increase of the pH value of HCl solution. When the strain rate is in the range of 66.2 s^{-1} to 75.9 s^{-1}, the peak strain decreased by 26.7% with the increase of pH value from 1.1 to 7.0. When the strain rate is in the range of 133.5 s^{-1} to 147.7 s^{-1}, the peak strain decreased by 28.4% with the increase of pH value from 1.1 to 7.0. Equation (6) shows the linear fitting relationship of peak strain with the pH value. As the strain rate increased, the slope of the linear fitting equation gradually increased. The results show that the dynamic peak strain of sandstone samples became more sensitive to the pH value at a high strain rate. In addition, as the strain rate increases, the increase rate of the slope of the fitting equation gradually decreases and finally tends to -1.14

$$\varepsilon_d = \begin{cases} 1.50 \times 10^{-2} + 2.13 \times 10^{-5} \dot{\varepsilon}, & R^2 = 0.94, \\ 1.59 \times 10^{-2} + 2.28 \times 10^{-5} \dot{\varepsilon}, & R^2 = 0.95, \\ 1.82 \times 10^{-2} + 2.57 \times 10^{-5} \dot{\varepsilon}, & R^2 = 0.96, \\ 1.99 \times 10^{-2} + 3.57 \times 10^{-5} \dot{\varepsilon}, & R^2 = 0.92, \end{cases} \tag{5}$$

$$\varepsilon_d = \begin{cases} 2.36 \times 10^{-2} - 1.05 \times 10^{-3} \mathrm{pH}, & R^2 = 0.99, \\ 2.46 \times 10^{-2} - 1.12 \times 10^{-3} \mathrm{pH}, & R^2 = 0.99, \\ 2.51 \times 10^{-2} - 1.14 \times 10^{-3} \mathrm{pH}, & R^2 = 0.98, \\ 2.61 \times 10^{-2} - 1.14 \times 10^{-3} \mathrm{pH}, & R^2 = 0.99. \end{cases} \tag{6}$$

3.4. Variation of Dynamic Modulus of Elasticity. In order to describe the coupling relationship between the pH value and strain rate on elastic modulus, Figure 10 shows the spatial surface characterizing elastic modulus E. It can be seen from the figure that E is linearly correlated with the pH value and shows certain nonlinear characteristics with strain rate. Figure 11 shows the relationship between dynamic modulus of elasticity and strain rate of sandstone samples under different concentrations of HCl solutions and freeze-thaw cycles.

(1) When the the pH value was 7.0, the dynamic elastic modulus first decreased and then increased with the increase of strain rate. When the pH value decreased from 5.8 to 1.1, the dynamic elastic modulus varied little with the increase of strain rate. Therefore, the strain rate had no obvious effect on the dynamic elastic modulus under the coupling effect of different concentrations of HCl solutions and freeze-thaw cycles

(2) With the decrease of the pH value, the dynamic elastic modulus decreased obviously. Equation (7) shows the linear fitting relationship of elastic modulus with pH value. As the strain rate increased, the slope of linear fitting equation first decreases and then increases. When the strain rate ranges from 66.2 s^{-1} to 75.9 s-1, 86.6 s^{-1} to 97.1 s^{-1}, 107.7 s^{-1} to 120.3 s^{-1}, and 133.5 s^{-1} to 147.7 s^{-1}, the elastic modulus increased by 83.7%, 67.6%, 78.4%, and 87.9%respectively, with the increase of the pH value from 1.1 to 7.0. The results show that when the strain rate ranges from 86.6 s-1 to 97.1 s-1, the sensitivity of dynamic elastic modulus to pH value is the lowest. After that, with the increase of strain rate, the sensitivity of dynamic elastic modulus to the pH value increased

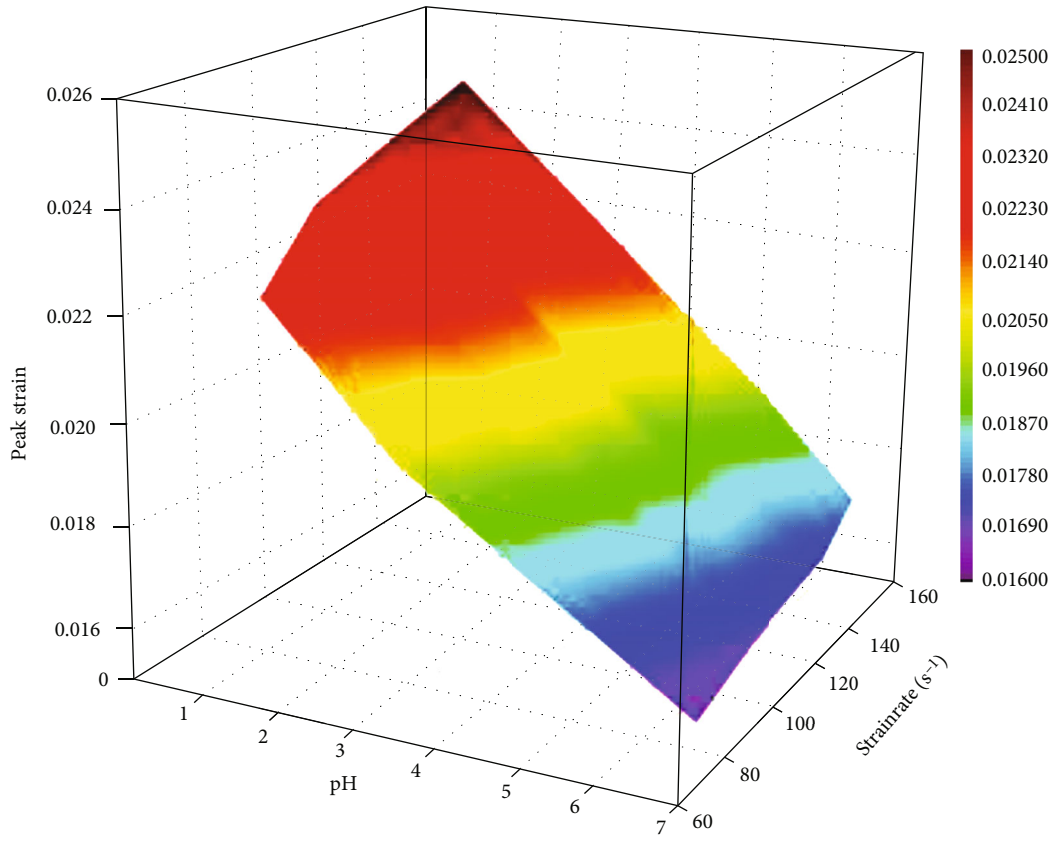

Figure 8: Coupling effect of pH value and strain rate on peak strain.

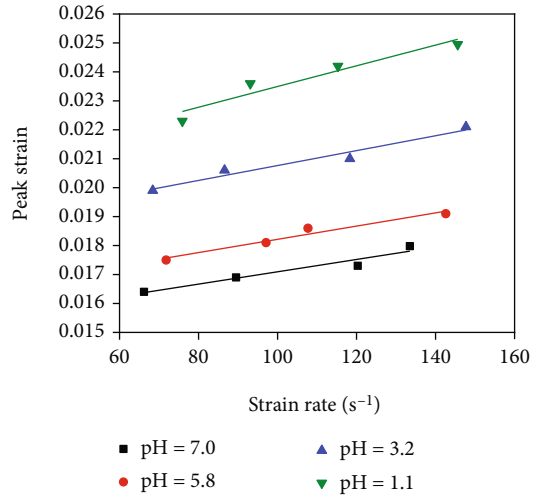

(a) Effect of strain rate on peak strain under different pH values

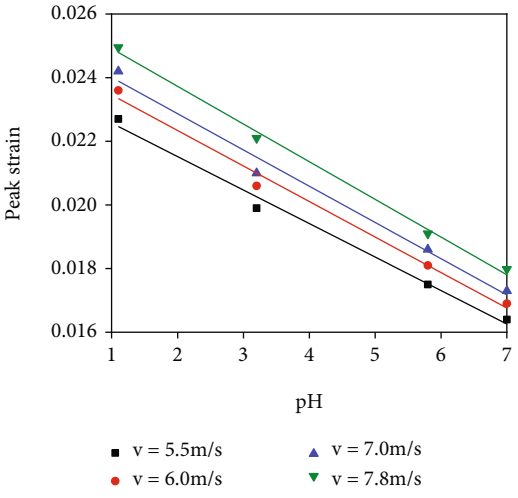

(b) Effect of pH value on peak strain under different strain rates

Figure 9: Variation curves of peak strain.

$$E = \begin{cases} 5.98 \times 10^8 + 1.01 \times 10^8 \text{pH}, & R^2 = 0.89, \\ 6.55 \times 10^8 + 9.36 \times 10^7 \text{pH}, & R^2 = 0.98, \\ 6.8 \times 10^8 + 9.53 \times 10^7 \text{pH}, & R^2 = 0.97, \\ 6.46 \times 10^8 + 1.16 \times 10^8 \text{pH}, & R^2 = 0.98. \end{cases} \quad (7)$$

4. Mesomechanism of Dynamic Mechanical Properties of Sandstone

The above test results showed that the strength and deformation characteristics of sandstones changed significantly under the coupling effect of different concentrations of HCl solutions

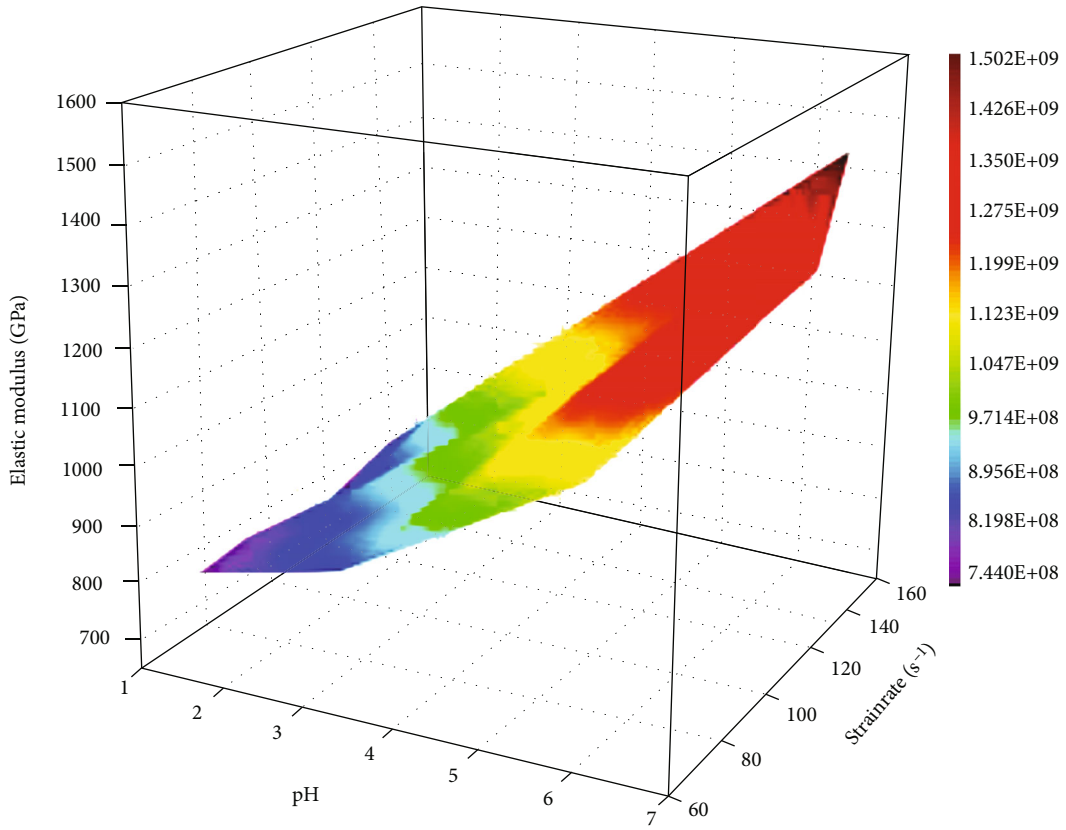

Figure 10: Coupling effect of pH value and strain rate on elastic modulus.

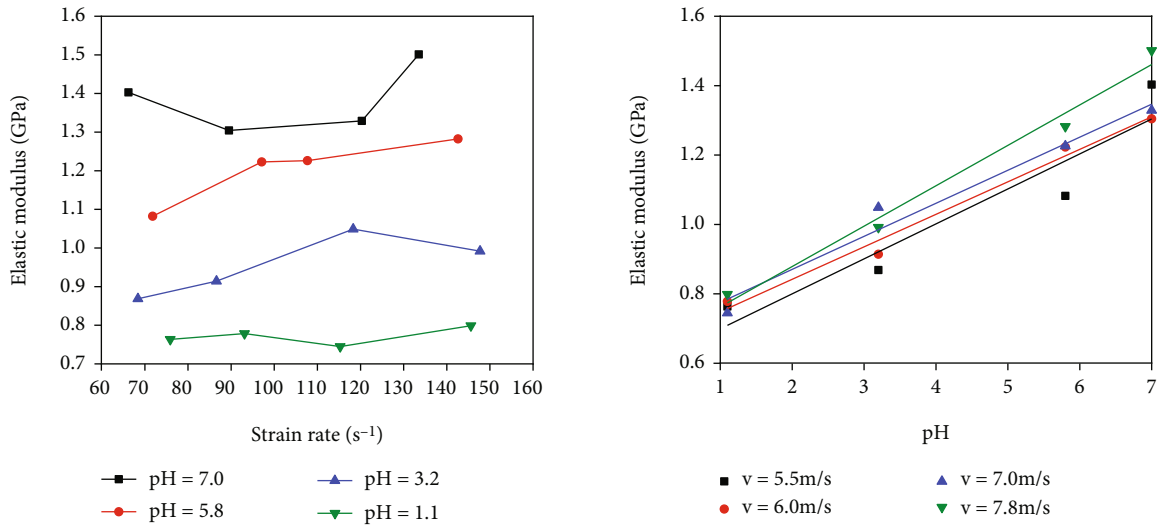

(a) Effect of strain rate on elastic modulus under different pH values (b) Effect of pH value on elastic modulus under different strain rates

Figure 11: Variation curves of elastic modulus.

and freeze-thaw cycles, and the damage evolution of rock material mechanical properties was closely related to the change of microstructure. Therefore, in order to accurately analyze the hydrochemical effect, X-ray diffractometer (XRD) and scanning electron microscopy (SEM) were used to confirm the changes of mineral composition and microstructure damage of samples, so as to verify the change law of rock mechanical properties.

4.1. Variation Law of Sandstone Composition. In order to determine the influence of HCl solution on the composition change of sandstone, X-ray diffraction was used to analyze the samples. Figure 12 shows the X-ray diffraction pattern of the sandstone corroded by various concentrations of HCl solutions. The main components of the samples in this test are quartz, kaolinite, and muscovite. Figure 13 shows the

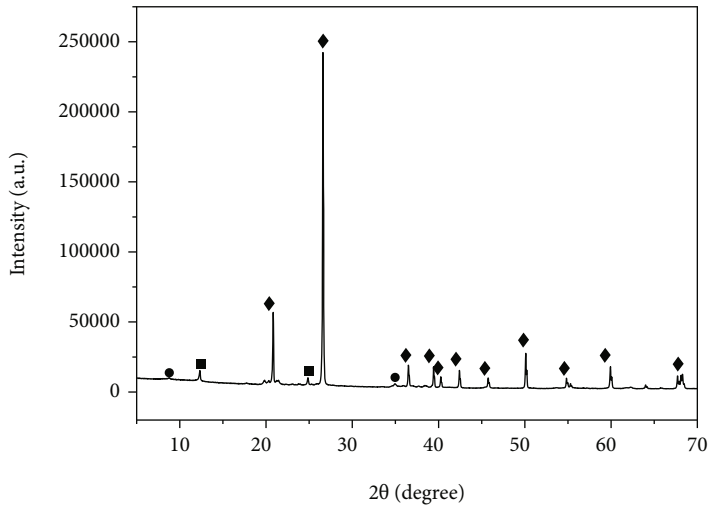

(a) 0 mol·L^{-1}pH = 7.2

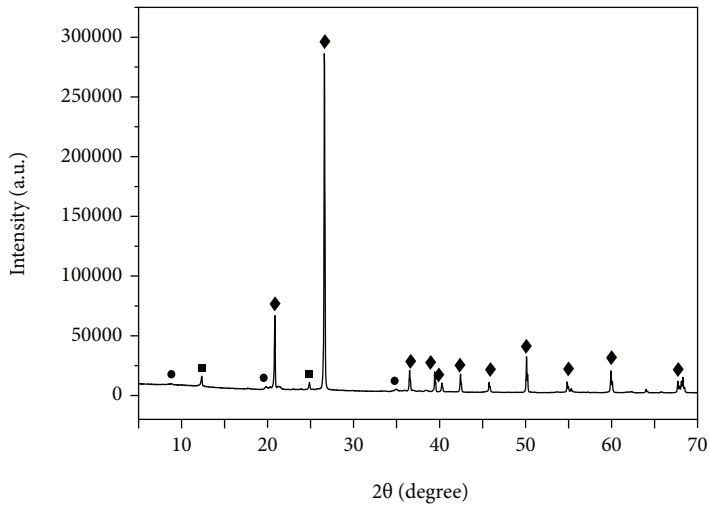

(b) 0.01 mol·L^{-1}pH = 5.6

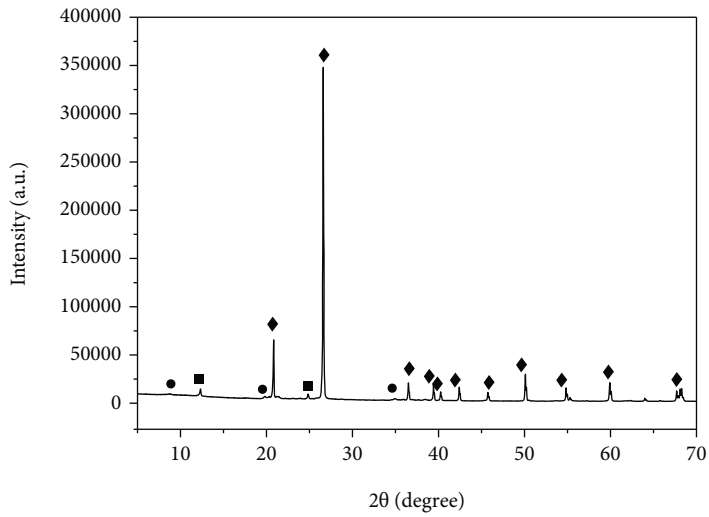

(c) 0.1 mol·L^{-1}pH = 3.2

Figure 12: Continued.

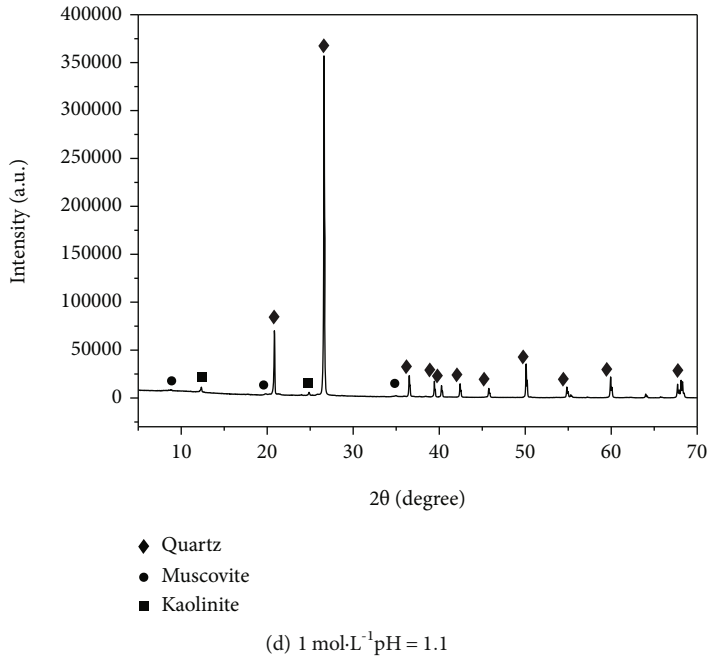

Figure 12: Mass fraction of sandstone component as it varies with the solution concentration.

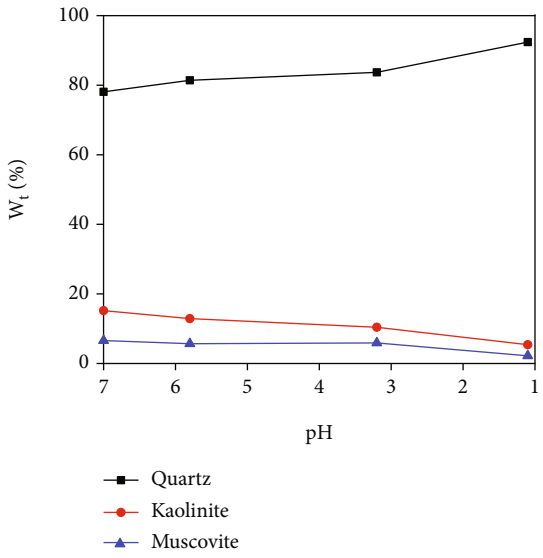

Figure 13: Variation curves of main mineral components with pH value.

variations of mineral composition W_t with pH value. The results are as follows.

The pH value of solution, the composition of solute, and the internal structure of rock are the main factors affecting the chemical corrosion of rock. In this paper, HCl solution is used to affect the chemical corrosion of the same sandstone after the same number of times. Therefore, the pH value of the solution is the main reason affecting the chemical corrosion of rocks. According to the XRD test results, the main components of the main possible chemical reactions of various mineral components in sandstone affected by HCl solution are shown in formula (8)–(11), which can be found in Liu et al. [34] and Lin et al. [35].

(1) The content of quartz in the sandstone was much greater than other mineral compositions, and 78.1% was in distilled water. In the range of pH 7.0 to 3.2, quartz content was relatively stable, showing a gradual upward trend. It increased from 78.1% to 83.7%, with a growth rate of 7.17%. When the pH value decreased to 1.1, it rose sharply from 83.7% to 92.4%, with the increase rate of 10.39%. The above situations might be caused by the hydrochemical reaction of quartz in distilled water and HCl solution:

$$SiO_2 + H_2O \longrightarrow H_4SiO_4 \quad (8)$$

$$SiO_2 + H^+ \longrightarrow Si^{4+} + 2H_2O \quad (9)$$

(2) Kaolinite was one of the main mineral content, and 15.2% was in distilled water. With the decrease of pH value, the content of kaolinite decreased gradually. In the range of pH 7.0 to 3.2, it decreased from 15.2% to 10.4%, and the rate of decline was 31.58%. When the pH value decreased to 1.1, it decreased from 10.4% to 5.4%, with a decrease rate of 48.08%. The results showed that when the pH value decreased to 1.1, the content of kaolinite decreased significantly. The following chemical reactions occurred in kaolinite affected by HCl solution:

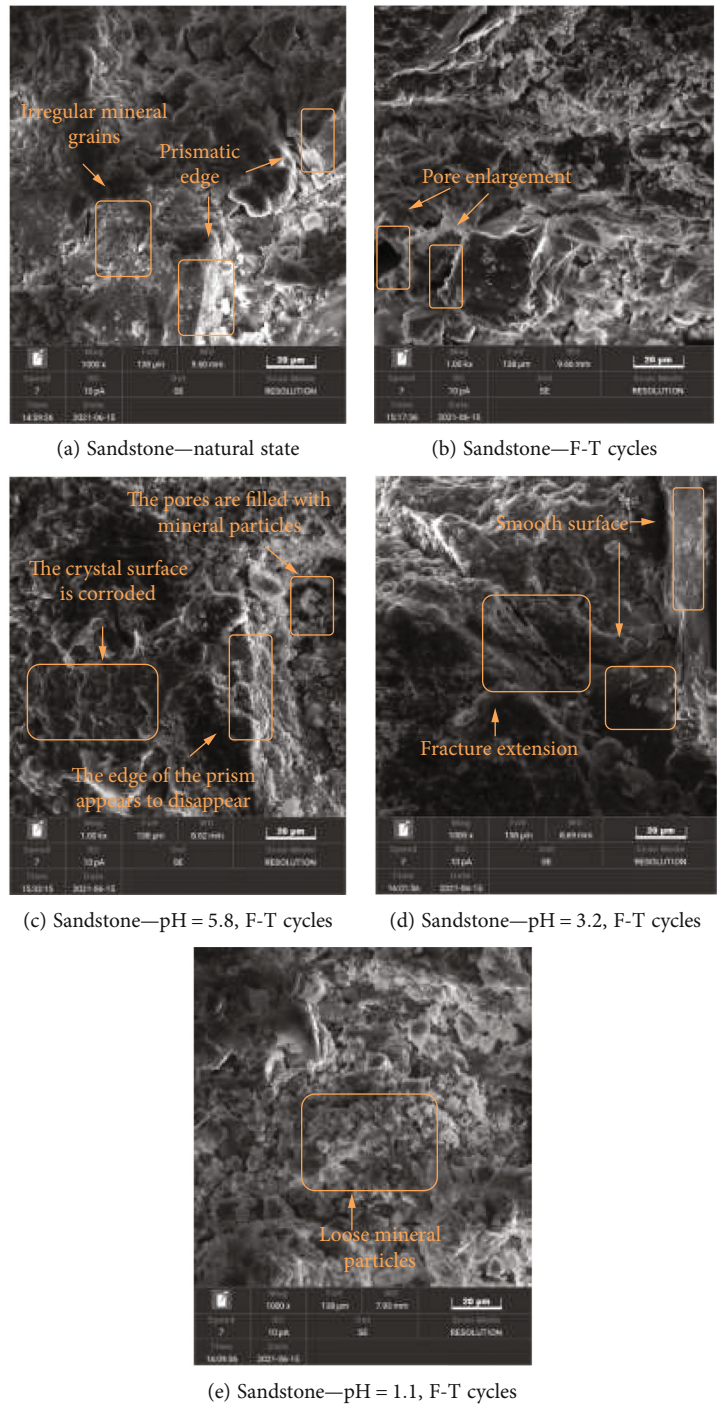

(a) Sandstone—natural state

(b) Sandstone—F-T cycles

(c) Sandstone—pH = 5.8, F-T cycles

(d) Sandstone—pH = 3.2, F-T cycles

(e) Sandstone—pH = 1.1, F-T cycles

Figure 14: Sandstone microscopic images under different test conditions.

$$Al_2Si_2O_5(OH)_4 + 6H^- \longrightarrow 2Al^{3+} + 2SiO_2 + 5H_2O \quad (10)$$

(3) The content of muscovite occupied the third place of the main mineral content, and 6.6% was in distilled water. Similarly, within the pH range of 7.0 to 3.2, the content of muscovite had little change, showing a slow downward trend. When the pH value decreased to 1.1, it decreased significantly from 5.9% to 2.2%, with a decrease rate of 62.71%. The following chemical reactions occurred in muscovite affected by HCl solution:

$$KAl_3Si_3O_{10}(OH)_2 + 10H^- = 3Al^{3+} + 3SiO_2 + K^+ + 6H_2O \quad (11)$$

Under the operation of freeze-thaw cycles, HCl solution has a considerable effect on sandstone samples. The fundamental reason for this is because during the freezing process, the solution in the pores expands after reaching the freezing point, causing pore fractures to form, and the expansion coefficients of mineral particles differ. It is also the cause of pore crack propagation. The contact area between the HCl solution and the mineral particles is increased after dissolution owing to the widening of pore fissures, and the chemical damaging impact is intensified. The sample is mainly composed of quartz, kaolinite, and muscovite. The chemical properties of quartz were relatively stable, and the hydrochemical effect was not obvious. With the increase of the concentration of HCl solution, the proportion of quartz content showed an increasing trend. Therefore, it could be seen that the hydrochemical reaction of quartz in distilled water and HCl solution was not the main factor for the significant change in its content. According to Equations (10) and (11), kaolinite and muscovite gradually decomposed and produced free SiO_2 particles under the corrosion of HCl solution. With the progress of hydrochemical reaction, the proportion of kaolinite and muscovite gradually decreased, and free SiO_2 particles were produced, making the proportion of quartz increase. With the deepening of hydrochemical reaction, the pore structure of the sandstone sample was destroyed, and the cementation between internal minerals became weak. With the decrease of pH value, the hydrochemical effect was strengthened, especially when the pH value decreased from 3.2 to 1.1. It showed that the mesomechanism of sandstone sample was consistent with the mechanism of mechanical properties.

4.2. Variation Law of Sandstone Microstructure. Mineral particles, cements, and pores are the fundamental components of rocks, and they also govern the macroscopic mechanical characteristics of rocks. The microstructure properties of sandstone were acquired using scanning electron microscope study of sandstone samples, as illustrated in Figure 14. The interior microstructure of the sample had changed significantly as a result of the coupling effect of the freeze-thaw cycles and the HCl solutions, as seen below:

(1) Microstructure of sandstone in natural state and freeze-thaw cycles state

In the natural state, there are some pores in the sandstone sample but the overall density is dense. There were many mineral crystal particles with uneven size and irregular distribution, but the degree of cementation between the particles was better. At the same time, the crystal surface was rough in the natural state. However, the internal cementation of the sandstone sample after the freeze-thaw cycles was weakened and the pores were enlarged and the surface was rougher.

(2) Microstructure of sandstone under freeze-thaw cycles and HCl solution corrosion

The irregular mineral particles inside the sample began to diminish as the pH reached 5.8. The surface looked to be eroded under the impact of the HCl solution. Simultaneously, the pores were filled with mineral particles, and the prismatic edge of the crystal began to dissolve. When the pH reached 3.2, the surface fractures began to grow and join to one another. The crystal particles deposited at the pore fractures grew, and the cementation between the crystal particles diminished gradually. When the pH was reduced to 1.1, the pores expanded substantially and the crystal volume shrank dramatically.

5. Conclusions

In this paper, the dynamic compression tests of sandstone samples corroded by HCl solutions of varying concentrations were performed using the SHPB system under four different impact loads over the same freeze-thaw cycles. The materials' composition and microstructure were examined using an X-ray diffractometer (XRD) and scanning electron microscopy (SEM). Based on the preceding analysis, the conclusions are reached:

(1) Under the coupling effect of freeze-thaw cycles and different concentrations of HCl solutions, the dynamic stress-strain curves of sandstone samples experienced four stages: initial compaction stage, linear elastic deformation stage, plastic deformation stage, and failure stage. With the decrease of pH value, the compaction stage gradually increased and the linear elastic deformation stage gradually decreased in the prepeak region

(2) In the same dynamic load, the pH value has a positive linear correlation with dynamic compressive strength and dynamic elastic modulus and a negative linear correlation with dynamic peak strain. With the increase of strain rate, the sensitivity of dynamic compressive strength and dynamic peak strain to the pH value increased. When the strain rate ranges from $86.6\,s^{-1}$ to $97.1\,s^{-1}$, the sensitivity of dynamic elastic modulus to the pH value is the lowest. After that, the dynamic elastic modulus increases with the increase of the strain rate. In the same concentration of HCl solution, the dynamic compressive strength and dynamic peak strain increased linearly with the increase of strain rate. With the decrease of the pH value, the sensitivity of dynamic compressive strength and dynamic peak strain to strain rate increased. However, the change of elastic modulus with strain rate was not obvious

(3) The findings of X-ray diffraction revealed that when the pH value declined, the quantity of quartz, the primary component, increased while the concentrations of kaolinite and muscovite, the subsidiary components, decreased. The concentrations of quartz, kaolinite, and muscovite altered dramatically when the pH was decreased to 3.2. The corrosion of HCl solution affected the content of each mineral component dramatically, which modified the mechanical characteristics of sandstone

(4) The particles in the crystal were impacted by the frost heaving force as a result of the freeze-thaw cycles, and pores and cracks formed. The internal mineral content of the sample and the HCl solution interacted with each other, resulting in the formation of pore fractures. The internal structure loosened, and the cementation deteriorated. Finally, the mechanical characteristics of sandstone were significantly reduced

Data Availability

Most of the data generated or analyzed during this study are included in this manuscript, and all of the data are available from the corresponding author on reasonable request.

Conflicts of Interest

The authors declare that they have no conflicts of interest.

Acknowledgments

Financial support for this work was provided by Fundamental Research Funds for the Central Universities (No. 2020ZDPYMS35).

References

[1] Q. Wang, M. He, S. Li et al., "Comparative study of model tests on automatically formed roadway and gob-side entry driving in deep coal mines," *International Journal of Mining Science and Technology*, vol. 31, no. 4, pp. 591–601, 2021.

[2] H. Jing, J. Wu, Q. Yin, and K. Wang, "Deformation and failure characteristics of anchorage structure of surrounding rock in deep roadway," *International Journal of Mining Science and Technology*, vol. 30, no. 5, pp. 593–604, 2020.

[3] T. Zhigang, Z. Chun, W. Yong, W. Jiamin, H. Manchao, and Z. Bo, "Research on stability of an open-pit mine dump with fiber optic monitoring," *Geofluids*, vol. 2018, 20 pages, 2018.

[4] C. Zhu, K. Zhang, H. Cai et al., "Combined application of optical fibers and CRLD bolts to monitor deformation of a pit-in-pit foundation," *Advances in Civil Engineering*, vol. 2019, 16 pages, 2019.

[5] J. Wu, H. Jing, Q. Yin, L. Yu, B. Meng, and S. Li, "Strength prediction model considering material, ultrasonic and stress of cemented waste rock backfill for recycling gangue," *Journal of Cleaner Production*, vol. 276, article 123189, 2020.

[6] G. Lin, M. Li, Y. Chen et al., "Dynamic tensile mechanical properties and fracture characteristics of water-saturated sandstone under the freezing effect," *International Journal of Geomechanics*, vol. 21, no. 5, p. 04021044, 2021.

[7] Y. Yu, "The effect of dynamic properties of rock on blasting under high strain rate," *Chinese Journal of Rock Mechanics and Engineering*, vol. 12, no. 4, pp. 345–352, 1993.

[8] A. Fakhimi, P. Azhdari, and J. Kimberley, "Physical and numerical evaluation of rock strength in Split Hopkinson Pressure Bar testing," *Computers and Geotechnics*, vol. 102, no. June, pp. 1–11, 2018.

[9] X. Liu, F. Dai, R. Zhang, and J. Liu, "Static and dynamic uniaxial compression tests on coal rock considering the bedding directivity," *Environment and Earth Science*, vol. 73, no. 10, pp. 5933–5949, 2015.

[10] N. Matsuoka, "Mechanisms of rock breakdown by frost action: An experimental approach," *Cold Regions Science and Technology*, vol. 17, no. 3, pp. 253–270, 1990.

[11] Y. Inada and K. Yokota, "Some studies of low temperature rock strength," *International Journal of Rock Mechanics and Mining Science and Geomechanics Abstracts*, vol. 21, no. 3, pp. 145–153, 1984.

[12] M. Bellanger, F. Homand, and J. M. Remy, "Water behaviour in limestones as a function of pores structure: Application to frost resistance of some Lorraine limestones," *Engineering Geology*, vol. 36, no. 1-2, pp. 99–108, 1993.

[13] G. M. Xu and Q. S. Liu, "Analysis of mechanism of rock failure due to freeze-thaw cycling and mechanical testing study on frozen-thawed rocks," *Yanshilixue Yu Gongcheng Xuebao/Chinese Journal of Rock Mechanics and Engineering*, vol. 24, no. 17, pp. 3076–3082, 2005.

[14] Y. Bai, R. Shan, Y. Ju, Y. Wu, P. Sun, and Z. Wang, "Study on the mechanical properties and damage constitutive model of frozen weakly cemented red sandstone," *Cold Regions Science and Technology*, vol. 171, article 102980, 2020.

[15] E. Kolay, "Modeling the effect of freezing and thawing for sedimentary rocks," *Environment and Earth Science*, vol. 75, no. 3, pp. 1–12, 2016.

[16] J. Li, R. B. Kaunda, and K. Zhou, "Experimental investigations on the effects of ambient freeze-thaw cycling on dynamic properties and rock pore structure deterioration of sandstone," *Cold Regions Science and Technology*, vol. 154, no. June, pp. 133–141, 2018.

[17] P. Wang, J. Xu, X. Fang, and P. Wang, "Energy dissipation and damage evolution analyses for the dynamic compression failure process of red-sandstone after freeze-thaw cycles," *Engineering Geology*, vol. 221, pp. 104–113, 2017.

[18] K. P. Zhou, B. Li, J. L. Li, H. W. Deng, and F. Bin, "Microscopic damage and dynamic mechanical properties of rock under freeze-thaw environment," *Transactions of Nonferrous Metals Society of China*, vol. 25, no. 4, pp. 1254–1261, 2015.

[19] Q. Ma, D. Ma, and Z. Yao, "Influence of freeze-thaw cycles on dynamic compressive strength and energy distribution of soft rock specimen," *Cold Regions Science and Technology*, vol. 153, no. May, pp. 10–17, 2018.

[20] J. Lu, K. Zhu, L. Tian, and L. Guo, "Dynamic compressive strength of concrete damaged by fatigue loading and freeze-thaw cycling," *Construction and Building Materials*, vol. 152, pp. 847–855, 2017.

[21] R. Liu, N. Huang, Y. Jiang, H. Jing, and L. Yu, "A numerical study of shear-induced evolutions of geometric and hydraulic properties of self-affine rough-walled rock fractures," *International Journal of Rock Mechanics and Mining Sciences*, vol. 127, article 104211, 2020.

[22] R. Liu, B. Li, Y. Jiang, and L. Yu, "A numerical approach for assessing effects of shear on equivalent permeability and nonlinear flow characteristics of 2-D fracture networks," *Advances in Water Resources*, vol. 111, pp. 289–300, 2018.

[23] J. Yu, W. Yao, K. Duan, X. Liu, and Y. Zhu, "Experimental study and discrete element method modeling of compression and permeability behaviors of weakly anisotropic sandstones," *International Journal of Rock Mechanics and Mining Sciences*, vol. 134, article 104437, 2020.

[24] T. Han, J. Shi, and X. Cao, "Fracturing and damage to sandstone under coupling effects of chemical corrosion and freeze–thaw cycles," *Rock Mechanics and Rock Engineering*, vol. 49, no. 11, pp. 4245–4255, 2016.

[25] T. Han, X. Wang, Z. Li, D. Li, F. Xing, and N. Han, "Laboratory investigation of the mode-I fracture of sandstone caused by a combination of freeze-thaw cycles and chemical solutions," *Bulletin of Engineering Geology and the Environment*, vol. 79, no. 7, pp. 3689–3706, 2020.

[26] X. Yang, A. Jiang, and M. Li, "Experimental investigation of the time-dependent behavior of quartz sandstone and quartzite under the combined effects of chemical erosion and freeze-thaw cycles," *Cold Regions Science and Technology*, vol. 161, no. March, pp. 51–62, 2019.

[27] F. Gao, Q. Wang, H. Deng, J. Zhang, W. Tian, and B. Ke, "Coupled effects of chemical environments and freeze–thaw cycles on damage characteristics of red sandstone," *Bulletin of Engineering Geology and the Environment*, vol. 76, no. 4, pp. 1481–1490, 2017.

[28] D. Qu, D. Li, X. Li, Y. Luo, and K. Xu, "Damage evolution mechanism and constitutive model of freeze- thaw yellow sandstone in acidic environment," *Cold Regions Science and Technology*, vol. 155, no. July, pp. 174–183, 2018.

[29] X. Li, D. Qu, Y. Luo, R. Ma, K. Xu, and G. Wang, "Damage evolution model of sandstone under coupled chemical solution and freeze-thaw process," *Cold Regions Science and Technology*, vol. 162, no. February, pp. 88–95, 2019.

[30] J. Zhang, H. Deng, A. Taheri, B. Ke, C. Liu, and X. Yang, "Degradation of physical and mechanical properties of sandstone subjected to freeze-thaw cycles and chemical erosion," *Cold Regions Science and Technology*, vol. 155, no. July, pp. 37–46, 2018.

[31] J. Xu, H. Pu, and Z. Sha, "Mechanical behavior and decay model of the sandstone in Urumqi under coupling of freeze–thaw and dynamic loading," *Bulletin of Engineering Geology and the Environment*, vol. 80, no. 4, pp. 2963–2978, 2021.

[32] M. Yu, S. Li, Q. Sun, and S. Wang, "Influence of grain size on the strain-rate-dependent dynamic response of sandstones," *Geomechanics and Geophysics for Geo-Energy and Geo-Resources*, vol. 7, no. 3, 2021.

[33] Q. Zhu, D. Li, and W. Wang, "Mechanical behavior and permeability evolution of sandstone with confining pressure after dynamic loading," *Geomechanics and Geophysics for Geo-Energy and Geo-Resources*, vol. 7, no. 3, 2021.

[34] X. Liu, W. Yuan, Y. Fu, Z. Wang, L. Miao, and W. Xie, "Tests on shear strength deterioration of sandstone under the action of chemical solution and drying-wetting cycles and analysis of chemical thermodynamics," *Yanshilixue Yu Gongcheng Xuebao/ Chinese Journal of Rock Mechanics and Engineering*, vol. 35, no. 12, pp. 2534–2541, 2016.

[35] Y. Lin, K. Zhou, J. Li, B. Ke, and R. Gao, "Weakening laws of mechanical properties of sandstone under the effect of chemical corrosion," *Rock Mechanics and Rock Engineering*, vol. 53, no. 4, pp. 1857–1877, 2020.

Hindawi
Geofluids
Volume 2021, Article ID 3645438, 13 pages
https://doi.org/10.1155/2021/3645438

Research Article

A Study of Millisecond Blasting on High Bench at Barun Iron Ore Operation

Pengfei Zhang,[1,2] **Runcai Bai**,[3] **Xue Sun**,[2] **Haoran Li**,[1] **Honglu Fei**,[4] **and Shijie Bao**[4]

[1]*School of Mining, Liaoning Technical University, Fuxin, Liaoning 123000, China*
[2]*School of Energy Engineering, Longdong University, Qingyang, Gansu 745000, China*
[3]*Institute of Technology and Equipment for the Development and Utilization of Mineral Resources, Liaoning Provincial College of Engineering, Liaoning Technical University, Fuxin, Liaoning 123000, China*
[4]*School of Science, Liaoning Technical University, Fuxin, Liaoning 123000, China*

Correspondence should be addressed to Pengfei Zhang; 704626564@qq.com, Runcai Bai; bairuncai@163.com, and Xue Sun; sunxue@163.com

Received 23 August 2021; Revised 16 September 2021; Accepted 26 October 2021; Published 3 December 2021

Academic Editor: Richeng Liu

To improve the productivity and efficient of modern large-scale open-cut mines, a number of technologies are developed and trialed, including new blasting equipment, larger blasting holes, high benches, air spacing, and short-delay blasting within holes. However, the relative blasting parameters need field calibration and further investigation of theories on these techniques are required. This paper studied the open-cut bench blasting at Barun Eboxi Mine of Baotou Iron and Steel Group via theoretical analysis on shock wave, numerical simulation, and field test. According to the technical conditions of the site, three sets of vertical boreholes at 310 mm diameter were drilled on 24 m high batter; and three sets of air-spaced charges were set up. The digital electronic detonator was used to initiate at millisecond intervals. The study found that under the condition of 24 m high bench, the use of intermediate air interval is beneficial to the rock fragmentation. The delay time within the hole is 3-8 ms. The bottom of the lower explosives and the top of the upper explosives were devised for initiation to optimize the initiation location. The peak effective stress points are 63.6%, 52.2%, and 8.9% higher, respectively. The field test of high-bench intrahole millisecond blasting in Barun Eboxi mine shows that the intrahole millisecond blasting parameters proposed in this study are feasible.

1. Introduction

Millisecond blasting can improve rock fragmentation while reducing vibration from blasting shoving wave. As bench blasting is a complicated engineer practice and there are many factors that can influence the results, only limited studies on the use of delayed detonation to achieve shock wave collision are available [1–3]. Hence, it is critical to investigate the parameters of millisecond blasting in boreholes. Reference [4] studied the influence of charge-up and millisecond time on blasting vibration via observation on shock waves. They suggested that the millisecond time is closely related to amplitude and range of local amplification effect. Reference [5] used laser dynamic caustics to study the dynamic behavior of cracks between different groups of slits in millisecond blasting holes. Results showed that under the millisecond time conditions, stress wave generated by the first blast hole induced tensile stress on the delayed blast hole wall; this helps crack initiation using the same amount of explosives. Reference [6] used Euler algorithm to establish a fully coupled numerical model of free surface air and water under different parameters and different mesh sizes. Comparison between simulation results and empirical formulas showed that the blasting shock wave propagation through different media is significantly different. At the same time, a method of using the "ratio of the explosive radius to the grid size" to determine the grid size was proposed. Reference [7] used conventional TNT explosives to conduct underwater explosion experiments. The peak pressure and specific impulse of the shock wave were considered as indicators to study the

effects of these three factors on the results of the numerical simulation. Subsequently, the mesh size under various explosive levels was determined. A regression model between explosive level and mesh size was also defined. Reference [8] proposed the concept of fine blasting, suggesting to study multidisciplinary blasting theories, blasting digitization, precise numerical simulation, modernization of fine blasting construction, and construction standardization. The study then quantitatively analyzed and finely controlled the release of explosive energy. This in turn provided theoretical support with blasting design and integrated the research of fine blasting with information technology. Reference [9] studied the influence of the initiation position on blasting-induced coal seam fracturing and permeability and analyzed the characteristics of detonation wave propagation, stress field distribution, and crack development at different initiation positions. In conjunction with the results from numerical simulation, it was concluded that simultaneous detonation at two points can expand the range of local fractures while increasing the detonation locations can shorten the detonation time and result in more uniformly distributed fractures.

Reference [10] suggested that the pressure generated by the collision of two opposite detonating waves during the double-point initiation of the hole is greater than the sum of the intensities of the two shock waves by calculating the range of rock blasting fragmentation in different ways. Most of the above literatures (Cai et al.) have studied the effects of blasting vibration waves, shock waves, and detonation waves on cracks and fractures. The investigation of blasting was mainly on mechanisms and experimental analysis of the initiation position in the hole. There is still a lack of relevant research on the stress field distribution and rock breaking mechanism of millisecond initiation in blasting holes on high benches.

Therefore, the detonation wave and shock wave collision can be used to adjust the explosive energy distribution to meet the requirements of different engineering practices by calibrating the parameters of delay time in the hole, the detonation position, and the detonation combination.

In this study, the 24 m bench expansion on the highwall side of Barun Mine was considered a field example. The shock wave empirical formula in literature [6] was used to express the change of shock wave overpressure during the explosion. At the same time, numerical simulation was used to investigate the rock fracturing mechanism from blasting [11–13]. ANSYS software simulated the detonation sequence parameters including middle-interval charged holes and detonation positions of the upper and lower charge packs. This revealed the distribution of the blasting stress field in the rock during the millisecond blasting on the high bench of Barun Mine.

2. Theory of Shock Wave and Millisecond Time Calculation

2.1. Theoretical Analysis on Shock Wave. The structure of the spaced charge in the hole is shown in Figure 1. According to the layered and segmented millisecond delay detonation method adopted in the field, the explosives in area D of

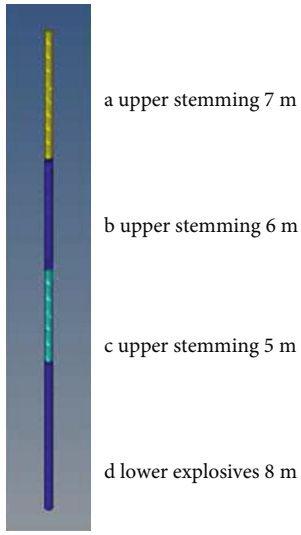

Figure 1: Model charge-up structure: (a) upper stemming; (b) upper explosives; (c) middle air compartment; (d) lower explosives.

Figure 1 detonates first after a millisecond; the detonator at the bottom of area B detonates the explosive after a delay, and the middle section uses air for separation. Under the initiation condition of zone D after t (t = assumed time), the detonation wave front becomes almost flat. Idealistically, the detonation wave will maintain a stable velocity and propagate along the hole. Since t is much smaller than the delay time, the unstable detonation zone generated by one end of the blast hole is much smaller compared to the delay of the entire blast hole. In the calculation, it can be considered that the entire blast hole is still dominated by stable detonation [9]. Based on the conservation law of medium mass between the shock wave front and the explosive air, the equation of the medium motion can be written as

$$\rho_1\left[\frac{\partial_u(R,t)}{\partial t}+\frac{u(R,t)\partial_u(R,t)}{\partial_R}\right]=-\frac{\partial_p(R,t)}{\partial_R},$$
$$\frac{\partial[R_u(R,t)]}{\partial_R}=0, \tag{1}$$
$$\pi\left(R_{\mathrm{m}}^2-R_{\mathrm{w}}^2\right)\rho_0=\pi\left(R^2m-R_{\mathrm{vp}}^2\right)\rho_1.$$

At blasting interface, $R=R_{\mathrm{vp}}$ and $p=p_{\mathrm{vp}}$, such that $2R_{\mathrm{vp}}R^*_{\mathrm{vp}}+aR^2_{\mathrm{vp}}=F(R_{\mathrm{vp}})$, where R_{w} is radius of detonation wave front, R_{vp} is radius of the exploded air, F is function, t is time, ρ_0 is initial density, and ρ_1 is density at any moment. For the closed explosion pressure of the extended charge:

$$p_{\mathrm{vp}}=*p_{\mathrm{w}}\left(\frac{R_{\mathrm{w}}}{R_{\mathrm{vp}}}\right)^6=\left(\frac{\rho_{\mathrm{w}}D^2}{8}\right)\left(\frac{R_{\mathrm{w}}}{R_{\mathrm{vp}}}\right)^6. \tag{2}$$

As exploded air expands, $p_{\mathrm{vp}}=2800(R_{\mathrm{k}}/R_{\mathrm{vp}})^{4/3}$. When $p_{\mathrm{vp}}=p_0$(i.e., $R_{\mathrm{vp}}=R_{\mathrm{vd}}$), expansion ends, in which p_{vp} is

pressure of exploded air, $*p$w is average detonation pressure of exploded air, R_w is radius of concentrated charge pack, ρ_w is explosive density, R_{vp} is radius of exploded air, and R_{vd} is blasting cavity radius.

Based on the theoretical analysis of shock wave, the peak pressure of detonation induced shock wave will decrease rapidly with the increase of the blasting center distance. Hence, it can be considered that when the blasting center distance increases to a threshold value, the impact of the shock wave pressure can be ignored. This paper conducted analysis on the change of shock wave peak pressure using the empirical formula of explosion shock wave proposed by Henrych [14]. Results were later compared against numerical calculation. The shock wave peak overpressure is the peak pressure P_f on the shock wave front minus the original pressure in the air P_0 (standard atmospheric pressure). The specific form of Henrych's empirical formula can be written as

$$\begin{gathered}\Delta P_{(t)} = \Delta P_f\left(1 - t/t_p\right)e^{-\alpha 0t/t_p},\\ \Delta P_f = 0.0662/Z + 0.405/Z^2 + 0.3288/Z^3,\\ Z = R/W^{1/3},\\ t_p = 0.001W^{1/3}\left(0.107 + 0.444Z + 0.264Z^2 - 0.129Z^3 + 0.0335Z^4\right),\end{gathered} \tag{3}$$

where ΔP_t is change of shock wave peak overpressure over time, ΔP_f is peak shock wave overpressure, Z is proportional explosion distance, R is the distance between blasting center to the measurement point (1-9 m), W is weight of emulsion explosive (240-250 kg), t_p is the duration of shock wave overexposure, t is the barotropic pressure, and α_0 is the attenuation coefficient.

When explosives are detonated, the medium is the same as the fluid and only longitudinal waves propagate in the medium, such that c_p can be considered close to infinity [15–17]. When $t = 0$, the medium instantly obtains the initial speed and keeps its speed unchanged, and it starts to move, $c_p = (E/\rho_0)/2$ and average pressure $p = Q_w/\Delta V$. ΔV approaches zero while p approaches infinity. Force at this stage can be expressed as $i = p\Delta t$. When the velocity field is considered in conjunction with potential function, it can be assumed that

$$\begin{aligned}u_x &= -\frac{\partial\varphi}{\partial x},\\ u_y &= -\frac{\partial\varphi}{\partial y},\\ u_z &= -\frac{\partial\varphi}{\partial z}.\end{aligned} \tag{4}$$

Under idealistic fluid motion, the continuous functions can be obtained:

$$\begin{aligned}\frac{\partial u_x}{\partial x} + \frac{\partial u_y}{\partial y} + \frac{\partial u_z}{\partial z} &= 0,\\ \frac{\partial^2\varphi}{\partial x^2} + \frac{\partial^2\varphi}{\partial y^2} + \frac{\partial^2\varphi}{\partial z^2} &= 0.\end{aligned} \tag{5}$$

Based on Green's formula [18], the kinetic energy of medium at the point of explosion is equal to the energy of the explosive:

$$Q_w = -\rho_0/2\int\varphi\partial\varphi/\partial n dF. \tag{6}$$

By substituting the spherical velocity field of r into Equation (4),

$$u_r = -\frac{\partial\varphi}{\partial x}C = 4\pi r^2 u_r. \tag{7}$$

By substituting Equation (7) into Equation (6),

$$\begin{aligned}u_x &= -\frac{\partial\varphi}{\partial x},\\ u_y &= -\frac{\partial\varphi}{\partial y},\\ u_z &= -\frac{\partial\varphi}{\partial z},\\ Q_w &== \frac{(r_w Q_w)^{1/2}}{r^2}.\end{aligned} \tag{8}$$

When the energy from explosion is converted to kinetic energy, the medium point starts to move. To better describe the movement process, strain energy (K) was introduced:

$$K = \rho_0 u^2 S \quad A_s = \frac{\sigma^2 s}{2E}. \tag{9}$$

By solving the above equation, the critical velocity can be expressed as

$$u_S = \sigma_s \cdot (\rho_0 E)^{-1/2}. \tag{10}$$

If $K < A_s$, the medium oscillates; otherwise, the medium will experience tensile failure.

2.2. Millisecond Time Calculation. By using theoretical calculation and reasonable selection of the differential interval time,

$$t = \frac{2w}{c_p} + \frac{w}{u_{tr}} + \frac{s}{u_r}. \tag{11}$$

The time to reach the formation of a new free surface can be optimized, so as to obtain the best blasting quality and shock absorption effect. The millisecond time [19] is 25 ms, which is consistent with the actual lagging time between holes. However, it does not explain the whole process of the mutual interference of the stress fields

generated by all the explosive packs. Thereby, this theory is not practical for the calculation of the microdifference in the hole. Pokrovsky [14] proposed that in the microdifference delayed blasting, the decisive factor on the rock fragmentation and the reduction of the seismic effect is the action time of the explosion air pressure ($t = a/c_p + t_{vp}$). This time is about 3~8 ms.

In the formula, t is millisecond time. It is equal to the time required for the formation of a free face, which can be further divided into three parts. The first part is the time required for the stress wave to travel from the center of the explosive pack to the free face and then back to the free face. The second part is the time required to form a crack approximately equal to the minimum chassis resistance line. The third part is the time required for 8-10 mm crack formation. u_{tr} is the speed of crack propagation, s is the crack width, u_r is the average speed of flying rock, a is the interval of explosive packs, and c_p is the speed of longitudinal wave in the medium.

In order to accurately calculate the differential time in the hole, it is based on the research of Zhendong et al. in literature [20].This paper modified the Hanukayev formula from two factors: (i) the formation time of the new free surface and (ii) the residual amount of the stress wave. According to Henry and Jianguo in literature [14], it is assumed that the pressure in the hole at the moment of explosion is p_0, and the moment when the explosion air freely flows out at the beginning, it can be assumed that the higher the pressure, the greater the rate of change, which can be expressed as $p = p(t) = p_0 e^{-\alpha t}$, $p(t)$ is the pressure in the hole, and α is the hypothetical index. The projectile of the rock body from blasting is assumed to be elliptical:

$$\frac{x^2}{a^2} + \frac{y^2}{b^2} = 1, \tag{12}$$

where $a = w \tan(\beta/2)$ and $b = w$.

According to the above formula, the weight of the flying body is $M = \rho_0 V = (\pi/2) H_w 2\rho_0 \tan(\beta/2)$. The pressure acting on the hole element can be therefore calculated as

$$dp = p0e - \alpha t R w \cos\delta d\delta dz. \tag{13}$$

Subsequently, the weight of the flying body can be estimated by integration of the above function. The force can be roughly described by the motion equation of the flying body: $M[d^2 v(t)/dt^2] = P(t)$.

Assume that $p = p_{(t)} = p_0 e^{-\alpha}$ is replaced by a quadratic parabola of $p_{(t)} = mt^2 + nt + l$. When $p_{(0)} = 1$, $p_{(tm)} = p_m << 1$ and $dp_{(tm)}/dt = 0$. Thus,

$$p(t) = (1 - p_m) t_2/t_2 m + 2(p_m - 1) t/t_m + 1. \tag{14}$$

By combining with the above formula of $P(t)$,

$$v(t) = \frac{(1 - p_m) t^2}{k\alpha^2 t^2 m} + \left[\frac{2(p_m - 1)}{k\alpha^2 t_m} + \frac{1}{k\alpha}\right] t. \tag{15}$$

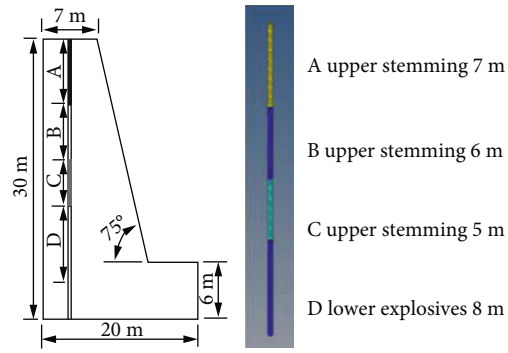

Figure 2: Model charge-up structure.

For $t = t_3$, $v(t_3) = v_p$, $p_0 = 4000\,\text{kg·cm}^{-2}$, and $v_p = 10$ cm. t_3 can be estimated as

$$t_3 = \left[T_3 w^2 \rho_0 \tan(\beta/2)\right]/Ø. \tag{16}$$

The coefficient t_3 in the formula is to consider the influence of some quantities appearing in the equation of motion but not included in the equation. As a first-order approximation, T_3 can be assumed as 80×10^{-6}. Single-row blasting [14] $V_p * = awH$is the blasting volume of a row in the blasting zone; the blasting volume of a single hole can be considered as the average value of the single-row blasting volume. According to Wenhai in literatures[21, 22], the most efficient delay time in the hole-by-hole millisecond blasting is at 25 ms. In summary, the dolomite blasting time within the hole was defined as $t = t_1 + t_2 + t_3 = 3 \sim 8$ ms.

3. Numerical Simulation on Millisecond Blasting and Field Validation

To improve the simulation process, the medium in the model was set as a homogeneous, continuous, and isotropic elastic-plastic material with no initial stress. A symmetrical model was established with the z-axis as the symmetrical plane at a bench height of 24 m, a length of 20 m, and a width of 15 m. The designed batter angle was 75°. ANSYS was used for simulation work via a hexahedral mesh generated by Hypermesh 14.0. When defining the boundary conditions, the section (shot hole surface) of the model was considered as the symmetrical boundary, and the other surfaces except the section are all nonprojection boundaries. The crest, surface, and toe of the batter were set as free face, as shown in Figure 2.

Three sets of numerical models were established based on the figure to represent the field conditions. Dynamic loading and rock yield time were quantitatively studied by using millisecond blasting while reasonably setting delay time, detonation sequence, and detonation location. A parametric study was also carried out on millisecond time of the digital electronic detonated. The detonation combinations can be seen in Table 1.

The dynamic experiments on many materials [23] show that the dynamic yield stress was significantly higher than the static yield stress. The Cowper-Symonds relationship is

Table 1: Simulation parameters of millisecond blasting in the hole.

	B-section delay time	3 ms				5 ms				7 ms			
Parameters of millisecond blasting	B & D combined detonation	1	2	3	4	5	6	7	8	9	10	11	12
		D top & B bottom		D top & B top	D bottom & B bottom	D top & B top	D top & B bottom	D bottom & B top	D bottom & B bottom	D top & B top	D top & B bottom	D bottom & B top	D bottom & B bottom
	D-section detonation location	0	0	0	0	0	0	0	0	0	0	0	0
		0.5	0.5	0.5	0.5	0.5	0.5	0.5	0.5	0.5	0.5	0.5	0.5
		1.0	1.0	1.0	1.0	1.0	1.0	1.0	1.0	1.0	1.0	1.0	1.0
		1.5	1.5	1.5	1.5	1.5	1.5	1.5	1.5	1.5	1.5	1.5	1.5

a simple empirical formula between the dynamic yield stress and strain rate ([24, 25]; [26]), which was proposed on the basis of a large number of experiments. This study investigated the feasibility of complete restart numerical simulation technology and the Lagrangian [27] numerical algorithm on multistage rock blasting simulation. The constitutive model of rock material was not studied in detail, such that a bilinear kinematic hardening model (plastic kinematic constitutive model) was used for rock material based on the Cowper-Symonds relationship [28]. This is a commonly used model for rock and soil simulation. The expression is as follows:

$$\sigma_Y = \left[1 + \left(\frac{\varepsilon *}{C}\right)^{1/P}\right]\left(\sigma_0 + \beta E_{\mathrm{P}} \cdot \varepsilon_{\mathrm{eff}}^{p}\right), \tag{17}$$

where σ_0 is the initial yield strength. C and P are constant related to material properties, $C = 35$ and $P = 3$. $\varepsilon *$ is strain rate, and $\beta = 1$ (adjustable parameter). E_{P} is the modulus of hardening (24 MPa), $\varepsilon^{\mathrm{P}}{}_{ij}$ is plastic strain rate, and $\varepsilon^{\mathrm{P}}{}_{\mathrm{eff}}$ is equivalent plastic strain, which can be calculated as $\varepsilon^{\mathrm{P}}{}_{\mathrm{eff}} = \int_0^t (2\varepsilon^{\mathrm{P}}{}_{ij}/3)^{1/2} dt$.

The elements of rock and blast hole filling were defined as "∗sect-lag"; and rock and stemming materials were assumed to be subject to the constant-stress solid element algorithm (see Tables 2 and 3 for details).

The element of the spaced air in the hole was defined as "∗sect-ale". Mat-Null material model (5) was used to represent air; and other parameters were set as default. The state equation of air is the ideal air equation (∗EOS-001). This equation is a linear polynomial, and the material parameters at initial state were defined using thermodynamics:

$$p = \frac{(\gamma - 1)\rho E}{\rho_{\mathrm{air}}}, \tag{18}$$

where γ is the adiabatic index (=1.4), $\rho_{\mathrm{air}} = 1.29$ g/L, ρ is the density at certain time, and E is the specific internal energy[29]. The JWL [24] equation was used for emulsion explosives, which can precisely describe the expansion process of detonation products. This equation has an extensive database for various explosives and is expressed as

Table 2: Blocking material parameters.

Density (g/cm^3)	Elastic modulus (GPa)	Poisson's ratio	Yield strength (MPa)	Tangent modulus (MPa)
1.85	1.2	0.38	0.8	0.1

Table 3: Dolomite material parameters.

Density (g/cm^3)	Elastic modulus (GPa)	Poisson's ratio	Tensile strength (MPa)	Compressive strength (MPa)
2.43	5	0.30	4	80

$$P = A\left[\frac{1-w}{R_1 V}\right]e^{-R_1 V} + B\left[\frac{1-w}{R_2 V}\right]e^{-R_2 V} + \frac{\mathrm{wE}}{V}, \tag{19}$$

where P is the required pressure and E is internal energy of detonation product per unit volume (assumed as 50 GPa). According to Min et al. in the literature [23, 30–32], ρ and v were obtained, respectively, at values of 1.2 g·cm^{-3} and 0.4 cm·μs^{-1}. V is volume of detonation product, $A = 2.14 \times 1011$, $B = 1.82 \times 109$, $R_1 = 4.15$, $R_2 = 0.95$, and $w = 0.5$.

3.1. Determination of Detonation Location and Combination. Detonation location was investigated first while keeping other parameters the same. Although simultaneous initiation method is the most efficient way for rock fragmentation, it is difficult to be achieved due to clamping effect of the lower rock. Intermediate initiation and two-end initiation methods within the hole are more effective than bottom-end initiation method considering the length of the charge from the deep-hole blasting and superposition of detonation waves. Based on the engineering practice, this paper simulated the single-point detonation with initiation point at the bottom of the hole. This section discusses the change of the effective stress in the intermediate air interval at various millisecond time intervals (3-8 ms). Rock strengths at Barun Mine were obtained by conducting laboratory experiments on the rock specimen collected from the toe of 1548 slope, at an average uniaxial compressive strength of 35 MPa and ultimate tensile strength of 4 MPa. The average tensile strength was used as the critical value of the failure criterion. In other words, the colored area

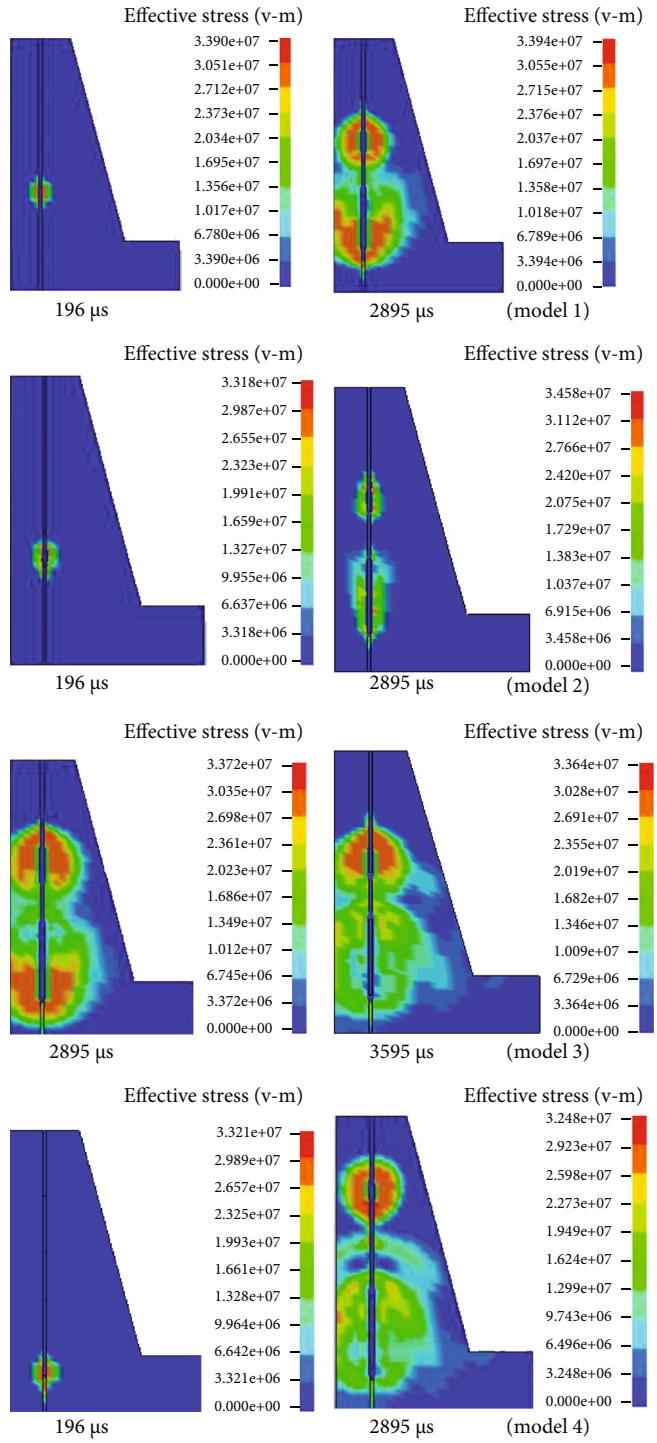

Figure 3: Equivalent stress cloud at different times.

under the stress of the rock mass corresponding to the blast hole is in a critical or plastic strain state.

Figure 3 shows the changes in the Mises stress cloud diagram of high-bench blasting at various conditions. The explosives at the bottom of the blasting hole detonated first, and the detonation wave propagated from bottom to top. By then, the stress wave extended outward in a "teardrop-shape" in the rock mass. The stress subsequently decreased as decaying of detonation wave energy. When $t = 2199\,\mu s$ in model 3, the bottom 8 m explosives were detonated first and the stress wave of the bottom explosive began to propagate in the 5 m air interval while the upper explosives were set to detonate 3 ms later. Since then, part of detonation wave from upper explosives propagated towards the surface, whereas the other parts started to propagate downwards along the upper 6 m explosives. When $t = 2895\,\mu s$, the stress

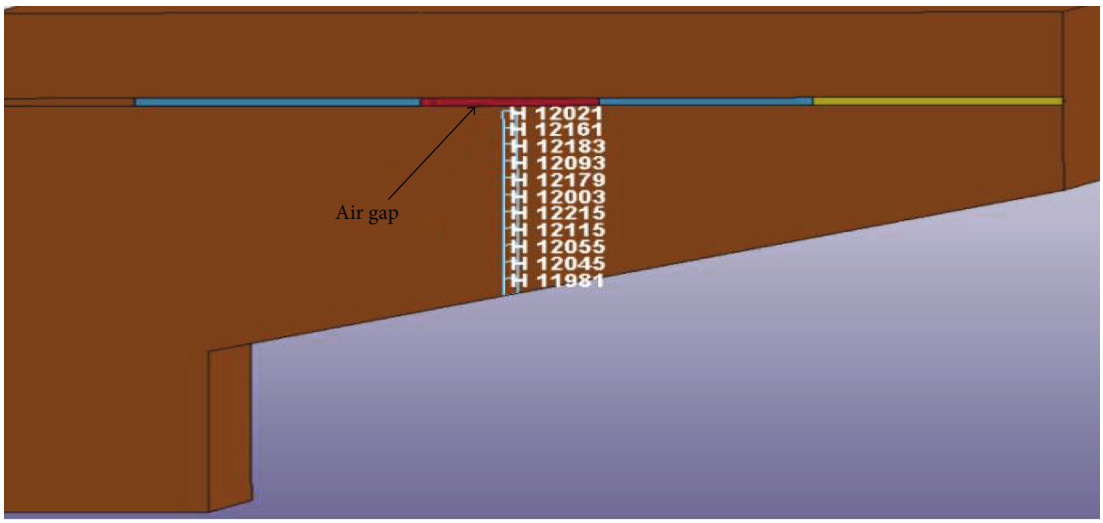

Figure 4: Locations of equidistant monitoring points in the air compartment.

waves of the upper and lower explosives collided and superimposed. At this point, the bottom explosives that detonated first completed full detonation. The decaying stress area started to increase and expand again. Subsequently, it propagated until the delaying of the stress area was less than the yield strength of the rock mass; and the whole explosion process was completed. The changes in the Mises stress cloud diagram of high-bench blasting at different times in model 3 show that the detonation wave superimposition of the upper and lower explosives induced stress superposition. This resulted in the stress decay rate in the rock body slower than the previous period. At this stage, the air interval in the blasting hole played a critical role in prolonging the detonation time such that the rock was subjected to a longer lasting stress. This in turn achieved an ideal rock breaking effect. Results from other models are similar to those shown in model 3, such that they are not discussed here.

The delayed detonation in the high step hole adopts air interval detonation. This is because the air had lower resistance to the rock mass, such that the explosion energy of the upper and lower sections can be directed to intermediate section first, which can effectively store energy while prolonging the effective time of detonation air. Thereby, this part of the corresponding rock mass was far away from the explosive energy, so that the explosion stress distribution was relatively small.

Therefore, the equidistant interval was used in the intermediate air interval to determine monitoring point locations H12021~H11981, as shown in Figure 4. The stress curve of different monitoring units was calculated by the LS-prepost postprocessor; and the peak effective stress in each unit was obtained. By then, the trend of Miss stress in the units during blasting was obtained from the model.

Based on the field experience and combination of initiation methods, the initiation position was determined to be 0.5 m from the bottom explosives and gradually increased the bottom initiation position by every 0.5 m. In this simulation, the bottom initiation positions were selected as 0.0 m, 0.5 m, 1.0 m, and 1.5 m from the hole base. According to the stress time curve diagram of each point, the peak value of the overall waveforms under all cases rose first and then decreased with increasing time, although the time interval when the peak stress was over rock strength was different for each case. As the distance between the monitoring point and the air column increases, the rate of stress reduction at the monitoring point, that is, the degree of flatness of the curve, was different. Schemes 4-1 and 4-2 have steeper slopes than the curves of 3-1 and 3-2.

As there are variations during numerical calibration, Scheme 3.2 had most fluctuation with a range between 0.2 MPa and 0.4 MPa; this variation was within the tolerant level. The other curves were relatively flat, and the curve in Scheme 4-1 had the flattest slope. The flatness of the curve reflected the uniformity of the explosion energy distribution, such that Scheme 4.1 had the most uniformed explosion energy distribution. This was a more effective utilization of explosion energy. At 1 m initiation position, the peak effective stress of the element was greater than the dynamic tensile strength of the rock, which means the element had yielded and "flaking" had occurred. If one unit does not yield, it can be considered that the blasting process produced a large block (>1 m) than since the distance between the selected units was 1.0 m. It is very likely that the blasting plan should be improved based on the parameters of the mining equipment. From Scheme 4-1 in Figure 5, it can be seen that all units yielded; while the peak effective stresses of some units in Scheme 3.1 were lower than the dynamic tensile strength of the rock, which may result in larger blocks.

Based on the field experience at Barun Mine and the authors' experience on millisecond blasting, the initiation time of the upper and lower charges in the hole was set between 3 ms and 8 ms delay time.

With different initiation parameters, the bottom initiation distance was set as 0 m, 0.5 m, 1.0 m, and 1.5 m. Results showed that under Schemes 3-1, 3-2, 4-1, and 4-2, the average peak effective stresses are at the monitoring points (see

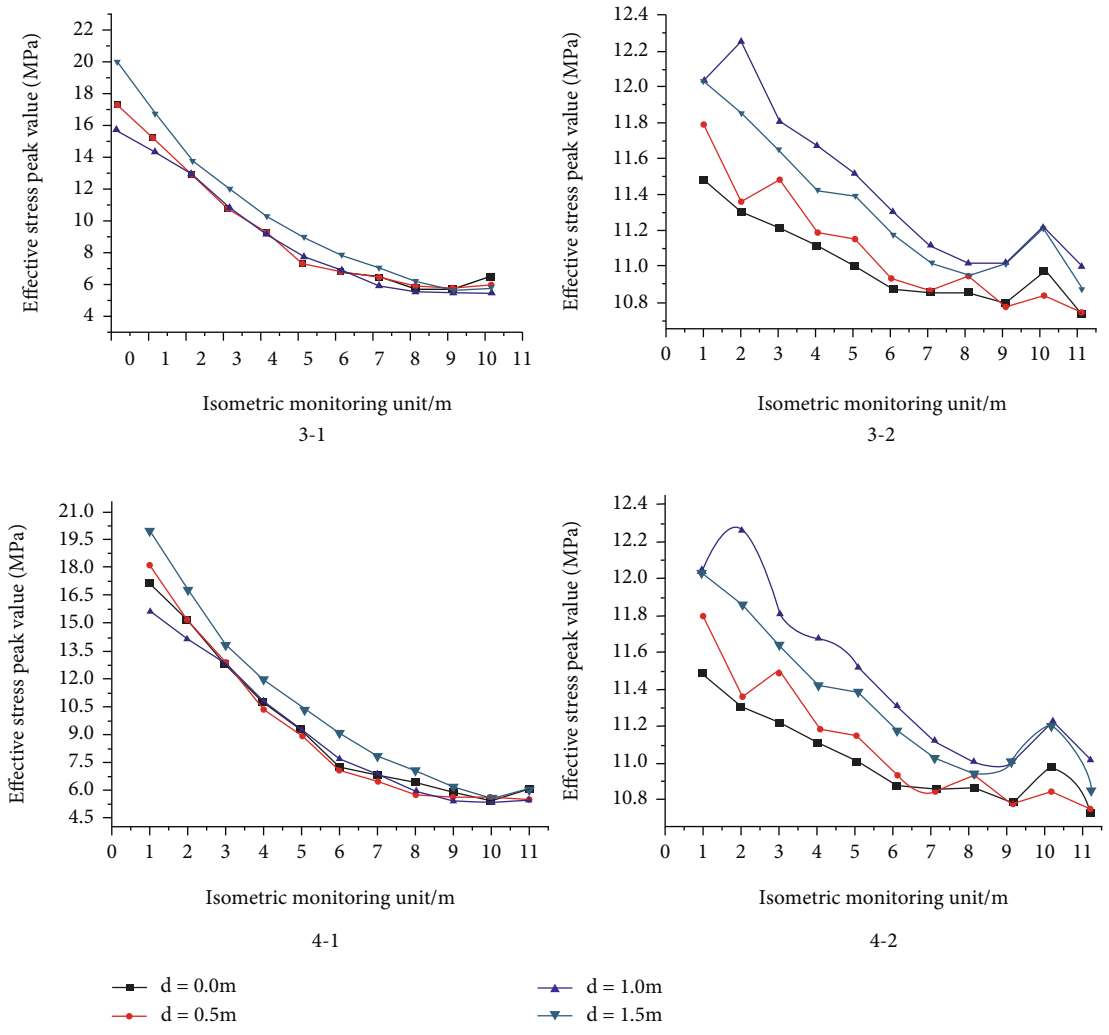

(a) 3 ms

Figure 5: Continued.

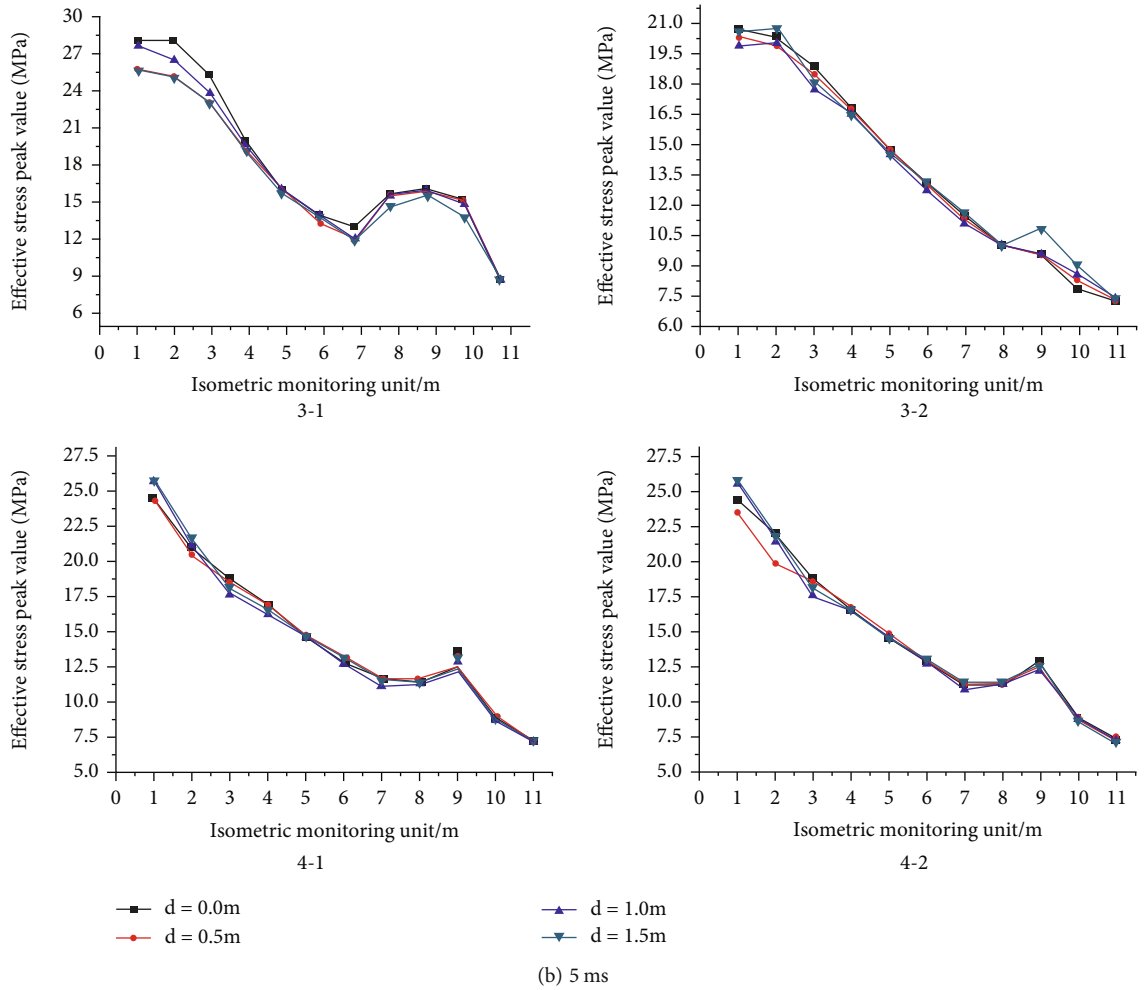

(b) 5 ms

Figure 5: Continued.

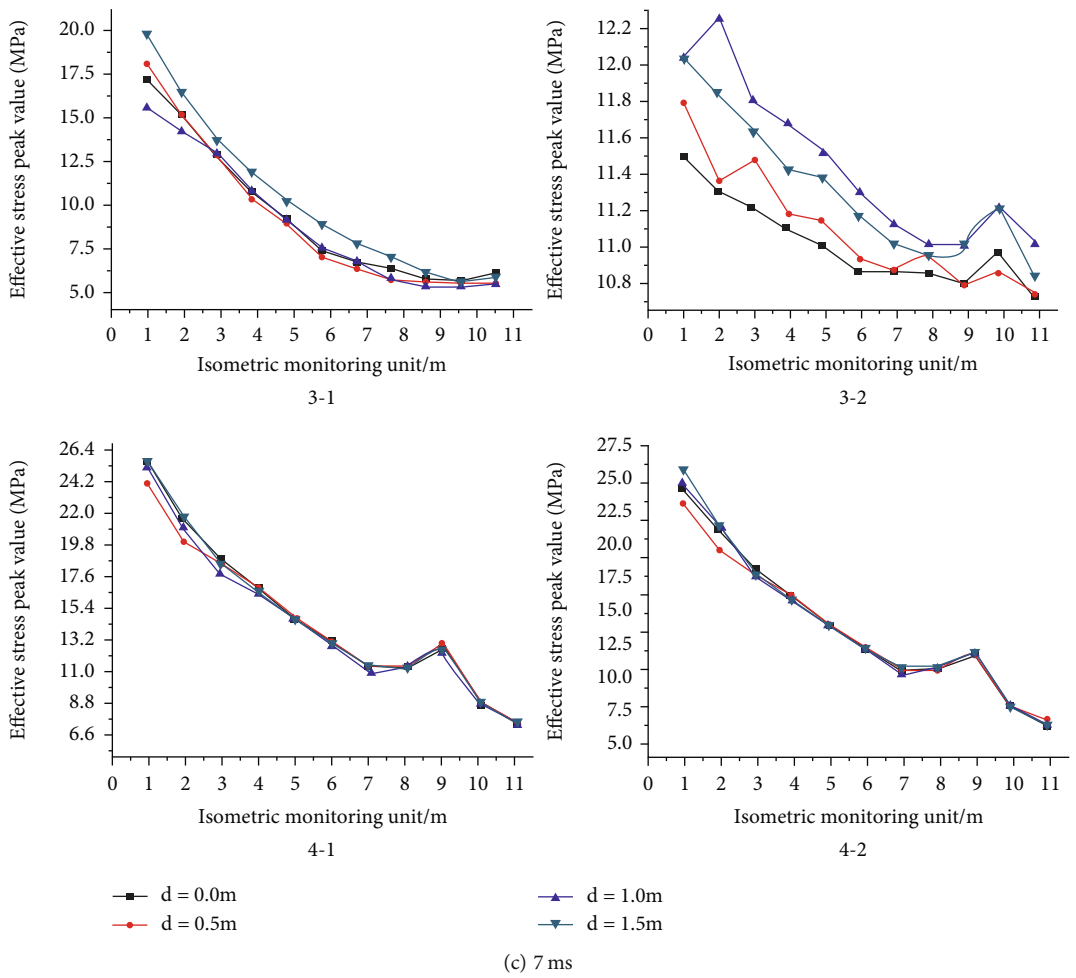

(c) 7 ms

Figure 5: Peak effective stress diagram at equidistant monitoring points of interval air column.

Table 4: Peak effective stress of the inspection points under the millisecond blasting.

Initiation method	Peak effective stress (MPa)				
	Initiation location 0 m	0.5 m	1.0 m	1.5 m	Difference between maximum and minimum
3-1	9.37	9.25	9.05	10.36	1.31
3-2	10.02	10.09	14.50	13.23	4.48
4-1	15.80	15.40	15.55	15.46	0.40
4-2	14.38	14.14	14.18	14.45	0.07
Difference between maximum and minimum	6.43	6.15	6.50	5.10	///

Table 4 for details). It also shows that under the same bottom detonation distance, the detonation method had an impact on the peak effective stress at each monitoring point, with a variation between 5.10 and 6.50 MPa. On the contrary, under the same detonation method and different bottom detonation distances, the peak effective stress of each monitoring unit varied from 0.07 MPa to 4.48 MPa, while the millisecond initiation sequence influenced the fragmentation and was larger than the bottom initiation distance. Considering the changes in the peak effective stress values at each point around the intermediate air space, the intensity of the full stress field, and the duration, the best millisecond initiation parameter was determined, i.e. millisecond time of 3~8 ms. Based on model 3, the initiation distance was determined to be 1 m.

3.2. Field Test. Barun Mine is a subsidiary of Baotou Iron and Steel Group. The main drilling equipment of Barun Mine is a KY-310 roller drilling rig. The prestrip equipment mainly includes ER9350 large hydraulic shovel Liebherr and 4410 large electric truck. It is a modern superpit. The lithology at the site is mainly dolomite, slate, and Quaternary. Due to the requirement of pit boundary optimization, the highwall needs to be expanded towards the north. To improve the efficiency of the expansion, Barun Mine decided to utilize the upper existing 12 m high bench, modification of

Figure 6: Rock fragmentation at front of high-bench blasting.

Figure 7: Rock fragmentation at the crest of high-bench blasting.

drilling rig, and production process. The upper 12 m bench was expanded to a 24 m high bench without the change of original mine design parameters. Thus, 24 m boreholes through two benches were drilled at one time. This would increase the efficiency of blasting. Due to the height of the benches at Barun Mine, the factors including blast reliability improvement were considered; such improvement was achieved by setting initiation points at top and bottom of the blasting hole. However, with the increase in bench height, the length of the explosives in the blasting hole also decreased. It was required to redetermine the parameters of explosives in the upper and lower segments of the blast hole.

The blasting zone was located on the north side of the pit at the level of 1548. The bench lithology is mainly medium strength dolomite. Blasting holes had a diameter of 310 mm and a chassis resistance line of 10 m. To reduce the influence of blasting vibration, the short delay time in the holes was set as 3~8 ms and the detonation was carried out between the rows. The charging method was interval charging with 7 m stemming. There were 71 blast holes in total, and the rock blasting volume was 66 134.88 t. Based on the field test results, it can be seen that the average block size satisfied the requirements of shoveling. The block diameter was about 20 cm, and the forward moving was about 20 m. The back and side movements were limited by other in-rock masses, such that the distance was relatively small, at approximately 3 m. The reasonable fragmentation size was acceptable and uniform, which satisfied the capacity of mining equipment. The throwing distance of the blasted rock was greater than 25 m. The on-site blasting results are shown in Figures 6 and 7.

4. Conclusion

Under the condition of 24 m bench and large vertical drilling at Barun Mine, multiple analytical and numerical models were constructed to analyze the distribution of blasting stress in the rock mass at various initiation sequence and locations. The millisecond blasting initiation parameters provided a theoretical basis for high-bench blasting; and the following conclusions were drawn:

(1) Based on numerical simulation and field test, it was concluded that the effective stress duration was longer when the lower end of the lower explosives was detonated first and the millisecond time interval between

the holes is 3~8 ms. The delayed detonation at the top of the upper grain is reasonable, which can result in sufficient rock fragmentation. This provided a favorable analysis and technical support for the development of the millisecond blasting at Barun Mine

(2) By comparing the peak stresses of same detonation sequence under different detonation locations with the same detonation location under different detonation sequences, it was found that the millisecond initiation sequence was the key factor affecting the rock fragmentation. Thereby, the emerging high-precision digital electronic detonators provide sufficient preciseness for millisecond blasting in high-bench holes. Moving forward, the advantages of electronic detonators will be further utilized to specific working conditions, aiming at improving the blasting efficiency of open-cut operations

List of Symbols

a: Interval of explosive packs, m
C and P: Constant related to material properties, $C = 35$ and $P = 3$
E_p: Modulus of hardening, MPa
E: Internal energy of detonation product per unit volume, GPa
F: Function
ΔP_t: Change of shock wave peak overpressure over time, MPa
ΔP_f: Peak shock wave overpressure, MPa
P: The required pressure, MPa
p_{vp}: Pressure of exploded air, MPa
$*p_w$: Average detonation pressure of exploded air, MPa
R_w: Radius of detonation wave front, m
R_{vp}: Radius of the exploded air, m
R_{vd}: Blasting cavity radius, m
R_w: Radius of concentrated charge pack, m
R: The distance between blasting center to the measurement point, m
s: Crack width
t_p: Duration of shock wave overexposure, ms
t: Time, ms
t_1: Barotropic pressure, MPa
t_2: Millisecond time, ms
u_{tr}: Speed of crack propagation
u_r: Average speed of flying rock
W: Weight of emulsion explosive, kg
Z: Proportional explosion distance, $m/kg^{1/3}$
ρ_0: Initial density, kg/m^3
ρ_1: Density at any moment, kg/m^3
ρ_w: Explosive density, kg/m^3
α_0: Attenuation coefficient
c_p: Speed of longitudinal wave in the medium, m/s
σ_0: Initial yield strength
$\varepsilon *$: Strain rate
β: 1 (adjustable parameter)
$\varepsilon^p{}_{ij}$: Plastic strain rate
$\varepsilon^p{}_{eff}$: Equivalent plastic strain.

Data Availability

The data basically comes from the mining data of the Baiyun Obo rare earth mine. This article makes a corresponding study on the delay time in the hole.

Additional Points

Highlights. The delayed detonation at the top of the upper grain is reasonable, which can result in sufficient rock fragmentation. This provided a favorable analysis and technical support for the development of the millisecond blasting at Barun Mine. The emerging high-precision digital electronic detonators provide sufficient preciseness for millisecond blasting in high-bench holes. Moving forward, the advantages of electronic detonators will be further utilized to specific working conditions, aiming at improving the blasting efficiency of open-cut operations

Conflicts of Interest

The authors declared that they have no conflicts of interest in this work.

Acknowledgments

The work of this paper is supported by the Research and application of 24 m high step expansion blasting technology in Baiyun Eboxi Mine.

References

[1] L. Zhendong, F. Yong, and W. Lu, "Analysis of explosion energy transmission and rock breaking effect under dual-point initiation in a hole," *Chinese Journal of Rock Mechanics and Engineering*, vol. 38, pp. 1–13, 2019.

[2] G. Qidong, L. Wenbo, and L. Zhendong, "Study on the control effect of the initiation position in the hole on the energy transmission of the explosion in rock blasting," *Chinese Journal of Geotechnical Engineering*, vol. 42, no. 11, pp. 2050–2058, 2021.

[3] L. Wu, L. Hongwei, and N. Huajun, "Experimental study on the influence of millisecond delay time on rock breaking effect," *Pyrotechnics*, vol. 8, no. 4, pp. 52–57, 2020.

[4] C. Shihai, S. Hu, and C. Shaofeng, "Study on the influence of millisecond time and cylindrical charge characteristics on blasting vibration effect," *Chinese Journal of Rock Mechanics and Engineering*, vol. 36, no. S2, pp. 3974–3983, 2017.

[5] Y. Zhongwen, Z. Shichun, and Q. Peng, "Crack propagation mechanism of short-delay blasting in slit charge bag," *Journal of China Coal Society*, vol. 43, no. 3, pp. 638–645, 2018.

[6] Z. Sherong, L. Hongbi, and G. Wang, "Comparative analysis of grid size effects in numerical simulation of air and underwater explosion shock waves," *Journal of Hydraulic Engineering*, vol. 46, no. 3, pp. 298–306, 2015.

[7] H. Liangliang, H. Ruiyuan, and L. Shichao, "Numerical simulation study of underwater explosion shock wave," *Chinese Journal of High Pressure Physics*, vol. 34, no. 1, pp. 1–13, 2020.

[8] X. Xie, "Development status and prospect of fine blasting," *Engineering Science of China*, vol. 16, no. 11, pp. 14–19, 2014.

[9] G. Deyong, Z. Chao, and Z. Tonggong, "The influence of the initiation position of deep-hole shaped energy blasting on coal

seam fracturing and anti-reflection," *Journal of China Coal Society*, vol. 1078, 2020.

[10] L. Zhendong, W. Lu, and F. Yong, "Explosion energy distribution under lateral initiation conditions and its influence on rock breaking effect," *Explosion and Shock*, vol. 37, no. 4, pp. 661–670, 2017.

[11] L. Qiyue and L. Xiuquan, "The construction method of ANSYS three-dimensional complex model based on SURPAC," *Mining and Metallurgical Engine*, vol. 34, no. 5, pp. 1–5, 2014.

[12] L. Tong, C. Ming, and Y. Zhiwei, "Research on the energy transfer efficiency of blasting explosion with different coupling media," *Explosion and Shock*, vol. 41, no. 6, pp. 1–13, 2021.

[13] W. Dong, C. Ming, and Y. Zhiwei, "Research on the blasting damage area of rock mass based on the dynamic characteristics of strain rate," *Engineering Science and Technology*, vol. 53, no. 1, pp. 67–74, 2021.

[14] J. Henry and X. Jianguo, *Explosive Dynamics and Its Applications*, Science Press, Beijing, 1981.

[15] S. Wu, J. Li, J. Guo, G. Shi, Q. Gu, and C. Lu, "Stress corrosion cracking fracture mechanism of cold-drawn high-carbon cable bolts," *Materials Science and Engineering: A*, vol. 769, pp. 1–10, 2020.

[16] S. Wu, H. L. Ramandi, H. Chen, A. Crosky, P. Hagan, and S. Saydam, "Mineralogically influenced stress corrosion cracking of rockbolts and cable bolts in underground mines," *International Journal of Rock Mechanics and Mining Sciences*, vol. 119, pp. 109–116, 2019.

[17] S. Wu, X. Zhang, J. Li, and Z. Wang, "Investigation for influences of seepage on mechanical properties of rocks using acoustic emission technique," *Geofluids*, vol. 2020, Article ID 6693920, 10 pages, 2020.

[18] Q. Qihu, "Several progress in rock explosion dynamics," *Chinese Journal of Rock Mechanics and Engineering*, vol. 28, no. 10, pp. 1945–1968, 2009.

[19] L. Xiaoming, Z. Wenhai, and J. Wenbin, "Optimal delay control of millisecond blasting for rock breaking mechanism," *Journal of Harbin Institute of Technology*, vol. 49, no. 2, pp. 158–163, 2017.

[20] L. Zhendong, W. Lu, and H. Hu, "The influence of blasting free surface on the peak of vibration induced by millisecond blasting on slope," *Chinese Journal of Rock Mechanics and Engineering*, vol. 35, no. 9, pp. 1815–1822, 2016.

[21] Z. Wenhai, *Selection of hole-by-hole initiation delay time for deep-hole bench blasting in open-pit mine*, Fuzhou University, 2015.

[22] S. Jianfeng, Z. Dongwang, and H. Xiaowu, "Model test study on the best time delay between drilling and blasting holes," *Metal Mine*, vol. 6, pp. 19–22, 2015.

[23] C. Yu, L. Liangzhong, and H. Yimin, "Study on the detonation product of aluminum-containing explosives JWL equation of state," *Explosion and Shock*, vol. 19, no. 3, pp. 274–279, 1999.

[24] R. Yang, D. Chenxi, and G. Yang, "Experimental study on crack propagation characteristics of milli second blasting," *Explosion and Shock Wave*, vol. 36, no. 24, pp. 98–103, 2017.

[25] Z. Wenjun, N. Hongxin, and S. Wang, "Optimization of preprocessing for engineering blasting simulation based on HyperMesh," *Computer Aided Engineering*, vol. 29, no. 4, pp. 50–56, 2020.

[26] Q. Gao, W. Lu, and L. Zhendong, "Research on the control effect of the initiation position in the hole on the energy transmission of the explosion in rock blasting," *Chinese Journal of Rock Engineering*, vol. 42, no. 11, pp. 2050–2059, 2020.

[27] R. Cai, Y. Li, C. Zhang et al., "Damage assessment of prefabricated prestressed channel slab under plane charge blast," *Journal Engineering Structures*, vol. 246, p. 113021, 2021.

[28] J. Chen, Y. Zhao, H. Zhao, J. Zhang, C. Zhang, and D. Li, "Analytic study on the force transfer of full encapsulating rockbolts subjected to tensile force," *International Journal of Applied Mechanics*, vol. 13, no. 9, 2021.

[29] Q. He, L. Zhu, and L. Yingchun, *Simulating hydraulic fracture re-orientation from oriented perforations in heterogeneous rocks with an improved discrete element method*, Rock Mechanics and Rock Engineering, 2021.

[30] G. Min, W. Canhua, and L. L. Xun, "Determination and function of main blasting parameters in hard rock excavation," *Journal of China Coal Society*, vol. 40, no. 7, pp. 1526–1533, 2015.

[31] J. Chen, P. Liu, H. Zhao, C. Zhang, and J. Zhang, "Analytical studying the axial performance of fully encapsulated rock bolts," *Engineering Failure Analysis*, vol. 128, p. 105580, 2021.

[32] J. Chen, H. Zhao, F. He, J. Zhang, and K. Tao, "Studying the performance of fully encapsulated rock bolts with modified structural elements," *International Journal of Coal Science and Technology*, vol. 8, no. 1, pp. 64–76, 2021.

Hindawi
Geofluids
Volume 2021, Article ID 9808238, 14 pages
https://doi.org/10.1155/2021/9808238

Research Article

Experimental Study of the Water-Sediment Two-Phase Seepage Characteristics in Rock Fractures and the Influencing Factors

Kui Di,[1] Ming Li,[1] Xianbiao Mao,[1] Zhanqing Chen,[1] Lianying Zhang,[2] and Yu Han[1]

[1]*State Key Laboratory for Geomechanics and Deep Underground Engineering, China University of Mining and Technology, Xuzhou, 221116 Jiangsu, China*
[2]*School of Civil Engineering, Xuzhou University of Technology, Xuzhou, 221018 Jiangsu, China*

Correspondence should be addressed to Ming Li; mingl@cumt.edu.cn

Received 12 August 2021; Accepted 22 September 2021; Published 25 November 2021

Academic Editor: Andri Stefansson

The water-sediment two-phase seepage in coarse fractures is one of the major factors to trigger mine water inrush disasters. Based on seepage mechanics theory, a mechanical model of the water-sediment two-phase seepage in coarse fractures was established. An experimental system was also developed to study the seepage characteristics under various conditions. The relationships between the absolute value of the pressure gradient and the seepage velocity were analyzed during the test process. The nonlinear characteristics of the seepage test were revealed. In addition, variation laws of the absolute value of the pressure gradient with the sand volume fraction and the sand particle size were illustrated, which were related to the loss of pressure during the particle movement. The impacts of the sand volume fraction and the sand particle size on the equivalent fluidity and β-factor of non-Darcy flow were discussed and analyzed. It was determined that the local turbulence was the main reason for the change of nonlinear variation characteristics of seepage parameters.

1. Introduction

Water inrush is one of the major disasters affecting coal mine safety production. It causes the direct cost of tens of billions of yuan every year in China. Therefore, it is of great significance to find clear water inrush disaster mechanisms and effectively control the disasters for the construction of green mines in China [1, 2]. Water-sediment two-phase flow in course fractures is the precursor of mine water inrush disasters. It is the key to study seepage characteristics of the water-sediment mixture to reveal the mine water inrush mechanism.

The formation of fissure channels and the seepage of water-sediment mixture are two core factors of mine water inrush disasters. The fissure channels are caused by the surrounding rock deformation during the roadway driving and the mining of the working face [3–5]. The surface of the fracture is usually coarse. The water-sediment mixture mainly exists in old roofs or water-rich areas [6, 7]. The content of the water-sediment mixture is mainly water, and the content of sand is less in Eastern China, while thick sand layers usually exist above coal seams in Northwest China. A complete channel penetrating fractures will form after the overburden failure [8]. Then, the overlying thick land layers will flow to fractures along with the water and thus trigger water and sand inrush disasters. Many scholars used numerical calculation methods to reveal the complete process of water-sediment two-phase flow, and they adopted the software, such as ANSYS, FLAC, PFC, and COMSOL, to study the seepage fields and stress fields [9–12]. However, the numerical calculation results have limited guidance value for actual engineering, due to inaccurate mechanical parameters and simplified models. Therefore, scholars are trying to find more scientific methods to study mechanical problems of water-sediment two-phase seepage.

Limited by the testing equipment, the water-sediment two-phase seepage experiments took water and prefabricated parallel fractures as research objects [13]. With the development of test equipment and the signal acquisition system, water-sediment two-phase seepage experiments in coarse fractures were carried out and a series of research results were achieved [14–16]. Based on a large number of

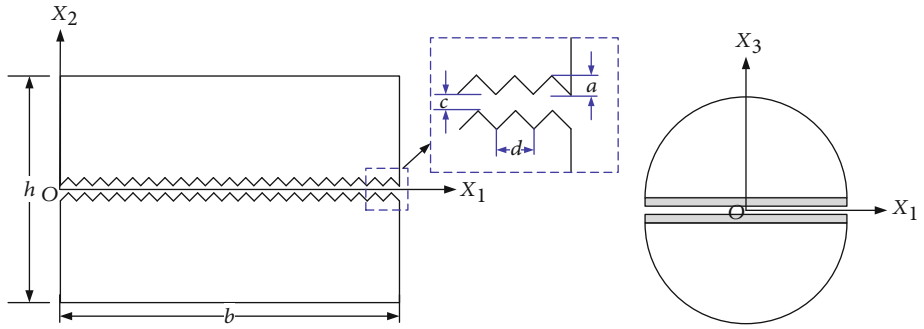

Figure 1: Structure and size of the fracture specimen.

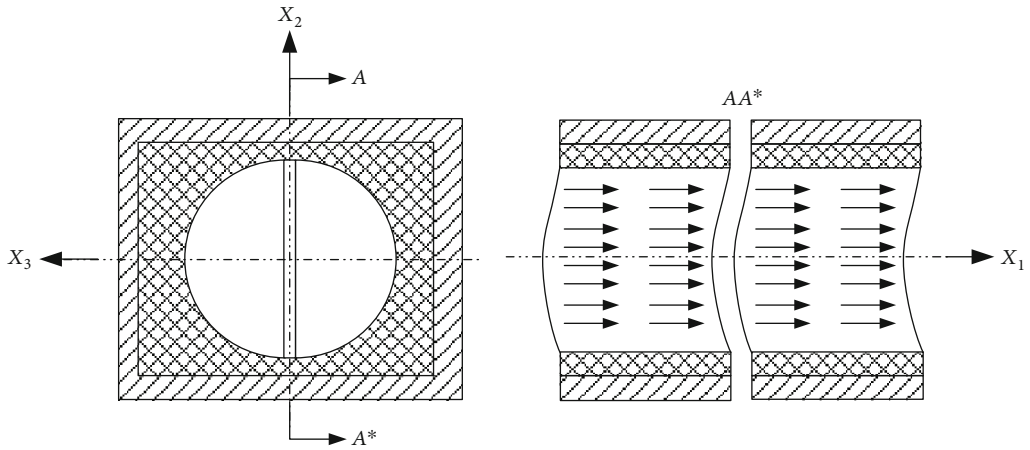

(a) Installation methods of specimens (b) Seepage velocity distribution

Figure 2: Water-sediment seepage principles inside the fissures.

studies on the water-sediment seepage process in coarse fractures, scholars mainly study the factors affecting the seepage characteristics, including fracture roughness, fracture aperture, sediment concentration, and sand particle size [17–21]. However, the current studies on fracture seepage mainly focus on a single-fluid seepage field and rarely involve the liquid-solid two-phase flow in fractures [22, 23]. When the particle concentration is relatively low, the particle cannot be treated as the quasi-fluid and the interphase forces cannot be ignored. At the point, water-sediment transport can be treated neither as two-fluid seepage nor as single-fluid seepage. The research on particle phase and continuous phase flow in fractures is rare.

At present, there is rare research involving the liquid-solid two-phase flow in fractures. In the paper, a mechanical model of water-sediment two-phase seepage in coarse fractures was established based on the seepage mechanics theory. A testing system was built to simulate water-sediment two-phase seepage in coarse fractures. Then, the mechanical test was carried out by using prefabricated coarse fracture specimens. The water-sediment two-phase seepage characteristics and the influencing factors were studied systematically. The test results are aimed at revealing the water and sediment inrush mechanism and providing references for water-sediment inrush disaster prediction and control.

2. Experimental Principles and Introduction

2.1. Preparation of Coarse Fracture Specimens. Natural rock specimens are generally used to get fissure surfaces by fracture splitting in fluid flow experiment in fractures. The obtained fractures are relatively close to the actual fractures but cannot be used to describe geometrical characteristics and construct the numerical model. Meanwhile, the composition of natural rock is complex and may easily cause a water-soluble phenomenon to occur, which will affect the experimental results. On this basis, Ni-Cr alloys (06Cr19Ni10 GB/T 20878-2007) were used to make coarse fracture specimens in this experiment. Figure 1 shows the sizes of fracture specimens. The height (b) is 100 mm, and the diameter (h) is 70 mm + 2a + c. The projections of the fissure surfaces on the longitudinal section are continuous and uniform distributed isosceles triangles. The height of the triangle (a) is 1 m. The distance between two fissure surfaces (d) is 2 mm. The fissure aperture (c) is 0.8 mm. The fissures are anastomosed between two fissure surfaces. Water and quartz sand were used as the liquid phase and solid phase, respectively, for the experiment.

2.2. Experimental Principles and the Test System Establishment. Water and sediment belong to solid-liquid two-phase mixtures. The flow of water and sediment in fractures is complex turbulent flow. In this paper, a generalized

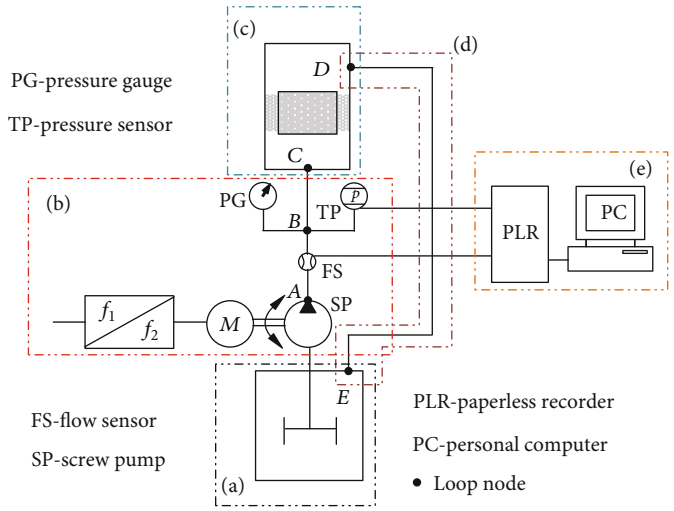

Figure 3: The water-sediment seepage testing system in fissures (a: the stirring system; b, d: the water-sediment transport system; c: permeameter; and e: control panel).

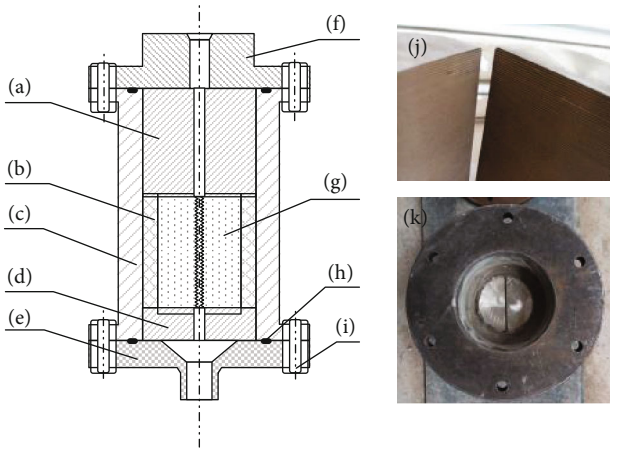

Figure 4: Seepage system and specimen installation method (a: upper water-conducting transition plate; b: high water material; c: cylinder tube; d: lower water-conducting transition plate; e: conical base; f: capping; g: fissure specimen; h: O-shaped rubber seal ring; i: bolt; j: coarse fissure surface; k: the inner of the seepage system).

flow-seepage was used to simplify actual flow of water and sediment. Taking the direction parallel to crack length as the X_1 axis and the direction of crack aperture as the X_2 axis, the coordinate system $OX_1X_2X_3$ was established according to right-hand grip rule, as shown in Figure 1.

In actual flow, the distributions of water flow rate $\vec{v}$, sand flow rate $\overrightarrow{v^{\mathrm{p}}}$, hydraulic pressure p, and sediment concentration (fractional volume Φ) are uniform. This is because fracture surfaces have unilateral constraints to water and sediment.

In seepage mechanics, the normal distributions of flow velocities among fractures are usually not considered along the fissure surfaces, and the seepage velocity (the average seepage velocity along the fracture width direction) is used to replace the permeability velocity. The water phase seepage velocity was marked as $\vec{V}$, the sand phase seepage velocity was marked as $\overrightarrow{V^{\mathrm{p}}}$, and the distance between two fissure surfaces was marked as c; then, the following equations could be obtained.

$$\vec{V} = \frac{1}{c}\int_0^c \vec{v}\,\mathrm{d}x_2, \tag{1}$$

$$\overrightarrow{V^{\mathrm{p}}} = \frac{1}{c}\int_0^c \overrightarrow{v^{\mathrm{p}}}\,\mathrm{d}x_2, \tag{2}$$

where x_2 is the local coordinate. The transformation relation between x_2 and X_2 is given as follows:

$$x_2 = X_2 - X_2^*, \tag{3}$$

where X_2^* is the coordinate of X_2, the point of intersection between the lower fissure surface and cross section.

As shown in Figures 1 and 2, the seepage velocities $\vec{V}$ and $\overrightarrow{V^{\mathrm{p}}}$ were one dimension less than the actual flow velocities $\vec{v}$ and $\overrightarrow{v^{\mathrm{p}}}$. To facilitate the analysis, the physical quantity was assumed to be constant along the direction of X_3. Thus, the actual flow velocities $\vec{v}$ and $\overrightarrow{v^{\mathrm{p}}}$ were two-dimensional, while the seepage velocities $\vec{V}$ and $\overrightarrow{V^{\mathrm{p}}}$ were one-dimensional, that is,

$$\vec{v} = \vec{f}_{\mathrm{v}}(X_1, X_2; t), \tag{4}$$

$$\overrightarrow{v^{\mathrm{p}}} = \overrightarrow{f_{\mathrm{v}}^{\mathrm{p}}}(X_1, X_2; t), \tag{5}$$

$$\vec{V} = \vec{F}_{\mathrm{v}}(X_1; t), \tag{6}$$

$$\overrightarrow{V^{\mathrm{p}}} = \overrightarrow{F_{\mathrm{v}}^{\mathrm{p}}}(X_1; t). \tag{7}$$

In seepage experiments, the distributions of flow velocities along direction X_2 were unavailable, so flow velocities in fissures

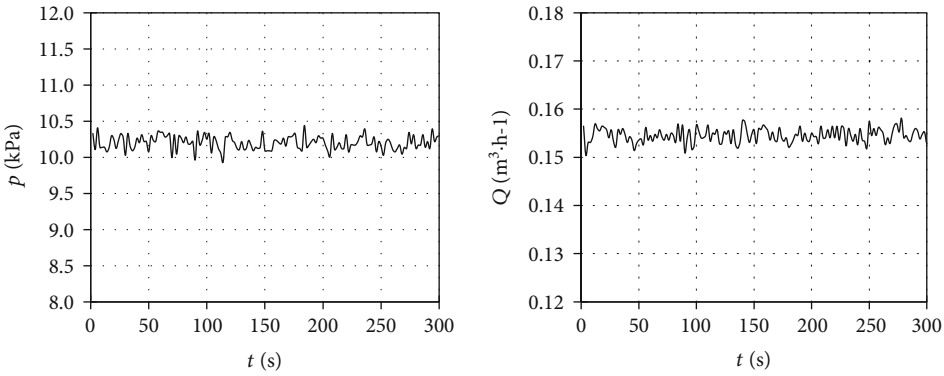

(a) Pressure-time (b) Flow-time

Figure 5: Pressure-time curve and flow-time curve ($n = 200$ r/min).

were measured. The experimental phenomena and water-sediment flow laws were explained and analyzed by viewpoints and theory of seepage mechanics.

During the seepage of water and sediment in two parallel fissure surfaces, the water was the Newtonian fluid, while the sediment was the non-Newtonian fluid. The fissure surfaces are curved surfaces generated by polyline translation.

$\vec{e}_i (i = 1, 2, 3)$ was the base vector of the coordinate system $OX_1X_2X_3$; then, the seepage velocity was $\vec{V} = V\vec{e}_1$ and $\overrightarrow{V^{\mathrm{p}}} = V^{\mathrm{p}}\vec{e}_1$. The sum of the water flow and sediment flow in fissures could be obtained by the following equation:

$$Q = V\Phi^{\mathrm{w}}hD + V^{\mathrm{p}}\Phi hD, \tag{8}$$

where Φ^{w} is the volume fraction of water and Φ is the volume fraction of sediment. Due to

$$\boldsymbol{\Phi}^{\mathrm{w}} + \boldsymbol{\Phi} = 1, \tag{9}$$

equation (8) could be transformed into

$$Q = [V(1 - \Phi^{\mathrm{w}}) + V^{\mathrm{p}}\Phi]hD. \tag{10}$$

Therefore, the seepage velocity of the water-sediment mixture could be obtained by

$$V = \frac{Q}{hD} = V(1 - \Phi^{\mathrm{w}}) + V^{\mathrm{p}}\Phi. \tag{11}$$

To realize accurate measurement of flow in fissures, the following boundary conditions should be met for water-sediment flow.

$$V_2|_{X_3=\pm D/2} = 0,\ V_3|_{X_3=\pm D/2} = 0, \tag{12}$$

$$V_2^{\mathrm{p}}\big|_{X_3=\pm D/2} = 0,\ V_3^{\mathrm{p}}\big|_{X_3=\pm D/2} = 0. \tag{13}$$

In the experiment, $X_3 = \pm D/2$ was set as the closed boundary without mass transfer.

To realize the boundary conditions in equations (12) and (13), high water seal materials were used around two specimens with fissure surfaces. A rigid frame was arranged outside the high water materials, as shown in Figure 2(a). The seepage velocity of fluids was parallel to the X_1 axis, as shown in Figure 2(b).

According to principles in Figure 2, a water-sediment seepage test system in fissures was designed, as shown in Figure 3. The system consists of a stirring system (a in Figure 3), a water-sediment transport system (b and d in Figure 3), a self-developed permeameter (c in Figure 3), and a control panel (e in Figure 3). Figure 4 shows the installation methods of the permeameter and specimens. Manual control was used for the relative positions between fissure surfaces. Firstly, the specimen was sealed in the cylinder tube. A 0.8 mm copper wire was placed on the fissure surface along both sides of the specimen. High water materials were filled between the specimen and cylinder tube.

2.3. Calculation Methods of Characterization Parameters. The water-sediment mixture flow in coarse fissures belongs to typical non-Darcy flow. In the experiment, the equivalent fluidity I_{e} and the β-factor of non-Darcy flow were chosen as characterization parameters.

The inner diameter of pipe-segment ABC was d_{tube}, and the average flow velocity could be obtained by

$$V_{\mathrm{tube}} = \frac{4Q}{\pi d_{\mathrm{tube}}^2}. \tag{14}$$

The seepage velocity in fissures could be calculated by

$$V = \frac{Q}{BD}. \tag{15}$$

On the precondition that linear loss and local loss were neglected, the Bernoulli equation was given as follows:

$$\frac{p_{\mathrm{tube}}}{\rho^* g} + \frac{V_B^2}{2g} = \frac{p_1}{\rho^* g} + \frac{V^2}{2g} + \Delta H, \tag{16}$$

where ρ^*, ρ, and ρ^{p} are densities of water-sediment mixture, water, and sand, respectively, and $\rho^* = \rho^{\mathrm{p}}\Phi + \rho(1 - \Phi)$.

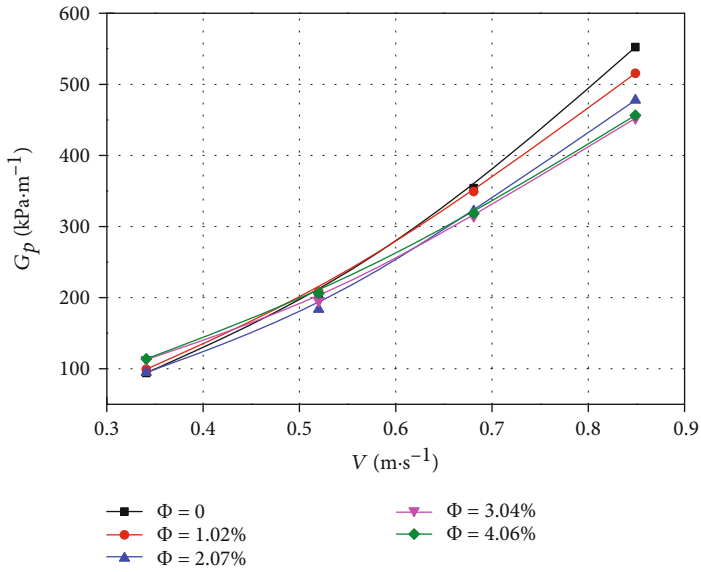

(a) D_p = 0.02-0.06 mm

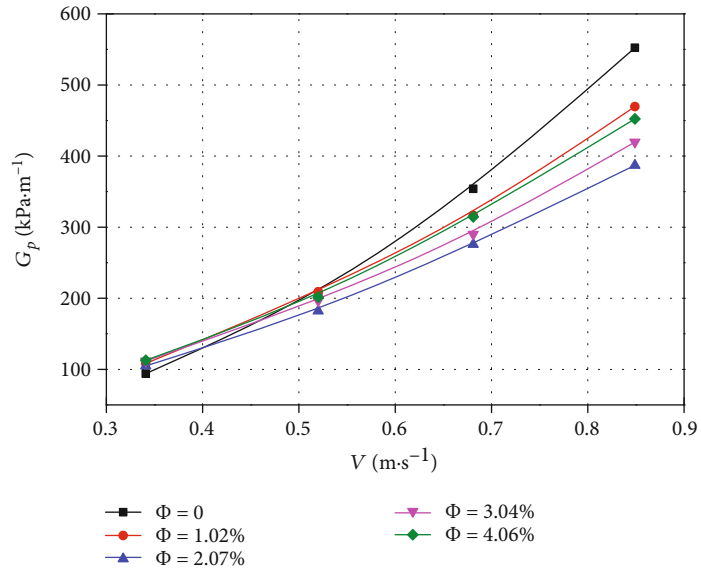

(b) D_p = 0.06-0.10 mm

Figure 6: Continued.

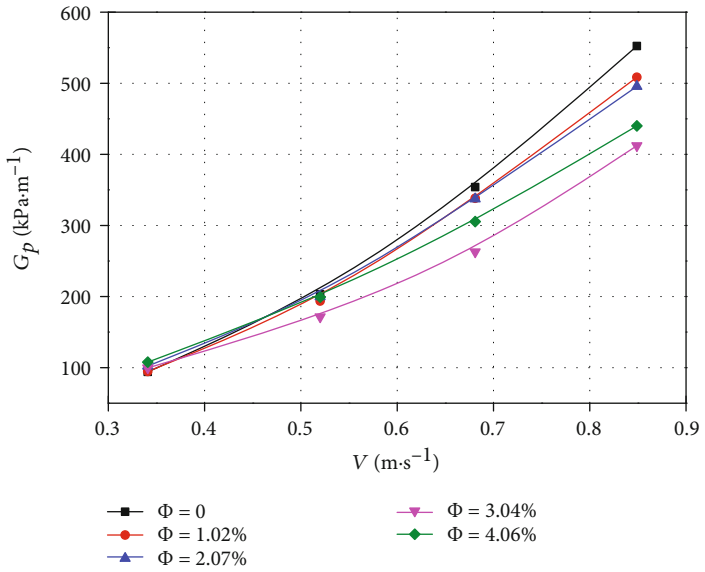

(c) D_p = 0.10-0.14 mm

FIGURE 6: G_p Abs-V curves.

g is the acceleration of gravity. p_1 is the pressure at fissure entrance. ΔH is the height difference between point B and the middle of the fissure surface (ΔH was about 1.1 m in this system). Equation (16) could be used to get the pressure p_1 at the entrance of the fracture.

The outlet of the fracture was open, so the pressure p_2 was approximately equal to zero. Then, the average pressure gradient of water-sediment mixture along X_1 was given:

$$\left.\frac{\partial p}{\partial x}\right|_{\text{average}} = -\frac{p_1}{L}. \tag{17}$$

That is, the absolute value of the pressure gradient G_p could be calculated by

$$G_p = \frac{p_1}{L}, \tag{18}$$

The water-sediment mixtures were treated as power law fluids. The power exponent was marked as n. Then, in steady-state flow, the equivalent fluidity I_e, β-factor of non-Darcy, seepage velocity V, and absolute value of pressure gradient G_p could meet the following relation:

$$\frac{1}{I_e} V^n + \rho^* \beta V^2 = -\frac{p_2 - p_1}{L}. \tag{19}$$

Considering $p_2 = 0$, equation (19) could be simplified as

$$\frac{1}{I_e} V^n + \rho^* \beta V^2 = \frac{p_1}{L}. \tag{20}$$

According to equation (18), equation (21) could be obtained.

$$\frac{1}{I_e} V^n + \rho^* \beta V^2 = G_p. \tag{21}$$

By introducing the symbol λ_1 and λ_2, equation (22) could be obtained.

$$\begin{cases} \lambda_1 = \dfrac{1}{I_e}, \\ \lambda_2 = \rho^* \beta. \end{cases} \tag{22}$$

Then, equation (21) could be transformed into

$$\lambda_1 V^n + \lambda_2 V^2 = G_p. \tag{23}$$

In this experiment, four groups of screw pump rotation speeds were set. The flow and the pressure at the entrance were Q_i and p_1^i, respectively. The corresponding seepage velocity V_i and the absolute value of the pressure gradient were G_p^i, $i = 1, 2, 3, 4$.

The functional was constructed as follows:

$$\Pi = \sum_{i=1}^{4} \left(\lambda_1 V_i^n + \lambda_2 V_i^2 - G_p^i\right)^2 = 0. \tag{24}$$

To take the minimum value of Π, equation (25) could be obtained.

$$\begin{cases} \left(\sum_{i=1}^{4} V_i^{2n}\right)\lambda_1 + \left(\sum_{i=1}^{4} V_i^{2+n}\right)\lambda_2 = \left(\sum_{i=1}^{4} V_i^n G_p^i\right), \\ \left(\sum_{i=1}^{4} V_i^{2+n}\right)\lambda_1 + \left(\sum_{i=1}^{4} V_i^4\right)\lambda_2 = \left(\sum_{i=1}^{4} V_i^2 G_p^i\right). \end{cases} \tag{25}$$

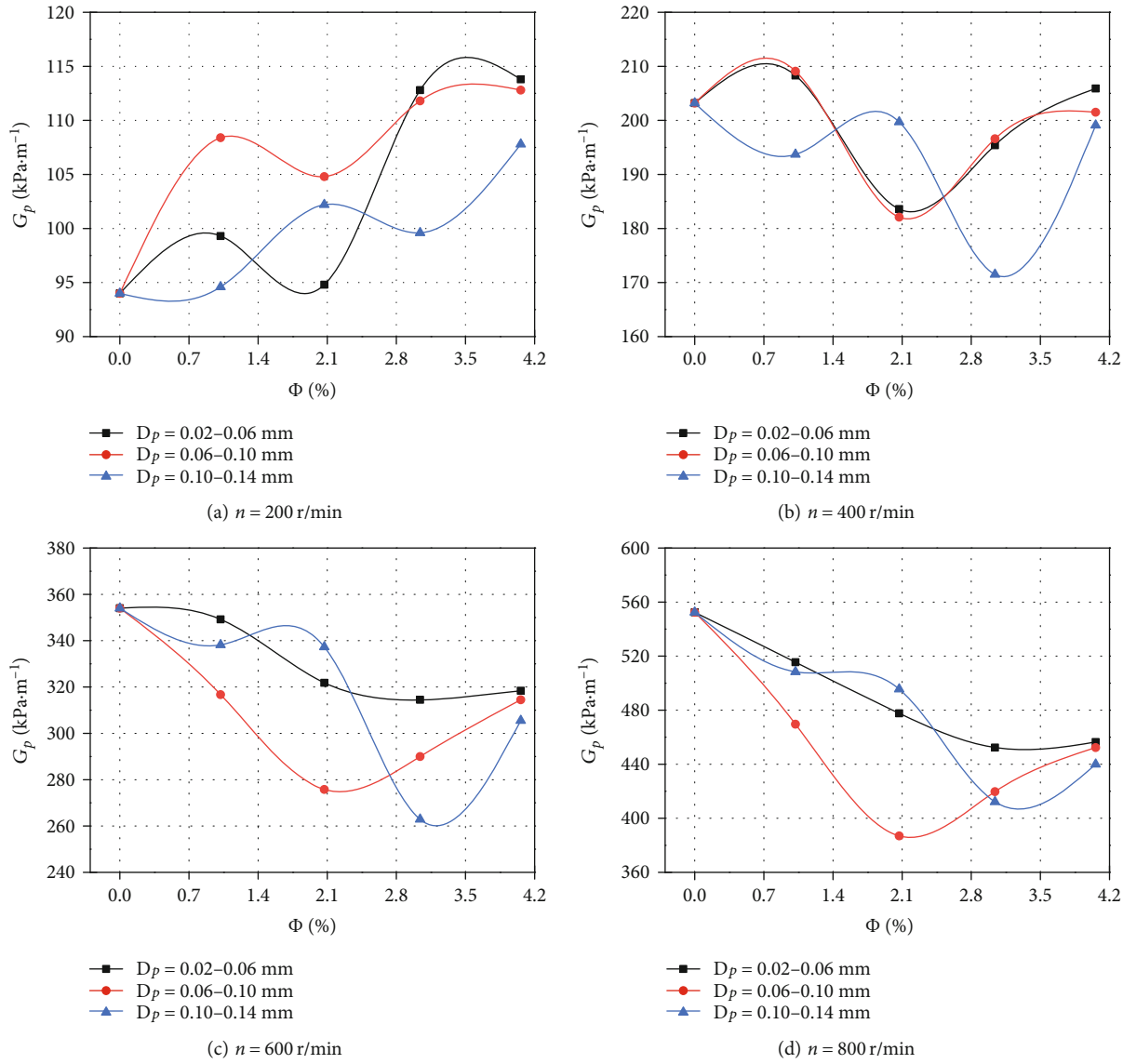

Figure 7: G_p-Φ curves.

The solution of equation (25) was calculated as follows:

$$\begin{cases} \lambda_1 = \dfrac{\left(\sum_{i=1}^{4} V_i^n G_p^i\right)\left(\sum_{i=1}^{4} V_i^4\right) - \left(\sum_{i=1}^{4} V_i^{2+n}\right)\left(\sum_{i=1}^{4} V_i^2 G_p^i\right)}{\left(\sum_{i=1}^{4} V_i^{2n}\right)\left(\sum_{i=1}^{4} V_i^4\right) - \left(\sum_{i=1}^{4} V_i^{2+n}\right)\left(\sum_{i=1}^{4} V_i^{2+n}\right)}, \\ \lambda_2 = \dfrac{\left(\sum_{i=1}^{4} V_i^{2n}\right)\left(\sum_{i=1}^{4} V_i^2 G_p^i\right) - \left(\sum_{i=1}^{4} V_i^n G_p^i\right)\left(\sum_{i=1}^{4} V_i^{2+n}\right)}{\left(\sum_{i=1}^{4} V_i^{2n}\right)\left(\sum_{i=1}^{4} V_i^4\right) - \left(\sum_{i=1}^{4} V_i^{2+n}\right)\left(\sum_{i=1}^{4} V_i^{2+n}\right)}. \end{cases} \tag{26}$$

By using equation (22), the equivalent fluidity I_e and β -factor of non-Darcy flow could be obtained as follows:

$$I_e = \frac{1}{\lambda_1}, \tag{27}$$

$$\beta = \frac{\lambda_2}{\rho^*}. \tag{28}$$

2.4. The Testing Scheme and Methods. In this experiment, the sediment particle size D_p and the sediment volume fraction (concentration) Φ were selected as variables to study water-sediment two-phase seepage characteristics in coarse fractures. There were three groups of D_p, that is, 0.02-0.06 mm, 0.06-0.10 mm, and 0.10-0.14 mm. Φ values were divided into five groups, that is, 0%, 1.02%, 2.07%, 3.04%, and 4.06%.

The whole process is as follows:

(i) The first step is to pour water into the stirring pool with the inner diameter of D_{pool}. The depth of water was H_w. Then, the volume of water was $B_w = (\pi/4) D_{pool}^2 H_w$. The sediment volume required for the test could be converted according to Φ, that is,

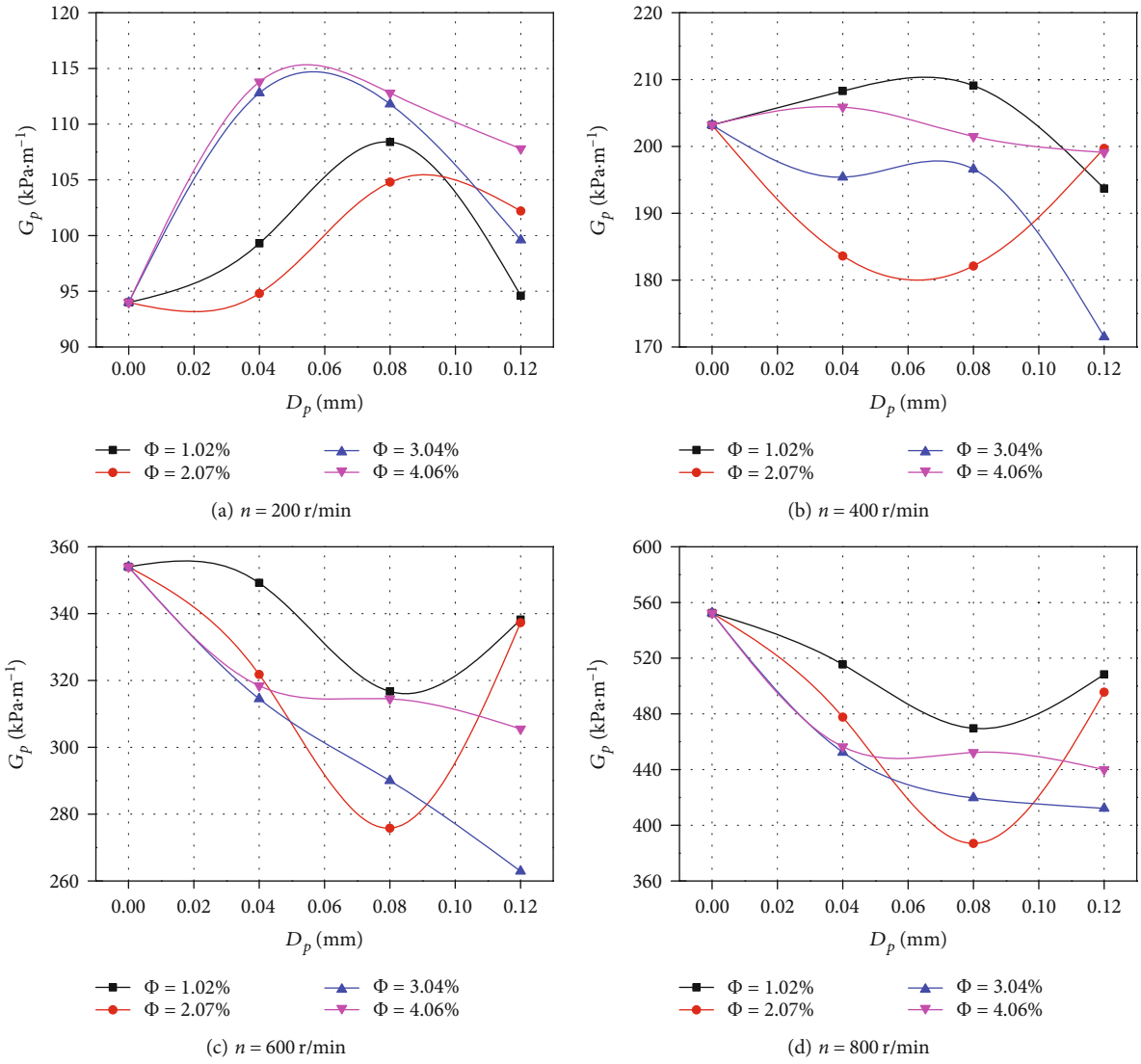

Figure 8: G_p-D_p curves.

$$B^p = \frac{1-\Phi}{\Phi} B^w. \tag{29}$$

According to the density of sand, the quality of sand could be calculated as follows:

$$m^p = \rho^p B^p. \tag{30}$$

By substituting equation (29) into equation (30), equation (31) could be obtained.

$$m^p = \frac{1-\Phi}{\Phi} \rho^p B^w. \tag{31}$$

(ii) The second step was to turn on the motor to drive the stirring impeller to make sand particles mix in the water. After a certain period of stirring, the screw pump was started to extract water-sediment mixtures. The sand concentration (volume fraction) $\tilde{\Phi}$ was measured. If there was a big difference between $\tilde{\Phi}$ and Φ, a hand pump was used to lift the container. At this point, the sand concentration would be measured again. After the relative error between $\tilde{\Phi}$ and Φ was no more than 5%, the handle of the reversing valve of the hand pump was placed at the neutral position to stop the movement of the double-acting hydraulic cylinder

(iii) The screw pump was connected to the permeameter by a hose to form a penetration channel. The permeameter was connected with the stirring pool to form a backflow channel

(iv) VVVF (Variable Voltage and Variable Frequency) was used to adjust the screw pump rotation speed

to $n_1 = 200(\mathrm{r/min})$. The real-time flow and pressure displayed by the paperless recorder were observed. After the flow and pressure became stable, the flow Q_1 and pressure in pipeline p_1' were recorded

(v) The screw pump rotational speeds were adjusted to $n_2 = 400(\mathrm{r/min})$, $n_3 = 600(\mathrm{r/min})$, and $n_4 = 800(\mathrm{r/min})$, and the corresponding flows $Q_i(i = 2, 3, 4)$ and pressures $P_i'(i = 2, 3, 4)$ were recorded

(vi) The screw pump was closed and Φ was changed. Steps (i) to (v) were repeated

(vii) The screw pump was closed and D_p was changed. Steps (i) to (vi) were repeated

(viii) According to above steps, the water-sediment seepage tests were completed for three groups of sediments with different particle sizes and five groups of sediments with different volume fractions. The penetration test was carried out with the fracture width of 0.8 mm, D_p of 0.02-0.06 mm, and Φ of 4.06%. Figure 5 shows the pressure-time curve and flow-time curve. It could be seen that when the screw pump rotational speed became stable, the volume flow of the water-sediment mixture changed slightly, and the average value was relatively stable. This showed that the fracture resistance had little effect on screw pump displacement

3. Pressure Gradient Change Characteristics of Water-Sediment Two-Phase Seepage in Coarse Fractures

3.1. Nonlinear Characteristics of Water-Sediment Two-Phase Seepage. Figure 6 shows the change curves of absolute values of pressure gradient G_p of water-sediment mixtures with the flow rate V in coarse fractures under different sand particle sizes D_p and sand concentrations Φ. As V increased, G_p increased gradually. A remarkable nonlinear relationship existed between G_p and V, proving that the water-sediment two-phase seepage in fracture specimens belonged to the typical non-Darcy flow.

3.2. Variation Laws of Pressure Gradient with the Sand Volume Fraction. Figure 7 shows change curves of the pressure gradient G_p with the sand volume fraction Φ under various screw pump rotational speeds n. When n were 200 r/min and 400 r/min, change characteristics of curves were similar. When n were 600 r/min and 800 r/min, the characteristics of curves varied a lot.

In Figures 7(a) and 7(b), under low rotational speeds and three kinds of sand particle sizes, the absolute value of G_p firstly increased, then decreased, and increased again with the change of sand particle volume fraction Φ. When $D_p = 0.02 \sim 0.06$ mm and $D_p = 0.06 \sim 0.10$ mm, monotone intervals of G_p-Φ curves were consistent. When $D_p = 0.10 \sim 0.14$ mm, monotone intervals changed significantly, presenting that the whole of the curve shifted to the right. The comparison of two groups of curves indicated that when $n = 200$ r/min, three groups of G_p-Φ curves showed an overall upward trend, while with $n = 400$ r/min, they showed horizontal fluctuations.

Table 1: Parameters involved in water-sediment seepage in rock fractures under various conditions.

D_p (mm)	Φ (%)	$I_e(\mathrm{m}^{n+2} \cdot \mathrm{s}^{2-n} \cdot \mathrm{kg}^{-1})$	β (m^{-1})
0	0	5.06×10^{-7}	$6.87E+05$
0.02-0.06	1.02%	$1.46E-08$	$5.72E+05$
	2.07%	$1.91E-08$	$5.41E+05$
	3.04%	$7.17E-09$	$4.11E+05$
	4.06%	$6.40E-09$	$3.98E+05$
0.06-0.10	1.02%	$7.59E-09$	$4.39E+05$
	2.07%	$6.03E-09$	$3.01E+05$
	3.04%	$5.91E-09$	$3.35E+05$
	4.06%	$6.67E-09$	$4.00E+05$
0.10-0.14	1.02%	$2.68E-08$	$5.96E+05$
	2.07%	$1.25E-08$	$5.33E+05$
	3.04%	$1.04E-08$	$4.01E+05$
	4.06%	$6.82E-09$	$3.88E+05$

In Figures 7(c) and 7(d), under high rotational speeds and three kinds of sand particle sizes, the change of G_p with Φ firstly decreased and then increased, showing an overall downward trend.

Comparisons of each group of curves indicated that the curves of pressure gradient absolute values and sand particle volume fraction had multiple monotonicity. When the flow velocity was low, sand movement increased the pressure loss of the water-sediment flow in fractures. As the flow velocity increased, the pressure loss also decreased.

3.3. Variation Laws of Pressure Gradient with the Sand Particle Size. In the water-sediment mixture, the sand particle size could affect the pressure gradient. Figure 8 gives variation laws of G_p with D_p under various conditions.

In Figure 8(a), with n of 200 r/min and various Φ, the absolute values of G_p first increased and then decrease with the increase in D_p, showing an overall upward trend with different positions of extreme points of G_p. Compared with the two groups of curves with Φ values of 1.02% and 2.07%, the maximum values of curves with Φ of 3.04% and 4.06% shifted to the right. When n increased to 400 r/min in Figure 8(b), G_p-D_p curves had obvious differences under four kinds of Φ, showing horizontal fluctuations on the whole.

As n increased to 600 r/min in Figure 8(c), the variation trends of two kinds of curves with Φ of 1.02% and 2.07% were relatively consistent. G_p first decreased and then

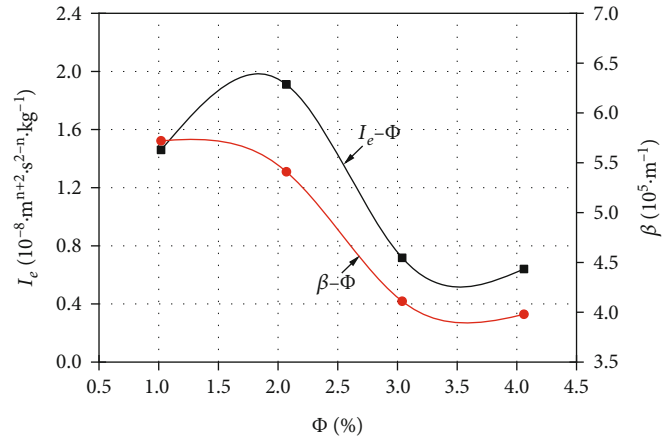

(a) D_p = 0.02~0.06 mm

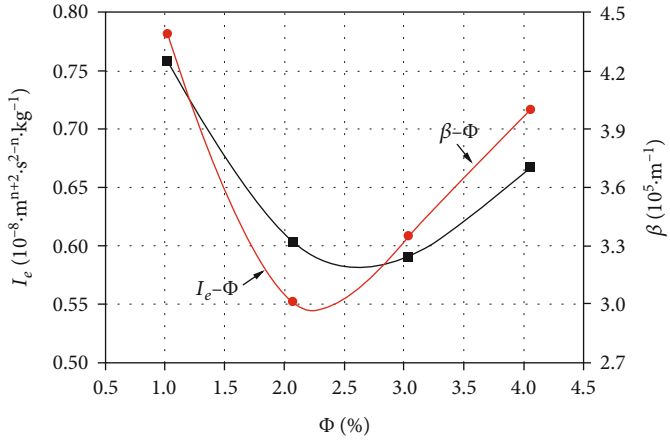

(b) D_p = 0.06~0.10 mm

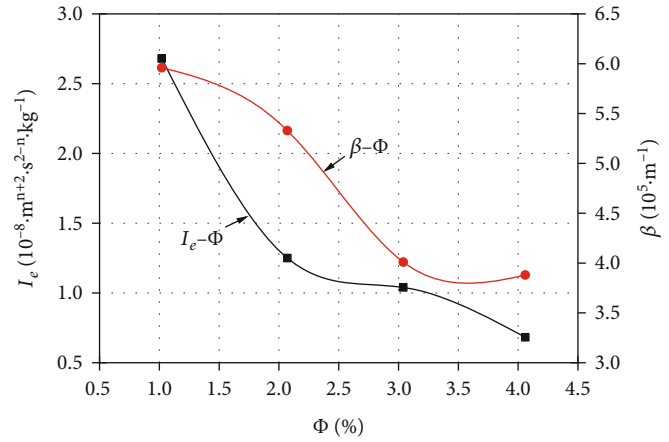

(c) D_p = 0.10~0.14 mm

Figure 9: Variation curves of seepage parameters with the sand volume fraction.

increased with the increase in D_p. When Φ were 3.04% and 4.06%, G_p decreased with the increase in D_p. When $n = 800$ r/min, the change characteristics of the lower curve were basically the same with those when $n = 600$ r/min. That is, under low Φ, G_p first decreased and then increased with the increase in D_p, while under high Φ, G_p reduced gradually with the increase in D_p.

On the whole, the variation of sand particle size could significantly change the characteristics of pressure gradient. Meanwhile, the changes of the rotational speed of the pump and sand concentration could also affect the pressure gradient. When the flow velocity was low and the particle size was large, the particle movement caused loss of pressure. As the flow velocity increased, the pressure loss became weak gradually.

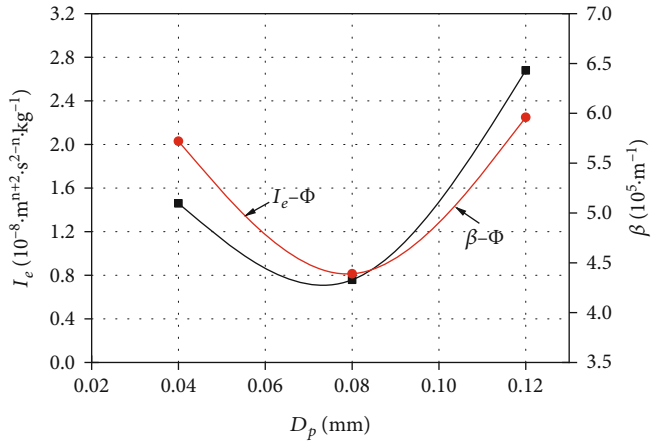

(a) $\Phi = 1.02\%$

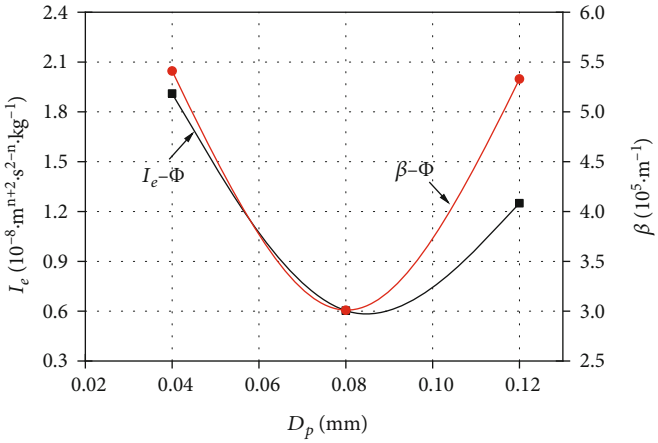

(b) $\Phi = 2.07\%$

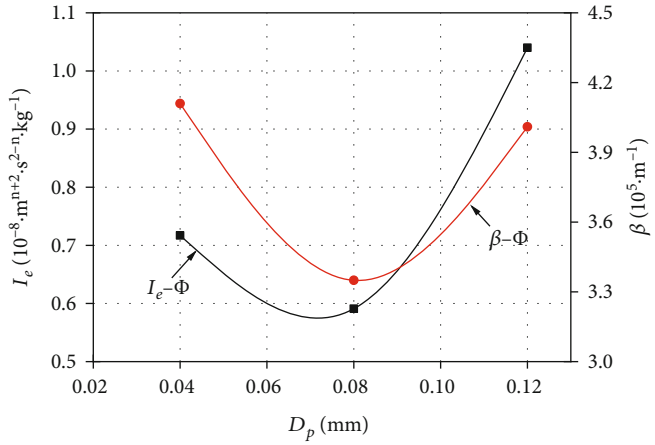

(c) $\Phi = 3.04\%$

Figure 10: Continued.

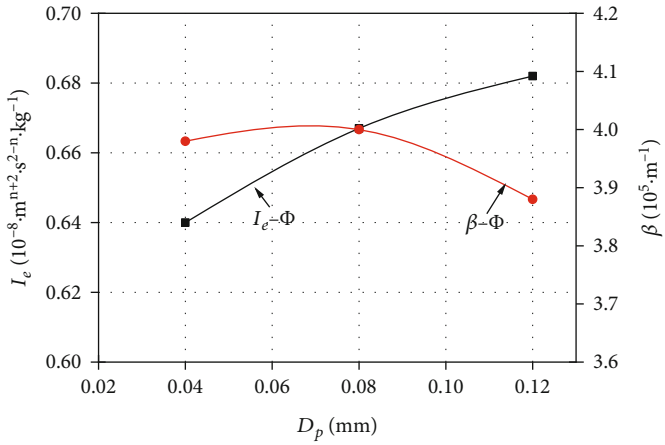

(d) $\Phi = 4.06\%$

Figure 10: Variation laws of I_e and β-factor with D_p.

4. Change Characteristics of Parameters Involved in the Water-Sediment Two-Phase Seepage in Coarse Fractures

Based on the experimental results and calculations, the equivalent fluidity I_e and β-factor of non-Darcy flow were obtained under various particle sizes D_p and sand volume fraction Φ, as shown in Table 1.

4.1. Variations Laws of Seepage Parameters with Sand Volume Fraction. According to the data in Table 1, variation curves of the equivalent I_e and β-factor of non-Darcy flow with the sand volume fraction were obtained under three kinds of particle sizes, as shown in Figure 9.

Figure 9 shows that variation laws of I_e and β-factor of non-Darcy flow with Φ were basically the same, proving that the two factors could represent the same seepage characteristics. With D_p between 0.02 and 0.06 mm, as Φ increased, I_e and β-factor showed an overall decreasing trend. When Φ increased from 1.02% to 2.07%, I_e showed a small increase, while β-factor was basically unchanged. When Φ increased from 3.04% to 4.06%, I_e and β-factor were basically unchanged. When Φ increased from 2.07% to 3.04%, I_e and β-factor decreased by over 60%. When $D_p = 0.06$ ~0.10 mm, I_e and β-factor increased with Φ, showing the trend of first decreasing and then increasing. When $D_p =$ 0.10~0.14 mm, I_e and β-factor decreased rapidly with the increase in Φ.

4.2. Variation Laws of Seepage Parameters with the Sand Particle Size. Based on the experimental results, variation laws of I_e and β-factor with D_p were obtained, as shown in Figure 10.

Figure 10 indicates that variation laws of I_e and β-factor with D_p were basically the same. When $\Phi = 1.02\%$, 2.07%, and 3.04%, I_e and β-factor first decreased and then increased with the increase in D_p. When $\Phi = 4.06\%$, I_e increased with the increase in D_p and the increase became slow gradually, while β-factor first increased and then decreased and the overall amplitude of variation was not obvious.

4.3. Analysis and Discussions. In seepage mechanics, the equivalent fluidity I_e refers to the ratio of the flow and cross-sectional area. It is used to represent the seepage capacity of the mixtures. The larger the value, the stronger the seepage capacity. β-factor of non-Darcy flow is used to represent nonlinear characteristics of seepage in fractures. The larger the value, the more obvious the nonlinear characteristics. Compared with the water phase seepage flow, the sand particle size and the sand concentration (volume fraction) are important factors affecting the water-sediment flow in fractures, which has been illustrated in the experiment.

In the fixed mixtures with various sand particle sizes, the higher the sand volume fraction, the narrower the overall permeable channel of the fracture and the lower the permeability of the fracture, resulting in a smaller equivalent fluidity I_e. Meanwhile, the narrow permeable channel reduced the nonlinear characteristics of the seepage, macroscopically characterized by the decrease in β-factor of non-Darcy flow, as shown in Figures 9(a) and 9(c). However, remarkable solid-liquid two-phase seepage characteristics existed when the water-sand mixture passed through the narrow channel, which led to significant nonlinear changes in seepage parameters under certain conditions. As shown in Figure 9(b), when $D_p = 0.06$~0.10 mm, the solid-liquid two-phase seepage might cause turbulent flow to occur in the local channel, as the sand volume fraction increased from 2.07% to 3.04%, causing sudden changes in variation laws of seepage parameters.

When the sand volume fraction was fixed in the water-sediment mixture, variations of the sand particle sizes could lead to uncertain nonlinear seepage characteristics in the seepage process. The increase in the particle size firstly narrowed the local permeable channels, weakened the whole seepage capacity in fractures, and lowered the nonlinear seepage characteristics of the medium. As the particle size further increased, the overall migration capacity of the water-sediment mixture increased. The overall impact

capacity of the mixture on the channel section enhanced. The equivalent fluidity of the sandstones became larger. Meanwhile, local turbulence could be found around the particles, leading to the increase in the equivalent fluidity I_e in the channel of fractures and β-factor of non-Darcy flow. The processes are shown in Figures 10(a)–10(c). When the volume fraction of the water-sediment mixture reached a certain level, the influences of the particle clusters composed of fine particles and the large-volume particles on the overall seepage characteristics were basically unchanged; that is, the change characteristics of I_e and β-factor of non-Darcy flow were not obvious, as shown in Figure 10(d).

5. Main Conclusions

To further clarify the mechanism of mine water inrush hazards, this paper carried out an experiment to study mechanical characteristics of the water-sediment two-phase seepage in prefabricated coarse fractures. The nonlinear characteristics of the water-sediment seepage in fractures were studied systematically, and the influencing factors were analyzed in detail. The main research conclusions are as follows:

(i) Based on theory of seepage mechanics, the formulas for the principle of the water-sediment two-phase seepage in fractures were deduced. The mechanical model was established. A system was developed to conduct the water-sediment seepage test, and the characterization parameters were determined and analyzed

(ii) Variation laws of the absolute values of the pressure gradients with the seepage velocities were systematically analyzed under various conditions. The nonlinear relationships were clarified. On this basis, it was determined that the water-sediment two-phase seepage test was a typical non-Darcy flow experiment

(iii) The impacts of the sand volume fraction and the sand particle size on the absolute values of the pressure gradients were significant. When the particle size was fixed and the pump rotational speed was slow, the pressure gradient first increased, then decreased, and increased again with the change of the sand volume fraction. When the pump rotational speed was high, the pressure gradient first decreased and then increased. When the sand volume fraction was fixed, the absolute value of pressure gradient changed from first increasing and then decreasing to first decreasing and then increasing, as the speed of the pump changed from high to low. This was related to the pressure loss caused by the sand particle movement

(iv) During the seepage process of the water-sediment seepage in fractures, the change characteristics of equivalent fluidity I_e and β-factor of non-Darcy flow with the sand volume fraction and the sand particle size were basically the same. When the particle size was fixed, with the higher sand volume fraction, both I_e and β-factor decreased. When $D_p = 0.06\sim0.10$ mm, they first decreased and then increased. When the sand volume fraction was fixed, they first decreased and then increased with the increase in the sand particle size. When the sand volume fraction was relatively high, they changed slightly

Data Availability

The data used to support the findings of this study are included within the article.

Conflicts of Interest

The authors declare that they have no conflict of interest.

Acknowledgments

This study was funded by the National Natural Science Foundation of China (grant number 52074240).

References

[1] W. Sun, W. Zhou, and J. Jiao, "Hydrogeological classification and water inrush accidents in China's coal mines," *Mine Water and the Environment*, vol. 35, no. 2, pp. 214–220, 2016.

[2] S. Dong, H. Wang, X. Guo, and Z. Zhou, "Characteristics of water hazards in China's coal mines: a review," *Mine Water and the Environment*, vol. 40, no. 2, pp. 325–333, 2021.

[3] J. Chen, J. Zhao, S. Zhang, Y. Zhang, F. Yang, and M. Li, "An experimental and analytical research on the evolution of mining cracks in deep floor rock mass," *Pure and Applied Geophysics*, vol. 177, no. 11, pp. 5325–5348, 2020.

[4] S. Yin, J. Zhang, and D. Liu, "A study of mine water inrushes by measurements of in situ stress and rock failures," *Natural Hazards*, vol. 79, no. 3, pp. 1961–1979, 2015.

[5] Y. Qin and J. Lu, "Prediction of coal mine water hazards: a case study from the Huainan coalfield," *Arabian Journal of Geosciences*, vol. 12, no. 3, p. 83, 2019.

[6] G. Zhang, K. Zhang, L. Wang, and Y. Wu, "Mechanism of water inrush and quicksand movement induced by a borehole and measures for prevention and remediation," *Bulletin of Engineering Geology and the Environment*, vol. 74, no. 4, pp. 1395–1405, 2015.

[7] W. Yang, L. Jin, and X. Zhang, "Simulation test on mixed water and sand inrush disaster induced by mining under the thin bedrock," *Journal of loss prevention in the process industries*, vol. 57, pp. 1–6, 2019.

[8] S. Lei, X. Feng, and W. Shidong, "Water-sand mixture inrush through weakly cemented overburden at a shallow depth in the Yili coal mining area," *Arabian Journal of Geosciences*, vol. 14, no. 12, p. 1103, 2021.

[9] Y. Wang, F. Geng, S. Yang, H. Jing, and B. Meng, "Numerical simulation of particle migration from crushed sandstones during groundwater inrush," *Journal of hazardous materials*, vol. 362, pp. 327–335, 2019.

[10] F. Du, G. Jiang, and Z. Chen, "A numerical simulation study of the migration law of water-sand two-phase flow in broken rock mass," *Geofluids*, vol. 2018, 12 pages, 2018.

[11] J. Wang, Y. Zhang, Z. Qin, S. Song, and P. Lin, "Analysis method of water inrush for tunnels with damaged water-resisting rock mass based on finite element method-smooth particle hydrodynamics coupling," *Computers and Geotechnics*, vol. 126, article 103725, 2020.

[12] W. Zhong, Y. Xiong, Z. Yuan, and M. Zhang, "DEM simulation of gas–solid flow behaviors in spout-fluid bed," *Chemical Engineering Science*, vol. 61, no. 5, pp. 1571–1584, 2006.

[13] B. Zhang, Q. He, Z. Lin, and Z. Li, "Experimental study on the flow behaviour of water-sand mixtures in fractured rock specimens," *International Journal of Mining Science and Technology*, vol. 31, no. 3, pp. 377–385, 2021.

[14] Q. Liu and B. Liu, "Experiment study of the failure mechanism and evolution characteristics of water–sand inrush geo-hazards," *Applied Sciences*, vol. 10, no. 10, p. 3374, 2020.

[15] Q. Yin, G. Ma, H. Jing et al., "Hydraulic properties of 3D rough-walled fractures during shearing: an experimental study," *Journal of Hydrology*, vol. 555, pp. 169–184, 2017.

[16] Z. Zhou, J. Zhang, X. Cai, S. Wang, X. Du, and H. Zang, "Permeability experiment of fractured rock with rough surfaces under different stress conditions," *Geofluids*, vol. 2020, 15 pages, 2020.

[17] J. Xu, H. Pu, J. Chen, and Z. Sha, "Experimental study on sand inrush hazard of water-sand two-phase flow in broken rock mass," *Geofluids*, vol. 2021, 9 pages, 2021.

[18] Y. Liu and S. Li, "Influence of particle size on non-Darcy seepage of water and sediment in fractured rock," *Springerplus*, vol. 5, no. 1, p. 2099, 2016.

[19] B. Guo, C. Wang, L. Wang, Y. Chen, and T. Cheng, "A modified cubic law for rough-walled marble fracture by embedding peak density," *Advances in Civil Engineering*, vol. 2020, 10 pages, 2020.

[20] F. Ye, J.-C. Duan, W.-X. Fu, and X.-Y. Yuan, "Permeability properties of jointed rock with periodic partially filled fractures," *Geofluids*, vol. 2019, 14 pages, 2019.

[21] T. Xiao, M. Huang, and M. Gao, "Triaxial permeability experimental study on deformation and failure processes of single-fractured rock specimens," *Shock and Vibration*, vol. 2020, 12 pages, 2020.

[22] Z. Chao, G. Ma, X. Hu, and G. Luo, "Research on anisotropic permeability and porosity of columnar jointed rock masses during cyclic loading and unloading based on physical model experiments," *Bulletin of Engineering Geology and the Environment*, vol. 79, no. 10, pp. 5433–5454, 2020.

[23] Y. Chen, W. Liang, H. Lian, J. Yang, and V. P. Nguyen, "Experimental study on the effect of fracture geometric characteristics on the permeability in deformable rough-walled fractures," *International Journal of Rock Mechanics and Mining Sciences*, vol. 98, no. July, pp. 121–140, 2017.

Hindawi
Geofluids
Volume 2021, Article ID 6669234, 9 pages
https://doi.org/10.1155/2021/6669234

Research Article

Analytical Solution for the Deformation and Support Parameters of Coal Roadway in Layered Roof Strata

Kai Wang,[1,2] **Bao-gui Yang**,[1] **Zhong-kui Wang**,[2] **and Xiao-long Wang**[1]

[1]*School of Energy and Mining Engineering, China University of Mining & Technology, Beijing 100083, China*
[2]*Gucheng Coal Mine of Shanxi Lu'an Mining Group, Changzhi, Shanxi 046204, China*

Correspondence should be addressed to Kai Wang; 2024613980@qq.com

Received 28 June 2021; Revised 17 August 2021; Accepted 9 October 2021; Published 25 October 2021

Academic Editor: Afshin Davarpanah

In order to meet the security and high-efficiency production needs, high-strength bolt (cable) reinforcement technology is usually used to maintain the stability of roadways. However, due to the great variability of lithology and mechanical properties, the failure form and stability of the layered roof in coal roadways are significant differences. The traditional supporting design method of the layered roof support in coal roadways is the engineering analogy method, which depends on experiences rather than theoretical analysis. Based on the theory of the elastic foundation beam and key stratum, this paper establishes a simplified analytical model of layered roof strata in coal roadways. Based on the Mohr-Coulomb theory, this paper gives the failure criteria of the layered roof strata, and the failure range of the layered roof strata is obtained. The length and pretightening force of bolt (cables) of the layered roof strata can be calculated based on the suspension theory and composite beam theory, which providing a quantitative theoretical basis for the determination of supporting parameters. Finally, as a case, the layered roof strata failure range and supporting parameters of the S1301 auxiliary transportation roadway in Gucheng coal mine are calculated.

1. Introduction

With the continuous innovation of energy mining technology [1], the support technology of roadway is also constantly innovating. However, due to the complex formation and changeable characteristics of the coal seam, the characteristics of the roadway roof strata are complex and changeable, which makes the stability control of roadway layered roof strata very difficult [2–7]. Therefore, it is very important to analyze the surrounding rock pressure and failure characteristics of the layered roof strata.

After excavation, due to the existence of the free surface and unbalanced surrounding rock pressure, the layered roof strata of rectangular coal roadways will bend and deform to the free surface. If the length and pretightening force of the bolt (cable) are not adequate, the layered roof strata in coal roadways will separate and even collapse [8, 9]. The study on the deformation mechanism and the supporting parameters of layered roof strata mainly depend on simulation tests, numerical simulations, and field measurements rather than theoretical analysis [10–13]. Zhang et al. [14] studied on the mining instability characteristics and failure modes of the layered roof with three types of weak intercalation which depended on simulation tests and proposed the control principle of the roadway surrounding rock. Sofianos and Kapenis [15], Sofians [16], and Lin [17] studied on the stability and deformation failure process of the layered roof, which was supported by bolts, based on the discrete element method. Jiang et al. [18] classified the roadways compound layered roof into seven types. The classification scheme of roof caving possibility was established, and the hidden danger level of the typical roadway compound layered roof structure was divided.

Based on the composite beam theory and elastic foundation beam model [6, 19–21], the deformation characteristics of the layered roof strata in rectangular roadways are analyzed in this study. Based on the Mohr-Coulomb theory, this paper gives the failure criteria of the layered roof strata, and the failure range of the layered roof strata is obtained. Finally, we can calculate the length and pretightening force

of the bolt (cable) based on the suspension theory and composite beam theory, which provides a quantitative theoretical basis for the determination of the supporting parameters.

2. Theoretical Background

2.1. Problem Definition. As the length of the roadway is far larger than the section size, the analytical model is idealized as a plane strain problem. This study assumes that the compound layered roof of roadways are composed of n-layer strata, numbered $1, 2 \cdots i \cdots n$ from bottom to top (Figure 1). After excavation, the bending deformation of layered roof strata may lead to separation or interlayer sliding of the compound layered roof. If there is no bolt (cable) support, the failure layered roof strata of coal roadways may lead to roof caving accident. After the application of bolt (cable), the fractured layered roof strata will be suspended in the upper stable roof stratum and form a self-stable structure.

According to the above discussion, the first step in calculating the length and pretightening force of the bolt (cable) is to analyze the internal force of the layered roof strata based on the composite beam theory and the elastic foundation beam model. Then, the range of the failure roof can be determined. Finally, the bolt (cable) support parameters are obtained based on the suspension theory and composite beam theory.

Here, we assume that a certain number of layered roof strata in coal roadways form the composite beam structure. For the roadway is a plane-symmetric structure, we can assume that the stress and deformation of the layered roof are also symmetric. Thus, the right part of the layered roof strata relative to the symmetrical axis is taken as the analysis object. Based on the elastic foundation beam theory [14], the composite elastic foundation beam model and its coordinate system are established (Figure 1).

Here, q is the load on the composite elastic foundation beam structure, l is half of the roadway width, σ_H is the horizontal stress, and k is the foundation characteristic coefficient of the elastic foundation beam.

2.2. Basic Equations. The Winkler hypothesis considers that the settlement amount of any unit point in the foundation surface is proportional to the pressure. Therefore, the foundation counterforce of the elastic foundation beam can be determined as follows:

$$R = -kY, \tag{1}$$

where Y is the settlement amount of the foundation, namely, the bending amount of the foundation beam, $k = k_0 b$, where b is the width of the beam, $b = 1\,\text{m}$, and k_0 is the Winkler foundation coefficient.

According to the above simplifications and the equilibrium conditions, the deformation differential equation of the composite elastic foundation beam is

$$\begin{cases} \text{EI}\dfrac{d^4Y}{dx^4} = q + \gamma h, & 0 \le x \le l, \\ \text{EI}\dfrac{d^4Y}{dx^4} = q + \gamma h - kY, & l \le x < \infty, \end{cases} \tag{2}$$

where EI is the bending stiffness of the composite elastic foundation beam, which can be obtained using formula (3), q is the load on the composite elastic foundation beam, γ is the unit weight of the composite elastic foundation beam, and h is the thickness of the composite elastic foundation beam.

$$\text{EI} = \sum_{i=1}^{n} \int_{y_i}^{y_{i-1}} E_i (y - \Delta)^2 dA, \tag{3}$$

where E_i is the elastic modulus of the ith roof stratum in the composite elastic foundation beam, y is the ordinate of any point in the composite elastic foundation beam, y_i is the ordinate of the upper boundary of the ith roof stratum, and Δ is the ordinate of the neutral axis, which can be calculated using the following equation:

$$\Delta = \frac{\sum_{i=1}^{n} \int_{y_i}^{y_{i-1}} E_i y dA}{\sum_{i=1}^{n} \int_{y_i}^{y_{i-1}} E_i dA}. \tag{4}$$

According to the relationship between the bending, rotation angle, moment, and shearing force of composite elastic foundation beam, the deflection, moment, and shearing force are calculated as follows:

$$\begin{cases} \theta = \dfrac{dy}{dx} = Y', \\ M = -\text{EI}\dfrac{d^2y}{dx^2} = -\text{EI}Y'', \\ F_s = -\text{EI}\dfrac{d^3y}{dx^3} = -\text{EI}Y''', \end{cases} \tag{5}$$

where θ is the rotation angle, M is the moment, and F_s is the shearing force of any section of the composite elastic foundation beam.

For the model is a symmetric structure, the rotation angle and shearing force are zero at the symmetrical axis ($x = 0$). Moreover, for the excavation influence of the roadway is relatively limited, the rotation angle is zero at infinity ($x \longrightarrow \infty$). These conditions are expressed as follows:

$$\begin{cases} Y' = Y''' = 0, & x = 0, \\ Y' = 0, & x \longrightarrow \infty. \end{cases} \tag{6}$$

Considering the continuity of analytical solutions, the bending, rotation angle, moment, and shearing force should be continuous while $x = l$; thus, the continuity condition can

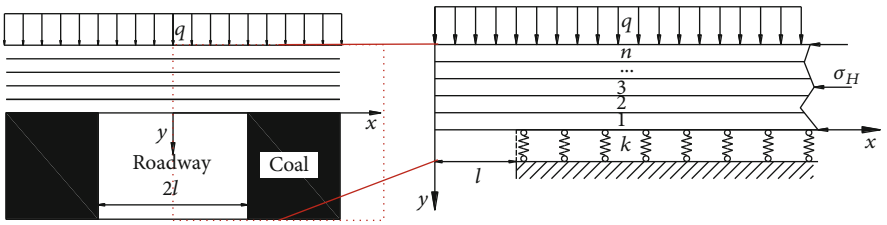

Figure 1: Analysis model of layered roof strata in coal roadway.

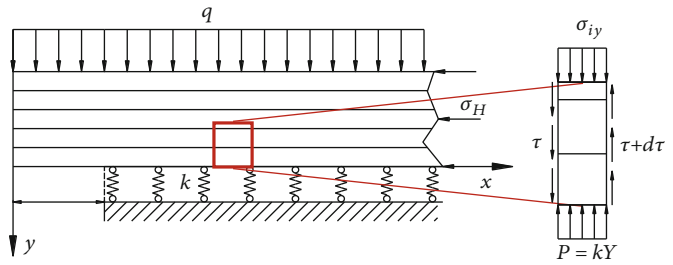

Figure 2: The analysis object of the composite beam and its force in the vertical direction.

Table 1: Rock properties of the roadway roof strata.

Rock strata	Lithology	Depth (m)	Thickness (m)
The 8th roof stratum	Siltstone	601.32	1.89
The 7th roof stratum	Medium sandstone	605.02	3.70
The 6th roof stratum	Fine sandstone	606.27	1.25
The 5th roof stratum	Siltstone	607.82	1.55
The 4th roof stratum	Fine sandstone	609.72	1.90
The 3rd roof stratum	Medium sandstone	612.02	2.30
The 2nd roof stratum	Fine sandstone	614.47	2.45
The 1st roof stratum	Sandy mudstone	615.29	0.82
3# coal	Coal	621.80	6.51

Table 2: Mechanical parameters of coal and rock.

Lithology	E (GPa)	γ (kN/m^3)	k (GN/m^2)	R_t (MPa)	R_c (MPa)	φ (°)
Medium sandstone	18.96	27.18	——	5.37	62.3	37.3
Fine sandstone	11.1	26.79	——	3.01	50.6	35.2
Siltstone	10.08	26.13	——	2.97	50.2	33.3
Sandy mudstone	10.59	26.23	——	2.57	26.65	32.1
Coal	1.29	14.60	0.06	0.57	5.3	30.1

be expressed by the following equations:

$$\begin{cases} \lim\limits_{x\longrightarrow l+} Y(x) = \lim\limits_{x\longrightarrow l-} Y(x), \\ \lim\limits_{x\longrightarrow l+} Y'(x) = \lim\limits_{x\longrightarrow l-} Y'(x), \\ \lim\limits_{x\longrightarrow l+} Y''(x) = \lim\limits_{x\longrightarrow l-} Y''(x), \\ \lim\limits_{x\longrightarrow l+} Y'''(x) = \lim\limits_{x\longrightarrow l-} Y'''(x). \end{cases} \tag{7}$$

3. Results

3.1. Deformation and Internal Force. The general solution of the differential equation (formula (2)) that satisfies the boundary condition (formula (6)) can be expressed as follows:

$$Y = \begin{cases} \dfrac{q+\gamma h}{24\mathrm{EI}}x^4 + A_1x^2 + A_2, & l \le x < \infty, \\ e^{-\beta(x-l)}[B_1\cos(\beta(x-l)) + B_2\sin(\beta(x-l))] + \dfrac{q+\gamma h}{k}, & 0 \le x \le l, \end{cases} \tag{8}$$

where A_1, A_2, B_1, and B_2 are undetermined constants that can be determined by the continuity conditions, formula (7). β is the characteristic coefficients, which can be expressed as

$$\beta = \sqrt[4]{\frac{k}{4\mathrm{EI}}}. \tag{9}$$

According to the continuity conditions (formula (7)), the undetermined constants of formula (8) can be expressed as

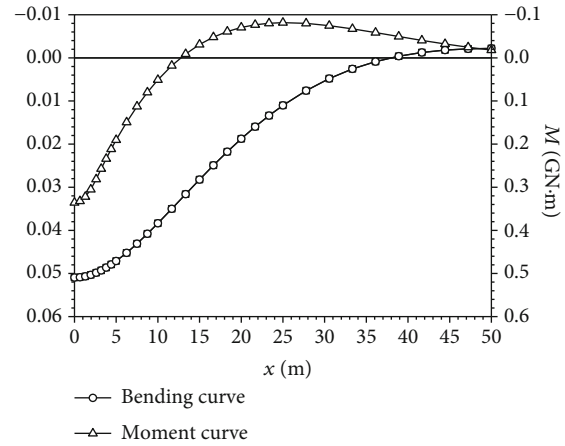

Figure 3: Deflection and bending moment curve of composite beam.

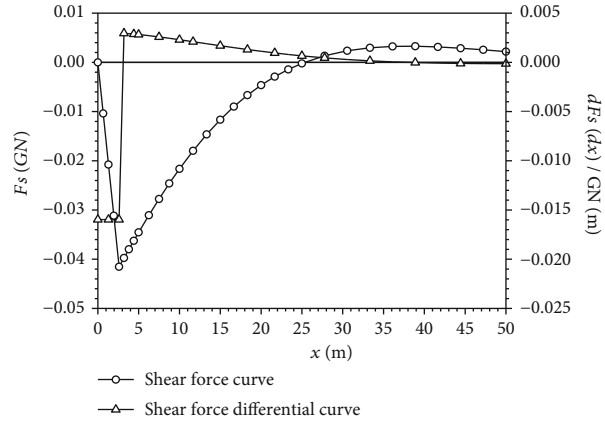

Figure 4: Shear force of composite beam and its differential curve.

follows:

$$\begin{cases} A_1 = -\dfrac{q+\gamma h}{12\mathrm{EI}}\dfrac{\beta^2 l^3 + 3\beta l^2 + 3l}{\beta^2 l + \beta}, \\ A_2 = \dfrac{q+\gamma h}{24\mathrm{EI}}\dfrac{\beta^3 l^4 + 4\beta^2 l^3 + 6\beta l^2 + 6l}{\beta^3} + \dfrac{q+\gamma h}{k}, \\ B_1 = \dfrac{q+\gamma h}{12\mathrm{EI}}\dfrac{2\beta^2 l^3 + 6\beta l^2 + 3l}{\beta^4 l + \beta^3}, \\ B_2 = -\dfrac{q+\gamma h}{12\mathrm{EI}}\dfrac{2\beta^2 l^3 - 3l}{\beta^4 l + \beta^3}. \end{cases} \tag{10}$$

In fact, the bending expressed by formula (8) includes two parts: the deformation caused by excavation and the initial deformation caused by the initial surrounding rock stress. Therefore, the deformation caused by excavation can be obtained as follows:

$$Y_e = \begin{cases} \dfrac{q+\gamma h}{24\mathrm{EI}}x^4 + A_1 x^2 + A_2 - \dfrac{q+\gamma h}{k}, & 0 \le x \le l, \\ e^{-\beta(x-l)}[B_1 \cos(\beta(x-l)) + B_2 \sin(\beta(x-l))], & l \le x < \infty. \end{cases} \tag{11}$$

According to formulas (5) and (8), the moment and shearing force value of the composite elastic foundation beam are obtained as follows:

$$M = \begin{cases} -\dfrac{q+\gamma h}{2}x^2 - 2A_1\mathrm{EI}, & 0 \le x \le l, \\ -2\beta^2\mathrm{EI}e^{-\beta(x-l)}(B_1 \sin(\beta(x-l)) - B_2 \cos(\beta(x-l))), & l \le x < \infty, \end{cases} \tag{12}$$

$$F_s = \begin{cases} -(q+\gamma h)x, & 0 \le x \le l, \\ -2\beta^3\mathrm{EI}e^{-\beta(x-l)}((B_2 - B_1)\sin(\beta(x-l)) + (B+B_2)\cos(\beta(x-l))), & l \le x < \infty. \end{cases} \tag{13}$$

3.2. Internal Force and Failure Analysis. According to the theory of the key stratum, the load of any strata in the compound layered roof generally affected by its adjacent strata in addition to itself. According to the definition and deformation characteristics of key stratum, when the key stratum deflects, the strata on the key stratum will undergo collaborative deformation, and the failure of the key stratum will lead to the synchronous failure of the strata on the key stratum. Practice shows that there are several key strata that play a major role in the stability control of the roadway, and there is a key stratum that plays a decisive role. Therefore, in order to calculate the failure range of the overlying strata, this article assume that the strata within the control range from the first key stratum to the decisive key stratum form the composite beam structure. Firstly, we assume that the first key stratum is the decisive key stratum. If the calculation result shows that the decisive key stratum is a failure and the composite beam structure does not meet the requirements of roadway stability, then we assume that the second key stratum is the decisive key stratum, and so on. The load (q) on the composite elastic foundation beam structure is the overlying rock strata gravity. Based on this hypothesis and idealization, the bending and deformation of the layered roof strata in coal roadways are calculated.

According to the deduction process of the bending normal stress and the uniaxial compression stress of a beam, the positive stress of any point of the roadway compound layered roof can be obtained as follows:

$$\sigma_i = -M\frac{E_i(y-\Delta)}{\mathrm{EI}} + \sigma_H. \tag{14}$$

According to the deduction process of the bending shear stress, the shear stress of any point of the roadway compound layered roof can be obtained as follows:

$$\tau_i = \frac{F_s}{2\mathrm{EI}}\left[\sum_{j=1}^{i-1} E_j\left(y_{j-1}{}^2 - 2y_{j-1}\Delta - y_j{}^2 + 2y_j\Delta\right) + E_i\left(y_{i-1}{}^2 - 2y_{i-1}\Delta - y^2 + 2y\Delta\right)\right], \tag{15}$$

where y is the ordinate of any point in the composite beam

and y_{i-1} is the ordinate of the upper boundary of layer $i-1$, namely, the ordinate of the lower boundary of layer i.

We take part of the composite beam as the analysis object and consider its force balance in the vertical direction (Figure 2).

The normal stress of any point in the vertical direction of the composite beam can be obtained as follows:

$$\sigma_{iy}=\begin{cases}\dfrac{1}{2\mathrm{EI}}\dfrac{dF_s}{dx}\left[\sum_{j=2}^{i}\int_{y_{j-1}}^{y}E_{j-1}\left({y_{j-2}}^2-2y_{j-2}\Delta-{y_{j-1}}^2+2y_{j-1}\Delta\right)dy+\sum_{j=1}^{i-1}\int_{y_{j-1}}^{y_j}E_j\left({y_{j-1}}^2-2y_{j-1}\Delta-y^2+2y\Delta\right)dy+\int_{y_{i-1}}^{y}E_i\left({y_{i-1}}^2-2y_{i-1}\Delta-y^2+2y\Delta\right)dy\right], & 0\le x\le l,\\ \left[kY+\dfrac{1}{2\mathrm{EI}}\dfrac{dF_s}{dx}\left[\sum_{j=2}^{i}\int_{y_{j-1}}^{y}E_{j-1}\left({y_{j-2}}^2-2y_{j-2}\Delta-{y_{j-1}}^2+2y_{j-1}\Delta\right)dy+\sum_{j=1}^{i-1}\int_{y_{j-1}}^{y_j}E_j\left({y_{j-1}}^2-2y_{j-1}\Delta-y^2+2y\Delta\right)dy+\int_{y_{i-1}}^{y}E_i\left({y_{i-1}}^2-2y_{i-1}\Delta-y^2+2y\Delta\right)dy\right]\right], & l\le x\le\infty.\end{cases}\tag{16}$$

In the plane rectangular coordinate system, the Mohr stress circle of any section in the composite beam can be expressed as

$$\tau^2=\left(\frac{\sigma_{ix}-\sigma_{iy}}{2}\right)^2+\tau_i^2-\left(\sigma-\frac{\left(\sigma_{ix}+\sigma_{iy}\right)}{2}\right)^2,\tag{17}$$

where σ and τ are the normal stress and shear stress of any section.

According to the Mohr-Coulomb criterion [22], the failure criterion of the layered roof strata can be expressed as follows:

$$\begin{cases}\tau^2\ge(\sigma+R_t)^2\left(\dfrac{1}{2}\sqrt{\dfrac{R_c}{R_t}-3}\right)^2+(\sigma+R_t)R_t, & \dfrac{R_c}{R_t}\ge 3\\ \tau^2\ge(\sigma+R_t)R_t, & \dfrac{R_c}{R_t}<3,\end{cases}\tag{18}$$

where R_c and R_t are the compressive and tensile strength of the rock, respectively.

Then, the failure criteria of the roadways layered roof strata can be expressed as follows:

$$f=\begin{matrix}\left(\dfrac{1}{2}R_c-\dfrac{1}{2}R_t-\sigma_{ix}-\sigma_{iy}\right)^2-\left(\dfrac{R_c}{R_t}+1\right)\left(\dfrac{1}{4}R_cR_t+\dfrac{1}{4}{R_t}^2+\sigma_{ix}\sigma_{iy}-{\tau_i}^2\right)\ge 0, & \dfrac{R_c}{R_t}\ge 3\\ \left(\sigma_{ix}+\sigma_{iy}-R_t\right)^2-4\left({R_t}^2+\sigma_{ix}\sigma_{iy}-{\tau_i}^2\right)\ge 0, & \dfrac{R_c}{R_t}<3.\end{matrix}\tag{19}$$

It should be noted that the yielding behavior of the surrounding rock and the failure criteria of the roadways layered roof strata is judged by the stress in the elastic state, which is not an exact elastic-plastic solution.

3.3. Bolt (Cable) Length and Its Pretightening Force

3.3.1. Calculation of the Bolt Length. According to the theory of composite beam, the supporting function of the bolts is to provide enough pretightening force to increase the friction force of the failure roof strata and prevent the strata from sliding or even separating. Therefore, the effective length of the bolt should be greater than the thickness of the failure roof strata. The length of the bolt is

$$L_b=L_{b1}+L_{b2},\tag{20}$$

where L_{b1} is the exposed length of the bolt, which typically takes 0.1-0.2 m. L_{b2} is the effective length of the bolt, which is larger than the thickness of the failure roof strata.

3.3.2. Calculation of the Bolt Pretightening Force. According to the composite beam theory, in order to prevent the sliding or even separating, the friction force provided by the bolt should be greater than the maximum shear stress generated by self-weight of the failure roof strata [23–25]. Thus, the bolt pretightening force can be expressed as follows:

$$F_b\ge\frac{3}{4}\frac{\left(\gamma_ih_i'+\sum_{j=1}^{i-1}\gamma_ih_i\right)l}{\tan\varphi_{\min}\left(h_i'+\sum_{j=1}^{i-1}h_i\right)}a_bb_b,\tag{21}$$

where i is the number of the failure roof strata; h_i' is the failure thickness of the ith roof stratum; a_b and b_b are the transverse and vertical distances of bolts, respectively; $\varphi_{\min}$ is the minimum value of the friction angle of the failure roof strata; and l is half of the roadway width.

3.3.3. Calculation of the Cable Length. According to the theory of composite beam and suspension, the function of cable is to suspend the failure roof strata in the upper stable strata and provide enough pretightening force to increase the friction force of the failure roof strata and prevent the strata from sliding or even separating. Thus, the effective length of the cable is

$$L_{c2}=\sum_{j=1}^{i}h_j,\tag{22}$$

where L_{c2} is the effective length of the cable, i is the number

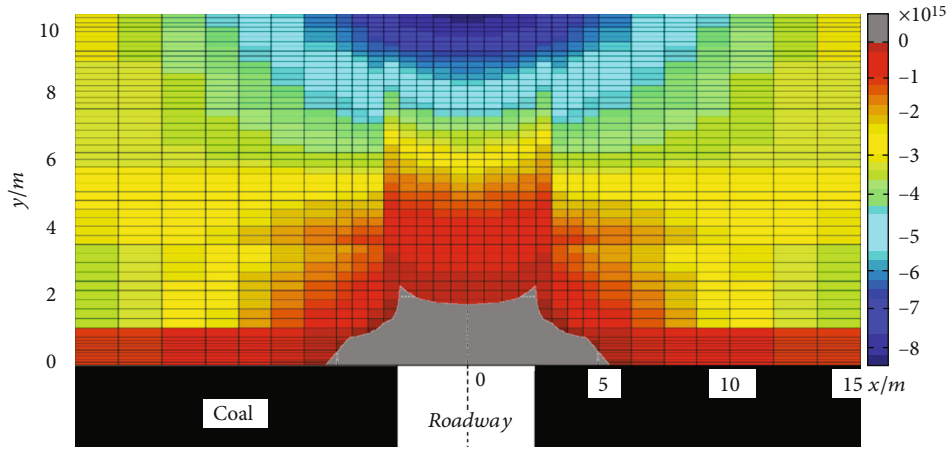

Figure 5: Failure factor cloud chart of the composite beam.

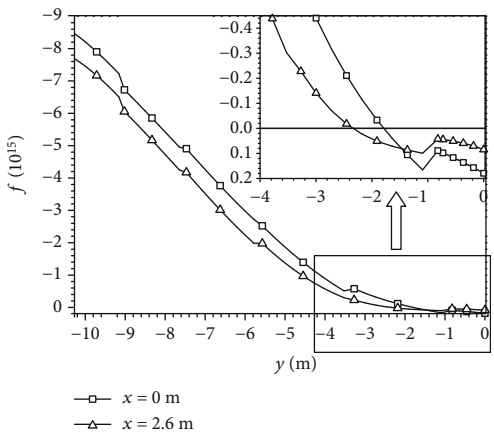

Figure 6: Breaking function curve of the composite beam.

of the failure roof strata, and h_j is the thickness of each failure roof stratum.

Therefore, the cable length (L_c) can be determined as follows:

$$L_c = L_{c1} + L_{c2} + L_{c3}, \tag{23}$$

where L_{c1} is the exposed length of the cable, which typically takes 0.2-0.3 m. L_{c2} is the effective length of the cable. L_{c3} is the anchor length, which can be determined by test according to the pretightening force.

3.3.4. Calculation of the Cable Pretightening Force. The essential role of the cable is to limit the plastic deformation of the surrounding rock and avoid separation or local roof collapse. Therefore, the cable pretightening force should be greater than the equivalent gravity of the failure roof strata, and the friction force provided by the cable support should be greater than the maximum shear stress between the failure roof strata.

Thus, the pretightening force of the cable can be obtained as follows:

$$F_c = \max\left\{a_c b_c \sum_{j=1}^{i} \gamma_j h_j, \quad F_b \frac{a_b b_b}{a_c b_c}\right\} f_a, \tag{24}$$

where F_c is the pretightening force of the cable, a_c is the cables equivalent spacing values, b_c is the cables row spacing values, γ_j is the unit weight of each failure roof stratum, and f_a is the safety factor, which typically takes 1.1-1.2.

It should be note that the failure range of the roadways layered roof strata is judged by the stress in the elastic state, and the stress of support structure varies with the development of surrounding rock. Thus, the support parameters are experience results that based on theoretical analysis.

4. Application

Taking the S1301 auxiliary transportation roadway of the Chinese Gucheng coal mine as an example, its width is 5.2 m ($2l = 5.2$ m), height is 3.6 m ($h = 3.6$ m), and buried depth is 615.3 m. The rock properties of the roadway roof strata is shown in Table 1, and the layered roof strata are numbered 1, 2…8 from bottom to top.

According to the geological data and field measurements, the horizontal stress is 9.1 MPa. The elasticity modulus, unit weight, foundation coefficient (Winkler's coefficient), and strength parameters of the roof strata are shown in Table 2.

4.1. Determination of Composite Beam Structure and Its Load. According to the key stratum theory, the 1st, 2nd, 3rd, and 4th key strata of the layered roof strata are the 1st, 2nd, 3rd, and 7th roof strata, respectively. Due to the low strength of the composite beam structure formed by the first and second key strata, the strata within the control range of the 1st, 2nd, and 3rd key strata can be taken as the research object directly, which means that the 3rd key stratum is the decisive key stratum. Namely, the first to sixth

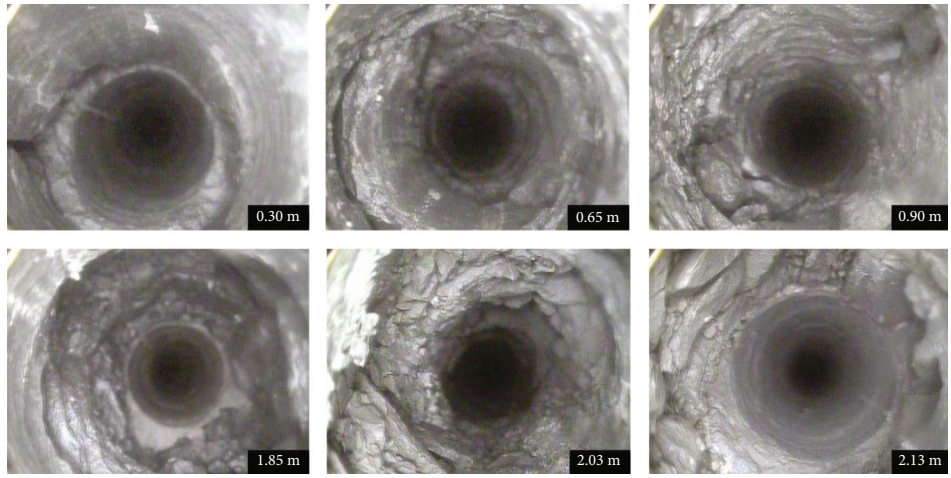

Figure 7: Endoscopic research results of roadway roof strata.

roof strata form the composite beam structure, and the load of the overlying strata is 15.7 MPa.

4.2. Neutral Axis and Bending Stiffness. The first step is to establish the coordinate system, with the boundary of the roadway roof as its x-axis and the central axis of the roadway as its y-axis. Then, the neutral axis ordinate and bending stiffness can be obtained ($\Delta = -5.01$ m, EI = 992.3 GN · m^2) by substituting the composite beam parameters into formulas (3) and (4).

4.3. Deflection and Internal Force Calculation of Composite Beam. After substituting the bending stiffness (EI), the overlying load (q) and the thickness (h) of the composite beam into formulas (9) and (10), and the coefficients of the bending and internal forces of the composite beam are $\beta = 0.06235\,\text{m}^{-1}$, $A_1 = -1.6909\,\text{m}^{-1}$, $A_2 = 0.31719$ m, $B_1 = 0.04984$ m, and $B_2 = 0.03649$ m.

According to formulas (11), (12), and (13), the deflection, bending moment, shear force, and shear force differential value of the composite beam can be determined, and the curves are shown in Figures 3 and 4.

According to Figures 3 and 4 and formulas (11)and (12), the bending and moment reach their maximum values in the middle of the roadway (while $x = 0$ m), $Y_e = 5.1$ cm and $M = 335.56 \times 10^6$N · m, respectively. And the shear force reach its maximum value in the side of roadway (while $x = 2.6$ m), $F_s = 41.53 \times 10^6$N.

4.4. Determination of the Failure Strata. According to the above analysis, the thickness of the composite beam is 10.27 m. Taking the composite beam on both sides of the roadway centerline, within 15 m, as the calculation model, the size of the numerical calculation model is 30 m × 10.27 m. Dividing the calculation model into 31 × 60 matrix grid by the software of MATLAB. According to equations (14)–(16), the stress state of each matrix point are obtained, respectively. The failure factors of each matrix point can be obtained by equation (19). The cloud chart of failure factor (as shown in Figure 5) and the curve of failure factor when $x = 0$ m and $x = 2.6$ m (as shown in Figure 6) can be obtained by MATLAB, which is a Coulomb-Mohr solution. It obvious that the maximum failure depth of the roof strata is 2.3 m according to Figures 5 and 6. Thus, according to the key stratum theory, the 1st-2nd layered roof of the roadway may break down. Namely, the effective length of the cable is $L_2 = 3.27$ m according to equation (22).

The endoscopic research technology was used to obtain the broken depth of the roof strata. The criterion for determination of the roof strata failure range is the thickness of the roof strata that loss integrity. The endoscopic research results (Figure 7) show that the roadway roof strata within 2.1 m is broken at different positions and loss its original integrity. Namely, the failure depth of roadway roof strata is 2.1 m.

4.5. Calculation of Bolt Length and Pretightening Force. According to Figures 5 and 6, the thickness of the damaged roof is 2.3 m, so the effective length of the bolt is 2.3 m, and the length of the bolt is 2.6 m. The transverse and vertical distances of bolts are 0.8 m × 0.8 m in this roadway. Due to the minimum friction angle of the damaged roof being 32.1°, the pre tightening force of the bolt is 120 kN according to formula (21).

4.6. Calculation of Cable Length and Pretightening Force. According to the above analysis, the 1st-2nd roof strata are likely to be damaged, the effective length of the cable can be determined to be $L_2 - 3, 27$ m, and the exposed length of the cable are 0.25 m. The spacing values of the cables are $a_c = 2.6$ m and $b_c = 0.8$ m, and the safety factor is $f_a = 1.15$. According to formula (24), the pretightening force of the cable should be greater than 210 kN. According to the pretightening force of the cable, the anchorage length can be determined by a pull-out test, which is 1.75 m. Thus, the length of the cable is $L = 5.3$ m.

5. Conclusion

(1) Based on the theory of the elastic foundation beam and key stratum, this paper establishes a simplified analytical model of layered roof strata in a coal roadway. Assuming that the roof strata within the control range from the first key stratum to the decisive key stratum form the composite beam structure. The analytical solution of deformation and internal force of the composite beam structure are obtained

(2) Based on the Mohr-Coulomb theory, the failure criteria of the layered roof strata is obtained; then, the failure range of the layered roof strata is determined. The length and pretightening of bolt (cable) can be calculated according to the suspension theory and composite beam theory, which provide a quantitative theoretical basis for the determination of bolt (cable) supporting parameters and a significant guiding for actual project

(3) Finally, a case is given to demonstrate the analysis and calculation process of the stress and supporting parameters of the layered roof strata in a coal roadway. The cloud chart of the composite beam failure factor and the curve of failure factors (when $x = 0$ m and $x = 2.6$ m) are obtained by MATLAB, which makes the process of determining the failure range of the layered roof strata simpler. Apart from this, the calculation result of the failure range is basically consistent with the endoscopic research results. To some extent, it proves the usefulness of the study. However, the theoretical calculation results still needs more case to verify

(4) It should be noted that the yielding behavior of the surrounding rock and the failure criteria of the roadways compound layered roof is judged by the stress in the elastic state, which is not an exact elastic-plastic solution. The supporting parameters are experience results based on theoretical analysis

Data Availability

The underlying data can be obtained from the corresponding author with the email of 2024613980@qq.com

Conflicts of Interest

The authors declare that they have no conflicts of interest.

References

[1] M. Yang, *Coal Mine Geology*, China Coal Industry Publishing House, Beijing, China, 2006.

[2] M. He, H. Xie, and P. Suping, "Study on rock mechanics in deep mining engineering," *Chinese Journal of Rock Mechanics and Engineering*, vol. 24, no. 16, pp. 2803–2813, 2005.

[3] H. Manchao, Y. Hesheng, J. Hongwen, W. Fangrong, and J. Haihe, *Theory and Practice of Bolt Supporting in China Coal Mines*, Science Press, Beijing, China, 2004.

[4] P. Małkowski, Z. Niedbalski, and T. Balarabe, "A statistical analysis of geomechanical data and its effect on rock mass numerical modeling: a case study," *International Journal of Coal Science and Technology*, vol. 8, no. 2, pp. 312–323, 2021.

[5] P. Małkowski, "The impact of the physical model selection and rock mass stratification on the results of numerical calculations of the state of rock mass deformation around the roadways," *Tunnelling and Underground Space Technology*, vol. 50, pp. 365–375, 2015.

[6] Q. Zhang, W. He, H.-Y. Zhang, H. Wang, and B.-S. Jiang, "A simple numerical procedure for the elasto-plastic coupling finite strain analysis of circular tunnels in strain-softening rock masses," *Computers and Geotechnics*, vol. 130, article 103921, 2021.

[7] Q. Zhang, B.-S. Jiang, S. Wang, X. R. Ge, and H.-q. Zhang, "Elasto-plastic analysis of a circular opening in strain-softening rock mass," *International Journal of Rock Mechanics and Mining Sciences*, vol. 50, pp. 38–46, 2012.

[8] K. Hongpu and J. Wang, *Rock Bolting Theory and Complete Technology for Coal Roadways*, China Coal Industry Publishing House, Beijing, China, 2007.

[9] Y. Liang, *Control of Surrounding Strata in Deep Mine Roadway and Practice in Huainan Area*, China Coal Industry Publishing House, Beijing, China, 2006.

[10] H. P. Kang, P. F. Jiang, and J. F. Cai, "Test and analysis on stress fields caused by rock bolting," *Journal of China Coal Society*, vol. 39, no. 8, pp. 1521–1529, 2014.

[11] K. Hongpu, J. Tieming, and F. Gao, "Design for pretensioned rock bolting parameters," *Journal of China Coal Society*, vol. 33, no. 7, pp. 721–726, 2008.

[12] Z. Yingda, "Mechanical mechanism of bolted structure forming in strong fissured surrounding rock," *Journal of China Coal Society*, vol. 36, no. 9, pp. 1435–1439, 2011.

[13] Z. Yingda, "The mechanics effect of bolt pretension in roadways surrounding rock," *Journal of China Coal Society*, vol. 33, no. 8, pp. 856–859, 2008.

[14] Z. Long, L. Guichen, and K. Jiaguang, "Influence of soft interlayer location in coal roof on stability of roadway bolting structur," *Rock and Soil Mechanics*, vol. 32, no. 9, pp. 273–278, 2011.

[15] A. I. Sofianos and A. P. Kapenis, "Numerical evaluation of the response in bending of an underground hard rock voussoir beam roof," *International Journal of Rock Mechanics and Mining Sciences*, vol. 35, no. 8, pp. 1071–1086, 1998.

[16] A. I. Sofians, "Analysis and design of an underground hard rock voussoir beam roof," *International Journal of Rock Mechanics and Mining Sciences & Geomechanics Abstracts*, vol. 33, no. 2, pp. 153–166, 1996.

[17] C. Lin, "Procedure analysis of numerical simulation for the failure mechanism of laminate roof," *Chinese Journal of Rock Mechanics and Engineering*, vol. 18, no. 4, pp. 392–396, 1999.

[18] L. S. Jiang, N. J. Ma, L. Bai, Y. J. Li, and L. Zhang, "Deformation and failure characteristics and roof caving hidden danger classification of roadways compound roof," *Journal of China Coal Society*, vol. 39, no. 7, pp. 1205–1211, 2014.

[19] F. Jincheng, *Analytical Analysis of Certain Deformation Problems and the Bolt Design in Coal Stope and Caverns*, University of Mining & Technology, Xuzhou China, 2014.

[20] H. Agrawal, S. Durucan, W. Cao, and W. Cai, "Evaluation of parameters affecting the energy accumulation in longwall

mining," *53rd US Rock Mechanics and Geomechanics Symposium*, 2019, p. ARMA-2019-0324, 2019.

[21] Q. Zhang, C.-H. Peng, R.-C. Liu, B.-S. Jiang, and M.-M. Lu, "Analytical solutions for the mechanical behaviors of a hard roof subjected to any form of front abutment pressures," *Tunnelling and Underground Space Technology*, vol. 85, pp. 128–139, 2019.

[22] Q. Minggao, S. Pingwu, and X. Jialin, "Mine pressure and rock strata control," *China University of Mining and Technology Press*, pp. 25-26, 2010.

[23] T. Majcherczyk, Z. Niedbalski, P. Małkowski, and Bednarek, "Analysis of yielding steel arch support with rock bolts in Mine Roadways Stability Aspect," *Archives of Mining Sciences*, vol. 59, no. 3, pp. 641–654, 2014.

[24] Z. Niedbalski, P. Małkowski, and T. Majcherczyk, "Monitoring of stand-and-roof-bolting support: design optimization," *Acta Geodynamica et Geomaterialia*, vol. 10, no. 2, pp. 215–226, 2013.

[25] F. Qiang, L. Weiwei, F. Shenggang, J. Binsong, and S. Linpo, "Analytical solution for deformation and internal force of hard roof in stope based on elastic foundation beam," *Journal of Mining & Safety Engineering*, vol. 34, no. 2, pp. 342–347, 2017.

Hindawi
Geofluids
Volume 2021, Article ID 3954097, 17 pages
https://doi.org/10.1155/2021/3954097

Research Article

Study on the Mechanical Behavior and Acoustic Emission Properties of Granite under Triaxial Compression

Jiaqi Guo,[1] **Pengfei Liu**,[1] **Junqi Fan**,[2] **and Hengyuan Zhang**[1]

[1]*School of Civil Engineering, Henan Polytechnic University, Jiaozuo 454000, China*
[2]*Research Institute for National Defense Engineering of Academy of Military Science PLA China, Luoyang 471023, China*

Correspondence should be addressed to Pengfei Liu; lpf546@163.com

Received 8 August 2021; Accepted 26 August 2021; Published 21 September 2021

Academic Editor: Richeng Liu

To study the rock mechanical behaviors and damage process mechanism of granite samples under triaxial stress, conventional triaxial compression tests were carried out on an RMT-150B rock mechanics testing machine and acoustic emission detector. The test results show that the strength of the granite sample has a good linear relationship with the confining pressure, the cohesion force c of the granite samples is 29.37 MPa, and the internal friction angle is 54.23° by calculation based on the Mohr-Coulomb strength criterion. The larger the initial confining pressure of the rock sample is, the larger the crack initiation stress (σ_{ci}) and dilatancy stress (σ_{cd}) of the granite specimen are, the larger the energy values at the crack initiation point and dilatancy point are, and the larger the peak energy storage and energy release rate at the failure are. In the case of a small initial confining pressure, the AE ringdowning counts and the cumulative AE ringing counts increase to their maximum instantaneously at the peak stress point, and the damage of the sample develops rapidly. While the initial confining pressure is high, the AE ringing counts and the cumulative AE ringing counts of the granite specimens increase evenly, and the deformation damage of the granite specimens is slow. Before the crack initiation point, AE signals are mainly low-energy and low-frequency friction-type AE events, while after the dilatation point, AE signals of samples are mainly high-frequency and high-energy fracture-type AE events. The failure mode of granite samples judged by acoustic emission parameters according to the distribution of characteristic values of AE parameters RA and AF is consistent with the reality. The AE b value of the granite sample is large when the confining pressure is low, and there will be a sudden drop, the decrease time is late, and the decrease rate is large. Under the same stress level, the larger the confining pressure is, the larger the damage variable D is.

1. Introduction

The stress concentration of surrounding rock in the high-stress area caused the energy stored in the rock mass to be released suddenly and violently in the process of underground engineering construction, and eventually, the surrounding rock will fracture loosening, spalling, ejecting and even bursting the rock, and other geological disasters will occur [1–3]. Such geological hazards have seriously threatened the safety, progress, and cost of underground engineering construction [4, 5]. Meanwhile, the study of the mechanical behavior and damage mechanism of deep buried hard rock under triaxial stress is of great significance for revealing underground engineering geological hazards, engineering stability control, and reasonable formulation of prevention and control measures [6, 7].

A large number of papers have studied in-depth and systematically researched on the mechanical properties and energy evolution characteristics of rock materials in triaxial compression. Martin and Chandler [8] obtained a complete stress-strain curve and failure mode of the hard rock by a large number of brittle rock load tests using a rigid testing machine. Zong et al. [9] obtained the law that peak strength, elastic modulus, and deformation modulus increase linearly with confining pressure by analyzing the stress-strain characteristics and strength deformation characteristics of

sandstone. The essence of failure of loaded rock is energy accumulation and release, so it is meaningful to study the law of energy evolution under different mechanical environments to reveal the failure mechanism of rock under load [10–12]. Based on this, Xie et al. [13, 14] analyzed the energy evolution mechanism and the influence of energy on rock strength in the failure process of rock under different mechanical states, the internal relationship between rock energy dissipation and release, and the rock strength, and the process of failure was established. Tian and Yu [15] carried out triaxial compression tests on limestone samples and revealed the energy conversion methods of the rock in each stage of the compression process. Zhang and Gao [16] analyzed the relationship between granite energy characteristics and stress, strain, and confining pressure through triaxial compression tests. The above research result has greatly promoted the development of the research on the energy evolution law in the process of loading failure of hard rock, but the above research has not linked the energy evolution with the fracture damage process of rock.

Acoustic emission monitoring technology is of great significance to study crack propagation and internal damage fracture behavior of brittle materials under complex stresses [17–19]. Eberhardt et al. [20] researched the failure process of granite through acoustic emission monitoring and found that the beginning of significant AE activity corresponds to the initiation of new cracks. Ganne et al. [21] proposed the four stages of acoustic emission energy accumulation in the rock fracture process through the AE test technology corresponding to the occurrence of microcracks, propagation accumulation, aggregation, and final failure; the material will show obvious characteristics of accelerated energy release before failure. Cai et al. [22] proposed that the frequency of acoustic emission in the spectrogram is related to the size of the fracture. A new method which is called the cumulative AE hit method which has been developed for objective determination of the crack stress was forwarded by Zhao et al. [23]. Zhang et al. [24] studied the variation law of acoustic emission b value of coal rock and showed that the b value would drop rapidly when the rock was failing. Tang and Xu [25], Eberhardt et al. [26], and Liu et al. [27] used AE events and ringing to characterize the damage of rock and studied the damage evolution law of rock. As can be seen from the above, acoustic emission technology plays an important role in the failure and instability mechanism of rock [28–30]. However, the research is mainly focused on uniaxial compression, and actual rock mass is more in the state of triaxial stress than uniaxial stress. Therefore, researches on acoustic emission characteristics of hard rock under different confining pressures are not in-depth and systematic enough.

To establish the relationship between AE parameters and the failure mechanism of hard rock, and further study the damage evolution law of hard rock under triaxial stress, in this paper, conventional triaxial compression tests under different confining pressures (5 MPa, 10 MPa, 15 MPa, and 20 MPa) for granite specimen were carried out. The mechanical properties and energy evolution mechanism of granite specimens under different confining pressures were studied. The crack initiation stress (σ_{ci}) and dilatancy stress (σ_{cd}) of hard rock were determined based on the law of linear energy dissipation. According to the results of AE monitoring, the characteristics of acoustic damage in the process of hard rock deformation and fracture under different initial confining pressures were studied. The types of granite specimen crack propagation under different loading times were clarified by judging the types of acoustic emission signals. The evolution law of the acoustic emission b value under different confining pressures was studied. The damage model D of granite was established in this paper. The research results of this paper are meaningful to the correct understanding of the mechanical properties and fracture mechanism of hard rock under triaxial stress and provide a theoretical basis for the selection of mechanical parameters of rock mass, engineering design calculation, and selection of support schemes in deep underground engineering.

2. Experimental Investigations

2.1. Experimental Instrument and Specimen. Conventional triaxial compression in this paper was carried out by the RMT-150B rock mechanics testing machine (as shown in Figure 1(a)). The instrument can apply a maximum confining pressure of 50 MPa, and the maximum axial stress is 1000 kN. In this study, the AE events of granite is monitored by DS-5 8-channel in the process of sample loading, as show in Figure 1(b). Meanwhile, in order to avoid attenuation of acoustic signal, butter was used as a coupling agent between the sensor and the sample, as shown in Figure 1(c), and a proper intensifying force was used to ensure good contact between the sensor and the granite sample. The sampling frequency was 3 MHz, the threshold value was set as 50, the amplification factor was set as 40 dB, and the frequency of acoustic emission sensor RS-2A was set as 150 kHz during the acquisition of acoustic emission signals.

The rock mass is complete relatively, without obvious defects, and the surface of the rock looks smooth. The original rock was processed into a cylinder with a diameter of 50 mm and a height of 100 mm, as shown in Figure 1(d). The machining accuracy of the granite samples was strictly in accordance with the standard of ISRM. The density of the granite is 2.63 g/cm^3 [31]. XRD analysis is widely used to testing the mineral compositions of the rock mass [32]. Therefore, in this study, XRD tests of granite powder were carried out by the Bruker X-ray diffractometer, as shown in Figure 2. Quartz and albite are hard and chemically stable; therefore, the higher the content, the greater the strength of the rock. The content of quartz and albite in the granite sample accounted for 71%, of which albite is 66% and quartz is 5%. In the sample, laumonite accounted for 25% and laumontite accounted for 4%.

2.2. Unloading Scheme. The rock sample was wrapped with a latex sleeve before loading; then, rigid cushion blocks with a diameter of 50 mm and a height of 25 mm were, respectively, placed on the upper and lower ends of the granite rock sample; finally, the rock sample was put into the pressure cylinder for loading. Rock samples were loaded to

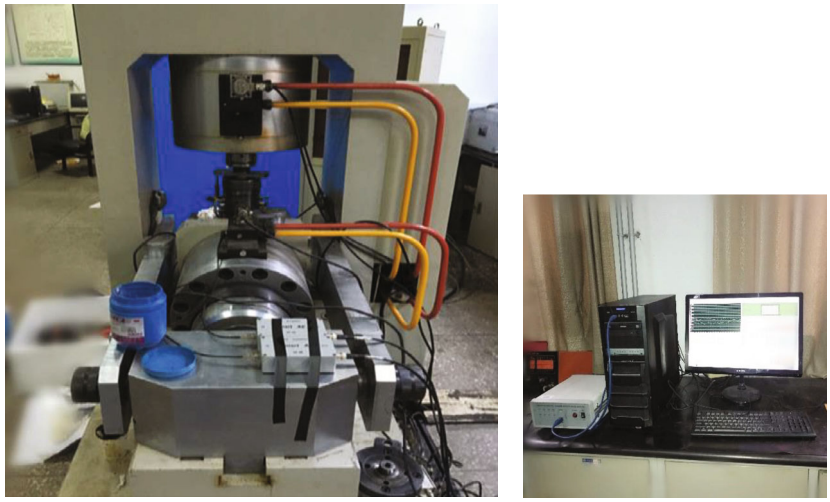

(a) RMT-150B rock mechanics test system (b) DS-5 AE system

(c) Acoustic emission probe (d) Rock specimens

Figure 1: Experimental instruments and rock specimens.

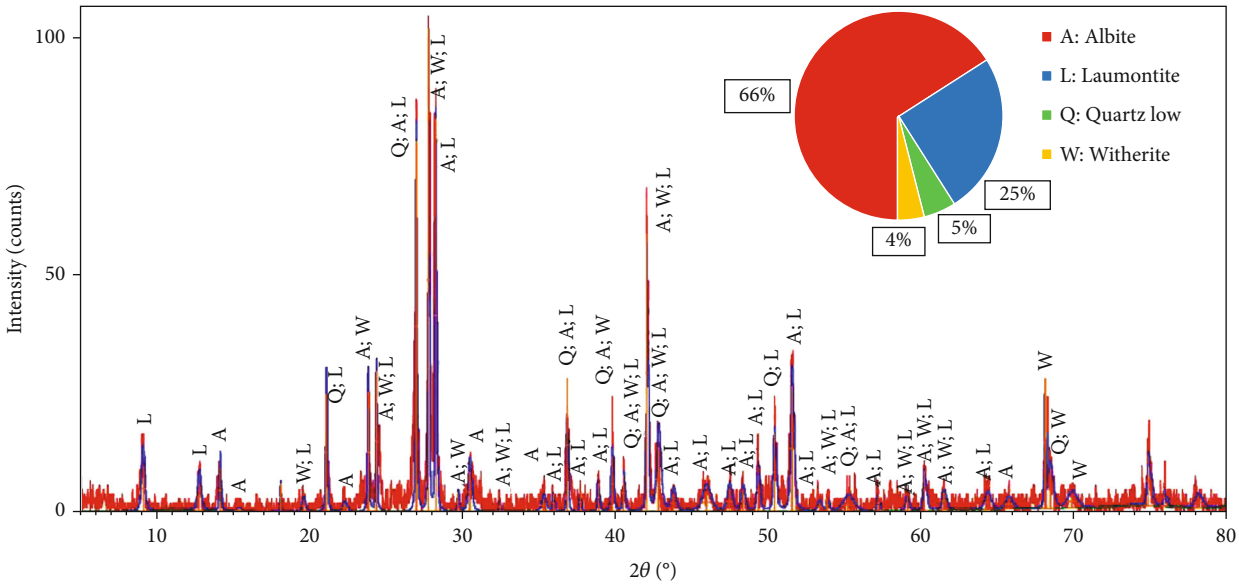

Figure 2: X-ray diffraction patterns of rock samples.

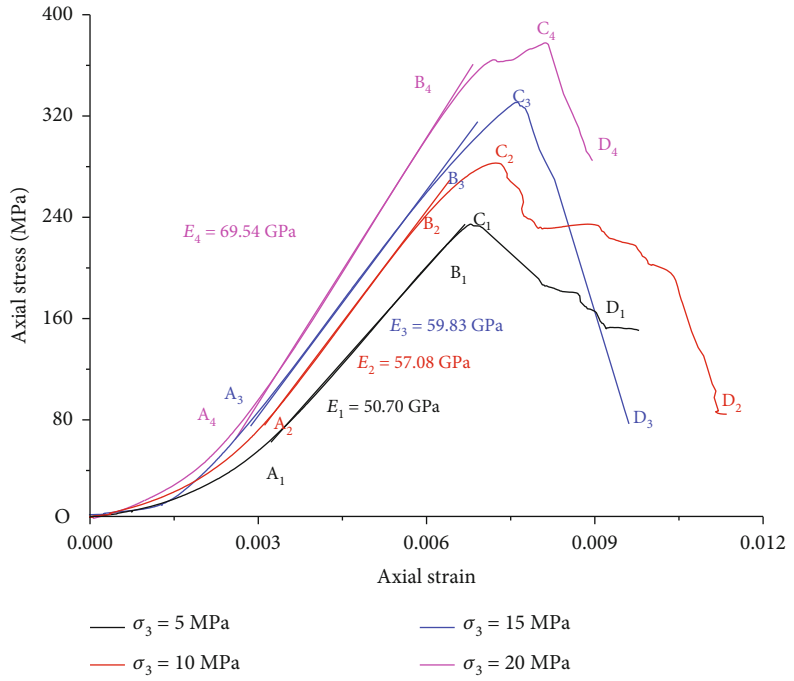

Figure 3: The stress-strain curve of granite.

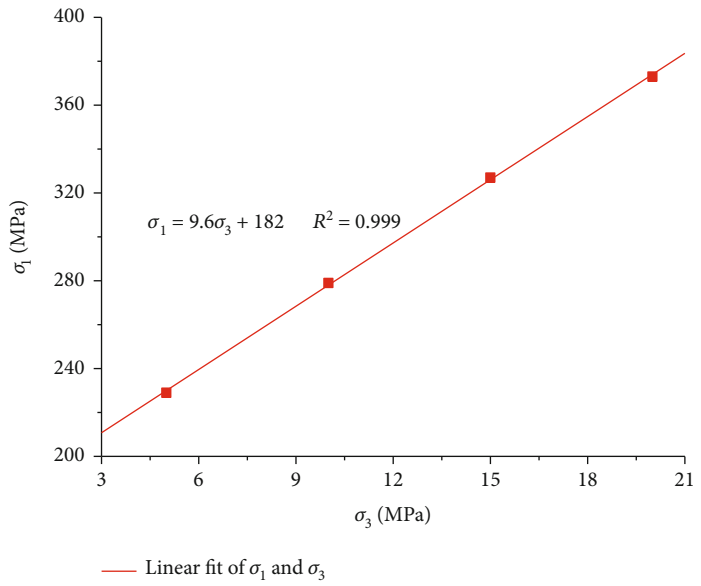

Figure 4: Relationship between confining pressures and peak stress.

predetermined confining pressures under hydrostatic pressure, four groups of initial confining pressures (5 MPa, 10 MPa, 15 MPa, and 20 MPa) were set in this paper, the loading rate of axial stress is 1.00 kN/s, and the loading rate of confining pressure is 0.500 MPa/s when applied to hydrostatic pressure. And then, axial compression was applied at a constant displacement load rate (0.005 mm/s) until rock samples were destroyed.

3. Experimental Analysis of Mechanical Properties of Granite

3.1. The Stress-Strain Curves of Granite. The complete stress-strain curves of granite samples under different initial confining pressures are shown in Figure 3.

It can be seen from Figure 3 that the stress-strain curves of the granite samples under different initial confining

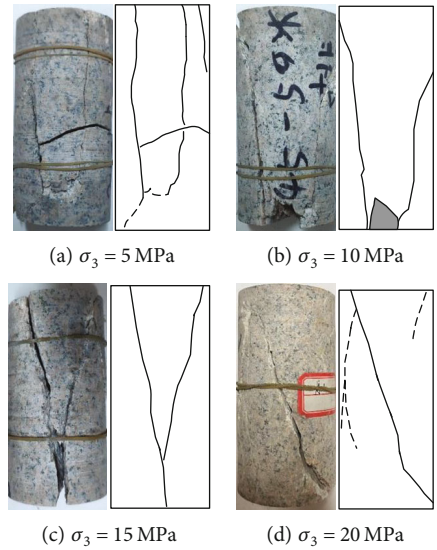

(a) $\sigma_3 = 5$ MPa (b) $\sigma_3 = 10$ MPa

(c) $\sigma_3 = 15$ MPa (d) $\sigma_3 = 20$ MPa

Figure 5: Fracture characteristics of granite samples under different confining pressures.

pressures all experienced the compaction stage (OA), linear elastic deformation stage (AB), plastic deformation stage (BC), and postpeak failure stage (CD). In the compaction stage (OA), the original holes and fissures inside the rock sample were compacted, and the stress-strain curves show obvious concaveness. When the sample enters the linear elastic stage (AB), in Figure 3, the elastic modulus (E_1) of the granite sample is 50.70 GPa, and the elastic modulus (E_4) of granite is 69.54 GPa, which indicates that the granite sample exhibits significant compression hardening. In the plastic deformation stage (BC), the stress-strain curve of samples becomes concave upward; the greater the confining pressure, the more obvious the prepeak yielding phenomenon and plastic deformation of the sample, and the specimen is gradually transformed from brittle to ductile. With the further application of the axial stress, the samples reach their peak point (C), and the peak stress and peak strain of the granite specimen both increase with the increase of the confining pressure.

3.2. The Strength Characteristics of Granite. Rock strength theory is aimed at expressing the yield and failure laws of rocks under complex stress conditions, which has always been a significant issue in the field of geotechnical engineering. And the Mohr-Coulomb strength criterion is the most authoritative strength theory [33] whose expression is shown in the following formula:

$$\sigma_1 = \xi\sigma_3 + \sigma_c. \tag{1}$$

In the formula, ξ is a constant and σ_c is the uniaxial compressive strength (MPa). According to formula (1), the fitting results are shown in Figure 4.

It can be seen from Figure 4 that the correlation coefficient R^2 of the triaxial compression test results fitted is 0.999, which has a good linear relationship. The parameters ξ and σ_c in equation (1) can both be expressed in terms of the strength parameters of the specimen, the cohesion (φ), and the angle of internal friction (c), whose expressions are shown in equations (2) and (3) as follows:

$$\xi = \frac{1 + \sin\varphi}{1 - \sin\varphi}, \tag{2}$$

$$\sigma_c = \frac{2c\cos\varphi}{1 - \sin\varphi}, \tag{3}$$

where φ is internal friction of the rock sample (°) and c is the cohesion force of the rock sample (MPa). Based on the fitting results in Figure 4 and equations (2) and (3), the cohesive force c of the granite specimen was calculated to be 29.37 MPa and the angle of internal friction φ was 54.23°.

3.3. Failure Characteristics of Granite under Different Confining Pressures. The granite presents a microdrum shape, resulting in an obvious expansion along the transverse direction during the fracture process of conventional triaxial loading. The crack sound of the granite specimen is heard clearly when it fails, which reflects the characteristics of hard rock failure. The photos of fracture characteristics of granite samples are shown in Figure 5.

It can be seen from Figure 5 that near the end of the sample, there are partially fractured surfaces on both sides of the main fracture surface; the end of the rock sample is more severely broken which is caused by the friction effect between the indenter of the testing machine and the end of the rock sample. The main forms of damage of granite specimens in triaxial compression are tensile and shear damage. As shown in Figure 5(a), two axial tensile failure surfaces appear in the rock sample, which shows that the damage of the specimen is compression-induced tensile cracking, and the extension of the tensile crack within the sample plays a dominant role in the damage of the granite specimens when the initial confining pressure is lower. When the initial confining pressure ranges from 10 to 20 MPa,

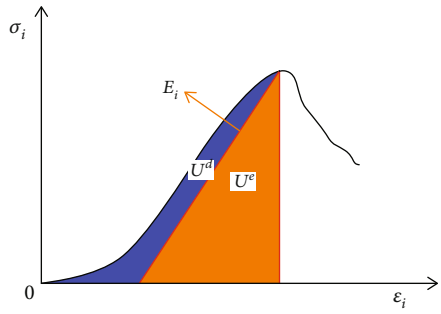

Figure 6: Relationship between dissipated energy and releasable strain energy

the failure of the rock sample ends with the formation of a macroscopic shear surface. As shown in Figure 4(b), the granite specimen fractured with a large number of splitting cracks in the axial direction; as shown in Figure 4(c), the rock sample shows typical Y-type conjugate shear failure; and as shown in Figure 4(d), the rock fracture pattern tends to be simplified, and the complex fracture pattern dominated by a tensile fracture gradually transforms into a single shear fracture pattern. Because the mineral particles inside the rock sample are bonded to each other and fit tightly under high pressure, which results in an increase in the cohesion of the granite sample, it is not prone to tensile fracture, and eventually, shear failure occurs. As show in Figure 4(d), the fracture angle of rock sample is 73°, which is close to the theoretical fracture angle of 72.3° predicted by the Mohr-Coulomb strength criterion ($\theta = 45° + \varphi/2$).

4. Energy Evolution of Granite under Different Confining Pressures

4.1. Principle of Energy Analysis. Rock loading failure is a process accompanied with energy absorption, storage, and dissipation [34, 35]. Assuming that the thermal energy generated by the external temperature change is not considered, the work done by the external force on the rock system is partly stored as elastic strain energy, and others are dissipated in the form of dissipation energy [36, 37] (as show in formula (4) and Figure 6). The rock will be destroyed when the elastic strain energy reaches its energy storage limit, a part of the stored elastic strain energy is converted into surface energy for the generation of new cracks, and the excess energy is used for rock kinetic energy, sound energy, thermal energy, and various kinds of radiation to be release to the outside world in other forms [14, 35].

$$W = U = U_e + U_d, \tag{4}$$

where U is the density of total energy (MJ/m^3), U_e is the density of elastic strain energy (MJ/m^3), and U_d is the density of dissipated energy (MJ/m^3). The schematic diagram of the relationship between the elastic strain energy U_e as shown in Figure 6.

Conventional triaxial compression tests were carried out in this paper, Therefore, it can be concluded that $\sigma_2 = \sigma_3$, formula (5) gives the calculation method of total energy U as follows:

$$U = \int_0^{\varepsilon_1} \sigma_1 d\varepsilon_1 + \int_0^{\varepsilon_2} \sigma_2 d\varepsilon_2 + \int_0^{\varepsilon_3} \sigma_3 d\varepsilon_3 = \int_0^{\varepsilon_1} \sigma_1 d\varepsilon_1 + 2\int_0^{\varepsilon_3} \sigma_3 d\varepsilon_3, \tag{5}$$

$$\begin{aligned} U_e &= \frac{1}{2E_i}\left[{\sigma_1}^2 + {\sigma_2}^2 + {\sigma_3}^2 - 2\mu(\sigma_1\sigma_2 + \sigma_2\sigma_3 + \sigma_1\sigma_3)\right] \\ &\approx \frac{1}{2E_0}\left[{\sigma_1}^2 + 2{\sigma_3}^2 - 2\mu\left(\sigma_1\sigma_3 + 2{\sigma_3}^2\right)\right], \end{aligned} \tag{6}$$

$$U_d = U - U_e, \tag{7}$$

where E_i is the elastic modulus at unloading; it can be replaced by the elastic modulus E_0 in the calculation [14].

4.2. Energy Evolution Process under Different Confining Pressures. According to formulas (5), (6), and (7), the evolution laws of total energy U, elastic strain energy U_e, and dissipated energy U_d of granite specimen during loading and damage under conventional triaxial stress path are obtained by using Origin software, as shown in Figure 7. Based on the conventional triaxial stress-strain characteristics of the sample, the stress-strain curve can be divided into the initial compression stage (OA), elastic deformation stage (AB), stable fracture growth stage (BC), unstable fracture growth stage (CD), and failure stage (DE).

(1) *Initial compression stage (OA)*: the energy absorbed by the rock sample is basically transformed into the dissipated energy U_d that causes the microcracks inside the rock to close and frictionally slip, at which point there is essentially no stored energy within the sample.

(2) *Elastic deformation stage (AB)*: the original cracks of the sample were compacted; there is no energy dissipation phenomenon in the rock sample. The elastic strain energy stored increases with the occurrence of elastic deformation, and the increase in elastic strain energy is constant. In this stage, the higher the confining pressure is, the higher the elastic strain energy storage rate is.

(3) *Stable fracture growth stage (BC)*: at this stage, the energy is still continuously inputted to the specimen, and the input energy is mainly stored in the form of releasable strain energy. There is a large number of microcracks in the sample initiation and development, but the initiation speed of microcracks in the sample is stable at this time, so the internal dissipation energy of the sample increases linearly at this stage. The crack initiation stress and dilation stress of the sample can be determined by the law of linear energy dissipation (as show in Figure 7). According to Figures 7(a) and 7(b), the crack initiation stress and dilatancy stress of granite samples increase with the increase of confining pressure.

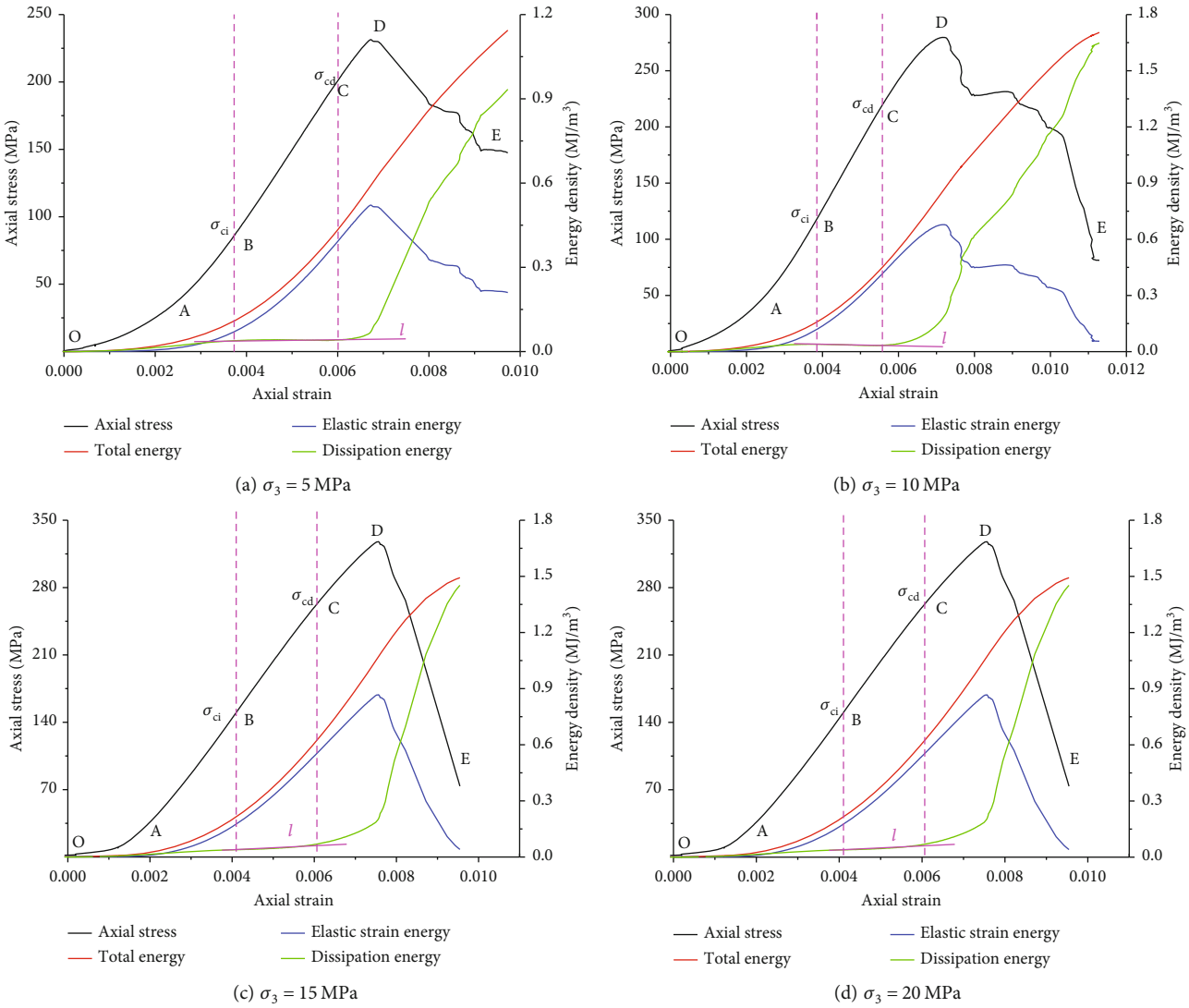

Figure 7: Energy evolution characteristics of granite under different confining pressures.

(4) *Unstable fracture growth stage (CD)*: the microcracks inside the rock sample begin to accelerate expansion and penetrate. The growth rate of elastic energy decreases sharply, and the growth rate of dissipated energy increases gradually. At the end of the unstable fracture growth stage, the elastic strain energy reaches the energy storage limit of the specimen, and the dissipation energy increases significantly.

(5) *Failure stage (DE)*: the sample can still absorb energy from the outside after the axial stress reaches its peak stress. However, at this time, the elastic strain decreased sharply, and the dissipated energy increases rapidly due to plastic deformation, macroscopic crack penetration, and slippage dislocation of macroscopic cracks which dissipate a large amount of energy. Finally, the strength of the whole rock structure is lost, and the rock is destroyed. At this stage, the greater the confining pressure is, the faster the energy release rate of the granite sample is. In Figure 7(a), the energy release rate of the granite sample is 377.69 MJ/m^3, and in Figure 7(d), the energy release rate of the granite sample is 904.92 MJ/m^3.

4.3. Analysis of Energy at Characteristic Points. The threshold stress of the granite sample was determined according to the law of linear energy dissipation in Section 3.2, and the relationship between the confining pressure of the sample and the total energy, elastic strain energy, and dissipated energy was obtained at the threshold stress and peak stress point, as shown in Figure 8.

According to Figure 8, each energy of the specimen under different times is highly correlated with the confining pressure. (1) At the crack initiation point, the confining pressure has a greater impact on the total energy U and elastic strain energy U_e of the granite specimen. The energy

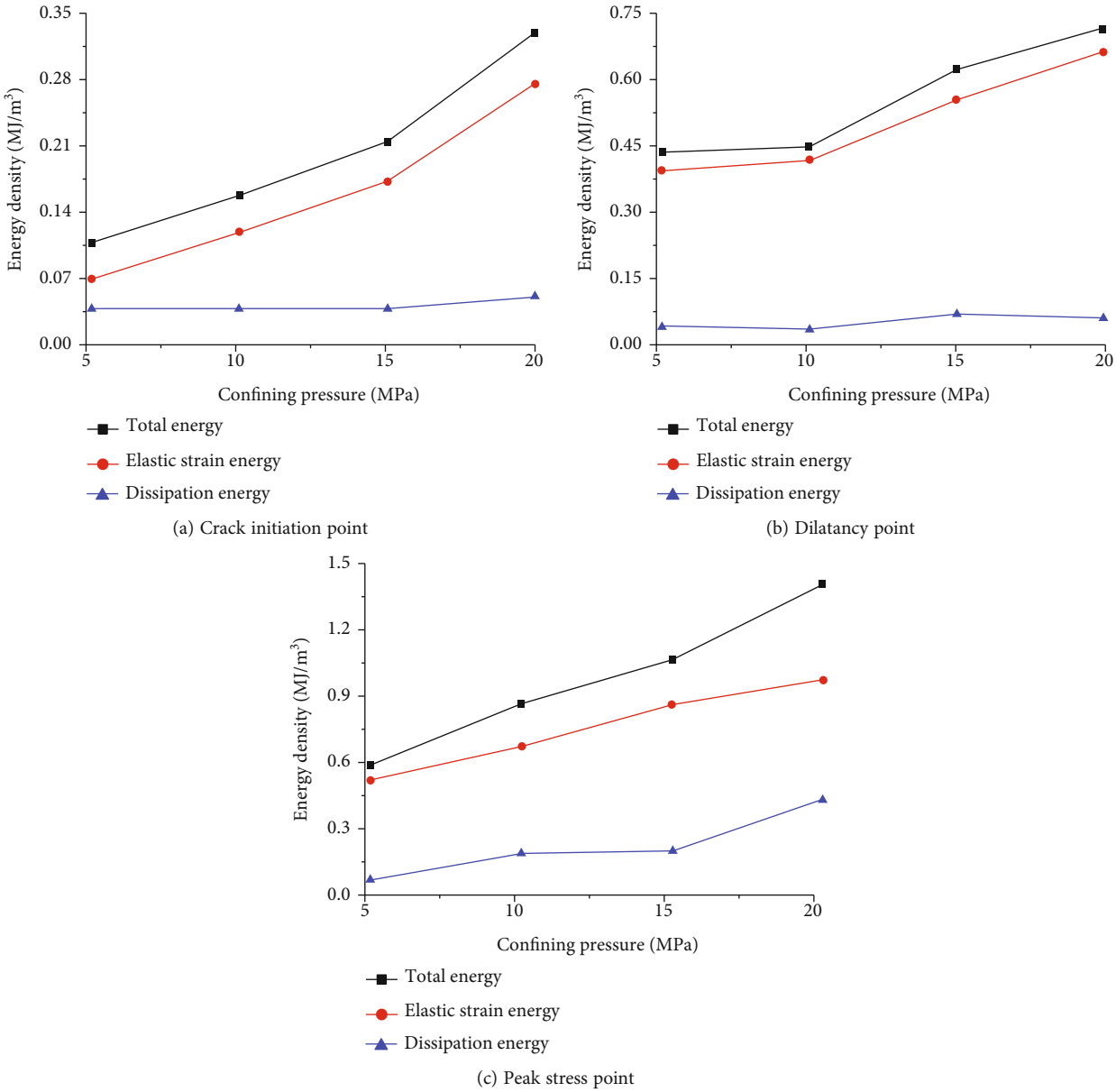

Figure 8: The relationship between confining pressure and energy at different characteristic points.

absorbed and stored by the sample increases linearly, and its growth rate is 0.011 (MJ/m^3)/MPa, while the change trend of absorbed and stored energy with confining pressure is steep, which is only 0.023 (MJ/m^3)/MPa when the confining pressure is greater than 15 MPa. The change of dissipated energy at the crack initiation point is not significant, and the value of dissipated energy is both 0.039 MJ/m^3. (2) At the expansion point, when the confining pressure is less than 10 MPa, the change trend of total energy and elastic strain energy of granite sample is slow, and the energy growth rate is 0.002 (MJ/m^3)/MPa and 0.005 (MJ/m^3)/MPa, respectively. However, the growth rates of total energy and elastic strain energy are 0.027 (MJ/m^3)/MPa and 0.022 (MJ/m^3)/MPa, respectively, when the confining pressure is larger. At this time, the change of dissipated energy is still not significant; the dissipated energy is both 0.039 MJ/m^3. (3) At the peak point, the overall linear law of the total energy, elastic strain energy, and confining pressure of the granite sample is more significant; when the confining pressure is larger than 15 MPa, the dissipated energy of the sample increases significantly. As shown in Figures 8(b) and 8(c), the greater the confining pressure is, the more energy is dissipated by the granite sample in the process of damage and failure, and the damage deformation of the sample is sufficient relatively. A large amount of energy was absorbed in the rock specimen when the confining pressure is high. At this time, the limit energy storage capacity of the rock sample is reduced. Therefore, the sample will release a large amount of energy and have a large energy

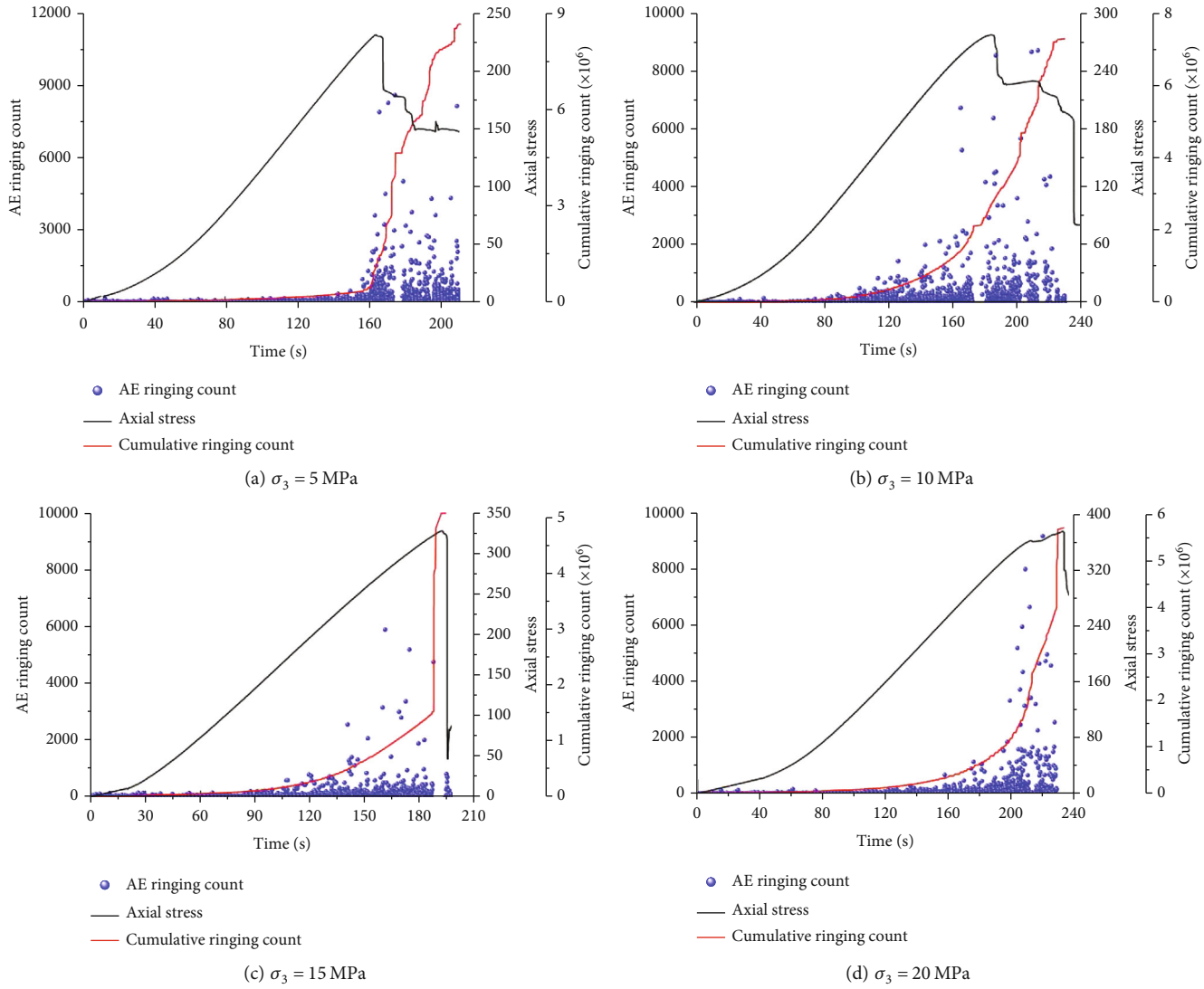

Figure 9: AE ringing count characteristics of granite specimens.

release rate when it is broken. This phenomenon has been confirmed in dynamic disasters such as rock bursts during the construction of a high geostress environment of underground engineering.

5. Damage Analysis of Hard Rock with AE Parameters

Acoustic emission of rock is an elastic wave released by the propagation of original cracks and defects in rock materials and the formation, initiation, evolution, expansion, and fracture of new microcracks during the process of loading [38, 39]. The acoustic emission of rock contains the evolution information of the failure process inside the rock, and the rock will show different acoustic emission signals and crack propagation characteristics under different stress levels. The analysis of the relationship between the acoustic emission signals and the characteristics of crack propagation in the process of rock fracture is helpful to the study of the internal fracture mechanism of rock under the three-direction stress path, which is of great significance to the further prediction and prevention of rock mass disasters [40, 41].

5.1. Qualitative Damage Analysis of Hard Rock with AE Parameters

5.1.1. The AE Ring Count Characteristics of Granite. Acoustic emission technology is of great significance to the study of material damage and fracture processes. Ringing count is a parameter that can better reflect the changes in material damage and fracture processes among many acoustic emission parameters, because it is proportional to the strain energy released by dislocation movement, inclusion and second phase particle peeling, and fracture and crack propagation in the rock material [18, 19]. Figure 9 shows AE ringing counts and cumulative ringing counts in the deformation and failure process of granite samples.

It can be seen from Figure 9, at the initial loading stage, there were small amounts of AE events in the granite specimen during the compaction stage due to the original cracks

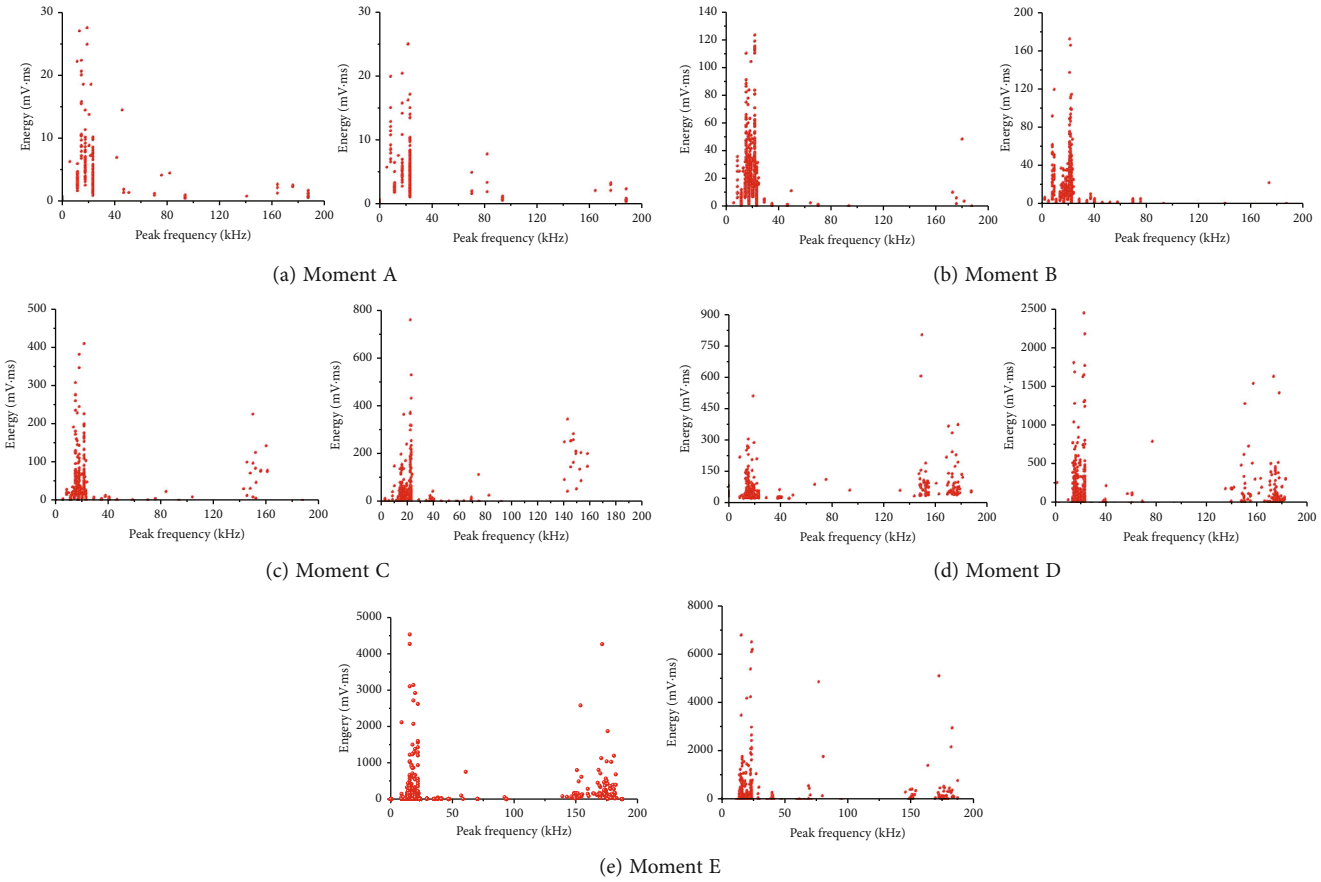

Figure 10: The relationship between peak frequency and energy under different moments.

inside the sample beginning to close and the frictional effect of rough crack surfaces occurring. With continuous loading, the sample enters the elastic deformation stage; at this time, acoustic emission events are still rare, because the stress in the granite specimen is not enough to product new cracks, and the generation of acoustic emission events is caused by the dislocation and grain slip between closed microcrack surfaces. When the sample enters the stage of stable microcrack growth, the cracks in the sample initiate, bifurcate, and develop stably, and the old cracks also enter the state of stable development. Acoustic emission events in the sample begin to increase, and the cumulative ringing count increases linearly. With the further application of axial load, internal microcracks of the sample accelerate extension, aggregation, and penetration; the acoustic emission event of the sample becomes active; and the cumulative ringing count curve is concave. At the peak stress, AE events are hyperactive, the AE ringing counts reach their maximum value, and the cumulative ringing counts increase suddenly.

When the confining pressure is small (see Figure 9(a)), the AE ringing counts are small in the prepeak stage, and the cumulative ringing count is only 0.46×10^6. The cumulative ring count increases sharply from 0.46×10^6 to 6.27×10^6 from the peak point to the failure process of the sample. When the confining pressure is large (see Figure 9(d)), the AE activity of the sample is relatively active before it fractures, and its cumulative ringing count has reached 2.24×10^6. In the case of low confining pressure, the granite specimen undergoes brittle failure when the axial stress reaches it material strength; therefore, the AE ringing counts increase to its maximum value instantaneously in the failure stage; on the contrary, the axial stress reaches the strength of the rock material and plastic deformation occurs. However, the strength of the rock material is greatly enhanced due to the confining pressure effect. At this time, the specimen still has a strong bearing capacity, the internal damage of the sample continues to develop, and the load-bearing capacity of the sample is gradually reduced while the deformation increases gradually. Finally, the specimen reaches its ultimate bearing capacity at the peak stress and ductile failure occurs; the acoustic emission ringing count grows more evenly in this process.

5.1.2. Acoustic Emission Types under Different Confining Pressures and Moments. Acoustic emission ringing count can qualitatively reflect the degree of the internal damage of the sample during the conventional triaxial loading failure process, and the type of acoustic emission signal can be judged by the frequency and energy of the acoustic emission signal, which can further investigate the type of damage within the specimen. There are two types of AE events in the process of rock deformation and damage under stress

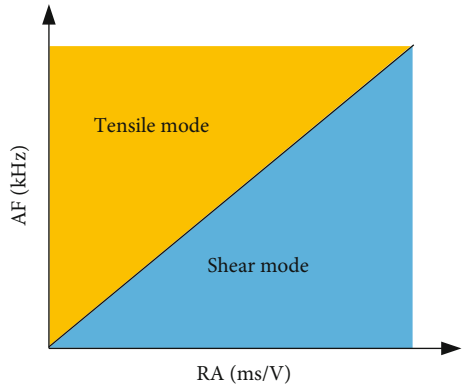

Figure 11: Relationship between RA value and AF value.

[42]. The first is the friction-type acoustic emission event caused by the closure of original cracks and the friction between material particles, which has low frequency and weak energy. The other is the fracture-type acoustic emission event caused by the expansion of new cracks, and this kind of acoustic emission has relatively high frequency and energy. Two types of AE events correspond to friction and fracture mechanisms, respectively. Figure 10 shows the relationship between the peak frequency and the acoustic emission energy of the specimen at the end of the compaction stage (point A), the crack initiation point (point B), the dilatancy point (point C), the peak stress point (point D), and the failure point (point E) under the initial confining pressure which is 5 MPa and 20 MPa.

According to Figure 10, the peak frequency and energy of acoustic emission signals at different times with the same confining pressure have great differences. In Figures 10(a1), to 10(d1), with the application of axial load, the energy value of the acoustic emission signal keeps increasing. The maximum acoustic emission energy at moment A is 28 mV·ms, the maximum value of acoustic emission energy is 420 mV·ms at the moment of C, and the maximum acoustic emission energy at moment E is as high as 4610 mV·ms, which is 171.79 times higher than that at the moment of A. At the same time, as the loading-applied AE high-frequency signal points increase, the frequencies of acoustic emission signals of the samples are concentrated in the range of 8.8~23.4 kHz at the moment A and moment B (see Figures 10(a) and 10(b)), which are dominated by low-frequency and low-energy friction-type acoustic emission events. At moment C, a small number of high-frequency signal points appear in the sample, which indicates that before the crack initiation point, AE events are mainly induced by the crack closure and interparticle friction in the granite sample. At moments D and E (see Figures 10(d) and 10(e)), a large number of high-frequency signal points appear. At this time, the acoustic emission model gradually transform from low-frequency and low-energy friction-type AE events to high-frequency and high-energy fracture-type AE events, and the above process is consistent with the deformation and damage process of the sample under triaxial loading. The AE signals of granite samples gradually evolve to high-frequency and high-energy regions under a low confining pressure. When the confining pressure is high, in Figures 10(d), the density of high-frequency and high-energy region points is the largest, while in Figure 10(e), the number of high-frequency and high-energy signal points is significantly reduced, and more intermediate frequency signals appear, which indicate that high confining pressure inhibits the generation of tension cracks.

5.1.3. The Relationship between RA and AF Parameters with Failure Mode. According to the research, the value of RA and average frequency (AF) in acoustic emission parameters can reflect the failure type of the rock material, where the value of RA can be obtained by dividing the rising time by the amplitude value of acoustic emission, and the average frequency AF is obtained by the ratio of ringing count and duration. Generally speaking, the AE signal has a low AF value and high RA value when the shear crack is initiated in the sample; otherwise, if the tensile crack is initiated, the AE event has a high AF value and low RA value [43], as shown in Figure 11.

The RA value and AF value of the granite samples were calculated, and the scatter distribution diagram is drawn, as shown in Figure 12.

As can be seen from the distribution of points in Figure 12, with the increase of confining pressure, the distribution region tends to approach the horizontal axis. In Figure 12(a), the points cover the entire longitudinal axis, which are mainly concentrated in the interval of $10 < AF < 80$. At this time, the AE signal has a lower RA value and a higher AF value, which indicates that the tensile crack of the sample is developed, when the confining pressure is $0 < RA < 40$. At this time, the difference between the acoustic emission signals AF and RA is small, and the tensile cracks and shear cracks are relatively developed in the sample; when the confining pressure is 15 MPa, the points are mainly concentrated near the horizontal axis and are dense relatively in the interval of (0, 40); the cracks produced by specimen failure are mainly shear cracks. In Figure 12(d), the points are all over the entire horizontal axis, the maximum value of AF decreases from 100 to about 70, and the RA value of the acoustic emission signal is much larger than the AF value. At this time, the shear crack of the sample is relatively developed, and the ultimate performance is typical shear failure. The failure modes of rock samples under different confining pressures determined above are consistent with the actual situation.

5.1.4. The Characteristic of AE b Value under Different Confining Pressures. Acoustic emission is a phenomenon of acoustic waves monitored by the release of strain energy during rock deformation and failure. Therefore, the acoustic emission event can be regarded as a kind of microseismic activity [44, 45]. Gutenberg and Richter [46] proposed the statistical relationship between earthquake magnitude and frequency distribution:

$$\lg N = a - bM, \tag{8}$$

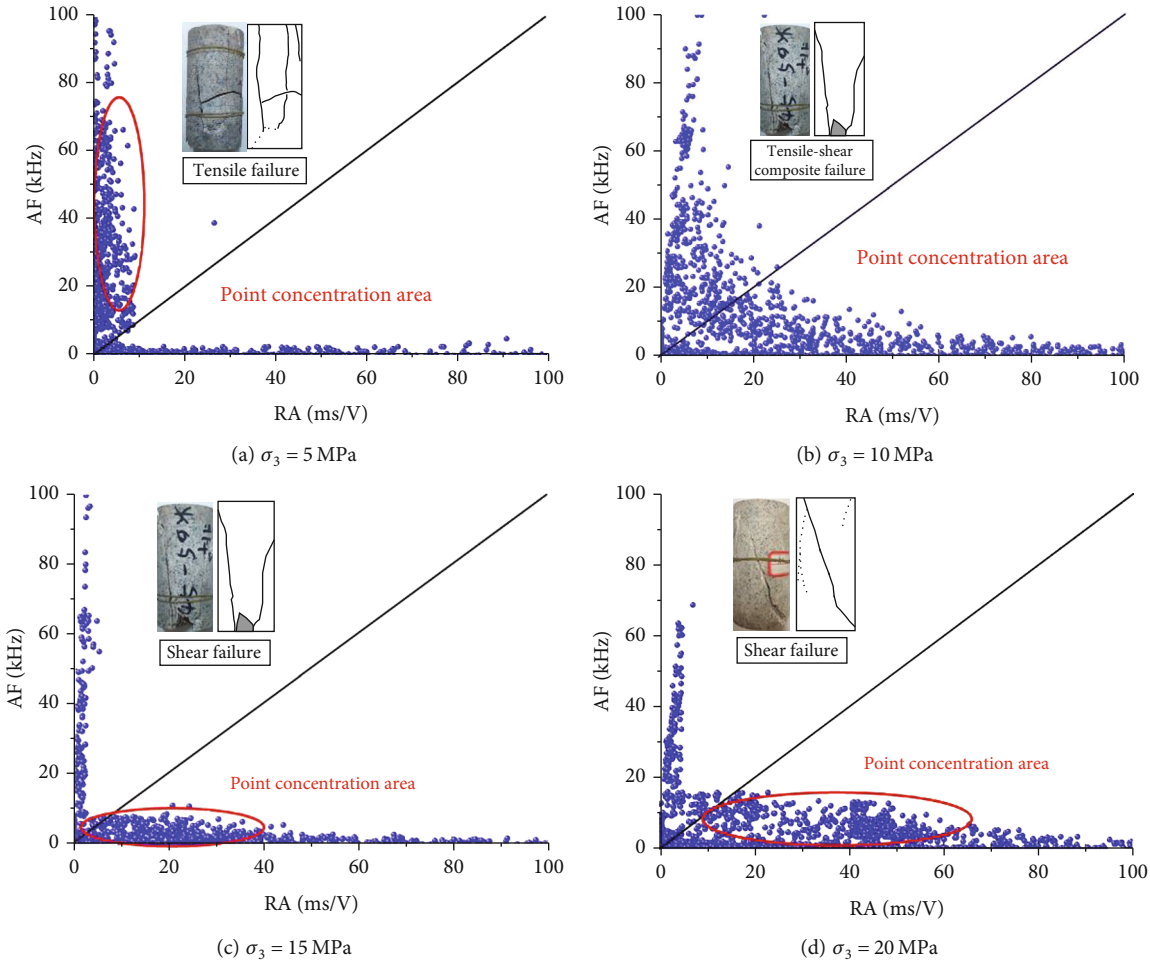

Figure 12: Distribution of AE parameters of RA versus AF.

where a and b are constants related to seismic activity characteristics; N is the number of earthquakes with magnitude in the range of ΔM, which can be considered as acoustic emission events of samples; and M is the magnitude of the earthquake, which can be replaced by the acoustic emission amplitude (dB) divided by 20; formula (8) can be rewritten as

$$\lg N = a - b\left(\frac{A_{\mathrm{dB}}}{20}\right), \tag{9}$$

where A_{dB} (dB) is the amplitude of the acoustic emission signal, N is the number of AE events, and a and b are constant. The b value of acoustic emission is a measure of the change of crack development, and the overall value and change trend of the b value are closely related to the internal crack development of rock. When the b value of acoustic emission is large, which indicates that the number of small events increases, and the development of internal rock cracks is a gradual and stable propagation. When the value of b is small, it means that the proportion of AE small events decreases, while the number of large events increases, which indicates that the crack inside the sample develops dramatically, and the rock may be damaged. In order to avoid large errors in the calculation, this paper selects 100 AE signals as a group of data to calculate the b value of AE by using the least-square method; the variation of the b value of samples during the conventional triaxial loading is shown in Figure 13.

As can be seen from Figure 13, in the early stages of loading, the b values of the sample under different confining pressures were low, and the AE amplitude was high and typically around 10–20 dB. Low b values and high amplitudes are due to the original holes and cracks in the rock samples which were compacted. In the elastic deformation stage, the AE amplitudes were low and below 10 dB. The b value of acoustic emission suddenly increases to its maximum value, and it fluctuates slightly near the maximum value. This indicates that the number of small AE events is increasing, the proportion of large and small events changes little at this stage, the development of internal cracks in the rock is slow, and the development of original cracks and regenerated cracks with different scales is relatively stable. As the load continues to increase, the b value of acoustic emission begins to decrease and reaches the minimum value at the peak

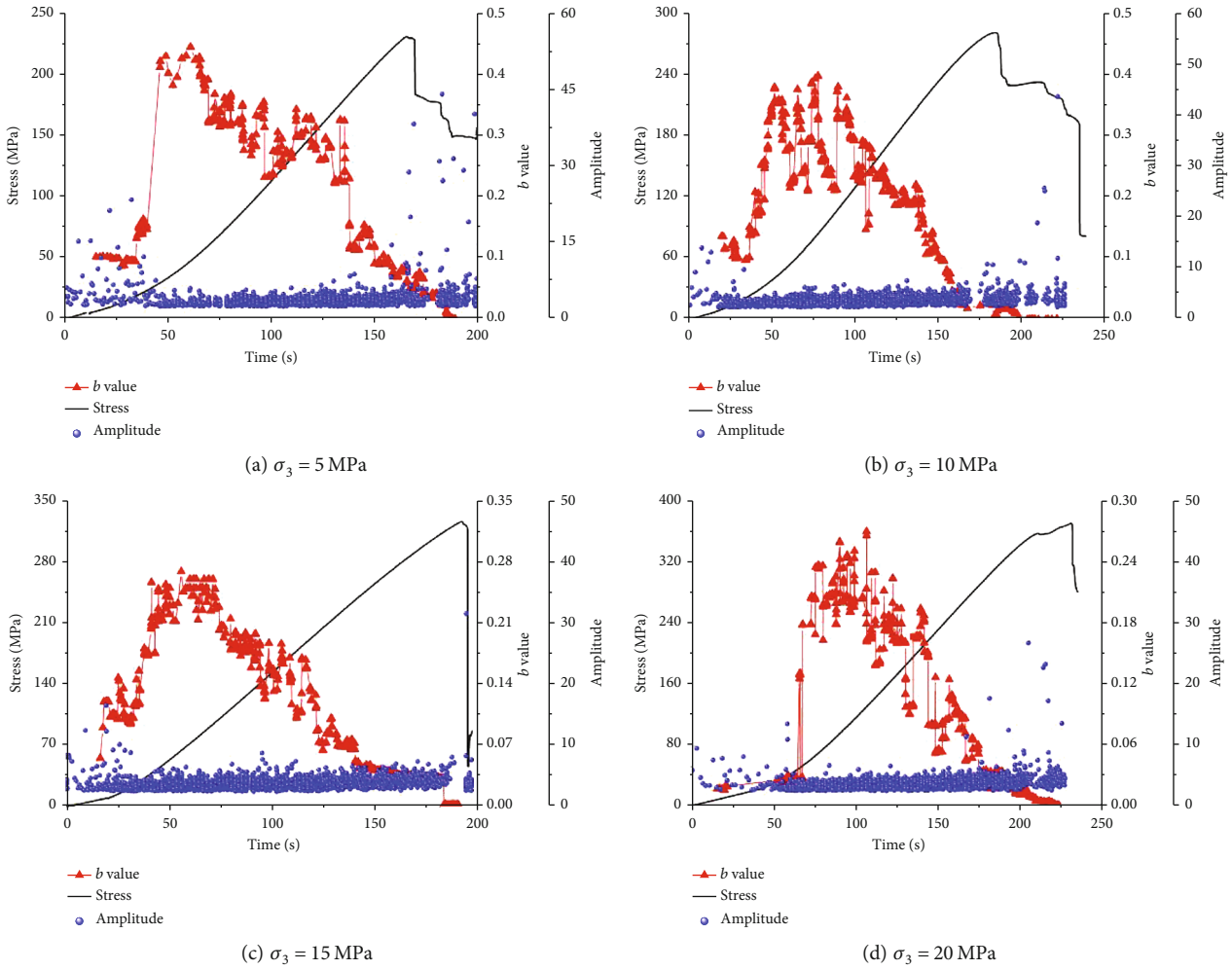

(a) $\sigma_3 = 5$ MPa

(b) $\sigma_3 = 10$ MPa

(c) $\sigma_3 = 15$ MPa

(d) $\sigma_3 = 20$ MPa

FIGURE 13: The relationship between time and b value under different confining pressures.

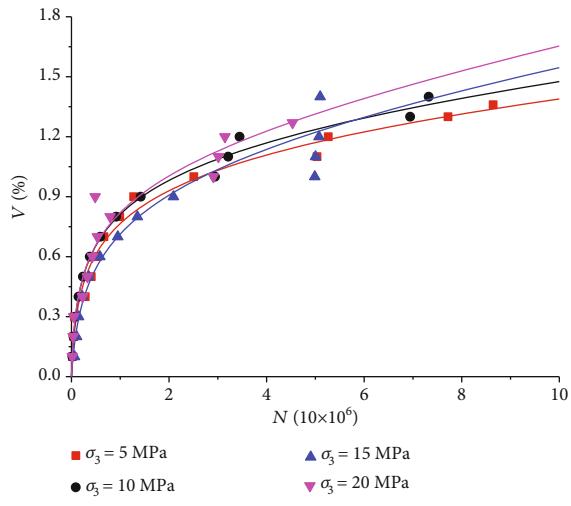

FIGURE 14: The relationship between N and V.

TABLE 1: Fitting results of V and N.

Confining pressure (MPa)	a	c	q	R^2
5	0.0127	0.224	27.822	0.982
10	0.0170	0.224	33.846	0.992
15	0.0307	0.248	14.712	0.966
20	0.0384	0.214	37.594	0.976

stress. In this process, the proportion of AE major events keeps increasing, the internal cracks of the sample accelerate the expansion, and the number of large-size cracks gradually increases, and finally, the failure occurs.

As seen Figure 13(a), the maximum value of the b value is 0.44, the b value of acoustic emission drops sharply at 79% σ_c, and then, the rate of decline is 3.65×10^{-3} s^{-1}. As seen Figure 13(d), the maximum value of the b value is 0.28, which begins to decrease at 59.3% σ_c, but the reduction rate is 9.46×10^{-4} s^{-1}. The above phenomenon is mainly due to the insufficient development of deformation and damage in the specimen under a small confining pressure, which shows

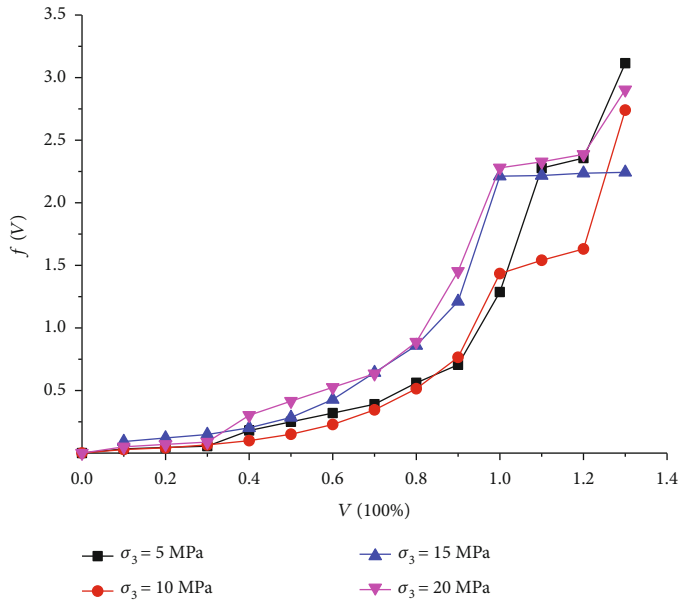

Figure 15: The relationship between $f(V)$ and V under different confining pressures.

the characteristics of brittle failure. Therefore, during the deformation and failure process, the b value is larger, and the b value will drop suddenly and decrease rapidly. In the case of a large confining pressure, due to the restraint of confining pressure and high stress level, the cracks of the specimen are fully developed and exhibit well ductility during the deformation and failure process. At this time, the b value is small, the decrease time of b value is early, and the rate of decrease is slower.

5.2. Damage Model of Granite under Triaxial Stress. From the above study, it is clear that acoustic emission parameters can qualitatively characterize the damage and failure of materials to a certain extent [47, 48]. The probability-density function $f(V)$ was introduced into this paper [2] to establish the relationship between acoustic emission events and corresponding stress level quantitatively, as shown:

$$f(V)dV = \frac{dN}{N_0}, \tag{10}$$

where V is the stress levels; it can be obtained by dividing the stress at a certain moment by the strength of the granite specimen under the corresponding confining pressure, N is the number of cumulative events, and N_0 is the number of total cumulative events. The relationship between V and N is shown in the following formula [49]:

$$V = \mathrm{aN} + c\ln(1 + qN). \tag{11}$$

Based on equation (11), the conventional triaxial compression test data of the sample were fitted, and the fitting results are shown in Figure 14.

As can be seen from Table 1, the correlation coefficient R^2 of the fitting results is distributed between 0.966 and 0.992, all of which are greater than 0.950. It indicates that the stress levels V and the number of cumulative events N under different confining pressures have a good logarithmic relationship, and the values of a, c, and q of equation (11) under different confining pressures were obtained through fitting. We substitute (11) into formula (10), through integral operation, as shown:

$$f(V) = \frac{1}{N_0}\left(\frac{1 + qN}{a + cq + aqN}\right). \tag{12}$$

From equation (12) and the fitting result in Figure 13, the relationship between $f(V)$ and V can be obtained as shown in Figure 15.

In order to study the damage variables D of granite in the postpeak stage, the stress level in the postpeak stage is defined as follows:

$$V = 1 + \frac{\sigma_{\max} - \sigma}{\sigma_{\max}}, \tag{13}$$

where $\sigma_{\max}$ is the peak stress of the granite specimen under the corresponding initial confining pressure (MPa). σ is the stress of the granite specimen at a certain point in the postpeak stage (MPa).

The damage variable D of the granite specimen can be obtained by integrating the probability-density function $f(V)$ as shown:

$$D = \int_0^V f(V)dV. \tag{14}$$

The damage curves of granite under different confining pressures can be obtained using Origin software to

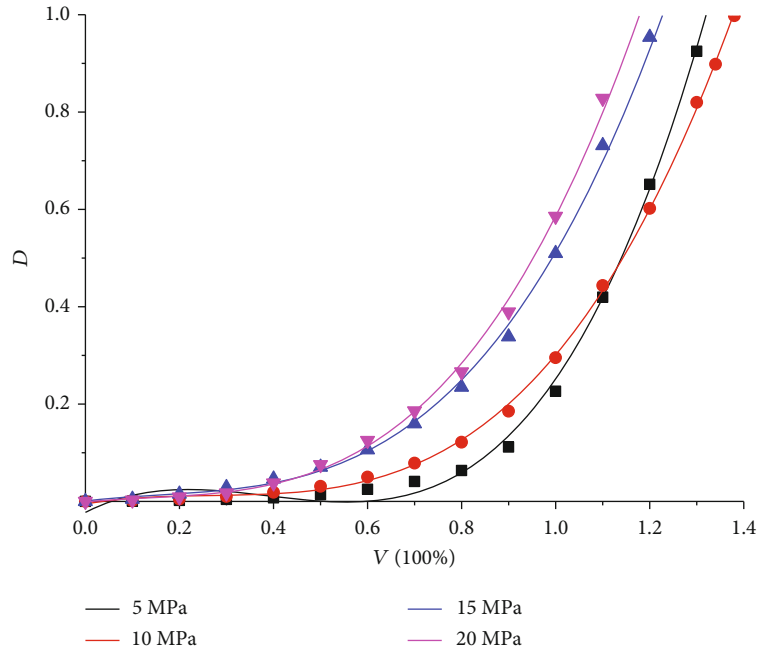

Figure 16: Damage curves of granite samples under different confining pressures.

integrate the $f(V)$-V curve, as shown in Figure 16 and formula (15).

$$\begin{aligned}
&\sigma_3 = 5\,\text{MPa} : D = 1.350V^3 - 1.570V^2 + 0.494V - 0.023,\ R^2 = 0.997,\\
&\sigma_3 = 10\,\text{MPa} : D = 0.712V^3 - 0.573V^2 + 0.167V - 0.005,\ R^2 = 0.999,\\
&\sigma_3 = 15\,\text{MPa} : D = 0.761V^3 - 0.369V^2 + 0.119V - 0.001,\ R^2 = 0.998,\\
&\sigma_3 = 20\,\text{MPa} : D = 0.783V^3 - 0.313V^2 + 0.088V - 0.001,\ R^2 = 0.999.
\end{aligned} \tag{15}$$

It can be seen from Figure 16 and formula (15) that there was a positively proportional linear relationship between D and the cubic polynomial in V; the correlation coefficients obtained by fitting are all greater than 0.99. As can be seen from Figure 16, the larger the initial confining pressure is, the larger the rock damage parameter D is under the same stress level, which is caused by the rock which will appear as a stick-slip phenomenon under the high confining pressure. When the stress level is greater than 1.1, the damage variable of the specimen at 5 MPa is greater than that at 10 MPa.

6. Conclusion

Conventional triaxial compression tests under different confining pressure were carried out in this paper. The following main results are obtained through the test results:

(1) The elastic modulus and plastic deformation of the granite sample are small, and the brittleness characteristics are significant when the confining pressure of the sample is low; conversely, the granite sample has obvious compression hardness and ductile characteristics. The peak stress and strain of the granite specimen increase linearly with the increase of the confining pressure of the sample. According to the Mohr-Coulomb strength criterion, the cohesion of the granite sample is 29.37 MPa and the internal friction angle is 54.23°

(2) The crack initiation (σ_{ci}) stress and dilatancy stress (σ_{cd}) of hard rock were determined based on the law of linear energy dissipation, which concluded that the σ_{ci} and σ_{cd} of granite specimens increase with the increase of confining pressure. Confining pressure has a significant promoting effect on the energy storage capacity of granite samples. At the crack initiation point and expansion point, the total energy and elastic strain energy of the specimen increase with the increase of the confining pressure, but the dissipated energy is less affected by the confining pressure. The value of each energy in the sample increases significantly with the increase of initial confining pressure at the peak stress. And the higher the confining pressure is, the faster the energy release of the sample is in the failure stage

(3) The ringing counts and cumulative ringing count increase rapidly to the maximum value near the peak stress while the confining pressure is small, and the specimen suddenly fails in a very short time. Conversely, when the ringing counts and cumulative ring counts increase more smoothly, the acoustic emission signal becomes active at the expansion point and the deformation damage of the sample is fully developed. Before the crack initiation point, AE signals are mainly low-energy and low-frequency friction-type AE events, while after the dilatation point, AE signals of samples are mainly high-

frequency and high-energy fracture-type AE events, and the acoustic emission signal has greater energy when the confining pressure is larger

(4) Typical tensile failure fracture occurs in granite samples under the low confining pressure, and tension-shear composite failure or typical shear failure is found in granite samples under high confining pressure, which is consistent with the failure mode of granite samples judged by acoustic emission parameters according to the distribution of characteristic values of AE parameters RA and AF. In the case of a low confining pressure, the acoustic emission b value of the granite sample is large, there will be a sudden drop, the decrease time is late, and the decrease rate is large. Under the same stress level, the larger the initial confining pressure is, the larger the damage variable D is

Data Availability

The data used to support the findings of this study are available from the corresponding author upon request.

Conflicts of Interest

The authors declare that there are no conflicts of interest regarding the publication of this paper.

Acknowledgments

This research was funded by the National Natural Science Foundation of China (51778215) and China Postdoctoral Science Foundation Funded Project (No. 2018M631114). The authors greatly appreciate the financial support from funding bodies.

References

[1] H. Han, D. Fukuda, H. Liu et al., "Combined finite-discrete element modellings of rockbursts in tunnelling under high in-situ stresses," *Computers and Geotechnics*, vol. 137, article 104261, 2021.

[2] Y. Wu, S. Li, D. Wang, and G. Zhao, "Damage monitoring of masonry structure under in-situ uniaxial compression test using acoustic emission parameters," *Construction and Building Materials*, vol. 215, pp. 812–822, 2019.

[3] M. He, F. Ren, and D. Liu, "Rockburst mechanism research and its control," *International Journal of Mining Science and Technology*, vol. 28, no. 5, pp. 829–837, 2018.

[4] J. Wang, G. Chen, Y. Xiao, S. Li, Y. Chen, and Z. Qiao, "Effect of structural planes on rockburst distribution: case study of a deep tunnel in Southwest China," *Engineering Geology*, vol. 292, article 106250, 2021.

[5] R. Xue, Z. Liang, and N. Xu, "Rockburst prediction and analysis of activity characteristics within surrounding rock based on microseismic monitoring and numerical simulation," *International Journal of Rock Mechanics and Mining Sciences*, vol. 142, article 104750, 2021.

[6] V. Kallimogiannis, H. Saroglou, and G. Tsiambaos, "Study of cracking process in granite," *Procedia Engineering*, vol. 191, pp. 1108–1116, 2017.

[7] S. Wang, L. Huang, and X. Li, "Analysis of rockburst triggered by hard rock fragmentation using a conical pick under high uniaxial stress," *Tunnelling and Underground Space Technology*, vol. 96, article 103195, 2020.

[8] C. D. Martin and N. A. Chandler, "The progressive fracture of Lac du Bonnet granite," *International Journal of Rock Mechanics and Mining Sciences & Geomechanics Abstracts*, vol. 31, no. 6, pp. 643–659, 1994.

[9] Y. Zong, L. Han, J. Wei, and S. Wen, "Mechanical and damage evolution properties of sandstone under triaxial compression," *International Journal of Mining Science and Technology*, vol. 26, no. 4, pp. 601–607, 2016.

[10] T. Zhou, Y. Qin, Q. Ma, and J. Liu, "A constitutive model for rock based on energy dissipation and transformation principles," *Arabian Journal of Geosciences*, vol. 12, no. 15, p. 492, 2019.

[11] D. Li, Z. Sun, T. Xie, X. Li, and P. G. Ranjith, "Energy evolution characteristics of hard rock during triaxial failure with different loading and unloading paths," *Engineering Geology*, vol. 228, pp. 270–281, 2017.

[12] H. P. Xie, J. F. Liu, Y. Ju, J. Li, and L. Z. Xie, "Fractal property of spatial distribution of acoustic emissions during the failure process of bedded rock salt," *International Journal of Rock Mechanics and Mining Sciences*, vol. 48, no. 8, pp. 1344–1351, 2011.

[13] H. Xie, L. Li, Y. Ju, R. D. Peng, and Y. M. Yang, "Energy analysis for damage and catastrophic failure of rocks," *Science China Technological Sciences*, vol. 54, Supplement 1, pp. 199–209, 2011.

[14] H. P. Xie, Y. Ju, and L. Li, "Criteria for strength and structural failure of rocks based on energy dissipation and energy release principles," *Chinese Journal of Rock Mechanics and Engineering*, vol. 17, pp. 3003–3010, 2005.

[15] Y. Tian and R. G. Yu, "Energy analysis of limestone during triaxial compression under different confining pressures," *Rock and Soil Mechanics*, vol. 35, no. 1, pp. 118–122, 2014.

[16] Z. Z. Zhang and F. GAO, "Confining pressure effect on rock energy," *Chinese Journal of Rock Mechanics and Engineering*, vol. 34, no. 1, pp. 1–11, 2015.

[17] H. Sun, L. Ma, W. Liu, A. J. S. Spearing, J. Han, and Y. Fu, "The response mechanism of acoustic and thermal effect when stress causes rock damage," *Applied Acoustics*, vol. 180, article 108093, 2021.

[18] Q. Wang, J. Chen, J. Guo, Y. Luo, H. Wang, and Q. Liu, "Acoustic emission characteristics and energy mechanism in karst limestone failure under uniaxial and triaxial compression," *Bulletin of Engineering Geology and the Environment*, vol. 78, no. 3, pp. 1427–1442, 2019.

[19] C. Khazaei, J. Hazzard, and R. Chalaturnyk, "Damage quantification of intact rocks using acoustic emission energies recorded during uniaxial compression test and discrete element modeling," *Computers and Geotechnics*, vol. 67, pp. 94–102, 2015.

[20] D. S. B. S. Eberhardt, D. Stead, B. Stimpson, and R. S. Read, "Identifying crack initiation and propagation thresholds in brittle rock," *Canadian Geotechnical Journal*, vol. 35, no. 2, pp. 222–233, 1998.

[21] P. Ganne, A. Vervoort, and M. Wevers, "Quantification of pre-peak brittle damage: correlation between acoustic emission

and observed micro-fracturing," *International Journal of Rock Mechanics and Mining Sciences*, vol. 44, no. 5, pp. 720–729, 2007.

[22] M. Cai, P. K. Kaiser, H. Morioka et al., "FLAC/PFC coupled numerical simulation of AE in large-scale underground excavations," *International Journal of Rock Mechanics and Mining Sciences*, vol. 44, no. 4, pp. 550–564, 2007.

[23] X. G. Zhao, M. Cai, J. Wang, P. F. Li, and L. K. Ma, "Objective determination of crack initiation stress of brittle rocks under compression using ae measurement," *Rock Mechanics and Rock Engineering*, vol. 48, no. 6, pp. 2473–2484, 2015.

[24] L. M. Zhang, S. Q. Ma, M. Y. Ren, S. Q. Jiang, Z. Q. Wang, and J. L. Wang, "Acoustic emission frequency and *b*-value characteristics in rock failure process under various confining pressures," *Chinese Journal of Rock Mechanics and Engineering*, vol. 34, no. 10, pp. 2057–2063, 2015.

[25] C. A. Tang and X. H. Xu, "Evolution and propagation of material defects and Kaiser effect function," *Journal of Seismological Research*, vol. 13, no. 2, pp. 203–213, 1990.

[26] E. Eberhardt, D. Stead, and B. Stimpson, "Quantifying progressive pre-peak brittle fracture damage in rock during uniaxial compression," *International Journal of Rock Mechanics and Mining Sciences*, vol. 36, no. 3, pp. 361–380, 1999.

[27] B. X. Liu, J. L. Huang, Z. Y. Wang, and L. Liu, "Study on damage evolution and acoustic emission character of coal-rock under uniaxial compression," *Chinese Journal of Rock Mechanics and Engineering*, vol. 28, Supplement 1, pp. 3234–3238, 2009.

[28] M. Cai, H. Morioka, P. K. Kaiser et al., "Back-analysis of rock mass strength parameters using AE monitoring data," *International Journal of Rock Mechanics and Mining Sciences*, vol. 44, no. 4, pp. 538–549, 2007.

[29] D. Triantis, "Acoustic emission monitoring of marble specimens under uniaxial compression. Precursor phenomena in the near-failure phase," *Procedia Structural Integrity*, vol. 10, pp. 11–17, 2018.

[30] S. Yang, H. Jing, and S. Wang, "Experimental investigation on the strength, deformability, failure behavior and acoustic emission locations of red sandstone under triaxial compression," *Rock Mechanics and Rock Engineering*, vol. 45, no. 4, pp. 583–606, 2012.

[31] J. Guo, P. Liu, J. Fan, X. Shi, and X. Huang, "Influence of confining pressure unloading rate on the strength characteristics and fracture process of granite using lab tests," *Advances in Materials Science and Engineering*, vol. 2021, Article ID 7925608, 16 pages, 2021.

[32] Q. Yin, R. Liu, H. Jing, H. Su, L. Yu, and L. He, "Experimental study of nonlinear flow behaviors through fractured rock samples after high-temperature exposure," *Rock Mechanics and Rock Engineering*, vol. 52, no. 9, pp. 2963–2983, 2019.

[33] P. Li, X. Li, Z. Guo, L. Ma, and J. Wang, "Variation of strength parameters of Beishan granite under triaxial compression," *Chinese Journal of Rock Mechanics and Engineering*, vol. 36, no. 7, pp. 1599–1610, 2017.

[34] C. D. Su and Z. H. Zhang, "Analysis of plastic deformation and energy property of marble under pseudo-triaxial compression," *Chinese Journal of Rock Mechanics and Engineering*, vol. 27, no. 1, pp. 136–142, 2008.

[35] G. Q. Guo, X. L. Liu, and C. S. Qiao, "Experimental study of mechanical properties and energy mechanism of karst limestone under natural and saturated states," *Chinese Journal of Rock Mechanics and Engineering*, vol. 33, no. 2, pp. 269–308, 2014.

[36] Y. Yang, Y. Ju, F. Li, F. Gao, and H. Sun, "The fractal characteristics and energy mechanism of crack propagation in tight reservoir sandstone subjected to triaxial stresses," *Journal of Natural Gas Science and Engineering*, vol. 32, pp. 415–422, 2016.

[37] N. Li, Y. Zou, S. Zhang et al., "Rock brittleness evaluation based on energy dissipation under triaxial compression," *Journal of Petroleum Science and Engineering*, vol. 183, article 106349, 2019.

[38] T. Shiotani, M. Ohtsu, and K. Ikeda, "Detection and evaluation of AE waves due to rock deformation," *Construction and Building Materials*, vol. 15, no. 5-6, pp. 235–246, 2001.

[39] N. B. Burud and J. M. C. Kishen, "Response based damage assessment using acoustic emission energy for plain concrete," *Construction and Building Materials*, vol. 269, article 121241, 2021.

[40] Z. Moradian, H. H. Einstein, and G. Ballivy, "Detection of cracking levels in brittle rocks by parametric analysis of the acoustic emission signals," *Rock Mechanics and Rock Engineering*, vol. 49, no. 3, pp. 785–800, 2016.

[41] X. Lei and T. Satoh, "Indicators of critical point behavior prior to rock failure inferred from pre- failure damage," *Tectonophysics*, vol. 431, no. 1-4, pp. 97–111, 2007.

[42] K. Zhao, D. Yang, C. Gong, Y. Zhuo, X. Wang, and W. Zhong, "Evaluation of internal microcrack evolution in red sandstone based on time-frequency domain characteristics of acoustic emission signals," *Construction and Building Materials*, vol. 260, article 120435, 2020.

[43] M. C. He, F. Zhao, S. Du, and M. J. Zheng, "Rockburst characteristics based on experimental tests under different unloading rates," *Rock and Soil Mechanics*, vol. 35, no. 10, pp. 2737–2747, 2014.

[44] Z. Zhang, R. Zhang, H. Xie, J. Liu, and P. Were, "Differences in the acoustic emission characteristics of rock salt compared with granite and marble during the damage evolution process," *Environmental Earth Sciences*, vol. 73, no. 11, pp. 6987–6999, 2015.

[45] C. Müller, T. Frühwirt, D. Haase, R. Schlegel, and H. Konietzky, "Modeling deformation and damage of rock salt using the discrete element method," *International Journal of Rock Mechanics and Mining Sciences*, vol. 103, pp. 230–241, 2018.

[46] B. Gutenberg and C. F. Richter, "Frequency of earthquakes in California," *Bulletin of the Seismological Society of America*, vol. 34, no. 4, pp. 185–188, 1994.

[47] X. Chi, K. Yang, and Z. Wei, "Investigation of energy and damage evolutions in rock specimens with large-scale inclined prefabricated cracks by uniaxial compression test and AE monitoring," *Advances in Civil Engineering*, vol. 2020, Article ID 8887543, 12 pages, 2020.

[48] A. Ishibashi, K. Matsuyama, N. Alver, T. Suzuki, and M. Ohtsu, "Round-robin tests on damage evaluation of concrete based on the concept of acoustic emission rates," *Materials and Structures*, vol. 49, no. 7, pp. 2627–2635, 2016.

[49] X. Zhou and J. Zhang, "Damage progression and acoustic emission in brittle failure of granite and sandstone," *International Journal of Rock Mechanics and Mining Sciences*, vol. 143, article 104789, 2021.

Hindawi
Geofluids
Volume 2021, Article ID 1872065, 6 pages
https://doi.org/10.1155/2021/1872065

Research Article

Mechanical Behavior of Frozen Porous Sandstone under Uniaxial Compression

Hong-Ying Wang[1] **and Qiang Zhang**[2]

[1]*School of Transportation Engineering, Jiangsu Vocational Institute of Architectural Technology, Xuzhou 221116, China*
[2]*State Key Laboratory for Geomechanics and Deep Underground Engineering, China University of Mining & Technology, Xuzhou 221116, China*

Correspondence should be addressed to Qiang Zhang; qzhang@cumt.edu.cn

Received 28 June 2021; Accepted 23 August 2021; Published 14 September 2021

Academic Editor: Zetian Zhang

The influence of low temperature on longitudinal wave velocity, uniaxial compression strength, tensile strength, peak strain, secant modulus, and acoustic emission characteristics of yellow sandstones was studied. The results show that the secant modulus increases with decreasing temperature when the axial strain is less than 0.6%, and a contrary influence performs for the subsequent stage due to the fracture of the pore ice. With the decrease in temperature, the uniaxial compression strength first increases and then remains at a relatively constant value of 34.44 MPa at about -40°C while the temperature ranges from -40°C to -70°C. The tensile strength shows an approximate linear increment as the temperature. The peak strain gradually increases with temperature in a three-stage piecewise linear form, and the increasing rate gradually decreases with the decreasing temperature. The phase transformation from liquid water at a temperature of 20°C to solid ice at a temperature of -3°C significantly increases the longitudinal wave velocity from 1.55 km/s to 3.36 km/s. When the temperature is lower than -10°C, the longitudinal wave velocity approximately increases linearly at a rate of 2.67×10^{-3} km /s · °C^{-1} with decreasing temperature.

1. Introduction

The mechanical properties of porous rock mass in a water-rich stratum at subzero temperature are of significance for the construction of highways, artificial freezing in a vertical shaft and metro, and storage and mining in cold regions such as the Tibet Plateau and Xinjiang district [1]. Subzero temperature can induce thermal effects, i.e., phase transition of water and frost heave, which results in significant changes in the mechanical properties of rocks [2]. The mechanical properties are a basic consideration for the design and stability evaluation of engineering. Therefore, the influence of temperature on the mechanical properties of rocks should be thoroughly investigated.

Many achievements have been obtained in the past decades. The experimental results denote that the strength, elastic modulus [3, 4], fracture toughness [5], and accumulative acoustic emission (AE) quantities [6] increase with decreasing temperature. The effects of cyclic loading-unloading [7], explosion [8], and chemical corrosion [9] decrease the strength, elastic modulus, and Poisson's ratio of rock samples. Additionally, the strength and modulus gradually decrease with the increase in frost-thaw cycle times [10–14]. A series of constitutive models have been proposed for frozen sandstone considering the loading ratio effect [7]. Among these studies, the frozen temperature is within -20~20°C according to the standard requirements of the International Society of Rock Mechanics (ISRM), and the red sandstone is widely used with a porosity less than 10% [15]. However, in particle engineering, the environment temperature is much lower than -20°C, and the porosity of rock samples is much larger than 10% [4].

Due to the much lower temperature and higher porosity, the rocks may perform different mechanical behaviors from

the conventional results, which has not been investigated. In this study, the experiments on frozen saturated yellow sandstones with a porosity of 13.08% at a wide range of temperature -70~20°C are conducted to investigate the mechanical behaviors, including compression strength, tensile strength, deformation characteristics, and AE characteristics according to the uniaxial compression test. This study can provide some references for the construction and development of structures in high porosity rocks in very cold regions.

2. Experimental Details

The yellow sandstone blocks with a porosity of 13.08% and a dry density of 2.10 g/cm^{-3} were retrieved from Daban district, Xinjiang, China, where the minimum temperature reaches -41°C. According to the requirements of ISRM, the parallelism was controlled within ±0.05 mm and the surface flatness within ±0.02 mm. Standard cylindrical specimens with a diameter of 50 mm and heights of 100 mm and 25 mm for compression and Brazilian Split tests were prepared. And samples with similar initial longitudinal wave velocity tested using RSM-SY6 were selected. Three rock samples were carried out for the same experimental condition to avoid the random error induced by the discreteness of rock.

The uniaxial compression tests were conducted with the electrohydraulic servocontrolled material testing machine MTS810, and the saturated samples were frozen using the low-temperature furnace MTS615.06 with a rate of -1.0°C/min. Eight temperature levels of 20, -3, -10, -20, -40, -50, -60, and -70°C were selected. When the environment temperature reached the preset value, the temperature was maintained for 30 mins. Then, the uniaxial compression tests were carried out with a loading rate of 0.002 mm/s. During the compression test process, the AE signal was detected and recorded using a DS5-8A.

3. Results and Analysis

3.1. Stress-Strain Behavior. Figure 1 shows the strain-stress curves at various temperatures. The elastic behavior is divided into two stages, i.e., hardening stage and weakening stage, by the inflection point of $\varepsilon_1 = 0.6\%$. For the specimens at a relatively high temperature (i.e., $T > -10°C$), an obvious compaction behavior is observed in the hardening stage. With the decrease in temperature, the compaction behavior becomes unsuspicious instead of an initial approximately linear behavior. For the specimens with $T < -20°C$, the initial elastic modulus increases more significantly than that for $T > -20°C$. When the temperature is lower than -30°C, the strain-stress curve turns from a concave shape to a convex curve. Contrary to the hardening stage, the secant modulus at the weakening stage decreases with the decreasing temperature. A brittle failure occurs with a sudden drop in strength when the peak strength is reached. The vibration in stress-strain behavior due to freezing temperature is mainly induced by the pore frozen ice, which fractures at an axial strain of 0.6% [16].

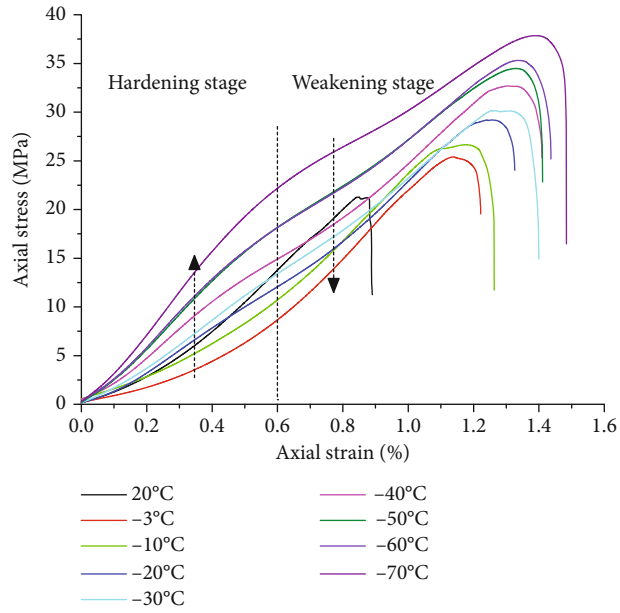

Figure 1: Uniaxial compressive stress-strain curves at various temperatures.

At the initial frozen stage within -3~-10°C, the volume and strength of ice significantly increases. Due to the filling of porous ice, the relative movement of the matrix is constrained, which enhances the whole stiffness and reduces the concentration effect. Thus, with the same axial strain, the potential sample cracks at a lower temperature are less than those at a higher temperature, which leads to the initial enhanced stress-strain behavior, i.e., the hardening stage. Once the strain reaches the critical strain of ice, fracture simultaneously occurs. Due to the enhanced strength for lower temperature frozen rock, the friction coefficient of the fracture surface would be much smaller than that of samples at a higher temperature. Thus, in the weakening stage, the stiffness of the sample at a lower temperature is less than that at a higher temperature.

3.2. Variations in Uniaxial Compression Strength and Tensile Strength. Figure 2 shows the evolutions of uniaxial compressive strength (UCS) and tensile strength with temperature. The UCS gradually increases with the decreasing temperature in a piecewise linear manner as shown in Figure 2(a). When the temperature decreases from 20 to -3°C, the UCS increases from an average value of 20.41 MPa to 23.69 MPa at an increase rate of 16.07%. Then, the UCS increases to 34.01 MPa at an increase rate of 43.56% for specimens subjected to temperatures within -3~-40°C, and the strength increases at an average rate of -0.28 MPa/°C with temperature. This is the same as the strength evolution of ice, which sharply increases within 0~-10°C, then remains as a linear increase at a smaller rate [17]. In fact, the increase in strength is mainly induced by the increasing ice strength. However, a larger volume expansion also induces internal force and potential cracks, if any. Thus, when the temperature is lower than -40°C, potential cracks may form inside the sandstone, which will induce the whole strength. Under

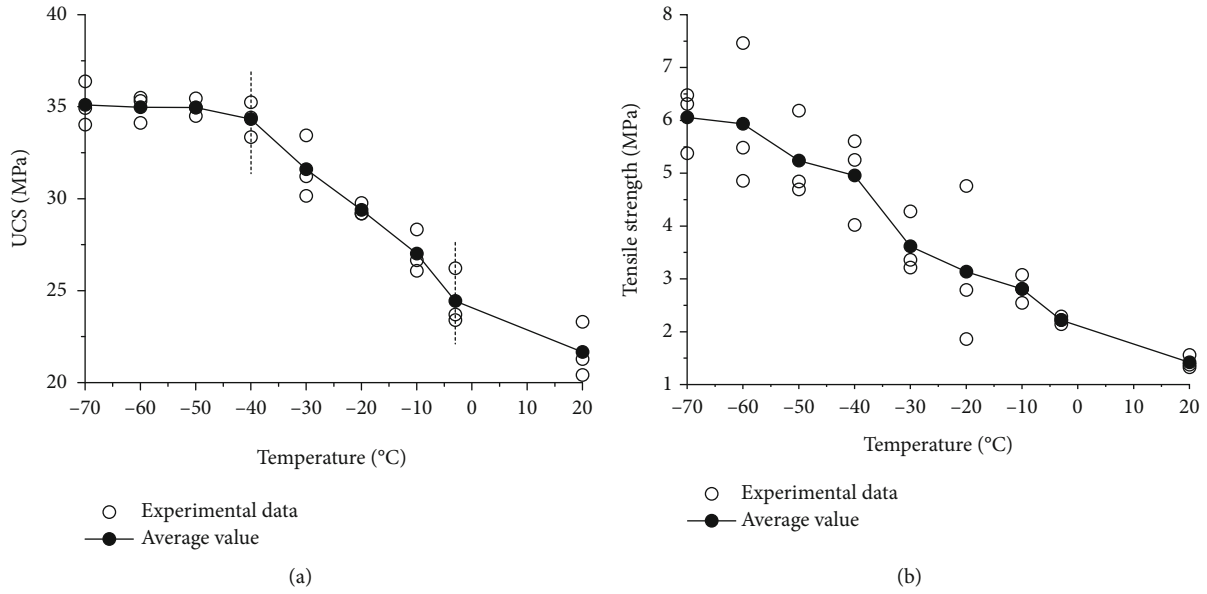

Figure 2: Evolutions of UCS and tensile strength with temperature: (a) UCS and (b) tensile strength.

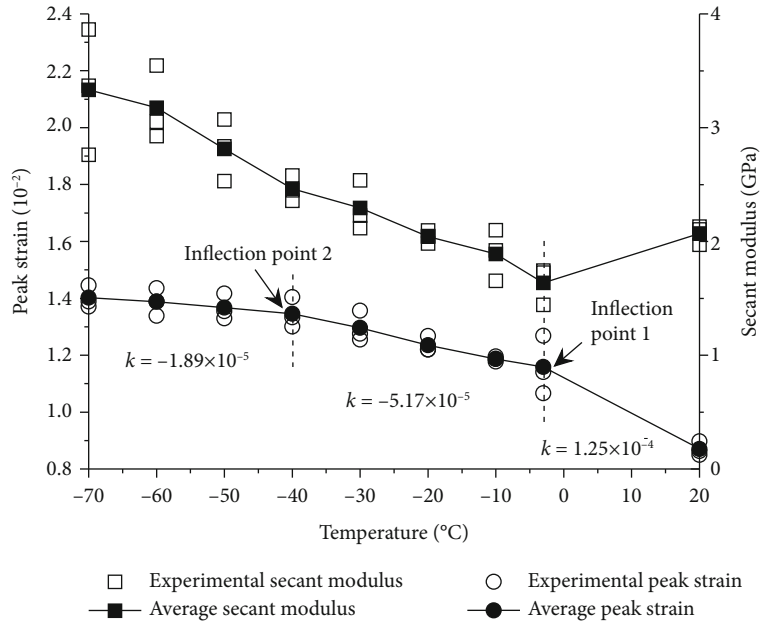

Figure 3: Evolution of peak strain and secant modulus with temperature.

the above two influences, a slight increase in UCS occurs with an average increase of 0.78 MPa for the specimen at -40°C and -70°C, and the mean UCS of specimens within -40~-70°C is 34.44 MPa. Thus, -40°C is the critical temperature, which distinguishes the influence of temperature on the strength of porosity yellow sandstone.

The tensile strength based on the Brazilian test is calculated by the formula as follows:

$$\sigma_t = \frac{2P}{\pi D t}, \tag{1}$$

where σ_t is the tensile strength, P is the peak load, D is the diameter of the disc, and t is the thickness of the disc.

The tensile strength of yellow sandstone samples changes significantly along with the temperature as shown in Figure 2(b). The tensile strength is 1.42 MPa, 2.22 MPa, 4.96 MPa, and 6.06 MPa corresponding to a temperature of 20°C, -3°C, -40°C, and -70°C, respectively, showing an approximate linear increase with the decreasing temperature. For the frozen samples, the average increasing rate of the tensile strength with temperature is 0.07 MPa/°C. However, when the temperature is lower than -40°C, the increasing rate in the tensile strength decreases. The average

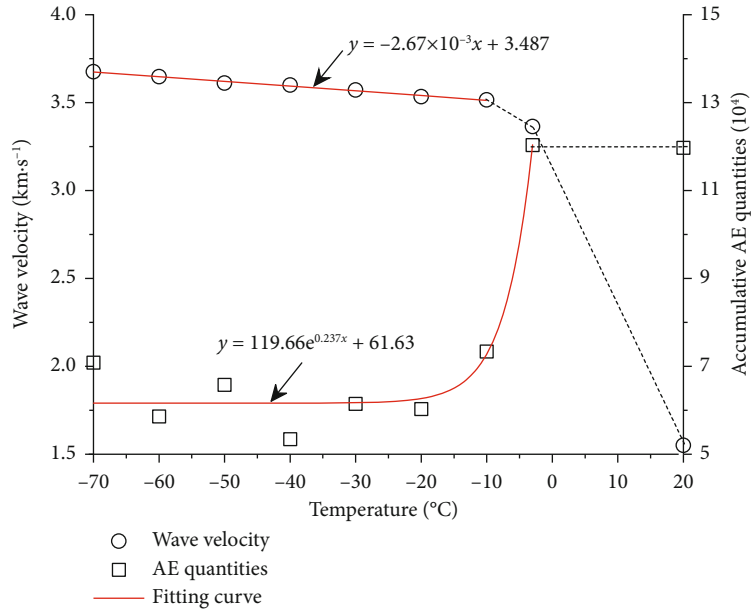

Figure 4: Influence of temperature on longitudinal wave velocity and AE characteristics.

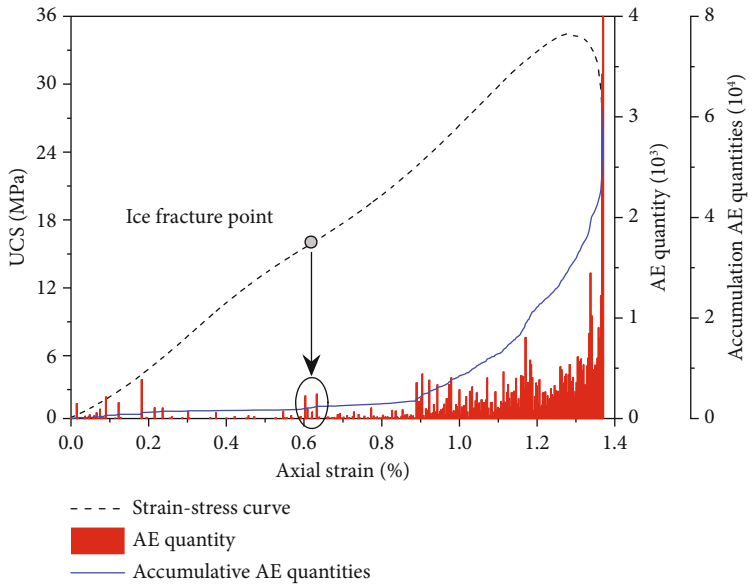

Figure 5: Acoustic emission characteristics of specimen at $T = -30^{\circ}C$.

increasing rate in the tensile strength is only 0.03 MPa/°C for samples within -40°C~-70°C.

3.3. Variations in Peak Strain and Secant Modulus. Figure 3 shows the evolutions of peak strain and secant modulus with temperature. Similar to the evolution of UCS, the peak strain (strain corresponds to the peak strength) gradually increases in a three-stage linear manner as temperature decreases by two inflection temperatures of -3°C and -40°C. When the temperature decreases from 20°C to -3°C, the peak strain increases from an average value of 0.87% to 1.16% with a rate of $-1.25 \times 10^{-4}{}^{\circ}C^{-1}$ with decreasing temperature. For temperatures within -10~-40°C and -40~-70°C, the peak strain decreases to 1.35% and 1.40% with the rates of $-5.17 \times 10^{-4}{}^{\circ}C^{-1}$ and $-1.89 \times 10^{-4}{}^{\circ}C^{-1}$, respectively. This is influenced by pore ice, which constrains the deformation of the rock matrix. A lower temperature corresponds to a larger stiffness of ice and a more significant constriction effect.

The secant modulus performs a two-piecewise characteristic with temperature. When the temperature decreases from 20°C to -3°C, the secant modulus decreases from 2.07 GPa to 1.64 GPa, at a decrease rate of 20.77%. This is mainly induced by the expansion damage during the phase transition of water. However, for the frozen samples, the secant modulus shows an approximate linear increase as the decreasing temperature. When the temperature decreases to -20°C, the secant modulus increases to

2.04 GPa, which approximately equals to that at $T = 20^{\circ}C$. Compared to the secant modulus at $T = -3^{\circ}C$, the secant modulus increases to an average value of 3.33 GPa for the specimen at $T = -70^{\circ}C$, at an increase rate of 103.05% with respect to that at $T = -3^{\circ}C$. The average increasing rate in the secant modulus is 0.025 MPa/°C for subzero temperature specimens.

3.4. Variations in Peak Strain and Secant Modulus. Figure 4 shows the influence of temperature on the longitudinal wave velocity and accumulative AE characteristics. The transformation from liquid water at a temperature of 20°C to solid ice at a temperature of -3°C in the pore of yellow sandstone increases the longitudinal wave velocity from 1.55 km/s to 3.36 km/s. When the temperature further decreases to -10°C, the velocity increases to 3.52 km/s [18] and keeps an average increasing rate of -2.67×10^{-3} km/s · °C^{-1} for the temperatures from -10 to -70°C. Thus, the initial solid stage of water significantly increases the longitudinal wave velocity. With the decrease in temperature when $T < -10^{\circ}C$, the increase in amplitude gradually decreases and remains at approximately a constant value.

During the initial freezing process, the accumulative AE qualities change a little, which increases from 11.97*e*4 to 12.03*e*4. With a further decreasing temperature from -3°C to -70°C, the accumulative AE quantities follow an exponentially decreasing manner with a decreasing decay rate. For specimens at $T = -30^{\circ}C$, the accumulative AE quantities are 6.15*e*4 at a decrease rate of 48.76% corresponding to that at $T = -3^{\circ}C$. Figure 5 shows the typical AE characteristics at $T = -30^{\circ}C$. Obviously, a series of significant AE rings occur at an axial strain of 0.6% corresponding to the ice fracture strain. Before this point, there is a silence period, in which only a few AE rings occur due to the compaction of initial cracks. The AE characteristics subsequently become active, and the AE ring quantity increases robustly after the fracture of ice.

4. Conclusions

A series of uniaxial compression tests and Brazilian tests were carried out at a wide range of temperature within -70~20°C. The results show that the stress-strain curves are divided into two stages by the axial strain of 0.6%, which corresponds to the approximate fracture point of ice. In the initial stage, the second modulus gradually enhances with the decreasing temperature; however, a decreasing modulus performs in the second stage. The uniaxial compressive strength firstly shows a linear increase for temperatures within -3~-40°C at an average rate of -0.28 MPa/°C. Then, the uniaxial compressive strength remains approximately constant value of 34.44 MPa subjected to temperatures within -40~-70°C. With the decreasing temperature, an approximate linear increase in tensile strength is performed. With the decrease in temperature, the peak strain shows a three-stage piecewise increasing characteristic, and the increasing rates of -1.25×10^{-4}°C^{-1}, -5.17×10^{-5}°C^{-1}, and -1.89×10^{-4}°C^{-1} correspond to the temperature ranges of -3~20°C, -20~-40°C, and -70~-40°C, respectively. The phase change from liquid water to solid ice significantly increases the longitudinal wave velocity, and an increasing rate of -2.67×10^{-3} km/s · °C^{-1} remains for specimens at a temperature that is lower than -10°C. The freezing water changes a little in accumulative acoustic emission quantities, and a further exponential decrease occurs for subzero samples.

Data Availability

Anyone who needs the data in the manuscript can contact the corresponding author with email address of qzhang@cumt.edu.cn.

Conflicts of Interest

The authors declare that they have no conflicts of interest.

Acknowledgments

The authors are grateful for the financial support from the National Natural Science Foundation of China (52074269) and China Postdoctoral Science Foundation (2020T130698).

References

[1] A. Kenji and H. Keisuke, "Storage of refrigerated liquefied gases in rock caverns: characteristics of rock under very low temperatures," *Tunnelling and Underground Space Technology*, vol. 5, no. 4, pp. 319–325, 1990.

[2] Y. Inada and K. Yokota, "Some studies of low temperature rock strength," *International Journal of Rock Mechanics and Mining Sciences & Geomechanics Abstracts*, vol. 21, no. 3, pp. 145–153, 1984.

[3] C. Park, J. Synn, H. Shin, D. Cheon, H. Lim, and S. Jeon, "An experimental study on the thermal characteristics of rock at low temperatures," *International Journal of Rock Mechanics and Mining Sciences*, vol. 41, no. 3, pp. 367-368, 2004.

[4] T. Yamabe and K. M. Neaupane, "Determination of some thermo-mechanical properties of Sirahama sandstone under subzero temperature condition," *International Journal of Rock Mechanics and Mining Sciences*, vol. 38, no. 7, pp. 1029–1034, 2001.

[5] N. Matsuoka, "Mechanisms of rock breakdown by frost action: an experimental approach," *Cold Regions Science and Technology*, vol. 17, no. 3, pp. 253–270, 1990.

[6] B. Liu, G. Zhang, W. Xu, and L. Liu, "Acoustic emission characterization of frozen sandstone in uniaxial compression test," in *50th US Rock Mechanics/Geomechanics Symposium*, Houston, Texas, 2016.

[7] N. Li, P. Zhang, W. Chen, and G. Swoboda, "Fatigue properties of cracked, saturated and frozen sandstone samples under cyclic loading," *International Journal of Rock Mechanics and Mining Sciences*, vol. 40, no. 1, pp. 145–150, 2003.

[8] J. Bonner, M. Leidig, C. Sammis, and R. Martin, "Explosion coupling in frozen and unfrozen rock: experimental data collection and analysis," *Bulletin of the Seismological Society of America*, vol. 99, no. 2A, pp. 830–851, 2009.

[9] X. Fang, J. Xu, and P. Wang, "Compressive failure characteristics of yellow sandstone subjected to the coupling effects of

chemical corrosion and repeated freezing and thawing," *Engineering Geology*, vol. 233, pp. 160–171, 2018.

[10] T. Chen, M. Yeung, and N. Mori, "Effect of water saturation on deterioration of welded tuff due to freeze-thaw action," *Cold Regions Science and Technology*, vol. 38, no. 2-3, pp. 127–136, 2004.

[11] W. Chen, X. Tan, H. H. Yu, K. Yuan, and S. Li, "Advance and review on thermo-hydro-mechanical characteristics of rock mass under condition of low temperature and freeze-thaw cycles," *Chinese Journal of Rock Mechanics and Engineering*, vol. 30, no. 7, pp. 1318–1336, 2011.

[12] M. Zhou and G. Meschke, "A multiscale homogenization model for strength predictions of fully and partially frozen soils," *Acta Geotechnica*, vol. 13, no. 1, pp. 175–193, 2018.

[13] M. Zhou and G. Meschke, "Strength homogenization of matrix-inclusion composites using the linear comparison composite approach," *International Journal of Solids and Structures*, vol. 51, no. 1, pp. 259–273, 2014.

[14] E. Liu, Y. Lai, M. Liao, X. Liu, and F. Hou, "Fatigue and damage properties of frozen silty sand samples subjected to cyclic triaxial loading," *Canadian Geotechnical Journal*, vol. 53, no. 12, pp. 1939–1951, 2016.

[15] M. Tang, Z. Wang, Y. Sun, and J. Ba, "Experimental study of mechanical properties of granite under low temperatures," *Chinese Journal of Rock Mechanics and Engineering*, vol. 29, no. 4, pp. 787–794, 2010.

[16] M. Zhang, *Experimental Study on Uniaxial Compressive Strength of Ice and Influence Factors*, Dalian University of Technology, 2012.

[17] D. M. Anderson and W. F. Weeks, "A theoretical analysis of sea-ice strength," *Transactions, American Geophysical Union*, vol. 39, no. 4, pp. 632–640, 1958.

[18] D. Draebing and M. Krautblatter, "P-wave velocity changes in freezing hard low-porosity rocks: a laboratory-based time-average model," *Cryosphere Discussions*, vol. 6, no. 5, pp. 1163–1174, 2012.

Hindawi
Geofluids
Volume 2021, Article ID 1207971, 14 pages
https://doi.org/10.1155/2021/1207971

Research Article

Influence of Clay on Solute Transport in Saturated Homogeneous Mixed Media

Albert Kwame Kwaw[1], **Zhi Dou**[1], **Jinguo Wang**[1], **Yuting Zhang**[1], **Xueyi Zhang**[1], **Wenyuan Zhu**[1] and **Portia Annabelle Opoku**[2,3]

[1]*School of Earth Science and Engineering, Hohai University, Nanjing 210098, China*
[2]*State Key Laboratory of Hydrology-Water Resources and Hydraulic Engineering, Hohai University, Nanjing 210098, China*
[3]*College of Hydrology and Water Resources, Hohai University, Nanjing 210098, China*

Correspondence should be addressed to Zhi Dou; dz.uriah@gmail.com and Jinguo Wang; wang_jinguo@hhu.edu.cn

Received 24 June 2021; Accepted 12 August 2021; Published 25 August 2021

Academic Editor: Richeng Liu

In this study, four homogeneous porous media (HPM1-HPM4), consisting of distinct proportions of sand-sized and clay-sized solid beads, were prepared and used as single fracture infills. Flow and nonreactive solute transport experiments in HPM1-HPM4 under three flow rates were conducted, and the measured breakthrough curves (BTCs) were quantified using conventional advection-dispersion equation (ADE), mobile-immobile model (MIM), and continuous time random walk (CTRW) model with truncated power law transition time distribution. The measured BTCs showed stronger non-Fickian behaviour in HPM2-HPM4 (which had clay) than in HPM1 (which had no clay), implying that clay enhanced the non-Fickian transport. As the fraction of clay increased, the global error of ADE fits also increased, affirming the inefficiency of ADE in capturing the clay-induced non-Fickian behaviour. MIM and CTRW performed better in capturing the non-Fickian behaviour. Nonetheless, CTRW's performance was robust. 12.5% and 25% of clay in HPM2 and HPM3, respectively, decreased the flowing fluid region and increased the solute exchange rate between the flowing and stagnant fluid regions in MIM. For CTRW, the power law exponent (β_{CTRW}) values were 1.96, 1.75, and 1.63 in HPM1-HPM3, respectively, implying enhanced non-Fickian behaviour. However, for HPM4, whose clay fraction was 50%, the β_{CTRW} value was 1.87, implying a deviation in the trend of non-Fickian enhancement with increasing clay fraction. This deviation indicated that non-Fickian behaviour enhancement depended on the fraction of clay present. Moreover, increasing flow rate enhanced the non-Fickian transport based on β_{CTRW}.

1. Introduction

Filled fractures are ubiquitous in the subsurface. Despite the narrow nature of such fractures compared to the size of the host rock, the fracture infills, most often sediments, are regarded as porous media through which fluid flow and solute transport occur. The sediment infills are in different forms ranging from purely sand to complex compositions of sand, silt, and clay. Previous studies have shown that sediments that fill the void spaces in single fractures have significant implications for flow and transport [1, 2]. Despite numerous studies, the role of clay, as a proportion of homogeneous mixed sediment infill, on the transport of solutes in single fractures is poorly understood. Below are extensive researches about the significance of clay on dissolved contaminant transport in natural and engineered systems.

At Sarnia in Ontario, Goodall and Quigley [3] detected pollution fronts beneath two young landfills built on dense silty clay formations. Crooks and Quigley [4] performed laboratory and field studies and compared the results of brine leachate through clay. In these studies, diffusion was identified as the main mechanism responsible for the migration of the dissolved chemical substances through the clays. Apart from diffusion, which is a physical process, clay also attenuates the transport of dissolved contaminants through chemical processes, for example, complexation and adsorption

[5–8], ultimately causing the groundwater cleanup time to be longer than expected [9–11].

To further understand the influence of clay on the contaminant transport behaviour in aquifer systems, researchers have paid much attention to scenarios where clays exist as lenses within aquifers [12, 13] and aquitards around aquifers [9, 14–20] in contact with dissolved plumes. These studies documented that clays occurring as lenses within aquifers and as aquitards near aquifers inhibited the transport of contaminants, yielding comparatively low concentrations of plumes at late times. In the context of groundwater quality, the occurrence of such low concentrations at times longer than expected is a problem and needs critical attention.

Solute transport modelling is essential. Nonetheless, the question of which model can quantify the migration of solutes in porous media remains challenging. The conventional advection-dispersion equation (ADE) model has been proposed to be adequate in modelling solute migration through homogeneous porous media [21]. However, in homogeneous porous media, there exist inherent heterogeneities [22, 23] and this gives breakthrough curves (BTCs) characterised by early arrival times and long late temporal tails. Hence, using the ADE solution to model the travel of solutes in such media may not be sufficient.

A mobile-immobile model (MIM), an improved version of the ADE model, was developed to resolve the nonequilibrium processes causing the anomalous transport behaviour of passive solutes. In the MIM model, long late-time tailing BTCs are ascribed to the trapping of portions of solutes in stagnant fluid regions. The transfer of solute between flowing and stagnant fluid regions is called the physical nonequilibrium process [24, 25]. Even though the MIM model is widely employed to model solute transport through homogeneous porous media [26–28], its validity is questionable in the sense that the transfer of solutes between the flowing and stagnant fluid regions, in reality, is a multiple-rate phenomenon and not a single rate suggested by the MIM model.

To address the issue of anomalous transport, the continuous time random walk framework (CTRW), a type of time nonlocal transport model, has been developed and widely used in modelling solute transport through different porous media. In homogeneous porous media, CTRW has been compared with MIM and/or ADE in many studies. For example, in a sand medium, Levy and Berkowitz [29] observed that the CTRW model performed better than the ADE model in terms of capturing the quick arrival time and long late temporal tailed BTCs. An analogous finding was reported by Cortis et al. [30] when they explored the transport behaviour of a conservative tracer through homogeneous porous media and fitted the observed BTCs with both ADE and CTRW models. Bromly and Hinz [31] conducted repacked sand experiments and discovered that the MIM model could not fit the measured BTCs, especially the long late temporal tails, while the CTRW model did. Zhang and Lv [32] also reported similar diffusive-flux of conservative solute in homogeneous media. Recently, Zaheer et al. [33] conducted solute displacement experiments in clay and documented that the CTRW model performs better in accounting for early breakthrough time and long late temporal tails than the ADE and MIM models. This implies that it is insufficient to use the classical ADE model and its variants to describe the transport behaviour of a solute through homogeneous porous media.

In order to choose a suitable model to quantify the transport of solutes in a sediment-filled fracture, the mechanism driving the solute in that fracture infill must be understood. However, in the case of homogeneous mixed media (with distinct fractions of clay and sand) filling a single fracture, the knowledge of solute transport behaviour is limited. To create well-controlled experimental conditions and have more access to the flow and transport data than in the field, we used an idealised one-dimensional physical model to represent the single fracture. It should be mentioned that the idealised single fracture employed in this study may not be the case in reality since natural filled single fractures have nonuniform apertures with rough surfaces. The objectives of this study are to (i) explore the effect of clay on solute transport characteristics in homogeneous mixed media as a single fracture infill, (ii) find an appropriate transport model that can describe the solute transport behaviour, and (iii) assess how distinct flow rates can impact the solute transport behaviour.

2. Materials and Methods

2.1. Experimental Set-Up and Materials. The experimental set-up (Figure 1) comprised a deionised water tank, a tracer tank, a peristaltic pump (BT101L + YZ15, Lead Fluid, China), flow control valves, connecting tubes, a column, two digital pressure gauges (HD-100G, China), and an automatic effluent collector (SBS-100, Huxi, China). The two tanks were joined to the column through the peristaltic pump using tubes and flow control valves. The peristaltic pump, whose flow control accuracy is ±0.5%, has a head pump flow ranging from 0.006 to 2300 mL/min. Valve A changed the flow from the deionised water tank to the tracer tank to inject the solute and vice versa to flush the column. The column, made of acrylic glass, served as the idealised single fracture. The column was 51 cm in length with an inner diameter and a thickness of 5 cm and 1 cm, respectively, with both ends sealed by flanges and shims to prevent water leakage. Both ends of the column had three metal pipes purposely to get a uniform distribution of flow in the column. The pressure gauge measured the pressure at the inlet and outlet of the column.

To avoid the effect of chemical reaction in the solute transport process, we used synthetic glass beads with no intragranular pore space to represent the porous media. Four homogeneous porous media (HPM1-HPM4), comprising different fractions of sand-sized and clay-sized particles, were prepared and used as single fracture infills. The sand-sized and clay-sized beads were spherical. The estimated hydraulic conductivities of high- and low-permeability beads were 1.94×10^{-2}°cm/s and 3.05×10^{-5}°cm/s. The range of sand and clay particle sizes, the proportions of sand and clay, and the porosity of the porous media are summarised in Table 1. Brilliant Blue FCF, commonly used as a colourant in foods and medications with a maximum optical

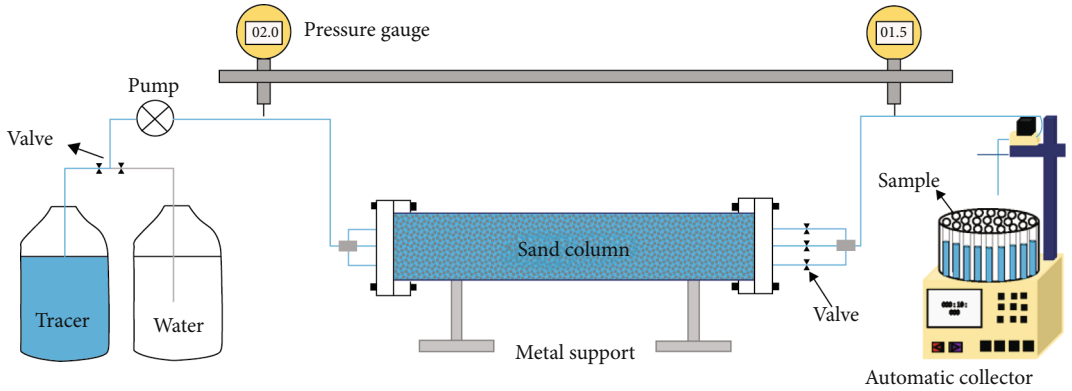

Figure 1: The experimental setup.

Table 1: Porous media properties.

Porous media	Particle size range of sand and clay (mm)	Mass proportions of sand and clay (%)	Porosity (n)
HPM1	0.355-0.5	100	0.368
HPM2	0.355-0.5, 0.071-0.09	87.5 : 12.5	0.316
HPM3	0.355-0.5, 0.071-0.09	75 : 25	0.285
HPM4	0.355-0.5, 0.071-0.09	50 : 50	0.230

absorption wavelength of 630 nm [34], was used as the non-reactive tracer.

2.2. Experimental Procedure. For each column experiment, the beads were washed and soaked in deionised water for 24 h purposely to remove any impurities on the surface of the beads. In filling the column, water was first poured into the column placed in a vertical position followed by the wet beads. Small quantities of the wet beads were poured and pressed firmly with a rod, and this was to obtain dense uniform media. Water was always above the beads throughout the filling, and the reason was to prevent air bubbles in the column. The column was laid horizontally on two metal supports and connected to the feed tanks, pump, and pressure gauges using the tubes and valves. Filters were placed at both ends of the column to prevent the beads from flowing out of the column. Deionised water was injected into the column until steady-state saturated flow was achieved.

An accurate description of a flow field is essential for studying the transport behaviour of solutes in porous media. In this study, flow experiments, with different pump rates (0.48, 0.72, 0.96, 1.20, 1.44, and 1.68 mL/min), were performed. To verify Darcian flow, since the groundwater flow is limited to Darcy's law, the hydraulic gradient (J) and specific discharge ($q = Q/A$) were estimated, where Q and A are the discharge rate (L^3T^{-1}) and inner cross-sectional area (L^2) of the column, respectively. The hydraulic gradient (J) was computed using

$$h = \frac{P}{\rho w g}, \tag{1}$$

$$J = \left(\frac{dh}{l}\right), \tag{2}$$

where h is the hydraulic head, p is the inlet or outlet pressure ($ML^{-1}T^{-2}$), ρ_w is the density of water (ML^{-3}), g denotes the acceleration due to gravity (LT^{-2}), dh is the difference between the inlet and outlet hydraulic heads, and l is the length of the column (L). Out of the six tested pump rates, three (i.e., 0.96, 1.44, and 1.68 mL/min) were used in the solute displacement experiments. Table 2 summarises the discharge rates and average flow velocities for the three pump rates in HPM1-HPM4.

A dimensionless number, Reynolds number (Re), was employed to assess the flow regime in HPM1-HPM4. The Reynolds number is simply a ratio of inertial force to viscous force and is given as

$$\mathrm{Re} = \frac{\rho q d}{\mu}, \tag{3}$$

where ρ, q, d, and μ denote the density of the fluid (ML^{-3}), specific discharge (LT^{-1}), the characteristic length of flow (L), and the dynamic viscosity of the fluid ($ML^{-1}T^{-1}$), respectively. The properties of water at 25°C (i.e., $\rho = 997.04\,kg/m^3$, $\mu = 0.89 \times 10^{-3}$ Pa·s) and $d = 5$ cm were used. In this study, d is the diameter of the column, representing the aperture of the filled single fracture. The aperture of a filled single fracture has also been used in a previous study by Qian et al. [1]. In their study, they documented that using the average grain size as the characteristic length may not be always convenient when the size of grains varies significantly, which was exactly the case in this study. The estimated Re values were less than some values within the range 1 and 10, signifying the Darcian flow regime [21] in HPM1-HPM4 for the six tested pump rates. Only Re values for 0.96, 1.44, and 1.68 mL/min are shown in Table 3. Moreover, the relation between hydraulic gradient and flow velocity was linear with the coefficient of determination (R^2) above 0.990 as shown in Figures 2(a)–2(d). The linear relationship implied Darcian flow in HPM1-HPM4. The verification of Darcian flow regime was done to ensure that there was no chaotic flow phenomenon in the packed media since such flow can

Table 2: Flow conditions in HPM1-HPM4 at 0.96, 1.44, and 1.68 mL/min.

Porous media	Pump rate (mL/min)	Discharge rate Q (mL/min)	Average flow velocity $\bar{v}^*$ (cm/min)
	0.96	0.7995	0.111
HPM1	1.44	1.2991	0.180
	1.68	1.5793	0.219
	0.96	0.8998	0.145
HPM2	1.44	1.3492	0.218
	1.68	1.6189	0.261
	0.96	0.8997	0.161
HPM3	1.44	1.2326	0.220
	1.68	1.4990	0.268
	0.96	0.8496	0.188
HPM4	1.44	1.2492	0.277
	1.68	1.4991	0.332

$\bar{v}^* = Q/\text{An}$, where n and A are the porosity and cross-sectional area of the column, respectively. A is 19.63 cm^2.

Table 3: Estimated Reynolds number (Re) for HPM1-HPM4 at 0.96, 1.44, and 1.68 mL/min.

Pump rate (mL/min)	HPM1 Re	HPM2 Re	HPM3 Re	HPM4 Re
0.96	0.380	0.428	0.428	0.404
1.44	0.618	0.642	0.586	0.594
1.68	0.751	0.770	0.713	0.713

induce a non-Fickian transport behaviour [35] even in homogeneous porous media [36].

After the verification of Darcian flow, a Brilliant Blue FCF solution, with a concentration of 4 mg/L, was injected continuously into the column, representing a step input boundary condition. The tracer injection continued until the effluent concentration was uniform and equivalent to the input concentration (C_0). The 4 mg/L solution was replaced with deionised water for the flushing of the tracer. The tracer injection and flushing were carried out using 0.96, 1.44, and 1.68 mL/min at a constant room temperature of 25°C. At the outlet of the column, effluents were collected in 10 mL-sized glass tubes placed in an automatic part collector (SBS-100, Huxi, China) over the entire period of the experiment. An ultraviolet-visible light spectrophotometer (HACH DR5000) was used to measure the absorbance (Ab) of the effluents at a wavelength of 630 nm. At this wavelength, a concentration above 4 mg/L was not detected by the spectrophotometer, hence the choice of 4 mg/L as the initial concentration in this study. The absorbance (Ab) values were then converted to concentrations (C) using the relation $\text{Ab} = 0.1397C - 0.0006$, with the coefficient of determination (R^2) above 0.999.

3. Inverse Models for Solute Transport

3.1. ADE Model. The ADE model is based on two assumptions. First, the ADE model treats the transition of solute particles as a Markovian process, meaning the present trait of the solute not dependent on its history [37]. Second, the ADE model adopts a Fickian-driven dispersive flux of a solute, with the coefficient of dispersion assumed to be constant in spatial and temporal scales [38]. For one-dimensional nonreactive solute transport through a homogeneous, isotropic, steady flow porous medium, ADE is given by [28]

$$\frac{\partial c}{\partial t} = D_{\text{ADE}} \frac{\partial^2 c}{\partial x^2} - \bar{v} \frac{\partial c}{\partial x}, \tag{4}$$

where C is the solute concentration (ML^{-3}), $\bar{v}$ is the average pore-water velocity (LT^{-1}), and D_x is the coefficient of hydrodynamic dispersion (L^2T^{-1}), t is time (T), and x is a distance (L). The analytical solution of ADE for flux type upstream boundary condition is given as [39]

$$c(x,t) = \frac{c_0}{2} \operatorname{erfc}\left(\frac{x - \bar{v}t}{2\sqrt{D_{\text{ADE}}t}}\right) + c_0 \sqrt{\frac{\bar{v}^2 t}{\pi D_{\text{ADE}}}} \exp\left(\frac{-(x-\bar{v}t)^2}{4D_{\text{ADE}}t}\right) - \frac{c_0}{2}\left(1 + \frac{\bar{v}x}{D_{\text{ADE}}} + \frac{\bar{v}^2 t}{D_{\text{ADE}}}\right) \exp\left(\frac{\bar{v}x}{D_{\text{ADE}}}\right) \operatorname{erfc}\left(\frac{x + \bar{v}t}{2\sqrt{D_{\text{ADE}}t}}\right), \tag{5}$$

where erfc means the complementary error function.

3.2. MIM Model. For the MIM model, which describes the physical nonequilibrium part applied in this study, the transport of a solute plume is modelled on the assumption that the porous media through which the plume migrates and has two different liquid phases: mobile (flowing) and immobile (stagnant). The migration of a solute in the flowing region is driven by an advection-dispersion process, while the immobile region exchanges its solute content with the mobile region through a rate-limited diffusion process and is described as a first-order process [25, 39]. For one-dimensional transport of a solute in the absence of chemical reaction, MIM is given as

$$\theta_m \frac{\partial c_m}{\partial t} + \theta_{im} \frac{\partial c_{im}}{\partial t} = \theta_m D_m \frac{\partial^2 c_m}{\partial x^2} - \theta_m v_m \frac{\partial c_m}{\partial x}, \tag{6}$$

$$\omega(c_m - c_{im}) = \theta_{im} \frac{\partial c_{im}}{\partial t}, \tag{7}$$

where θ_m, θ_{im}, c_m, and c_{im}, respectively, denote the amounts of water and concentration in the flowing and stagnant liquid regions; v_m and D_m, respectively, define the mean flow velocity and coefficient of hydrodynamic dispersion in the flowing fluid region; and ω is the first-order coefficient of mass transfer between the two flowing and stagnant liquid regions (T^{-1}). The flowing liquid fraction is expressed by a dimensionless $\beta = \theta_m/(\theta_m + \theta_{im})$.

3.3. CTRW Model. The idea of CTRW was introduced in electronics to explore transport in semiconductors [40] and later applied in geological media to study solute transport [41]. In porous media, a solute is transported by a fluid in which it dissolves through tortuous paths. This transport process is conceptualised by CTRW as particles randomly

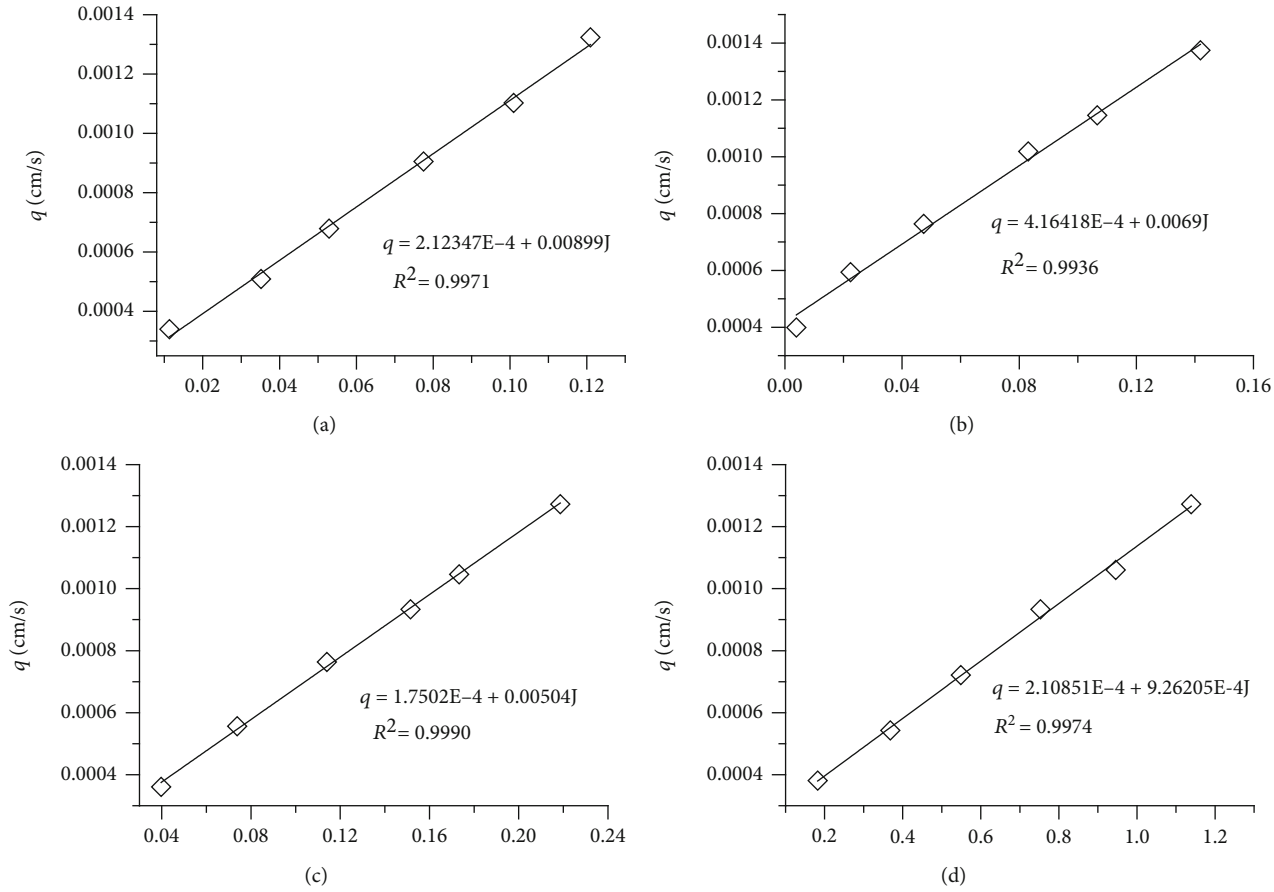

Figure 2: Relationship between hydraulic gradient and specific discharge for HPM1 (a), HPM2 (b), HPM3 (c), and HPM4 (d).

undergoing a series of "hops" and each "hop" is described by a displacement and waiting time. Here, the displacement of the particles is defined by the physical and chemical heterogeneous nature of the media, and the waiting times describe the durations of hopping events. The displacements and the waiting times are independent random variables, and their distributions are governed by a joint probability density function (PDF), represented by $\psi(s,t)$. For simplicity, the PDF is decoupled as $\psi(s,t) = P(s)\,\psi(t)$, where $P(s)$ defines the probability distribution of the distance travelled by the particles between sites and $\psi(t)$ is the probability rate for the transition time to cover the transition displacement [42].

As a solute migrates in porous media, a portion of the solute is held in immobile regions and later diffuses slowly out of the region to produce late temporal tailed BTCs, a mark of non-Fickian behaviour. The capturing of the waiting times of the solute held in the immobile region is the core of the CTRW model. This means that CTRW places more emphasis on the transition time distribution than the transition length since the residence times of fluids and solutes quantify transport in porous media. In this study, the concept of CTRW is summarised and the detail of the importance of waiting time distribution, which the CTRW model is all about, is documented in the publications [7, 43].

Assuming a Gaussian distribution for the transition displacement, the one-dimensional solute concentration defined in Laplace space for a uniform system is expressed as [44]

$$u\tilde{c}(x,u) - c_0(x) = -\tilde{M}(u)\left[v_\psi \frac{\partial}{\partial x}\tilde{c}(x,u) - D_\psi \frac{\partial^2}{\partial x^2}\tilde{c}(x,u)\right], \tag{8}$$

where

$$\tilde{M}(u) \equiv \bar{t}\,u\frac{\tilde{\psi}(u)}{1-\tilde{\psi}(u)}. \tag{9}$$

In the above equations, $\tilde{M}(u)$ is a memory function and is governed by the waiting time distribution [7]. $\tilde{M}(u)$ accounts for undetectable heterogeneities that exist at all scales, and u denotes the Laplace variable. $\tilde{c}(x,u)$ is Laplace transformed ensemble-average, normalised concentration, whereas c_0 and x denote the initial concentration and location in space, respectively. The characteristic time, transport velocity, and generalised coefficient of dispersion are defined by $\bar{t}$, v_ψ, and D_ψ, respectively. The transport velocity, v_ψ, is not equivalent to the average pore velocity, v, as both are reported to be similar in the classical ADE. Likewise, D_ψ is different from D in ADE.

Considering a unit constant flux boundary condition $\tilde{j} = u^{-1}$ at the inlet ($x = 0$) of a finite system of length 1 (i.e., $x = [0, 1]$), a zero concentration gradient boundary condition (i.e., $\partial\tilde{c}/\partial x = 0$) at the outlet ($x = 1$) and initial condition $c_0(x) = 0$, the resident concentration in the Laplace transform is given as

$$\tilde{c}(u,x) \equiv \frac{1}{u}\frac{(w-1)e^{q} + (w+1)e^{r}}{\left[(w+1)\tilde{M}v_{\psi} + 2u\alpha_{\psi}\right]e^{w/\alpha_{\psi}} + \left[(w-1)\tilde{M}v_{\psi} - 2u\alpha_{\psi}\right]}, \tag{10}$$

where

$$w = \sqrt{\frac{1 + \left(4u\alpha_{\psi}\right)}{\left(\tilde{M}v_{\psi}\right)}}, \tag{11}$$

$$q = \frac{[(1+w)x]}{2\alpha_{\psi}}, \tag{12}$$

$$r = \frac{2w - xw}{2\alpha_{\psi}}. \tag{13}$$

The behaviour of solute transport is quantified by the distribution of transition time, which can take on three different expressions, namely, asymptotic, truncated power law, and modified exponential models. In this study, only the truncated power model is discussed. The comprehensive description of the remaining models is documented in a publication by Cortis and Berkowitz [45]. To quantify the temporal regimes of transport in disordered media, characterised by heterogeneity at all scales, the transition time distribution of solute particles is defined by a truncated power law (TPL) [42]:

$$\psi(t) = \left\{t_1\tau_2^{-\beta}\exp\left(\tau_2^{-1}\right)\Gamma\left(-\beta, \tau_2^{-1}\right)\right\}^{-1}\frac{\exp\left(-t/t_2\right)}{\left(1 + t/t_1\right)^{1+\beta}}, \tag{14}$$

which transforms to Fickian behaviour at extended times. In Equation (14), $\tau_2 = t_2/t_1$ and $\Gamma()$ denotes the incomplete Gamma function. t_1 denotes the characteristic median transition time and sets the lower limit for the power law transport behaviour such that $t > t_1$. t_2 is a cutoff time for the truncated power-law transition time distribution function that corresponds to the largest heterogeneity length scale. For the time regime $t_1 \ll t \ll t_2$, $\psi(t)$ behaves in line with power law whereas $\psi(t)$ decreases exponentially for $t \gg t_2$ [42]. To find the memory function, TPL in Laplace transform (Equation (15)) [42] is substituted into Equation (9), with $\bar{t} = t_1$.

$$\tilde{\psi}(u) = (1 + \tau_2 u t_1)^{\beta}\exp\left(t_1 u\right)\frac{\Gamma\left(-\beta, \tau_2^{-1} + t_1 u\right)}{\Gamma\left(-\beta, \tau_2^{-1}\right)}. \tag{15}$$

For the truncated power law transition time distribution, the nature of solute transport (i.e., non-Fickian or Fickian) is dictated by the parameter β, where β is a constant exponent. The value of β is in three ranges, $0 < \beta < 1$, $1 < \beta < 2$, and $\beta > 2$. The nature of transport for the interval $0 < \beta < 1$ is extremely non-Fickian with early and long late-temporal tailed BTCs. For $1 < \beta < 2$, the mean of the plume migrates with steady velocity and yields non-Gaussian-shaped BTCs with long late-time tailings. When $\beta > 2$, the movement of the dissolved chemical species is already Fickian for $t \gg t_1$, and t_2 becomes insignificant in the solute migration process. In this case, the solute plume mass centre migrates with the average fluid velocity and yields a dispersion coefficient that is constant spatially and temporally [42].

3.4. Estimation of Parameters from Measured BTCs. The inverse models of ADE, MIM (from the nonlinear least-squares optimisation software CXTFIT2.0 [39]), and CTRW (from the CTRW Matlab Toolbox v.4.0 [44]), subject to an initial condition, Robin boundary condition at the inlet, and Neumann boundary condition at the outlet,

$$C(x, \cdot\, t = 0) = 0, \tag{16}$$

$$\left(v_x C - D\frac{\partial C}{\partial x}\right)|_{x=0} = v_x C_0, \tag{17}$$

$$\frac{\partial C}{\partial x}|_{x=L} = 0, \tag{18}$$

were fitted to the measured BTCs to obtain the transport parameters: v_{ADE}, D_{ADE} for the ADE model; v_{MIM}, D_{MIM}, β_{MIM}, and ω_{MIM} for the MIM model; and v_{CTRW}, D_{CTRW}, and β_{CTRW} for the CTRW framework. The values of v_{ADE} and D_{ADE} were used as the initial guesses for the CTRW inverse modelling. The choice of the Robin boundary condition at the upstream was based on mass conservation [46]. Besides, the infinite outlet condition applied to the finite system of length L was based on the assumption that the solute concentrations at the upstream were not altered by the downstream boundary [46]. The measured effluent concentrations (C) were normalised by the input concentration (C_0).

To assess the goodness of the fitted models, the coefficient of determination (R^2) and global error (E_j) were computed as

$$R^2 = 1 - \frac{\sum_{i=1}^{N}\left(C_i^o - C_i^f\right)^2}{\sum_{i=1}^{N}\left(C_i^o - \bar{C^o}\right)^2}, \tag{19}$$

$$Ej = \sqrt{\frac{1}{N}\sum_{i=1}^{N}\left(C_i^o - C_i^f\right)^2}, \tag{20}$$

where j is ADE, MIM, or CTRW model; C_i^o and C_i^f denote the observed and fitted tracer concentrations, respectively; $\bar{C^o}$ is the mean of the observed concentrations; and N represents the total number of observed concentrations obtained in a transport experiment.

4. Results and Discussion

4.1. Effect of Clay on Breakthrough Curves. The measured BTCs were analysed to explore the effect of clay on the nature of arrival and elution portions of the measured BTCs. The BTCs measured for HPM1-HPM4 at 1.68 mL/min are shown in Figure 3. The measured BTCs showed a non-Fickian transport behaviour (i.e., early breakthrough and long late temporal tails of the solute plumes). The distinct shaped BTCs, indicating a varying degree of non-Fickian characteristics, were due to microscale heterogeneity induced by the increasing fraction of clay. The poorly or highly interconnected pores created by the clay led to the evolution of high-velocity and low-velocity fluid regions [47].

In HPM1, the BTC was near Gaussian in shape with its elution limb exhibiting a weak late-temporal tail. The result was consistent with previous studies [22, 23, 29] that the transport behaviour of solutes in even uniformly packed porous media will not be Fickian as generally assumed for a classical advection-dispersion equation model. The near Gaussian-shaped BTC could be a result of the narrow distribution of solute advective velocities induced by the uniformly packed spherical-shaped solid grains. Moreover, the weak solute plume tail at late times implied the occurrence of a small diffusion-dominated fluid region. An analogous weak tail characteristic was reported in a recent study by Crevacore et al. [48] who employed a comparable shape of solid particles as the component of the porous medium. Compared to HPM1, the solute transport in HPM2 also displayed a near Gaussian-shaped BTC with a low degree of late temporal tail. However, the solute particles arrived at the measurement plane earlier than observed in HPM1, defining the spatial memory of the medium. This breakthrough time was enhanced by the presence of preferential pathways, characterised by high advective velocities, along which the solute particles migrated quickly with small residence time. The preferential pathways could result from the effect of bridging [29] induced by 12.5% of clay in HPM2.

In contrast, the non-Fickian characteristics (i.e., early breakthrough time and heavy late temporal tail) were more pronounced in HPM3 than in HPM2. The solute particles in HPM2 and HPM3 arrived at the measurement point earlier than that in HPM1. 12.5% and 25% fractions of clay in HPM2 and HPM3, respectively, were not enough to fill all primary pores between the sand particles; meaning, some pores were less filled or not filled at all. The unfilled pore spaces formed connected channels with enhanced hydraulic conductivity. The solute particles migrated along the preferential paths with relatively high velocities, explaining the earlier arrival times of solute in HPM2 and HPM3 compared to that in HPM1. The closeness of arrival times of solute in HPM2 and HPM3 could be attributed to the similarity in their preferential pathways along which the solute particles migrated. An increase in the proportion of clay from 12.5% to 25% in HPM3 did not only yield the earliest solute breakthrough time but also yield a solute elution limb, characterised by a heavy late temporal tail, compared to HPM1 and HPM2. This strong solute plume tailing was due to the increased stagnant fluid region, causing solute mass exchange between the flowing fluid regions. At early times, the stagnant fluid region served as a sink for the solute. The retention of the solute in the stagnant fluid region and subsequent release of held-up solute particles into the flowing fluid region delayed the mixing of the solute [27]. It is worth mentioning that the proportion of clay had a significant impact on the pace at which the solute diffused into and out of the stagnant fluid region.

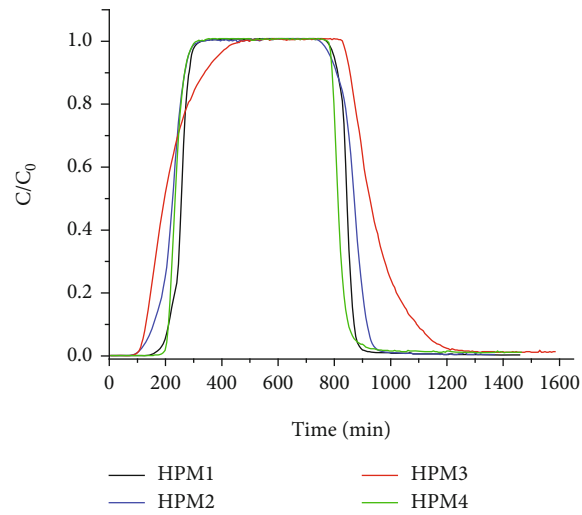

Figure 3: Measured BTCs in HPM1-HPM4 for 1.68 mL/min.

The solute transport in HPM1-HPM3 revealed an interesting trend of non-Fickian characteristics enhancement with an increasing proportion of clay. However, this trend did not continue in HPM4, consisting of equal fractions of sand and clay. The breakthrough time and late-temporal tail characteristics of HPM4 were almost the same as those of HPM1 even though HPM4 contained both sand and clay. Compared to HPM2 and HPM3, 50% of clay in HPM4 was enough to fill the primary pores between the sand particles, yielding well-connected and uniformly distributed pores with less immobile fluid regions. The well-connected and uniformly distributed pores explained the closeness of non-Fickian characteristics in HPM1 and HPM4. Our results indicated that in homogeneous mixed media, comprising sand- and clay-sized particles, the degree of non-Fickian transport of the solute was dependent on the proportion of clay present.

4.2. Inverse Modelling of Measured BTCs. To quantify the effect of clay on the solute transport in the filled single fracture, the BTCs measured in HPM1-HPM4 were analysed and interpreted using the inverse models of ADE, MIM, and CTRW. The representative fits to the BTCs for 1.68 mL/min are shown in Figures 4–7. The coefficient of determination (R^2) and global error (E_j) and the optimised transport parameters are presented in Tables 4 and 5, respectively.

The model of ADE performed relatively poorly in fitting the non-Fickian characteristics of the measured BTCs. In contrast, the models of MIM and CTRW showed a better

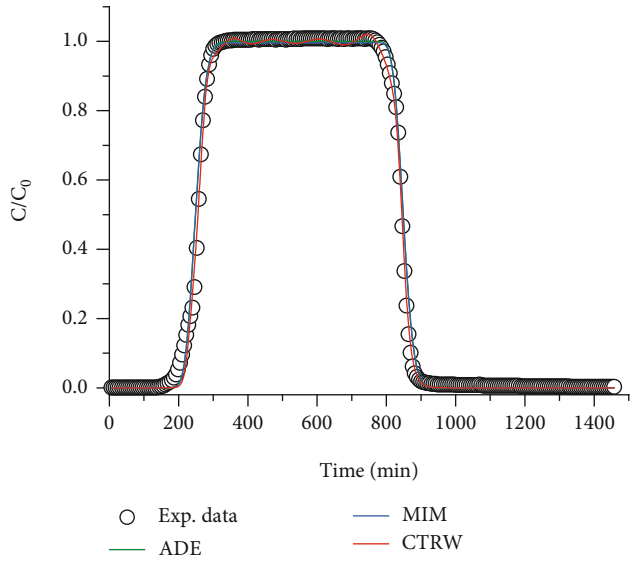

Figure 4: Measured BTCs fitted with the ADE, MIM, and CTRW models for HPM1 at 1.68 mL/min.

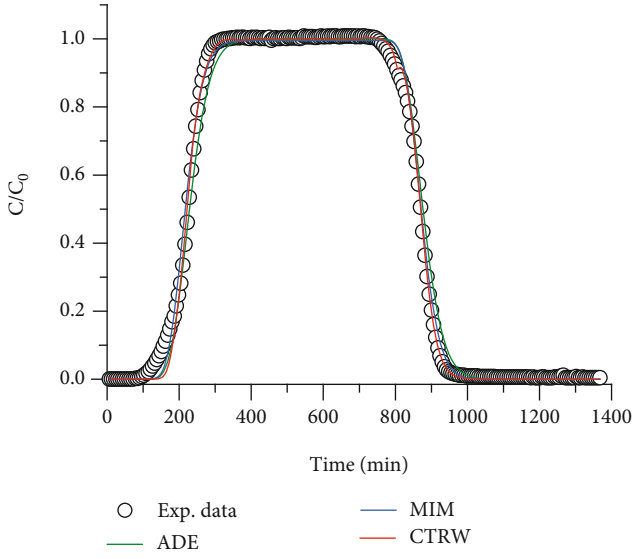

Figure 5: Measured BTCs fitted with the ADE, MIM, and CTRW models for HPM2 at 1.68 mL/min.

performance in describing the measured BTCs, especially early arrival and late temporal tails, than the ADE model. Compared to MIM, the fitted results of CTRW were better than MIM. While CTRW allows multiple rates of waiting times of solute particles, MIM assumes a single rate for all diffusion-driven solute mass exchanges between the mobile and immobile fluid regions, which explains MIM's relatively poor performance as discussed by Gao et al. [49]. According to Gao et al. [49], an alternative reason for the CTRW's best performance was its five fitting parameters, which enhanced the degree of freedom in fitting the measured BTCs compared to the two and four fitting parameters of ADE and MIM models, respectively. The largest and smallest values of coefficient of determination (R^2) and global error (E_j),

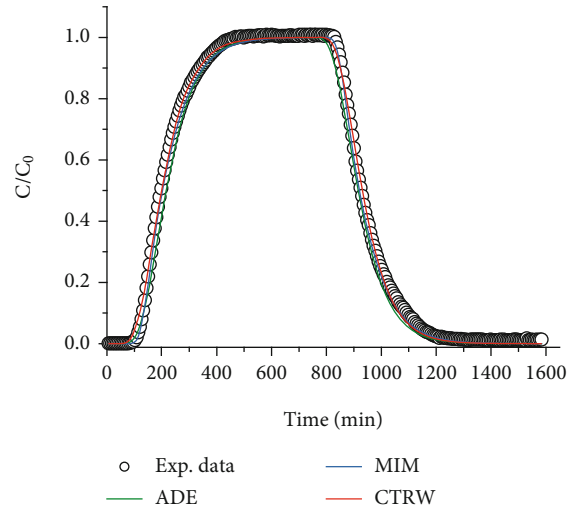

Figure 6: Measured BTCs fitted with the ADE, MIM, and CTRW models for HPM3 at 1.68 mL/min.

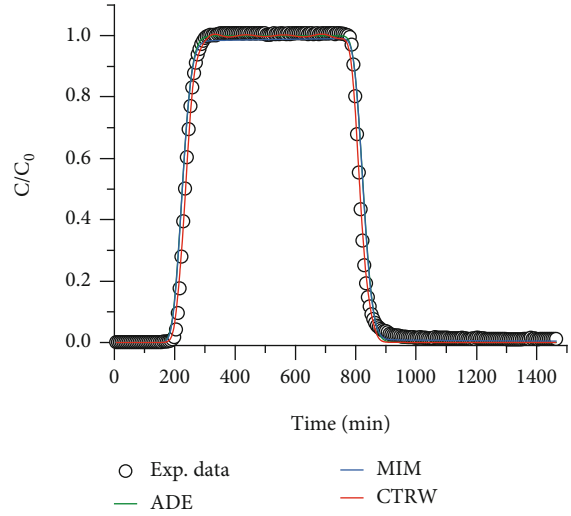

Figure 7: Measured BTCs fitted with the ADE, MIM, and CTRW models for HPM4 at 1.68 mL/min.

Table 4: Coefficient of determination (R^2) and global error (E_j) for assessing the goodness of the fitted ADE, MIM, and CTRW inverse models for 1.68 mL/min.

Porous media	ADE		MIM		CTRW	
	R^2	E_j	R^2	E_j	R^2	E_j
HPM1	0.9967	0.0273	0.9967	0.0272	0.9981	0.0206
HPM2	0.9937	0.0368	0.9971	0.0251	0.9973	0.0240
HPM3	0.9925	0.0374	0.9983	0.0178	0.9987	0.0159
HPM4	0.9910	0.0445	0.9913	0.0437	0.9983	0.0195

respectively, revealed the best performance of the CTRW model as shown in Table 4.

The ADE model produced an increasing global error. Adding 12.5%, 25%, and 50% of clay in HPM2-HPM4 led to increasing global error by 34.8%, 37%, and 63%, respectively. This showed that the classical ADE model could not

Table 5: Estimated parameters for the ADE, MIM, and CTRW models for HPM1-HPM4 at 1.68 mL/min.

Models	Parameters	HPM1	HPM2	HPM3	HPM4
ADE	v_{ADE} (cm/min)	0.204	0.219	0.220	0.225
	D_{ADE} (cm^2/min)	0.0470	0.204	0.852	0.0718
MIM	v_{MIM}(cm/min)	0.173	0.189	0.226	0.212
	D_{MIM} (cm^2/min)	0.0392	0.153	0.177	0.0626
	β_{MIM}	0.849	0.815	0.672	0.9400
	ω_{MIM} (min^{-1})	0.00419	0.00509	1.580	0.0178
CTRW	v_{CTRW} (cm/min)	0.208	0.303	0.365	0.248
	D_{CTRW} (cm^2/min)	0.0479	0.176	1.752	0.0722
	β_{CTRW}	1.96	1.75	1.63	1.87
	t_1 (min)	8.75×10^{-4}	3.86×10^{-3}	5.22×10^{-3}	1.51×10^{-3}
	t_2 (min)	3.42×10^{9}	8.63×10^{6}	1.52×10^{1}	9.53×10^{8}

quantify the characteristics of non-Fickian behaviour as the proportion of clay increased. For HPM1, which had no clay, the errors of the ADE and MIM models were very close with an error difference of 0.0001. However, as clay was considered in an increasing proportion in HPM2-HPM4, the error difference also increased (i.e., 0.0117, 0.0196, and 0.0008, respectively). HPM2 and HPM3 recorded large values, indicating the inefficiency of ADE to capture the enhanced non-Fickian characteristics. The results were consistent with the results by Scheibe et al. [50], who employed ADE and diffusion-driven mobile-immobile mass exchange model to quantify solute transport and found reasonable ADE fits for single particle-sized medium and poorer ADE fits for mixed media. The relatively low errors displayed by the MIM inverse model explained the presence of clay-induced physical nonequilibrium process, which was not accounted for in the classical ADE model.

The difference between the average flow velocities estimated from the flow experiments (Table 2) and the optimised transport velocities of the ADE model (Table 5) widened as the proportion of clay increased, and this could be explained by increasing microscale heterogeneity and the variation in flow velocities induced by the fractions of clay. As the clay was considered in varying fractions, the tortuosity of the porous media was enhanced and led to variable local velocities, which could be the reason for the widening of the difference between the average flow velocities and transport velocities. Moreover, comparing the velocity values obtained from the three inverse models (i.e., v_{ADE}, v_{MIM}, and v_{CTRW}), the v_{CTRW} values were higher. This contrast was expected because the average velocities of solute particles and water molecules in the porous media were not the same [7]. v_{CTRW} described the average solute particle whereas v_{ADE} and v_{MIM} expressed the average water velocity, hence the reason for the contrast.

The dispersion coefficient values (which quantify the spatial extent of solute through spreading) of ADE, MIM, and CTRW, as shown in Table 5, increased with a growing proportion of clay except for equal proportions of clay and sand. An increase in dispersion coefficient values with a growing proportion of clay except for equal proportions of clay and sand could be explained by the tortuosity of the media and a variation in velocity distribution. For HPM1, which contained only spherical sand-sized particles, there was a narrow distribution of local velocities due to less tortuous flow paths. Because the velocity distribution was narrow, the spatial extent of solute through spreading was also narrow, explaining its smaller dispersion coefficient value. 12.5% and 25% of clay in HPM2 and HPM3, respectively, aided in the evolution of more tortuous pathways, producing a wide range of local velocities. As the velocity distribution became broader, the spread of solute through the pores also widened, explaining the larger dispersion coefficient values of HPM2 and HPM3. However, 50% of clay was large to fill the pore spaces between the larger spherical sand-sized particles in HMP4, yielding a well-connected and even distribution of pores (with a narrow velocity distribution). The narrow velocity distribution resulted in less solute spreading, hence the smaller dispersion coefficient value of HMP4 compared to that of HPM2 and HPM3. In all, the dispersion coefficient values of the MIM model were less than those of the ADE model. The dispersion coefficient values of the MIM model only described the spreading of the solute particles in the flowing fluid region, whereas the ADE model merged both solute dispersion in the flowing fluid region and diffusive solute mass exchange between the flowing and stagnant fluid regions, hence the reason for the relatively low dispersion coefficient values of the MIM model. There was a wide range of stagnant fluid regions in the porous media. For HPM1-HPM4, the stagnant fluid regions were 15.1%, 18.5%, 32.8%, and 6%, respectively. An increasing spread of solute was reflected in the enhancement of the early breakthrough of BTCs. According to Dou et al. [51], the optimised dispersion coefficients might not be enough to describe non-Fickian transport since the process of solute spreading only quantifies the early arrival characteristic of BTCs and not the late temporal tail, which is mainly controlled by solute mixing. In other words, the spreading of the solute plume did not necessarily mean the true mixing of the solute plume.

The additional parameters (i.e., β_{MIM} and ω_{MIM}) in diffusion-driven mobile-immobile mass exchange models are not only for improving the degrees of freedom in fitting measured BTCs but also to explain the physical connection between microscale geometrical configuration and diffusion rates of solute mass exchange [52]. Therefore, to further understand the effect of clay fractions on the physical nonequilibrium solute transport that resulted in late temporal tailed BTCs, the optimised values of β_{MIM} and ω_{MIM} were analysed. As presented in Table 5, fitting the measured BTCs with the MIM model revealed a variation in the flowing fluid region β_{MIM}. In HPM1, the value of β_{MIM} was 0.849, which implied that 15.1% of the medium's fluid phase was stagnant. The occurrence of such a stagnant fluid regions was consistent with a previous study by Scheibe et al. [50] who observed trapped solute particles in the intergranular pore spaces in single particle-sized media when the simulated spatial solute distribution was visualised. The addition of clay (i.e., 12.5% and 25%) in HPM2 and HPM3, respectively, further reduced the fraction of the flowing region (β_{MIM}) and increased the fractions of immobile fluid region (1-β_{MIM}) in these two mixed media. For HPM2 and HPM3, the stagnant fluid region increased to 18.5% and 32.8%, respectively. However, for HPM4, which had 50% clay, the fraction of mobile region was 0.940, which implied that 6% of the medium's fluid phase was stagnant. The largest mobile fluid region of HPM4 resulted from well-connected and even distributed pores caused by 50% of clay which filled the primary pore spaces between the sand-sized particles. Compared to 1-β_{MIM} in HPM1, this 6% implied a reduction. The occurrence of stagnant fluid region showed a deviation from the Fickian solute transport behaviour. In addition, the variation in the stagnant fluid region indicated the significance of clay fractions in the development of stagnant fluid regions in mixed media consisting of sand and clay.

The presence of stagnant fluid regions, according to Padilla et al. [27], has a considerable effect on solute mixing in terms of contact areas between flowing and stagnant regions. Therefore, we analysed the interactions between stagnant and flowing fluid regions in terms of solute mass exchange expressed by first-order mass transfer coefficient (ω_{MIM}). In HPM1, which had no clay, the ω_{MIM} value was small, connoting a low diffusion-driven solute mass exchange between the flowing and stagnant fluid regions. The small rate of solute diffusion explained the weak tailed BTC. Because the synthetic glass beads were impermeable [53], the low solute mass exchange resulted from solute particles trapped in potential dead-end pore spaces and narrow pores caused by the packing process [54].

Compared to HPM1, the fraction of clay in HPM2-HPM4 enhanced the trapping of solute particles in the stagnant regions and increased the diffusive solute mass transfer between the flowing and stagnant fluid regions by 21%, 3761%, and 325%, respectively. These percentage increase values implied a higher degree of physical nonequilibrium process (i.e., mass exchange between mobile and immobile fluid regions), which reflected in the heavy late temporal tails, especially in HPM3. The heavy late-temporal tailed BTCs, a typical non-Fickian characteristic, implied an incomplete solute mixing process. The increasing trend of ω_{MIM} values with growing clay fraction in HPM2 and HPM3 created a notion that the larger the clay fraction in mixed media (consisting of sand- and clay-sized particles), the higher the diffusion-driven solute mass transfer between flowing and stagnant fluid regions. However, in HPM4, which had 50% of clay, the ω_{MIM} value was smaller compared to that of HPM3. This could be explained by the relatively less pore-scale heterogeneity in HPM4. An increasing rate of solute mass exchange between the two regions (with clay fraction less than the sand fraction) and a sudden drop in the solute mass transfer rate when both fractions were equal did show not only the significance of clay occurrence but also the importance of its proportion on non-Fickian characteristics enhancement in mixed media.

The study also analysed the non-Fickian behaviour of the solute in HPM1-HPM4, using the remaining optimised parameters (t_1, t_2, and β_{CTRW}) of the CTRW inverse model. The cut-off time values (t_2), which served as a limit of the transition from a power-law model to an exponential model, were large, implying that the solute transport during the entire period of the laboratory experiments was non-Fickian. Moreover, compared to the time scale of the experiments, the characteristic median transition time values (t_1) were small, and therefore, the transition time distribution was controlled mainly by the exponent of the power law (β_{CTRW}). As presented in Table 5, the β_{CTRW} values were in the range $1 < \beta_{CTRW} < 2$, implying a less non-Fickian transport behaviour. In this case, the solute transport velocity was steady, yet the coefficient of dispersion varied with the time scale. Even though the non-Fickian transport was less, the degree of non-Fickian characteristics (i.e., early arrival and late temporal tails) varied in HPM1-HPM4 as shown in Table 5. The variation in the degree of non-Fickian behaviour was due to a wide range of advective velocities and slow diffusion of solute particles into and out of stagnant fluid regions [29, 55, 56] induced by the fractions of clay.

This study has strengthened the understanding that the contribution of clay-induced physical heterogeneity is significant and cannot be neglected in solute transport through mixed media as also suggested by Liu et al. [57].

4.3. Effect of Flow Rate on Solute Transport Behaviour. Since the power law exponent (β_{CTRW}) expresses the nature of solute transport in porous media, the estimated β_{CTRW} values of the CTRW fits to the measured BTCs for 0.96, 1.44, and 1.68 mL/min were employed to assess the impact of flow rate on the solute transport behaviour. Figures 8(a)–8(f) show the measured BTCs fitted with the ADE, MIM, and CTRW models for HPM1 and HPM3. In HPM1, increasing the pump rate (0.96, 1.44, and 1.68 mL/min) yielded the power-law exponent (β_{CTRW}) values of 1.97, 1.974, and 1.96, respectively. The same trend was observed in HPM3. However, the β_{CTRW} values (1.74, 1.71, and 1.63) were smaller than those in HPM1. The closeness of β_{CTRW} values, especially in HPM1, indicated minor heterogeneity created by the flow rates.

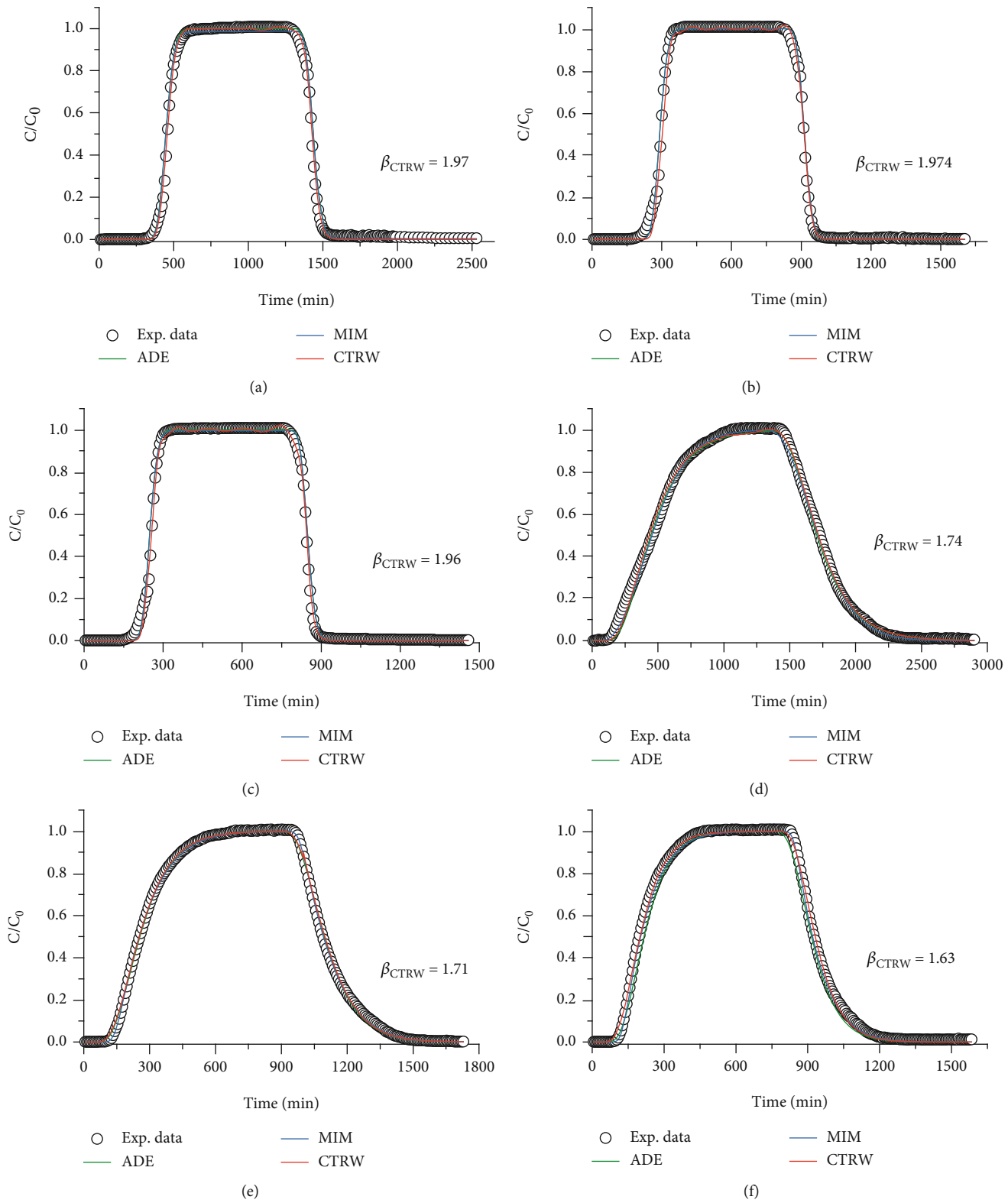

Figure 8: Measured BTCs fitted with the ADE, MIM, and CTRW models for HPM1: 0.96 mL/min (a), 1.44 mL/min (b), and 1.68 mL/min (c), and HPM3: 0.96 mL/min (d), 1.44 mL/min (e), and 1.68 mL/min (f).

For 0.96 mL/min, the β_{CTRW} value in HPM1 was close to the threshold defining the onset of Fickian transport. The reason could be the greater interaction between the advective dominated region and diffusion dominated region, leading to greater solute mixing. As the rate of flow increases, the interaction between the two regions lessens, which amplifies

non-Fickian behaviour [58]. This mechanism could be the reason for the relatively more non-Fickian transport as the flow rate increased, which was consistent with previous studies [29, 56]. The small yet significant distinction in the solute transport behaviour in the porous media at 0.96, 1.44, and 1.68 mL/min indicated the relevance of flow rate in enhancing non-Fickian solute transport, especially in the presence of clay, which was well quantified by the CTRW model with truncated power law transition time distribution.

5. Summary and Conclusions

To explore the influence of clay on solute transport in homogeneous mixed media as a single fracture infill, flow and nonreactive solute transport experiments in HPM1-HPM4 under three flow rates were conducted. The conventional ADE, MIM model, and CTRW framework with truncated power law transition time distribution were fitted to the measured BTCs to quantify the solute transport based on the optimised parameters. Our results allowed the following conclusions to be drawn.

The measured BTCs showed non-Fickian behaviour (i.e., early arrival times and long late temporal tails) in HPM1-HPM4. However, the non-Fickian behaviour was stronger in HPM2-HPM4 (which contained some fractions of clay) than in HPM1 (which contained no clay). This implied that the presence of clay enhanced the non-Fickian transport.

Fitting the classical ADE model to the measured BTCs yielded an increasing global error as the fraction of clay increased in HPM2-HPM4, affirming the inefficiency of classical ADE in capturing clay-induced non-Fickian transport. The models of MIM and CTRW performed better in describing the non-Fickian characteristics. However, CTRW's performance was robust.

Compared to HPM1, 12.5% and 25% of clay in HPM2 and HPM3, respectively, decreased the flowing fluid region and increased the solute transfer rate between the flowing and stagnant fluid regions in the MIM model. In addition, the CTRW model yielded power law exponent (β_{CTRW}) values of 1.96, 1.75, and 1.63 in HPM1-HPM3, respectively, implying enhanced non-Fickian behaviour with increasing clay fraction. However, for HPM4, whose clay fraction was 50%, the β_{CTRW} value was 1.87, indicating a deviation in the trend of non-Fickian enhancement with increasing clay fraction. This deviation showed that the enhancement of non-Fickian characteristics in homogeneous mixed media was dependent on the fraction of clay present.

Moreover, increasing flow rate enhanced the non-Fickian behaviour based on the optimised values of β_{CTRW}.

Our study has presented interesting results about the impact of clay and flow rate on nonreactive solute transport in homogeneous mixed media as an infill of a single fracture, which may be useful in groundwater contamination and remediation.

Data Availability

The data used to support the results of this research are available from the corresponding author upon request.

Conflicts of Interest

The authors declare that they have no conflicts of interest.

Acknowledgments

The study was financially supported by the National Key Research and Development Program of China (No. 2019YFC1804303) and the National Natural Science Foundation of China (Grant Nos. 41877171 and 41831289).

References

[1] J. Z. Qian, Z. Chen, H. B. Zhan, and S. H. Luo, "Solute transport in a filled single fracture under non-Darcian flow," *International Journal of Rock Mechanics and Mining Sciences*, vol. 48, no. 1, pp. 132–140, 2011.

[2] Z. Dou and Z. F. Zhou, "Modelling of solute transport in a filled fracture: effects of heterogeneity of filled medium," *Journal of Hydrodynamics*, vol. 27, no. 1, pp. 85–92, 2015.

[3] D. C. Goodall and R. M. Quigley, "Pollutant migration from two sanitary landfill sites near Sarnia, Ontario," *Canadian Geotechnical Journal*, vol. 14, no. 2, pp. 223–236, 1977.

[4] V. E. Crooks and R. M. Quigley, "Saline leachate migration through clay: a comparative laboratory and field investigation," *Canadian Geotechnical Journal*, vol. 21, no. 2, pp. 349–362, 1984.

[5] R. Haggerty, S. A. McKenna, and L. C. Meigs, "On the late-time behavior of tracer test breakthrough curves," *Water Resources Research*, vol. 36, no. 12, pp. 3467–3479, 2000.

[6] M. Zaheer, Z. Wen, H. Zhan, X. Chen, and M. Jin, "An experimental study on solute transport in one-dimensional clay soil columns," *Geofluids*, vol. 2017, 17 pages, 2017.

[7] B. Berkowitz and E. Zehe, "Surface water and groundwater: unifying conceptualization and quantification of the two water worlds," *Hydrology and Earth System Sciences*, vol. 24, pp. 1831–1858, 2020.

[8] Y. Chen, Z. Zhou, J. Wang, Y. Zhao, and Z. Dou, "Quantification and division of unfrozen water content during the freezing process and the influence of soil properties by low-field nuclear magnetic resonance," *Journal of Hydrology*, vol. 602, 2021.

[9] B. L. Parker, S. W. Chapman, and M. A. Guilbeault, "Plume persistence caused by back diffusion from thin clay layers in a sand aquifer following TCE source-zone hydraulic isolation," *Journal of Contaminant Hydrology*, vol. 102, pp. 86–104, 2008.

[10] M. Maghrebi, I. Jankovic, G. S. Weissmann, L. S. Matott, R. M. Allen-King, and A. J. Rabideau, "Contaminant tailing in highly heterogeneous porous formations: sensitivity on model selection and material properties," *Journal of Hydrology*, vol. 531, pp. 149–160, 2015.

[11] X. You, S. Liu, C. Dai, Y. Guo, G. Zhong, and Y. Duan, "Contaminant occurrence and migration between high- and low-permeability zones in groundwater systems: a review," *Science of The Total Environment*, vol. 743, p. 140703, 2020.

[12] S. W. Chapman, B. L. Parker, T. C. Sale, and L. A. Doner, "Testing high resolution numerical models for analysis of contaminant storage and release from low permeability zones," *Journal of Contaminant Hydrology*, vol. 136–137, pp. 106–116, 2012.

[13] F. Tatti, M. P. Papini, G. Sappa, M. Raboni, F. Arjmand, and P. Viotti, "Contaminant back-diffusion from low-permeability layers as affected by groundwater velocity: a laboratory investigation by box model and image analysis," *Science of The Total Environment*, vol. 622–623, pp. 164–171, 2018.

[14] W. P. Ball, C. Liu, G. Xia, and D. F. Young, "A diffusion-based interpretation of tetrachloroethene and trichloroethene concentration profiles in a groundwater aquitard," *Water Resources Research*, vol. 33, pp. 2741–2757, 1997.

[15] C. Liu and W. Ball, "Back diffusion of chlorinated solvent contaminants from a natural aquitard to a remediated aquifer under well-controlled field conditions: predictions and measurements," *Ground Water*, vol. 40, no. 2, pp. 175–184, 2002.

[16] S. W. Chapman and B. L. Parker, "Plume persistence due to aquitard back diffusion following dense nonaqueous phase liquid source removal or isolation," *Water Resources Research*, vol. 41, pp. 1–16, 2005.

[17] T. C. Sale, J. A. Zimbron, and D. S. Dandy, "Effects of reduced contaminant loading on downgradient water quality in an idealized two-layer granular porous media," *Journal of Contaminant Hydrology*, vol. 102, pp. 72–85, 2008.

[18] A. Rezaei, H. Zhan, and M. Zare, "Impact of thin aquitards on two-dimensional solute transport in an aquifer," *Journal of Contaminant Hydrology*, vol. 152, pp. 117–136, 2013.

[19] M. Yang, M. D. Annable, and J. W. Jawitz, "Solute source depletion control of forward and back diffusion through low-permeability zones," *Journal of Contaminant Hydrology*, vol. 193, pp. 54–62, 2016.

[20] X. You, S. Liu, C. Dai, G. Zhong, Y. Duan, and Y. Tu, "Acceleration and centralization of a back-diffusion process: effects of EDTA-2Na on cadmium migration in high- and low-permeability systems," *Science of The Total Environment*, vol. 706, p. 135708, 2020.

[21] J. Bear, *Dynamics of Fluids in Porous Media*, Dover Publications, Inc., New York, New York, 1972.

[22] F. Hoffman, D. Ronen, and Z. Pearl, "Evaluation of flow characteristics of a sand column using magnetic resonance imaging," *Journal of Contaminant Hydrology*, vol. 22, pp. 95–107, 1996.

[23] S. Oswald, W. Kinzelbach, A. Greiner, and G. Brix, "Observation of flow and transport processes in artificial porous media via magnetic resonance imaging in three dimensions," *Geoderma*, vol. 80, pp. 417–429, 1997.

[24] K. H. Coats and B. D. Smith, "Dead-end pore volume and dispersion in porous media," *Society of Petroleum Engineers Journal*, vol. 4, pp. 73–84, 1964.

[25] M. T. Van Genuchten and P. J. Wierenga, "Mass transfer studies in sorbing porous media I. Analytical solutions," *Soil Science Society of America Journal*, vol. 4, pp. 473–480, 1976.

[26] J. W. Bond and J. P. Wierenga, "Immobile water during solute transport in unsaturated sand columns," *Water Resources Research*, vol. 26, no. 10, pp. 2475–2481, 1990.

[27] I. Y. Padilla, T.-C. J. Yeh, and M. H. Conklin, "The effect of water content on solute transport in unsaturated porous media," *Water Resources Research*, vol. 35, pp. 3303–3313, 1999.

[28] N. Toride, M. Inoue, and F. J. Leij, "Hydrodynamic dispersion in an unsaturated dune sand," *Soil Science Society of America Journal*, vol. 67, p. 703, 2003.

[29] M. Levy and B. Berkowitz, "Measurement and analysis of non-Fickian dispersion in heterogeneous porous media," *Journal of Contaminant Hydrology*, vol. 64, pp. 203–226, 2003.

[30] A. Cortis, Y. Chen, H. Scher, and B. Berkowitz, "Quantitative characterization of pore-scale disorder effects on transport in "homogeneous" granular media," *Physical Review E*, vol. 70, article 041108, 2004.

[31] M. Bromly and C. Hinz, "Non-Fickian transport in homogeneous unsaturated repacked sand," *Water Resources Research*, vol. 40, pp. 1–12, 2004.

[32] X. Zhang and M. Lv, "Persistence of anomalous dispersion in uniform porous media demonstrated by pore-scale simulations," *Water Resources Research*, vol. 43, pp. 1–11, 2007.

[33] M. Zaheer, H. Ullah, S. A. Mashwani, E. U. Haq, S. H. A. Shah, and F. Manzoor, "Solute transport modelling in low-permeability homogeneous and saturated soil media," *Rudarsko-geološko-naftni zbornik*, vol. 36, pp. 25–32, 2021.

[34] M. Yang, M. D. Annable, and J. W. Jawitz, "Light reflection visualization to determine solute diffusion into clays," *Journal of Contaminant Hydrology*, vol. 161, pp. 1–9, 2014.

[35] D. Bolster, Y. Méheust, T. Le Borgne, J. Bouquain, and P. Davy, "Modeling preasymptotic transport in flows with significant inertial and trapping effects - the importance of velocity correlations and a spatial Markov model," *Advances in Water Resources*, vol. 70, pp. 89–103, 2014.

[36] D. R. Lester, G. Metcalfe, and M. G. Trefry, "Anomalous transport and chaotic advection in homogeneous porous media," *Physical Review E*, vol. 90, article 063012, 2014.

[37] J. H. Cushman, *The Physics of Fluids in Hierarchical Porous Media: Angstroms to Miles*, Theory and Applications of Transport in Porous Media, First, Springer Science+ Business Media Dordrecht, 1997.

[38] Y. Xiong, G. Huang, and Q. Huang, "Modeling solute transport in one-dimensional homogeneous and heterogeneous soil columns with continuous time random walk," *Journal of Contaminant Hydrology*, vol. 86, pp. 163–175, 2006.

[39] N. Toride, F. J. Leij, and M. T. van Genuchten, *The CXTFIT Code for Estimating Transport Parameters from Laboratory or Field Tracer Experiments*, vol. 121, Version 2.0. Research Report No. 137, U. S. Department of agriculture, Riverside (CA), 1995.

[40] H. Scher and M. Lax, "Stochastic transport in a disordered solid. II. Impurity conduction," *Physical Review B*, vol. 7, pp. 4502–4519, 1973.

[41] B. Berkowitz, H. Scher, and A. Abstract, "On characterization of anomalous dispersion in porous and fractured media conventional ADE is to make D time dependent," *This approach , to use D (t) to handle the same anomalous dispersion in the conventional and show that the D = D (t) generalizatio*, vol. 31, pp. 1461–1466, 1995.

[42] M. Dentz, A. Cortis, H. Scher, and B. Berkowitz, "Time behavior of solute transport in heterogeneous media: transition from anomalous to normal transport," *Advances in Water Resources*, vol. 27, pp. 155–173, 2004.

[43] Y. Zhang, D. Zhou, M. Yin et al., "Nonlocal transport models for capturing solute transport in one-dimensional sand columns: model review, applicability, limitations and improvement," *Hydrological Processes*, vol. 34, pp. 5104–5122, 2020.

[44] A. Cortis, S. Emmanuel, S. Rubin et al., *The CTRW Matlab toolbox v4.0: A Practical User's Guide*, pp. 1–28, Weizmann Institute of Science, Rehovot, Israel, 2020.

[45] A. Cortis and B. Berkowitz, "Computing "anomalous" contaminant transport in porous media: the CTRW MATLAB toolbox," *Ground Water*, vol. 43, pp. 947–950, 2005.

[46] M. T. van Genuchten and J. C. Parker, "Boundary conditions for displacement experiments through short laboratory soil columns," *Soil Science Society of America Journal*, vol. 48, pp. 703–708, 1984.

[47] B. Bijeljic, P. Mostaghimi, and M. J. Blunt, "Insights into non-Fickian solute transport in carbonates," *Water Resources Research*, vol. 49, pp. 2714–2728, 2013.

[48] E. Crevacore, T. Tosco, R. Sethi, G. Boccardo, and D. L. Marchisio, "Recirculation zones induce non-Fickian transport in three-dimensional periodic porous media," *Physical Review E*, vol. 94, article 053118, 2016.

[49] G. Gao, H. Zhan, S. Feng, G. Huang, and X. Mao, "Comparison of alternative models for simulating anomalous solute transport in a large heterogeneous soil column," *Journal of Hydrology*, vol. 377, pp. 391–404, 2009.

[50] T. D. Scheibe, Z. Hou, B. J. Palmer, and A. M. Tartakovsky, "Pore-scale simulation of intragranular diffusion: effects of incomplete mixing on macroscopic manifestations," *Water Resources Research*, vol. 49, pp. 4277–4294, 2013.

[51] Z. Dou, Z. Chen, Z. Zhou, J. Wang, and Y. Huang, "Influence of eddies on conservative solute transport through a 2D single self-affine fracture," *International Journal of Heat and Mass Transfer*, vol. 121, pp. 597–606, 2018.

[52] P. Gouze, Y. Melean, T. Le Borgne, M. Dentz, and J. Carrera, "Non-Fickian dispersion in porous media explained by heterogeneous microscale matrix diffusion," *Water Resources Research*, vol. 44, pp. 1–19, 2008.

[53] R. D. Swanson, A. Binley, K. Keating et al., "Anomalous solute transport in saturated porous media: relating transport model parameters to electrical and nuclear magnetic resonance properties," *Water Resources Research*, vol. 51, pp. 1264–1283, 2015.

[54] J. Bear and A. H.-D. Cheng, *Modeling Groundwater Flow and Contaminant Transport*, Springer Science & Business Media, 2010.

[55] B. Berkowitz, A. Cortis, M. Dentz, and H. Scher, "Modeling non-Fickian transport in geological formations as a continuous time random walk," *Reviews of Geophysics*, vol. 44, article RG2003, 2006.

[56] B. Berkowitz and H. Scher, "Exploring the nature of non-Fickian transport in laboratory experiments," *Advances in Water Resources*, vol. 32, pp. 750–755, 2009.

[57] D. Liu, A. P. Jivkov, L. Wang, G. Si, and J. Yu, "Non-Fickian dispersive transport of strontium in laboratory-scale columns: modelling and evaluation," *Journal of Hydrology*, vol. 549, pp. 1–11, 2017.

[58] A. Nissan, I. Dror, and B. Berkowitz, "Time-dependent velocity-field controls on anomalous chemical transport in porous media," *Water Resources Research*, vol. 53, pp. 3760–3769, 2017.

Hindawi
Geofluids
Volume 2021, Article ID 4901231, 17 pages
https://doi.org/10.1155/2021/4901231

Research Article

Exploring the Effect of Asperity Order on Mechanical Character of Joint Specimen from the Perspective of Damage

Zhouhao Yuan,[1] **Yicheng Ye**,[1,2] **and Binyu Luo**[1]

[1]*School of Resources and Environmental Engineering, Wuhan University of Science and Technology, Wuhan 430081, China*
[2]*Industrial Safety Engineering Technology Research Center of Hubei Province, Wuhan 430081, China*

Correspondence should be addressed to Binyu Luo; binyul@126.com

Received 22 May 2021; Accepted 16 July 2021; Published 16 August 2021

Academic Editor: Na Huang

The joint morphology is multiscale. The effect of each asperity order on the mechanical properties of joints is different. The shear mechanical properties of joint specimens are related to its surface damage characteristics. At present, there are still few studies on the effect of roughness on the shearing mechanical properties of joint from the perspective of damage of each asperity order. In this paper, the standard roughness profile was chosen as initial morphology. The standard roughness profile was decomposed into waviness and unevenness by the method combine the ensemble empirical mode decomposition (EEMD) and the cut-off criterion. Then, the joint specimen which contains waviness and unevenness and the specimen which only contains waviness were prepared by the 3D engraving technology. The 40 sets of joint specimens with different asperity order were subjected to direct shear tests under different normal stresses. Based on the 3D scanning technology and ICP iterative method, the damaged area and the damage volume were calculated. Based on the damage volume data and the acoustic emission (AE) data, the effect of asperity order to the joint mechanical behaviour was studied. The results indicate that (1) under low normal stress, the unevenness plays a control role in the failure mode of the joint specimen. Under low normal stress, the joint surface containing only waviness exhibits slip failure, and the joint surface with unevenness exhibits shear failure. With the increase of the normal stress, the failure mode of the specimen containing only waviness changes from slip failure to shear failure; (2) the unevenness controls the damage degree of the joint specimen. The damaged area, damage volume, AE energy rate, and accumulative AE energy of the joint specimen with unevenness are larger than those of the specimen with only waviness, and this difference increases with the normal stress increase; (3) the difference between the joint specimen with unevenness and specimen with only waviness mainly exists in the prepeak nonlinear stage and the postpeak softening stage. The characteristic parameters of acoustic emission generated in the postpeak softening stage of the joint specimen with unevenness are greater than those of the specimen with only waviness. This phenomenon can be used to explain the stress drop difference at the postpeak softening stage; (4) the AE b value can be used to evaluate the damage of joint specimens. Analysing the damage difference of each asperity order under different normal stresses is of great significance to the analysis of the influence of the morphology of the joint surface on the mechanical properties of the joint.

1. Introduction

The rock mass contains a large number of weak planes, such as rock joints, bedding planes, and fractures, caused by underground excavations and geothermal energy reservoir production [1–4]. The stability of the rock mass was controlled by the shear strength of these weak planes [5]. The shear strength of the rock joint was influenced by many parameters, such as normal stress, uniaxial stress, surface asperity, and joint match ratio. Among these parameters, the surface asperity is highly crucial [6–8].

The surface asperity is multiscale [9]. According to its geometric characteristic, the surface can be divided into primary asperity (waviness) and secondary asperity (unevenness). Patton [10] found that the effect of waviness and unevenness to the shear behaviour is different at first. In order to further explore their influence on the shear behaviour of the joint specimen, further shear tests were conducted

on the joint specimen. It is concluded that when the normal stress is low, the unevenness plays a key role in the shear behaviour; on the contrary, the waviness plays a control role in the shear behaviour of the joint specimen[11–15]. However, the research object of the abovementioned research is the joint specimen that contains both waviness and unevenness. In order to understand the influence of the waviness and unevenness on the shear behaviour of the joint specimens, it is necessary to decompose the joint surface into waviness and unevenness for analysis.

There are many ways to decompose the joint surface into waviness and unevenness, such as the Fourier series method [16–18], Gaussian filter method [19], different sampling interval method [20, 21], and wavelet analysis method [22–26]. The above methods have their own advantage and disadvantage it is still not known which one is the best up to now. Yang et al. [17, 18] identify the waviness and the unevenness of the joint surface by visual comparison. Jiang et al. [19] and Hong et al. [27] used the cut-off wavelength to distinguish the waviness and unevenness. Zou et al. [23], Wang et al. [24], Gui et al. [25], and Li et al. [26] proposed a critical cut-off level by the variance of the approximate component and think that, the critical decomposition is achieved when the standard deviation of the approximate component drops significantly. It is also proposed that the unevenness of the joint surface should obey the Gaussian distribution, and its distribution can be checked by the Shapiro-Wilk test method. At the same time, there is no unified criterion for the critical decomposition level of waviness and unevenness. Therefore, further research is needed in the decomposition method and critical decomposition level.

Yang et al. [18] reconstruct the joint surface containing the waviness and unevenness and the surface only containing the waviness by the Fourier series method and found that the waviness plays a control role in the normal displacement during the shear process. Hong et al. [28] divide the joint surface into waviness and unevenness by the Gaussian filtering method and then explore their mechanical contribution to the shear strength of the joint specimen under low normal stress and believed that identifying the degradation of the unevenness is important for evaluating the contribution of the waviness and unevenness to the peak shear strength. Yang et al. [18] proposed that there has a direct relationship between the damaged area caused by shearing and the shear strength under low normal stress. So the damage height of the joint specimen will affect the mechanical behaviour of the joint specimen. However, Yang et al. [18] and Hong et al. [28] analysed the damage of the joint specimen from two-dimensional rather than three-dimensional to capture the asperity damage.

The damaged area and damage volume of the joint surface can only reflect the damage ratio at the end of the shear test, and it is difficult to reflect the damage evolution process during the shearing process [29, 30]. Acoustic emission technology is widely used to study the damage of joint specimen during shear [31]. Zhou et al. [32] analysed the change rule of acoustic emission signal during the shear process and proposed that the changing law of AE events and energy rate was greatly affected by the roughness and normal stress. Moradian et al. [33] used acoustic emission technology to analyse the damage evolution during shear and found that joint specimen with more unevenness produced more AE energy. Meng et al. [34] analysed the acoustic emission signals of the joint specimen with different lithologies (granite, marble, cement, and similar materials) under different conditions (normal stress, shear rate) and proposed that the shear damage can be characterized by acoustic emission parameters (cumulative energy and cumulative events). Chen et al. [35] used 3D scan technology to quantify the shear damage volume and monitored the acoustic emission energy during the shear and then established the relationship between joint specimen damage volume and acoustic emission energy.

In summary, the asperity order shows an important effect on the shear behaviour of the joint specimen, which is mainly reflected in the contribution difference of the waviness and unevenness to mechanical characteristics of rock joints. It can be indicated that the damaged area is one of the factors affecting the shear strength of the joint specimen. However, current understanding about the impact of the asperity order on the damage degree of the joint specimen is still insufficient, and further research is needed to quantify the difference in the damage degree caused by the asperity order. Besides, the standard roughness profile was chosen as initial joint morphology, and the standard roughness profile was digitized by the gray-scale image processing method and decomposed into the waviness and unevenness by the method which combines the EEMD and cut-off level criterion. Six standard roughness profiles ($6^{\#}$~$10^{\#}$ standard profile) and their decomposed waviness component were chosen as the engraving path to prepare the joint specimen, and shear tests under different normal stresses were carried out. The acoustic emission system was used to monitor the damage of the joint specimen during shearing. The 3D scanning and ICP iteration method were used to quantify the damaged area and damage volume of the joint specimen; finally, the acoustic emission parameter AE-*b* value was used to characterize the influence of the asperity order on the damage of the joint specimen.

2. Test Method

2.1. Standard Roughness Profile Decomposition

2.1.1. The Method for Decomposition Standard Roughness Profile. In this paper, the standard roughness profile (Figure 1(a)) was chosen as the initial morphology and digitized by the gray-scale image processing method [36]. Then, the digitizing data was utilized to reconstruct the standard roughness profile in the origin software (Figure 1(b)). It can be found that the standard roughness profile and the reconstructed profile were similar by visual comparison.

The joint profile can be regarded as stationary signal patterns [37]. And the profile can be treated as the superposition of a series of simple sine and cosine waves. The ensemble empirical mode decomposition (EEMD) [38], as a mathematical method, has been widely used in signal processing. Thus, the EEMD can be used to decompose

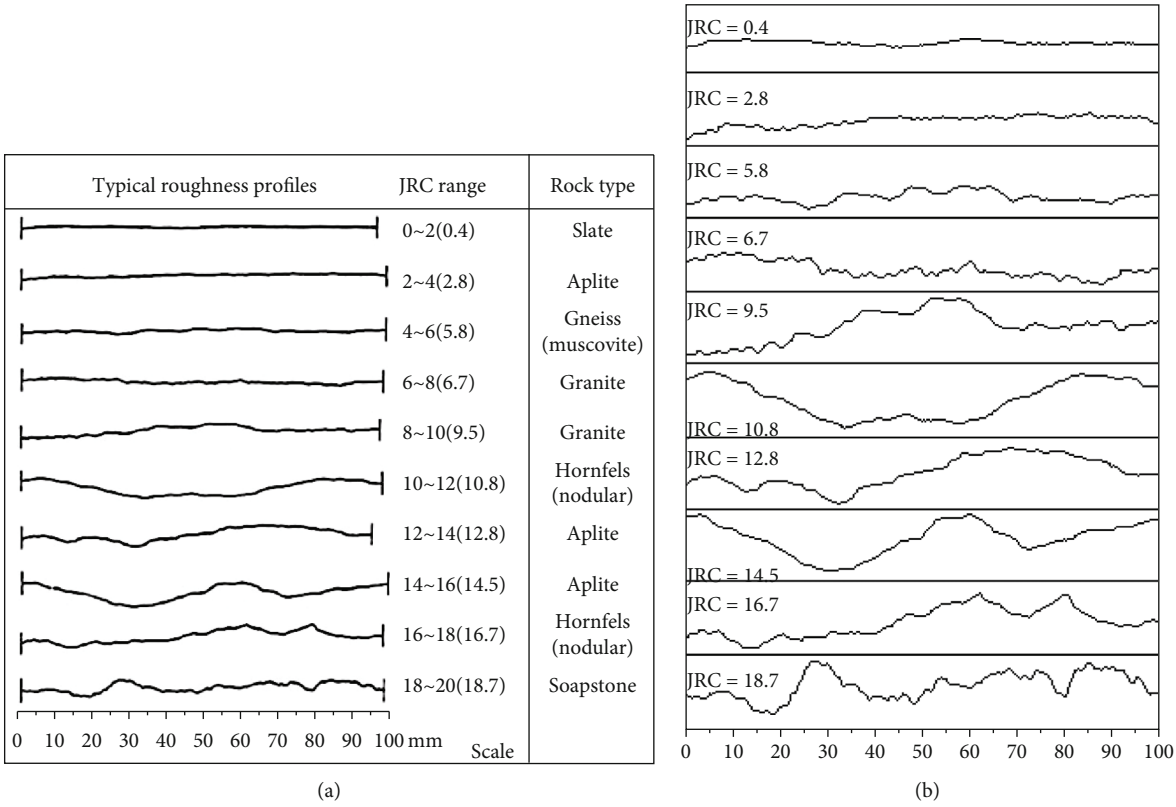

Figure 1: (a) The picture from Barton. (b) The picture reconstructed by the gray-scale image method.

the joint profile. The empirical mode decomposition (EMD) also can be used in signal processing. Unfortunately, the mode mixing will appear when using the EMD in signal processing. However, the EEMD can avoid the mode mixing by add white noise series in the corresponding IMFs. And the additional white noise series can erase each other in the final mean of the corresponding IMFs. The IMFs will stay within the natural dyadic filter windows, and this way can reduce the probability of mode mixing significantly and preserve the dyadic property. The proposed EEMD is developed as follows [39]: (1) add a white noise series to the target data, (2) decompose the data with added white noise into IMFs, (3) repeat steps 1 and 2 but with different white noise series, and (4) obtain the (ensemble) means of corresponding IMFs of the decompositions as the final result.

Like wavelet analysis [23], EEMD only decomposes the signal into approximate and detailed components. In order to decompose the standard roughness into primary asperity (waviness) and secondary asperity (unevenness), the cut-off level criterion with a clear mathematical definition is still needed. According to the description by the International Society of Rock Mechanics and Rock Engineering (ISRM), the waviness is defined by the dominating and large-scale overall wavy surface undulation to reflect the macroscopic fluctuations of the surface morphology, and the unevenness is defined by the generally randomly distributed small-scale unevenness. When the decomposition level is low, as the decomposition level increased, the approximate component became closer and closer to the macroscopic fluctuation in the standard roughness profile. And the approximate component is still similar to the standard roughness profile. However, when the decomposition level exceeded a certain level, part of the macroscopic fluctuation features was extracted as detailed components, and the similarity between the approximate component and the standard roughness profile declined rapidly, so the similarity can be chosen as a criterion to determine the cut-off level. In this paper, cosine similarity is used to judge the similarity between the approximate components and the original standard roughness profile because the unevenness can be regarded as a nonstationary random process following the Gaussian distribution [40]. In this study, the Kolmogorov-Smirnov (K-S) test [41] was chosen to verify the distribution of the unevenness.

2.1.2. The Decomposition Result of the Standard Roughness Profile. Combining the EEMD and the cut-off level criterion, the waviness and unevenness can be decomposed from the standard roughness profile, as shown in Figure 2. It can be seen that the waviness is characterized by large amplitude and low frequency, which can reflect the macroscopic fluctuation of the standard roughness profile, and the unevenness is characterized by small amplitude and high frequency. The characteristics of the waviness and the unevenness correspond to the qualitative description given by the ISRM, which means that the method which combines the EEMD and the cut-off level criterion can be used to decompose the standard roughness profile.

2.2. Joint Specimen Preparation and Test Plan. Considering the difficulty by the traditional way, such as tensile fracture,

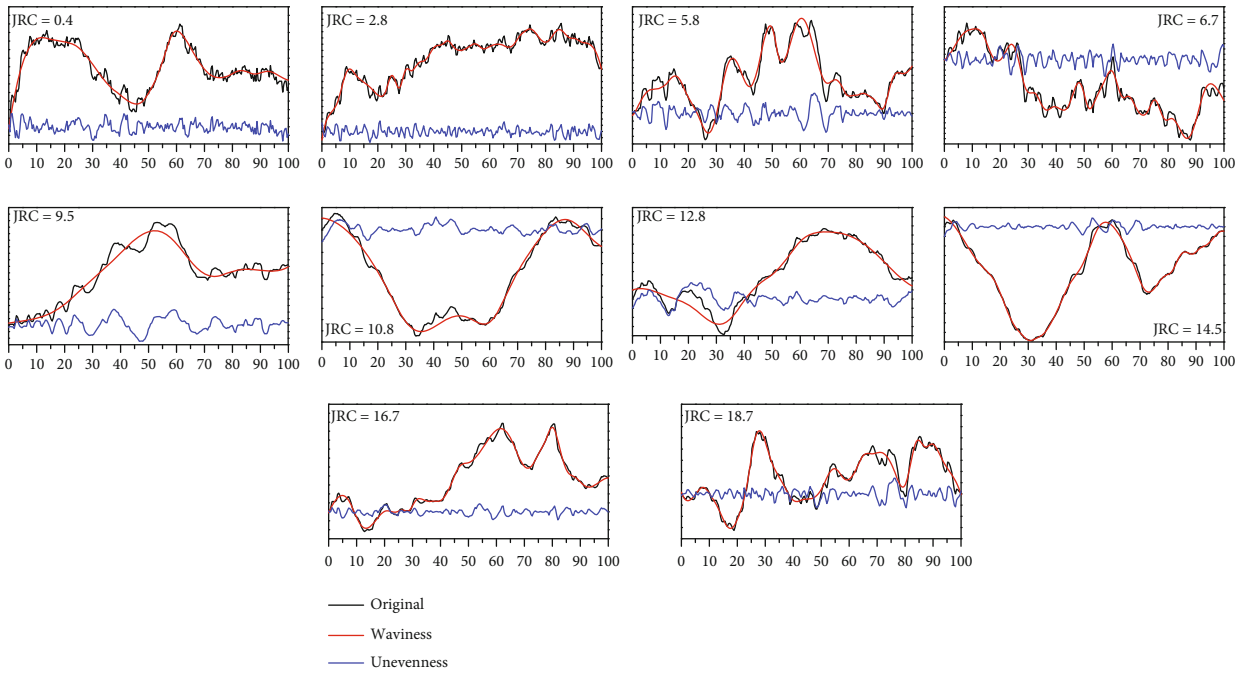

Figure 2: The decomposition result of the standard roughness profile.

saw flat joint with undulating or irregular surface, and silicon cast of the natural or stylized joint to produce large number of joint specimens with the same morphology, the 3D rigid engraving method [42, 43] was proposed in this study; this method can prepare a large number of joint specimens with the same morphology by rock material. Based on the digitized profile, the joint specimen containing standard roughness profile and the specimen containing only waviness were sculpted by the digital-control engraving machine (MK-6060). As shown in Figure 3, this machine is composed of the computer control system, spindle, operating table, cooling water circulation system, and milling cutter. The positioning accuracy of the spindle of this equipment is 0.1 mm. In order to ensure the accuracy of the joint surface, the distance between the engraving paths is set to 0.2 mm, and the diameter of the cutter head is 0.4 mm in this study.

The engraving process can be divided into 4 steps, just as shown in Figure 4.

$5^{\#}$~$10^{\#}$ standard roughness profile was chosen as initial surface morphology in this study. A total of 40 sets of joint specimens were prepared with the same raw material (red sandstone) whose mechanical parameter is shown in Table 1. Among these specimens, there are two types of specimen including only the waviness and specimen including the waviness and the unevenness.

A total of 40 sets of the joint specimen were subjected to the compression shear test, and the test plan is shown in Table 2. Three normal stresses (0.0125UCS, 0.05UCS, and 0.1UCS) were applied to the joint specimen which initial roughness coefficients equal to 9.5, 14.5, 16.7, and 18.7.Four normal stresses (0.0125UCS, 0.05UCS, 0.1UCS, and 0.2UCS) were subjected to the joint specimen which initial roughness coefficients equal to 10.8 and 12.8. In this study, the normal stress whose ratio to the uniaxial compressive strength is not more than 0.2 is regarded as low normal stress.

2.3. Test Procedure

2.3.1. Direct Shear Apparatus. The YZW-30A microcomputer-controlled electronic rock direct shear apparatus was adopted in this study. its maximum axial (tangential) load is 250 kN, and the load way includes displacement control and stress control, as shown in Figure 5(a). Thet loading process can be divided into two steps, normal stress loading and shear stress loading. At the normal stress loading process, the load rate is 0.3 mm/min. When the normal stress reaches the target value, the shear stress loading starts with a load rate of 0.3 mm/min until the shear displacement reaches 8 mm. Both normal stress loading and shear stress loading methods are displacement control methods.

2.3.2. Acoustic Emission Monitoring System. The acoustic emission monitoring system (Express-8, PAC) was used to monitor the damage during the whole shear process, as shown in Figure 5(b). It consists of an 8-channel acoustic emission signal acquisition system (Express-8), 4 preamplifiers (Figure 5(b), 2), 4 sensors (Figure 5(b), 3), and an acoustic emission signal processing system (AEWin). The AE sensors have a resonant frequency of 140 kHz and operating frequency range from 125 to 400 kHz. In order to eliminate the influence of noise generated by the test apparatus, the threshold was set to be 40 dB. The data acquisition frequency was set as 5 MHz. Four sensors were adhered on the lower part of the joint specimen. The distance between the probe and the bottom of the sample is about 35 mm, and the distance from the left and right sides of the joint specimen was both 10 mm, respectively, and the position can be seen in

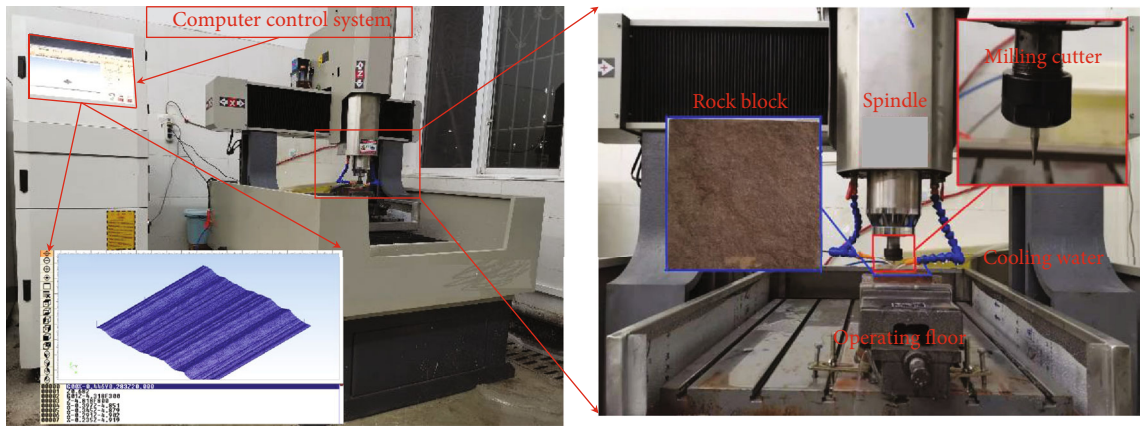

Figure 3: The 3D digital-control engraving machine.

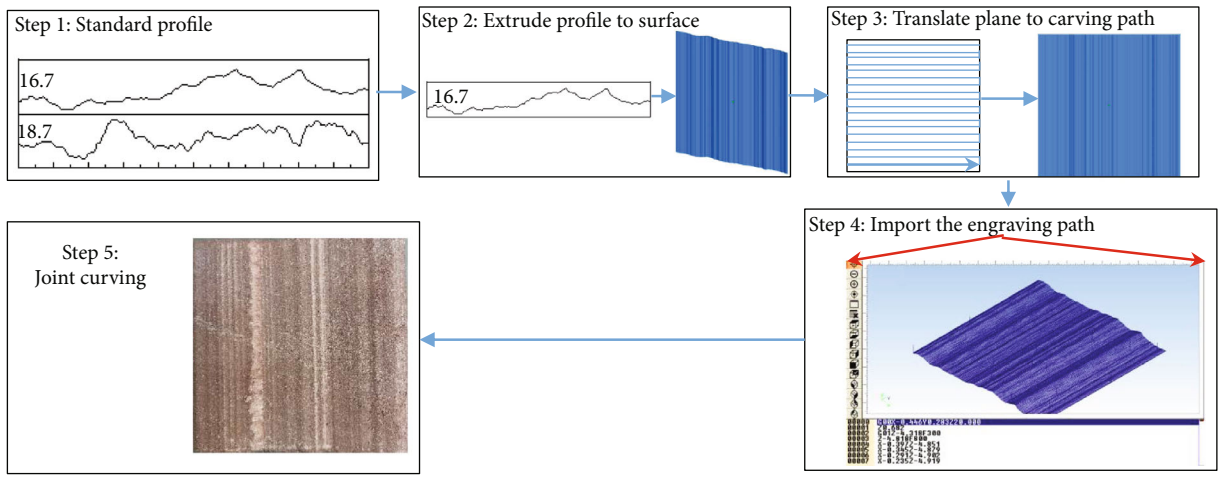

Figure 4: Schematic of the engraving process for a rock joint.

Table 1: The basic mechanical properties of the red sandstone.

σ_n (MPa)	c (MPa)	Φ (°)	E (GPa)
48	7.03	47.23	16.27

Figure 5(b), 4. In addition, a thin layer of Vaseline was applied to the interface between the rock specimen and the AE sensors for good acoustic coupling.

2.3.3. Surface Damage Characterization. A 3D light scanner (Cooper-Pro, Thunk3d, as shown in Figure 5(c)) was used to measure the surface morphology joint specimen before and after shear. The single frame accuracy, scanning range, and scanning speed of this scanner are 40 μm, 200 mm, and 0.3 s, respectively.

3. Results and Analysis

3.1. Test Result

3.1.1. Shear Behaviours. The shear stress against shear displacement for all joint specimens is shown in Figure 6.

Under low normal stress, the joint specimen which contains the unevenness shows higher peak shear strength and obvious postpeak stress drop as compared with the specimen only containing the waviness, as shown in Figure 6. The whole shear stress vs. shear displacement curve can be divided into 3 sections, climbing zone, gnawing zone, and slip zone. The whole curve only includes the climbing zone and the slip zone for the joint specimen only containing waviness. When the normal stress was 9.6 MPa, the postpeak stress drop became obvious for the joint specimen only containing waviness, and the whole curve also can be divided into 3 sections, climbing zone, gnawing zone, and slip zone, as shown in Figures 6(b) and 6(c). Under low normal stress, the difference of mechanical behaviour between the specimen containing unevenness and the specimen only containing waviness mainly appeared in the prepeak nonlinear stage and the postpeak stage.

3.1.2. Damage Characteristic. Figure 7 shows the joint surface which has a roughness coefficient equal to 9.5 after shear under different normal stress. We can find that the colour of the damaged area is lighter than the undamaged area. So the damaged area difference between the joint specimen

Table 2: The plan for the direct shear test.

Joint roughness	Asperity order	Normal stress
JRC = 9.5	Waviness+unevenness	0.6 MPa, 2.4 MPa, 4.8 MPa
	Waviness	0.6 MPa, 2.4 MPa, 4.8 MPa
JRC = 10.8	Waviness+unevenness	0.6 MPa, 2.4 MPa, 4.8 MPa, 9.6 MPa
	Waviness	0.6 MPa, 2.4 MPa, 4.8 MPa, 9.6 MPa
JRC = 12.5	Waviness+unevenness	0.6 MPa, 2.4 MPa, 4.8 MPa, 9.6 MPa
	Waviness	0.6 MPa, 2.4 MPa, 4.8 MPa, 9.6 MPa
JRC = 14.8	Waviness+unevenness	0.6 MPa, 2.4 MPa, 4.8 MPa
	Waviness	0.6 MPa, 2.4 MPa, 4.8 MPa
JRC = 16.7	Waviness+unevenness	0.6 MPa, 2.4 MPa, 4.8 MPa
	Waviness	0.6 MPa, 2.4 MPa, 4.8 MPa
JRC = 18.7	Waviness+unevenness	0.6 MPa, 2.4 MPa, 4.8 MPa
	Waviness	0.6 MPa, 2.4 MPa, 4.8 MPa

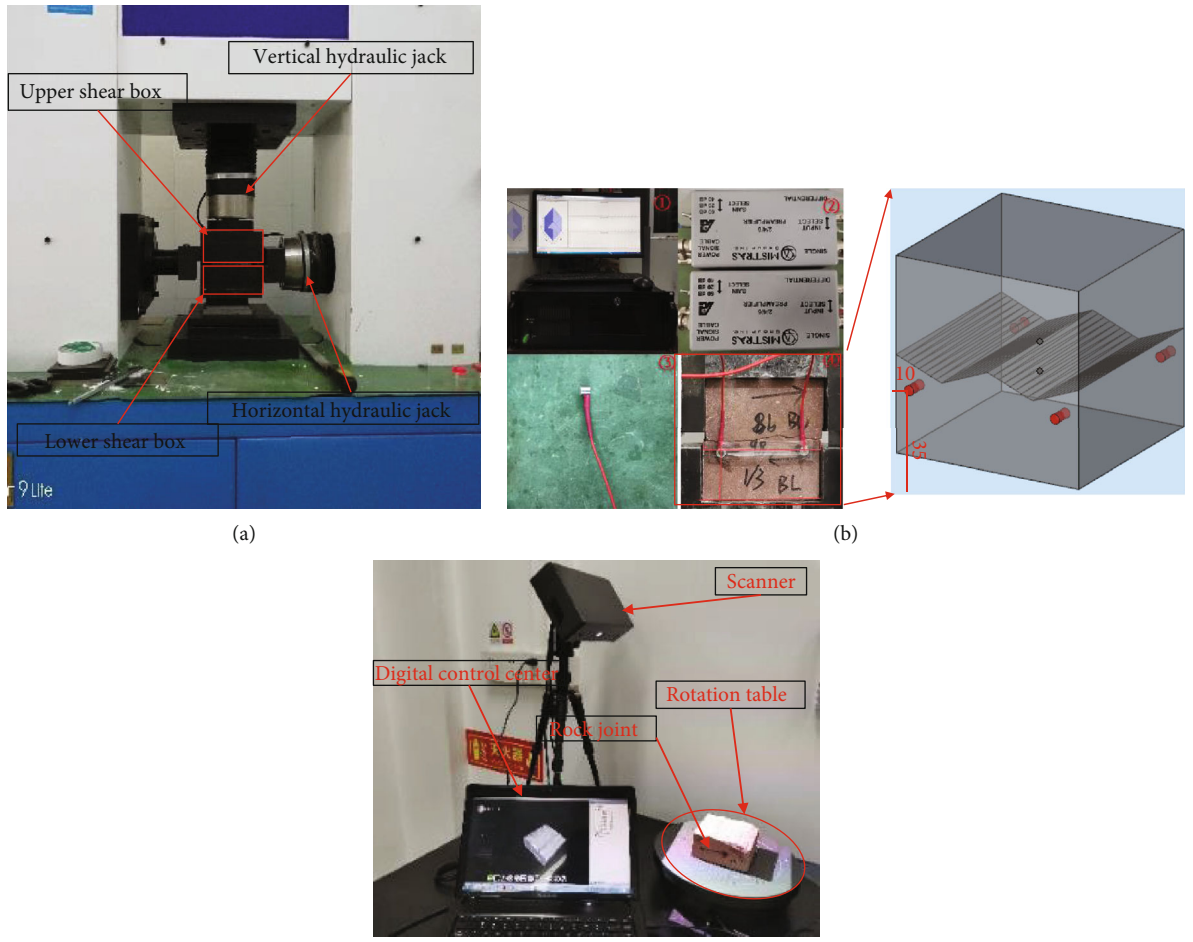

Figure 5: Test apparatuses. (a) Direct shear equipment (YZW-30A). (b) AE system (PAC Express-8). (c) 3D scan system (Cooper-Pro, Thunk3d).

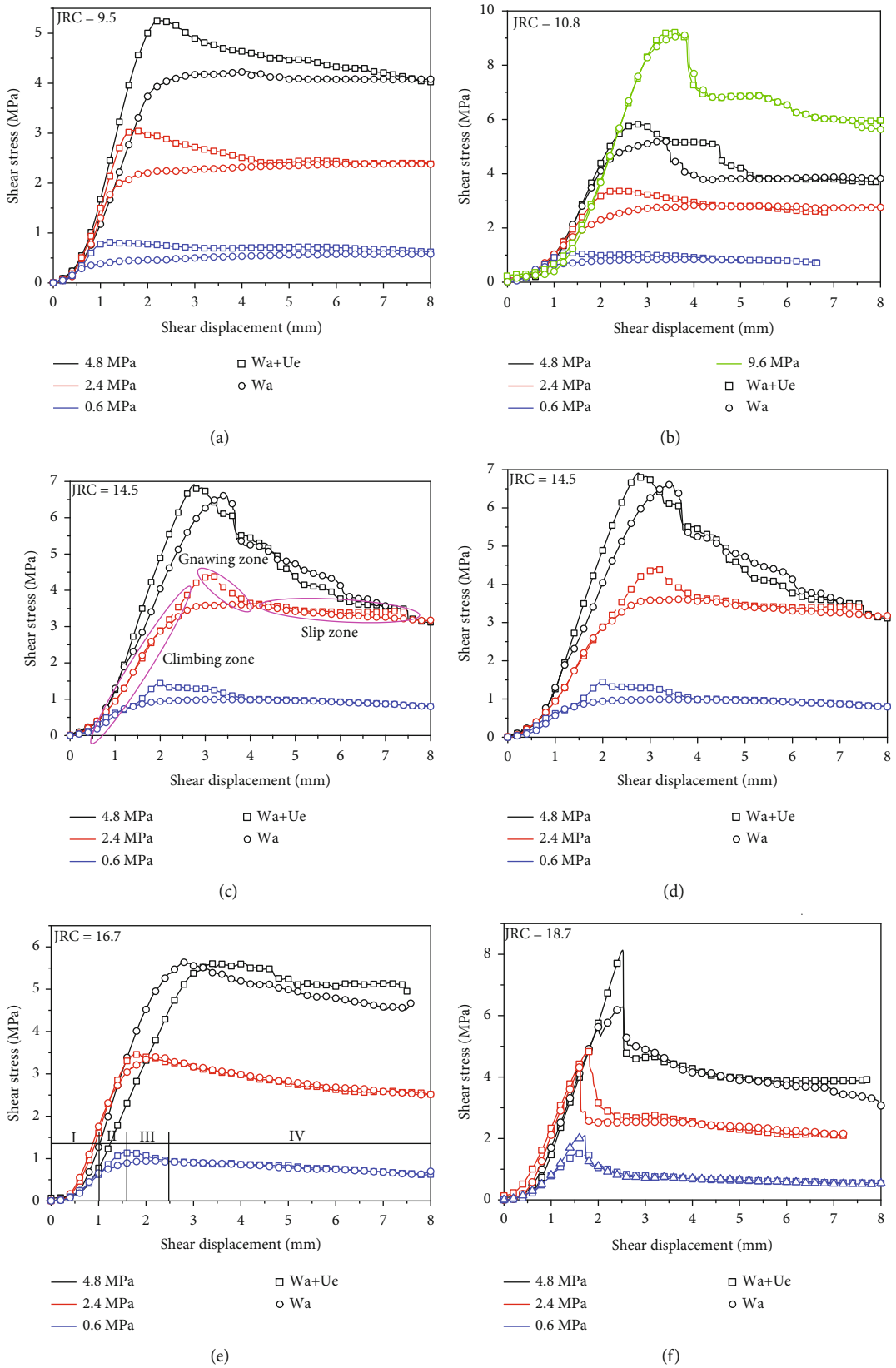

Figure 6: Shear stress-shear displacement curve under different normal stresses. Note: Wa means waviness; Ue means unevenness; I means the linear stage before peak shear stress; II means the nonlinear stage before peak shear stress; III means the nonlinear stage after the peak shear stress; IV means the residual stage.

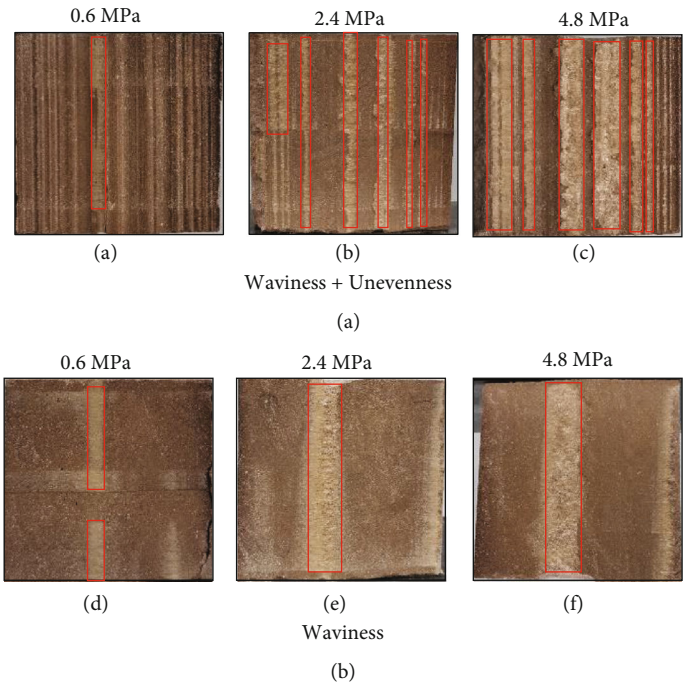

Figure 7: The joint surface after the shear test under different normal stresses.

containing unevenness and the specimen only containing waviness can be identified by visual comparison. The joint surface of the other specimen which has roughness coefficients equal to 10.8, 12.8, 14.5, 16.7, and 18.7 after shear under different normal stresses can be found in Appendix 1.

As shown in Figure 7, under low normal stress, there are only scratches that appear on the surface of the joint specimen only containing waviness, while there is obvious shear damage that appears on the surface of the joint specimen containing unevenness. When the normal stress was 9.6 MPa, the surface of the joint specimen that only contains waviness also shows obvious shear damage, as shown in Appendix 1. It can be inferred that, under low normal stress, the failure mode of the joint specimen only containing waviness is dominated by sliding wear, while the joint specimen containing unevenness is dominated by shear failure. The failure mode of the joint specimen only containing waviness changes from sliding wear to shear failure as the normal stress increases. Comparing Figures 7(a)–7(c) or Figures 7(d)–7(f), it can be seen that the damaged area increased with the increase of normal stress. This means that the damage degree increases with the increase of normal stress regardless of whether the joint specimen contains unevenness or not. Comparing Figures 7(a) and 7(d), Figures 7(b) and 7(e), or Figures 7(c) and 7(f), it can be seen that the damaged area of the joint specimen containing unevenness is larger than that of the joint specimen only containing waviness. And this difference increases with the normal stress increase.

3.1.3. Acoustic Emission (AE) Energy. The mechanical character difference is related to the damage difference between the two types of joint specimen. As shown in Figure 6, the mechanical character difference mainly appeared in the prepeak nonlinear stage and the postpeak stage. However, the damaged area and damage volume just reflect the damage degree at the end of the shear process. AE energy, a parameter which can reflect the damage generated during shear, was chosen to reflect the damage during the shear process. This section will analyse the effect of asperity order on the mechanical character of the joint specimen from the AE energy difference during the shear process.

Figure 8 shows the energy rate and the AE energy during the whole shear process. Figure 8 just shows the result of the specimen which roughness coefficient equal to 9.5; the result of the other specimen can be found in Appendix 2. It can be seen from Figure 8 that the energy rate vs. the shear displacement curve can be divided into 4 stages: nearly zero at the beginning, rising, falling rapidly, and keeping stable in the final. Correspondingly, the shear stress vs. the shear displacement can be divided into 4 stages: prepeak linear stage, prepeak nonlinear stage, postpeak stage, and residual stage. Comparing the stress stage and the energy rate stage, it can be found that different stress stages showed different energy rate characters. Prepeak linear stage: the shear stress is small, and the joint surface is still in an elastic state. Correspondingly, the energy rate is also low, which means that in this stage the joint specimen is hardly damaged. Prepeak nonlinear stage: in this stage, the shear stress increases rapidly with the increase of the shear displacement, and the specimen begins to climb along the surface. The energy will generate in the climb process, and the energy rate almost reaches the peak at the end of this stage; postpeak stage: at this stage, the shear stress decreases continually. And the decrease rate gradually decreases with the shear displacement increase. At the beginning of this stage, a large number of asperities were damaged, which produce a lot of acoustic emission events,

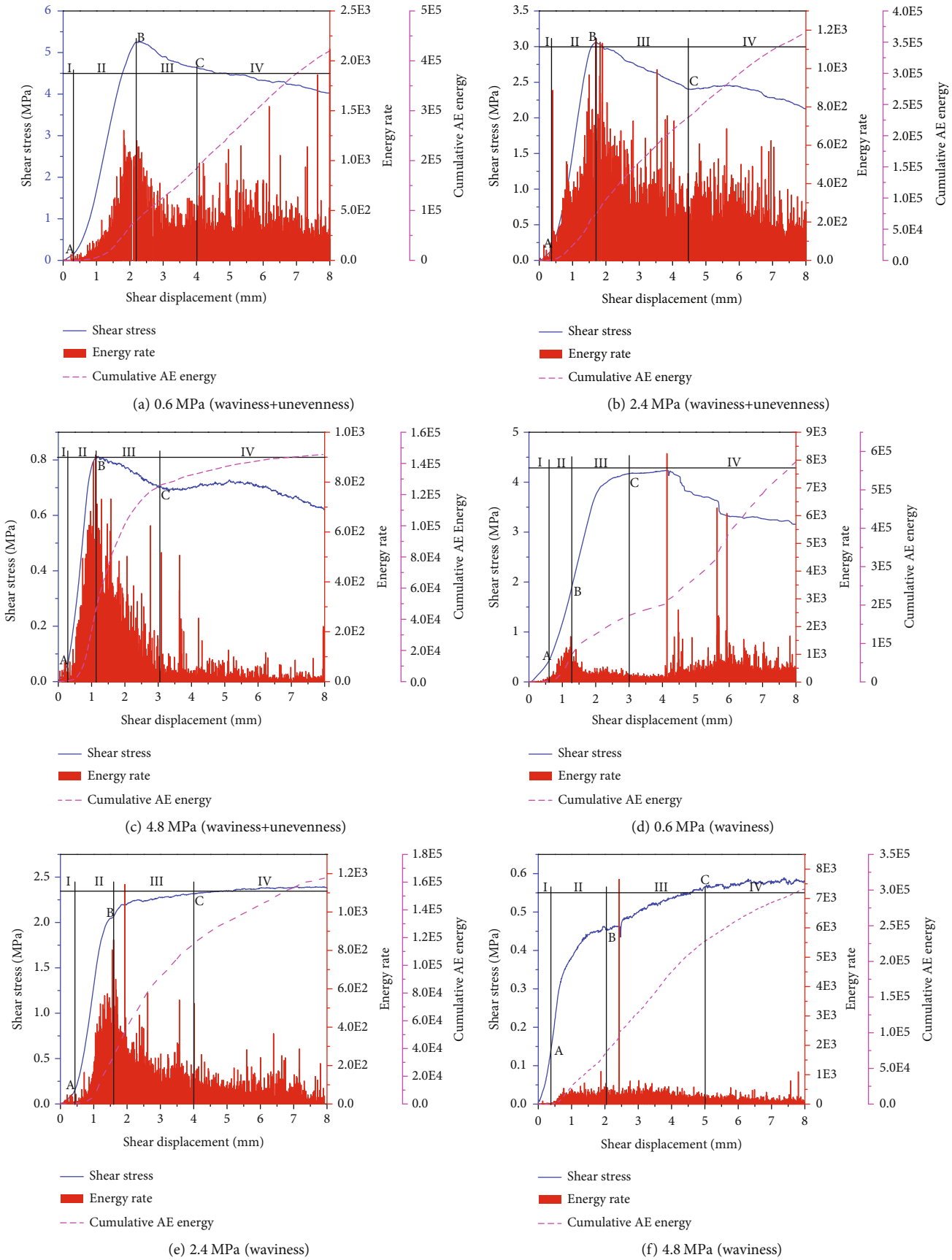

(a) 0.6 MPa (waviness+unevenness)

(b) 2.4 MPa (waviness+unevenness)

(c) 4.8 MPa (waviness+unevenness)

(d) 0.6 MPa (waviness)

(e) 2.4 MPa (waviness)

(f) 4.8 MPa (waviness)

Figure 8: Variation of AE parameters (energy rate and cumulative AE energy) with shear displacement for rock joint specimen (JRC = 9.5).

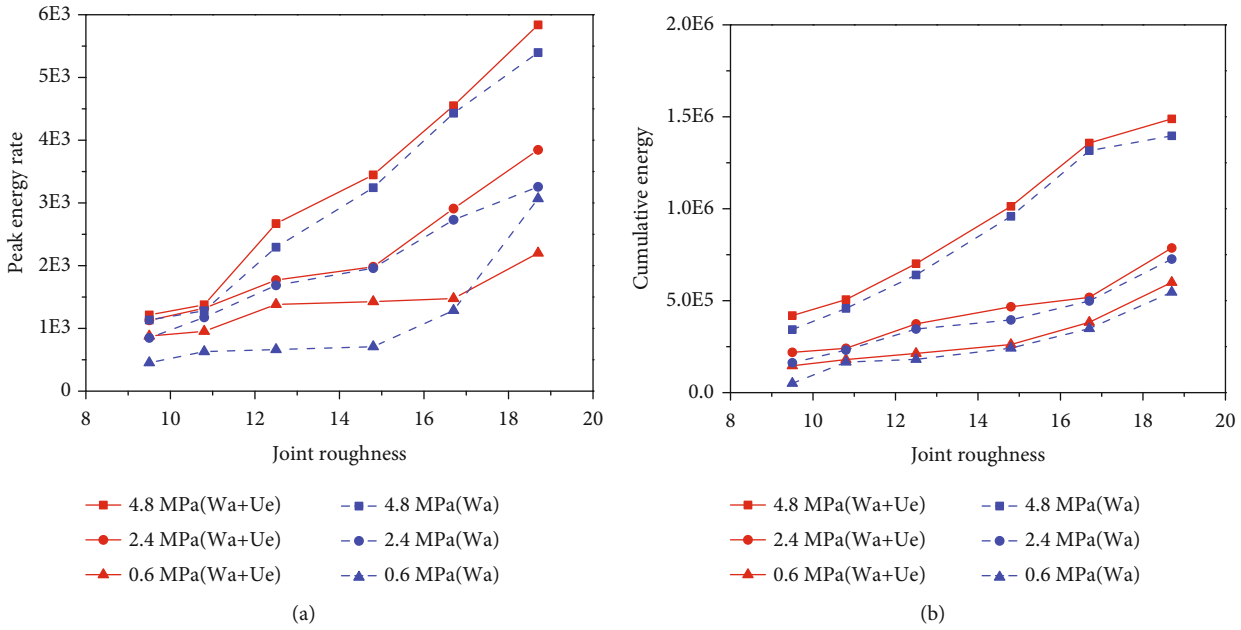

Figure 9: AE parameter for different specimens under different normal stresses: (a) peak energy rate and (b) cumulative AE energy.

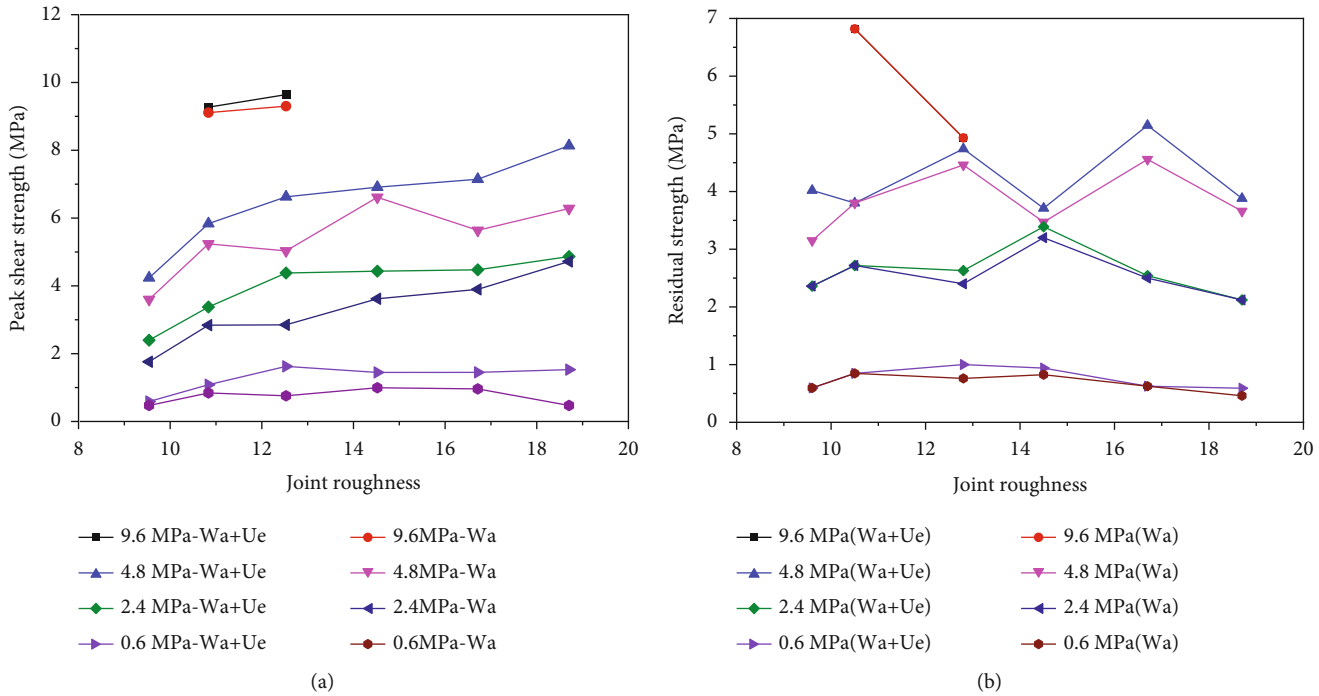

Figure 10: (a) Peak shear strength. (b) Residual shear strength. Note: Wa means waviness, and Ue means unevenness.

so the energy rate is still high. With the displacement increase, the number of the asperity which can provide resistance gradually decreased, which leads to the number of the asperity being sheared gradually decreasing. Therefore, the energy rate gradually decreased at the end of the postpeak stage. Residual stage: at this stage, the shear stress keeps stable. The asperity which can provide resistance has almost been damaged at the postpeak stage. And the contact rate is at a low level and almost unchanged. So the energy rate at this stage was basically stable at a relatively low level.

Figure 9 shows the peak energy rate and cumulative energy under different normal stresses. It can be seen that the peak energy rate and cumulative AE energy increased with the normal stress increases for the joint specimen with the same morphology, which indicates that the damage ratio increases with the normal stress. The peak energy rate and

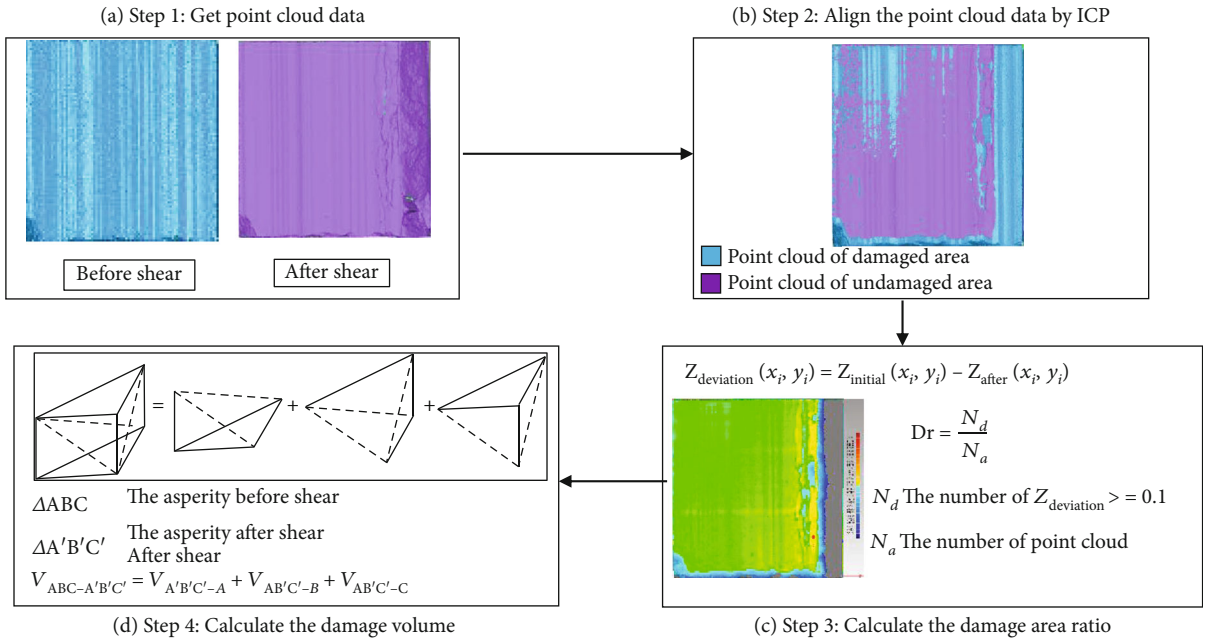

Figure 11: Schematic of calculating the damaged area ratio and damage volume.

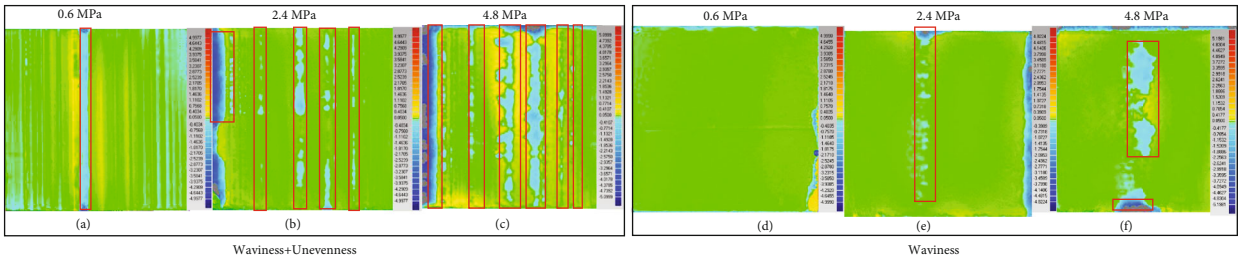

Figure 12: Surface height deviation under different normal stresses.

cumulative energy of the joint specimen containing unevenness were higher than those of the specimen only containing waviness, which means that the damage degree of the joint specimen containing unevenness was higher than that of the joint specimen only containing waviness.

3.2. Result Analysis

3.2.1. Asperity Order Effect on the Shear Strength. Figure 10 shows the peak shear strength and residual shear stress for different specimens under different normal stresses. It can be seen that (1) the peak shear strength and the residual shear stress of two types of joint specimens both increased with the surface roughness increase under the same normal stress. (2) The peak shear strength of the joint specimen containing unevenness was higher than that of the specimen only containing waviness. This difference in peak shear strength increased as the normal stress increased under low normal stress, which means that unevenness plays a control role in the mechanical behaviour under the low normal stress. When the normal stress is large, the difference in peak shear strength is almost zero, which means that waviness plays a control role in the mechanical behaviour under large normal stress.

The peak shear strength of the joint specimen was related to the average inclination angle of the surface [10, 44, 45]. According to the description by the ISRM, waviness is defined by the dominating and large-scale overall wavy surface undulation to reflect the macroscopic fluctuations of the surface morphology, and unevenness is defined by the generally randomly distributed small-scale unevenness. Comparing the waviness and the unevenness, the unevenness's inclination angle is larger than the waviness's. So the average inclination angle of the joint specimen containing unevenness is greater than that of the specimen only containing waviness. Therefore, the peak shear strength of the joint specimen containing unevenness is greater than that of the sample only containing waviness. At the residual stage, almost all the unevenness was cut off and the contact ratio in the residual stage was reduced due to the dilatancy; this makes the surface morphology of the joint specimen containing unevenness be similar to that of the joint sample only containing waviness.

3.2.2. Asperity Order Effect on the Damage Ratio. The mechanical character difference is related to the damage difference between the two types of the joint specimen. In order to characterize the damage difference between the two types

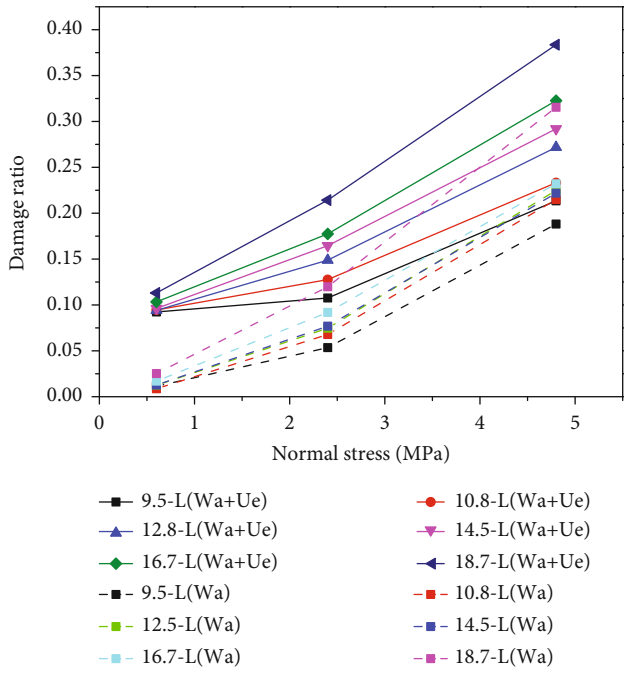

Figure 13: The damaged area ratio of the joint specimen with different asperity order under different normal stresses.

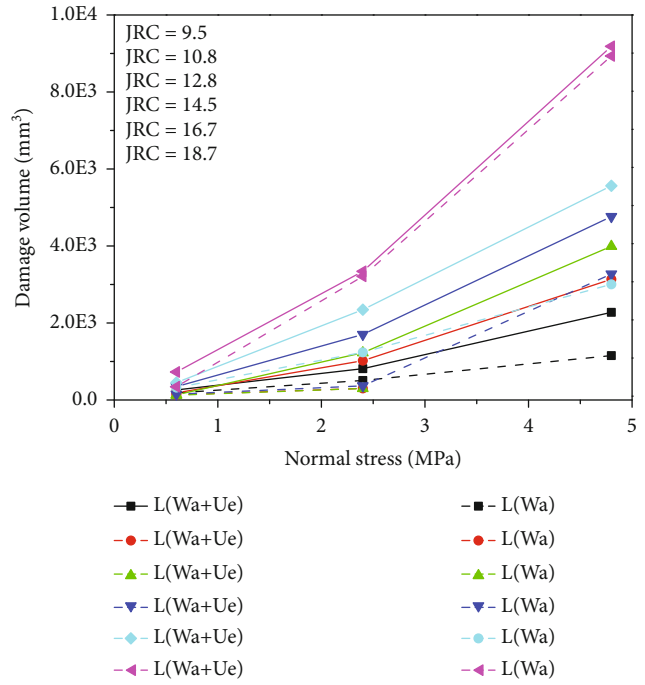

Figure 14: The damage volume of rock joint with different asperity order under different normal stresses.

of the joint specimen, the damaged area and damage volume were calculated in this section. The morphology of the damaged area is complex, so it is not easy to quantify the damaged area accurately through two-dimensional (2D) image analyses. In this study, a new method to quantify the joint damage ratio and damage volume was proposed [46]. The realization of this method can be divided into three steps [47]: (1) get the point cloud data of the joint surface before and after shear, (2) align the point cloud data of the joint surface before and after shear by the ICP algorithm, and (3) calculate the height deviation and damage volume by the Matlab code; the code can be found in Appendix 3. And the steps are shown in Figure 11.

Figure 12 shows the height deviation of the joint specimen which roughness equal to 9.5. The result of the other specimens can be found in Appendix 1.

Comparing Figures 12 and 7, it can be seen that the damaged area consists of the area in which the height deviation is larger. Generally, 5~6 measurements were needed to obtain the whole morphology. And errors can also occur during the alignment process. The combined three-dimensional error is difficult to be quantified. According to the accuracy of the scanning equipment and the test process, the test accuracy is set to 0.1 mm, which is consistent with Indraratna et al. [48] and Gui et al.'s [49] study. Based on this rule, the damaged area ratio was calculated.

Figure 13 shows the damaged area ratio of the joint specimen with different asperity order under different normal stress. It can be seen from Figure 13 that the damaged area ratio increased with the increase of the normal stress. The damaged area and the growth rate of the damaged area ratio of the joint specimen containing unevenness were greater than those of the joint specimen only containing waviness, under the condition of the same initial morphology. Thus, it can be concluded that, compared with the waviness, the unevenness is more prone to damage under low normal stress, resulting in a higher damaged area.

The damaged area ratio just reflects the proportion of the damaged area. It is difficult to reflect the damage degree accurately. The damage volume can reflect the damage degree in 3 dimensional, so it can reflect the damage degree more accurately compared with the damaged area. The calculation method of joint specimen damage volume mainly includes the following steps: (1) align the point cloud data before and after cutting by ICP iteration method and (2) triangulate the point data by the Delaunay triangulation method. In this paper, the joint surface asperities were discretized into triangles. $\triangle ABC$ represents the asperity before shearing, and $\triangle A'B'C'$ represents the asperity after shearing, as shown in Figure 11(d). The damage volume of the joint specimen is the sum of these volumetric elements $V_{ABC-A'B'C'}$. Among them, $V_{ABC-A'B'C'}$ is calculated by Equations (1) and (2). The damage volume of the joint specimen is calculated by Equation (3).

$$V_{ABC-A'B'C'} = V_{A'B'C'-A} + V_{AB'C'-B} + V_{ABC-C'}, \tag{1}$$

$$V_{ABC-A'B'C'} = \frac{1}{6} * \begin{vmatrix} 1 & 1 & 1 & 1 \\ x_a & x_b & x_c & x_d \\ y_a & y_b & y_c & y_d \\ z_a & z_b & z_c & z_d \end{vmatrix}, \tag{2}$$

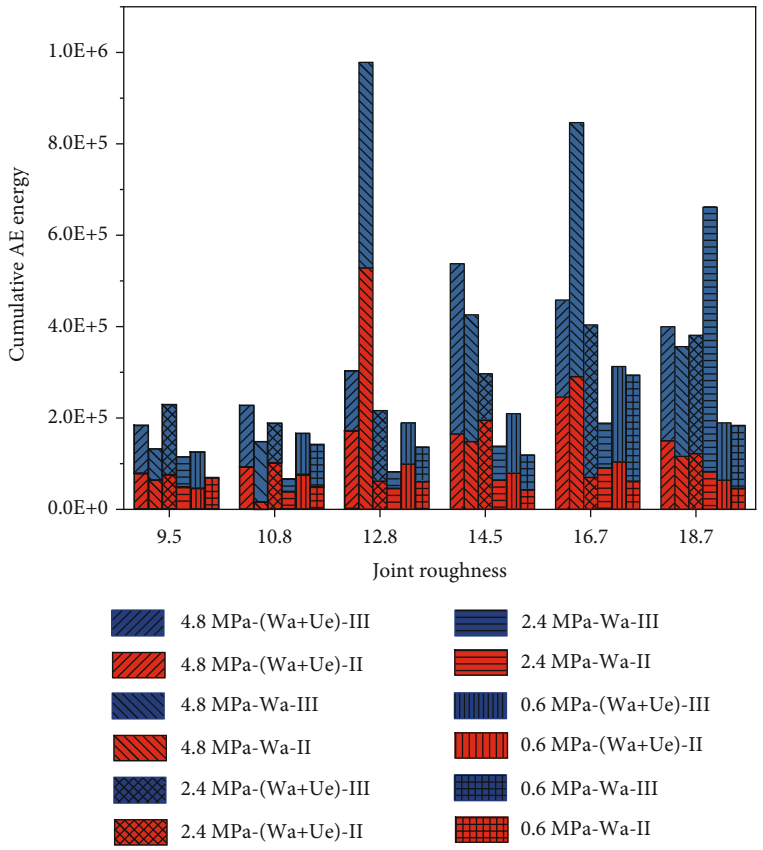

Figure 15: The cumulative AE energy in the second and third stages.

$$V = \sum V_{\mathrm{ABC-A'B'C'}}. \tag{3}$$

Based on the above method, the damage volume of the joint specimen can be calculated, and the calculation result is shown in Figure 14.

It can be seen that the damage volume increased with the increase of the normal stress; the damage volume of the specimen containing unevenness is larger than that of the joint specimen only containing waviness, and this difference increases with the normal stress increase. As shown in Figure 3, the average inclination angle of the specimen containing unevenness was higher than that of the specimen only containing waviness. Only the asperity's apparent dip angle is greater than a certain value; the asperity will be damaged during shearing [50]. Thus, compared with the waviness, the unevenness is more prone to be damaged. With the increase of the normal stress, more and more unevenness undergo shear failure, while the joint specimen containing waviness only undergoes slip wear failure, leading to a bigger difference in damage volume.

3.2.3. Asperity Order Effect on the Damage Energy. In fact, the difference in the shear mechanical properties of these two types of joint specimens mainly appeared in the prepeak nonlinear stage and the postpeak stage (the second and third stages), as shown in Figure 6. Therefore, further research was carried out on the acoustic emission energy of these two stages. The cumulative energy of acoustic emission in the second and third stages is shown in Figure 15.

It can be seen that under the condition of the same normal stress, the damage ratio and the cumulative energy generated in the second and third stages increased with the increase of the joint roughness coefficient. The rougher the joint surface, the less probability of shear failure occurring, the higher the energy accumulated before failure, and the greater the energy released when the joint surface fails. Under the same conditions, the cumulative energy produced in the third stage was higher than that in the second stage. In the prepeak nonlinear stage, the acoustic emission energy released by the joint specimen containing unevenness was higher than that of the joint specimen only containing waviness. In the postpeak stage, the unevenness on the surface of the joint specimen was sheared, which results in the energy released in the third stage being higher than that in the second stage.

Acoustic emission b value [51] is used as a characterization of the proportion of large-amplitude acoustic emission events and small-amplitude acoustic emission events in the entire section, which can be used to represent the damage degree of the joint specimen. The expression is shown in

$$\lg N = a - b\frac{A_{\mathrm{dB}}}{20}, \tag{4}$$

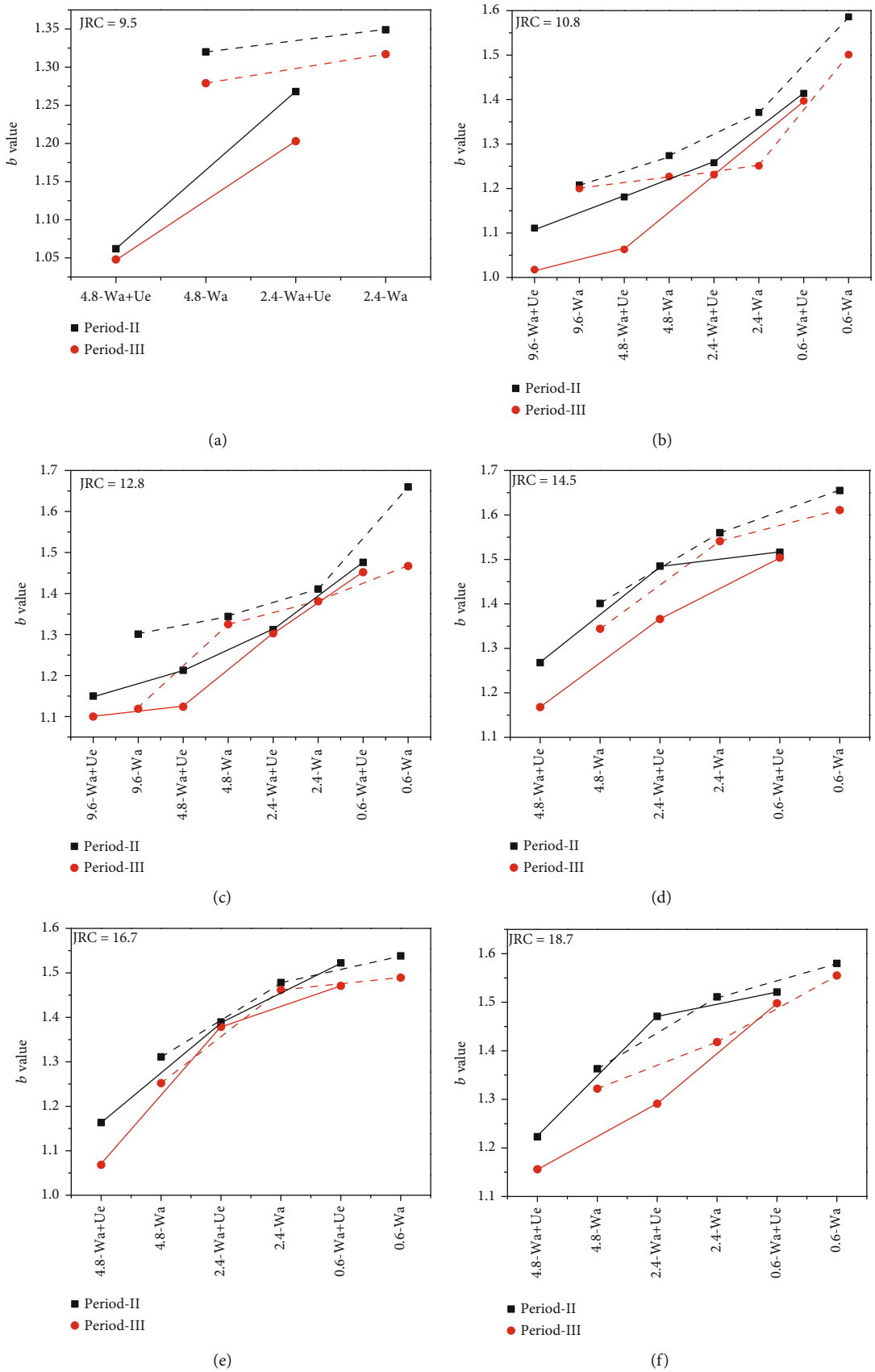

Figure 16: The AE-*b* value. (a) JRC = 9.5. (b) JRC = 10.8. (c) JRC = 12.8. (d) JRC = 14.5. (e) JRC = 16.7. (f) JRC = 18.7.

where A_{dB} is the peak amplitude of the AE hits in dB, $A_{dB} = 10 \log A_{max}^2 = 20 \log A_{max}$, A_{max} is the peak amplitude of the AE events in μv, and N is the number of acoustic emission events whose amplitude is greater than or equal to A_{dB}.

The b value is used to analyse the damage that occurs in the second and third shear stages of the joint specimen, and the analysis result is shown in Figure 16.

It can be seen from Figure 16, under the condition of the same morphology, the AE-b value of joint specimen at the second period was greater than that at the third period, which means that the damage degree at the second period was less than that at the third period. For the same shearing period, as the normal stress increased, the value of b gradually decreased, which means that the degree of joint damage increased with the increase of normal stress; besides, the b value of the joint specimen containing the unevenness was smaller than that of the specimen only containing the waviness, indicating a greater damage degree.

4. Conclusions

In this research, the experimental investigation on the damage of the joint specimen with different asperity order was carried out to better understand the effect of asperity order on the mechanical properties. The standard roughness profile was used as the initial surface morphology, and the method combining the EEMD and cut-off level criterion was used to decompose the standard roughness profile into waviness and unevenness; two types of joint specimens, respectively, containing unevenness and only containing waviness were prepared using 3D engraving technologies and were subjected to shear tests under different normal stresses. The following conclusions can be drawn.

Under low normal stress, unevenness plays a key role in the failure mode. The joint specimen containing unevenness mainly suffered from shear failure, and the shear stress-shear displacement curve can be divided into 3 sections: climbing zone, gnaw zone, and slip zone; while the joint specimen only containing waviness suffered from sliding wear damage, and the shear stress-shear displacement curve can be divided into 2 sections: climbing zone and slip zone. When the normal stress is larger, the failure model of the joint specimen only containing waviness changes from sliding wear to shear failure.

Under low normal stress, unevenness plays a key role in the damaged area and damage volume. The damaged area, volume, and AE energy of the joint specimen containing the unevenness are larger than the specimen containing only the waviness. And the difference between them increases with the increase of normal stress.

Under low normal stress, the mechanical character difference between the joint specimen containing unevenness and only containing waviness mainly existed in the prepeak nonlinear stage and the postpeak stage. The AE energy of the joint specimen containing the unevenness is larger than that of the joint specimen only containing waviness.

The AE-b value can be used to characterize the damage degree. The smaller the b value, the greater the damage degree. The AE-b value of the joint specimen containing the unevenness is smaller than that of the specimen only containing the waviness; the AE-b value of the joint specimen at the postpeak stage is smaller than that of the joint specimen at the prepeak nonlinear stage.

Data Availability

All data and code generated or used during the study appear in the submitted article.

Conflicts of Interest

The authors declare that there is no conflict of interest regarding the publication of this paper.

Acknowledgments

This work was supported by (1) the scientific research project funded by the Department of Education of Hubei Province (Grant No. Q20201109), (2) Natural Science Foundation of Hubei Province (Grant No. 2020CFB123), and (3) Hubei Province Key Field R&D Program Project (Grant No. 2020BCA082).

Supplementary Materials

Appendix 1: damaged area. Appendix 2: AE energy. Appendix 3: Matlab code for calculating the damage volume of the joint surface after shear test. *(Supplementary Materials)*

References

[1] S. Huang, Z. Lu, Z. Ye, and Z. Xin, "An elastoplastic model of frost deformation for the porous rock under freeze-thaw," *Engineering Geology*, vol. 278, article 105820, 2020.

[2] C. Wang, Y. Jiang, R. Liu, C. Wang, Z. Zhang, and S. Sugimoto, "Experimental study of the nonlinear flow characteristics of fluid in 3D rough-walled fractures during shear process," *Rock Mechanics and Rock Engineering*, vol. 53, no. 6, pp. 2581–2604, 2020.

[3] R. Liu, N. Huang, Y. Jiang, H. Jing, and L. Yu, "A numerical study of shear-induced evolutions of geometric and hydraulic properties of self-affine rough-walled rock fractures," *International Journal of Rock Mechanics and Mining Sciences*, vol. 127, article 104211, 2020.

[4] G. Han, H. Jing, Y. Jiang, R. Liu, and J. Wu, "Effect of cyclic loading on the shear behaviours of both unfilled and infilled rough rock joints under constant normal stiffness conditions," *Rock Mechanics and Rock Engineering*, vol. 53, no. 1, pp. 31–57, 2020.

[5] Z. Tao, Y. Shu, X. Yang, Y. Peng, Q. Chen, and H. Zhang, "Physical model test study on shear strength characteristics of slope sliding surface in Nanfen open-pit mine," *International Journal of Mining Science and Technology*, vol. 30, no. 3, pp. 421–429, 2020.

[6] Z. C. Tang, Z. F. Zhang, and Y. Y. Jiao, "Three-dimensional criterion for predicting peak shear strength of matched discontinuities with different joint wall strengths," *Rock Mechanics and Rock Engineering*, vol. 54, no. 6, pp. 3291–3307, 2021.

[7] Y. Zhao, C. Zhang, Y. Wang, and H. Lin, "Shear-related roughness classification and strength model of natural rock joint based on fuzzy comprehensive evaluation," *International Journal of Rock Mechanics and Mining Sciences*, vol. 137, article 104550, 2021.

[8] L. Ban, W. Du, T. Jin, C. Qi, and X. Li, "A roughness parameter considering joint material properties and peak shear strength model for rock joints," *International Journal of Mining Science and Technology*, vol. 31, no. 3, pp. 413–420, 2021.

[9] ISRM, "International Society for Rock Mechanics Commission on Standardization of Laboratory and Field Tests: suggested methods for the quantitative description of discontinuities in rock masses," *International Journal of Rock Mechanics and Mining Sciences and Geomechanics Abstracts*, vol. 6, no. 15, pp. 319–368, 1978.

[10] F. D. Patton, "Multiple models of shear failure in rock," in *Proceedings of the First Congress of ISRM*, Lisbon, 1966.

[11] N. Barton, "Review of a new shear-strength criterion for rock joints," *Engineering Geology*, vol. 7, no. 4, pp. 287–332, 1973.

[12] L. Jing, E. Nordlund, and O. Stephansson, "An experimental study on the anisotropy and stress-dependency of the strength and deformability of rock joints," *International Journal of Rock Mechanics and Mining Sciences & Geomechanics Abstracts*, vol. 29, no. 6, pp. 535–542, 1992.

[13] D. D. Kana, D. J. Fox, and S. M. Hsiung, "Interlock/friction model for dynamic shear response in natural jointed rock," *International Journal of Rock Mechanics and Mining Sciences & Geomechanics Abstracts*, vol. 33, no. 4, pp. 371–386, 1996.

[14] H. S. Lee, Y. J. Park, T. F. Cho, and K. H. You, "Influence of asperity degradation on the mechanical behavior of rough rock joints under cyclic shear loading," *International Journal of Rock Mechanics and Mining Sciences*, vol. 38, no. 7, pp. 967–980, 2001.

[15] X. M. Zhu, H. B. Li, and B. Liu, "Experimental study of shear strength of joints with first-order and second-order asperities," *Chinese Journal of Rock Mechanics and Engineering*, vol. 30, no. 9, pp. 1810–1818, 2011.

[16] Z. Nie, X. Wang, D. L. Huang, and L. H. Zhao, "Fourier-shape-based reconstruction of rock joint profile with realistic unevenness and waviness features," *Journal of Central South University*, vol. 26, no. 11, pp. 3103–3113, 2019.

[17] Z. Y. Yang, C. C. Di, and K. C. Yen, "The effect of asperity order on the roughness of rock joints," *International Journal of Rock Mechanics and Mining Sciences*, vol. 38, no. 5, pp. 745–752, 2001.

[18] Z. Y. Yang, A. Taghichian, and W. C. Li, "Effect of asperity order on the shear response of three-dimensional joints by focusing on damage area," *International Journal of Rock Mechanics and Mining Sciences*, vol. 47, no. 6, pp. 1012–1026, 2010.

[19] Z. Jiang, P. Cao, X. Fan, Y. He, and W. Fan, "Evolution of joint morphology subjected to shear loads based on Gaussion filtering method," *Journal of Central South University (Science and Technology)*, vol. 45, no. 6, pp. 1975–1982, 2014.

[20] X. G. Liu, W. C. Zhu, Q. L. Yu, S. J. Chen, and R. F. Li, "Estimation of the joint roughness coefficient of rock joints by consideration of two-order asperity and its application in double-joint shear tests," *Engineering Geology*, vol. 220, pp. 243–255, 2017.

[21] X. Liu, W. Zhu, Y. Liu, Q. Yu, and K. Guan, "Characterization of rock joint roughness from the classified and weighted uphill projection parameters," *International Journal of Geomechanics*, vol. 21, no. 5, article 04021052, 2021.

[22] M. Sharifzadeh, S. A. Mehri, and Y. Mirzaeian, "Multi-scale joints roughness characterization using wavelet and shear modeling," in *ISRM Regional Symposium-7th Asian Rock Mechanics Symposium*, Seoul, Korea, October 2012.

[23] L. C. Zou, L. R. Jing, and V. Cvetkovic, "Roughness decomposition and nonlinear fluid flow in a single rock fracture," *International Journal of Rock Mechanics & Mining Sciences*, vol. 75, pp. 102–118, 2015.

[24] M. Wang, Y. F. Chen, G. W. Ma, J. Q. Zhou, and C. B. Zhou, "Influence of surface roughness on nonlinear flow behaviors in 3D self-affine rough fractures: lattice Boltzmann simulations," *Advances in Water Resources*, vol. 96, pp. 373–388, 2016.

[25] Y. Gui, C. Xia, W. Ding, X. Qian, and S. Du, "Modelling shear behaviour of joint based on joint surface degradation during shearing," *Rock Mechanics and Rock Engineering*, vol. 52, no. 1, pp. 107–131, 2019.

[26] Y. Li, S. Sun, and C. Tang, "Analytical prediction of the shear behaviour of rock joints with quantified waviness and unevenness through wavelet analysis," *Rock Mechanics and Rock Engineering*, vol. 52, no. 10, pp. 3645–3657, 2019.

[27] E. S. Hong, I. M. Lee, G. C. Cho, and S. W. Lee, "New approach to quantifying rock joint roughness based on roughness mobilization characteristics," *KSCE Journal of Civil Engineering*, vol. 18, no. 4, pp. 984–991, 2014.

[28] E. S. Hong, T. H. Kwon, K. I. Song, and G. C. Cho, "Observation of the degradation characteristics and scale of unevenness on three-dimensional artificial rock joint surfaces subjected to shear," *Rock Mechanics and Rock Engineering*, vol. 49, no. 1, pp. 3–17, 2016.

[29] F. Meng, L. N. Y. Wong, H. Zhou, Z. Wang, and L. Zhang, "Asperity degradation characteristics of soft rock-like fractures under shearing based on acoustic emission monitoring," *Engineering Geology*, vol. 266, article 105392, 2020.

[30] Y. Zong, L. Han, Q. Meng, and Y. Wang, "Strength properties and evolution laws of cracked sandstone samples in re-loading tests," *International Journal of Mining Science and Technology*, vol. 30, no. 2, pp. 251–258, 2020.

[31] H. Ran, Y. Guo, G. Feng, T. Qi, and X. Du, "Creep properties and resistivity-ultrasonic-AE responses of cemented gangue backfill column under high-stress area," *International Journal of Mining Science and Technology*, vol. 31, no. 3, pp. 401–412, 2021.

[32] X. P. Zhou and Y. X. Zhang, "Study on the property of acoustic emission straight shearing test of rock joint in Dachang Tongkeng mine," *Chinese Journal of Rock Mechanics and Engineering*, vol. 21, no. 5, pp. 724–727, 2002.

[33] Z. A. Moradian, G. Ballivy, P. Rivard, C. Gravel, and B. Rousseau, "Evaluating damage during shear tests of rock joints using acoustic emissions," *International Journal of Rock Mechanics & Mining Sciences*, vol. 47, no. 4, pp. 590–598, 2010.

[34] F. Z. Meng, H. Zhou, Z. Q. Wang et al., "Characteristics of asperity damage and its influence on the shear behavior of granite joints," *Rock Mechanics and Rock Engineering*, vol. 51, no. 2, pp. 429–449, 2018.

[35] Y. Chen and Z. Zhao, "Correlation between shear induced asperity degradation and acoustic emission energy in single granite fracture," *Engineering Fracture Mechanics*, vol. 235, article 107184, 2020.

[36] R. Yong, J. Ye, Q. F. Liang, M. Huang, and S. G. Du, "Estimation of the joint roughness coefficient (JRC) of rock joints by vector similarity measures," *Bulletin of Engineering Geology & the Environment*, vol. 47, no. 10, pp. 1–15, 2018.

[37] C. Pickering and A. Aydin, "Modeling roughness of rock discontinuity surfaces: a signal analysis approach," *Rock Mechanics and Rock Engineering*, vol. 49, no. 7, pp. 2959–2965, 2016.

[38] Z. Wu and N. E. Huang, "Ensemble empirical mode decomposition: a noise-assisted data analysis method," *Advances in Adaptive Data Analysis*, vol. 1, no. 1, pp. 1–41, 2009.

[39] N. E. Huang, Z. Shen, S. R. Long et al., "The empirical mode decomposition and the Hilbert spectrum for nonlinear and non-stationary time series analysis," *Proceedings of the Royal Society*, vol. 454, no. 1971, pp. 903–995, 1998.

[40] C. C. Xia, "The waviness characteristics and mechanical effects of topography of rock structure faces," *Journal of Tongji University*, vol. 21, no. 3, pp. 371–377, 1993.

[41] J. Lu, "Polarization spectrum sensing exploiting eigenvalue based goodness-of-fit detection," in *2020 IEEE 5th International Conference on Signal and Image Processing (ICSIP)*, pp. 955–959, Nanjing, China, October 2020.

[42] Q. Jiang, B. Yang, F. Yan, C. Liu, Y. Shi, and L. Li, "New method for characterizing the shear damage of natural rock joint based on 3D engraving and 3D scanning," *International Journal of Geomechanics*, vol. 20, no. 2, pp. 1–15, 2020.

[43] H. Zhou, G. T. Cheng, Y. Zhu et al., "Study on anisotropy of shear characteristics of rock joint based on 3D carving technique," *Rock and Soil Mechanics*, vol. 40, no. 1, pp. 118–126, 2019.

[44] Q. Z. Zhang, M. R. Shen, and W. Q. Ding, "Study on the mechanical properties of rock mass discontinuity under shear condition," *Hydrogeology & Engineering Geology*, vol. 39, no. 2, pp. 42–47, 2012.

[45] P. H. S. W. Kulatilake, G. Shou, T. H. Huang, and R. M. Morgan, "New peak shear strength criteria for anisotropic rock joints," *International Journal of Rock Mechanics and Mining Sciences and Geomechanics Absatracts*, vol. 32, no. 7, pp. 673–697, 1995.

[46] Q. Jiang, L. B. Song, F. Yan, C. Liu, B. Yang, and J. Xiong, "Experimental investigation of anisotropic wear damage for natural joints under direct shearing test," *International Journal of Geomechanics*, vol. 20, no. 4, article 04020015, 2020.

[47] S. K. Singh, S. Raval, and B. P. Banerjee, "A robust approach to identify roof bolts in 3D point cloud data captured from a mobile laser scanner," *International Journal of Mining Science and Technology*, vol. 31, no. 2, pp. 303–312, 2021.

[48] B. Indraratna, S. Thirukumaran, E. T. Brown, W. Premadasa, and W. Gale, "A technique for three-dimensional characterisation of asperity deformation on the surface of sheared rock joints," *International Journal of Rock Mechanics and Mining Sciences*, vol. 70, pp. 483–495, 2014.

[49] Y. Gui, C. Xia, W. Ding, X. Qian, and S. Du, "A new method for 3D modeling of joint surface degradation and void space evolution under normal and shear loads," *Rock Mechanics & Rock Engineering*, vol. 50, no. 10, pp. 2827–2836, 2017.

[50] G. Grasselli, J. Wirth, and P. Egger, "Quantitative three-dimensional description of a rough surface and parameter evolution with shearing," *International Journal of Rock Mechanics and Mining Sciences*, vol. 39, no. 6, pp. 789–800, 2002.

[51] X. Lei, "Evolution of *b*-value and fractal dimension of acoustic emission events during shear rupture of an immature fault in granite," *Applied Sciences*, vol. 9, no. 12, article 2498, 2019.